

# Characterization, Modeling, and Performance of Geomaterials



*Edited  
by*

Xiong Zhang, Ph.D  
Xiong Yu, Ph.D, P.E.  
Hongyuan Fu, Ph.D  
Jie Zhang, Ph.D, P.E.

**ASCE**



GEOTECHNICAL SPECIAL PUBLICATION NO. 189

# CHARACTERIZATION, MODELING, AND PERFORMANCE OF GEOMATERIALS

---

SELECTED PAPERS FROM THE 2009 GEOHUNAN INTERNATIONAL CONFERENCE

---

August 3–6, 2009  
Changsha, Hunan, China

HOSTED BY  
Changsha University of Science and Technology, China

CO-SPONSORED BY  
ASCE Geo-Institute, USA  
Asphalt Institute, USA  
Central South University, China  
Chinese Society of Pavement Engineering, Taiwan  
Chongqing Jiaotong University, China  
Deep Foundation Institute, USA  
Federal Highway Administration, USA  
Hunan University, China  
International Society for Asphalt Pavements, USA  
Jiangsu Transportation Research Institute, China  
Korea Institute of Construction Technology, Korea  
Korean Society of Road Engineers, Korea  
Texas Department of Transportation, USA  
Texas Transportation Institute, USA  
Transportation Research Board (TRB), USA

EDITED BY  
Xiong Zhang, Ph.D  
Xiong Yu, Ph.D, P.E.  
Hongyuan Fu, Ph.D  
Jie Zhang, Ph.D, P.E.



Published by the American Society of Civil Engineers



Library of Congress Cataloging-in-Publication Data

Characterization, modeling, and performance of geomaterials : selected papers from the 2009 GeoHunan International Conference, August 3-6, 2009, Changsha, Hunan, China / hosted by Changsha University of Science and Technology, China ; co-sponsored by ASCE Geo-Institute, USA ... [et al.] ; edited by Xiong Zhang ... [et al.].

p. cm. -- (Geotechnical special publication ; no. 189)

Includes bibliographical references and indexes.

ISBN 978-0-7844-1041-7

1. Road materials--Congresses. 2. Soil mechanics--Congresses. 3. Roads--Subgrades--Congresses. 4. Geosynthetics--Congresses. I. Zhang, Xiong, 1971- II. Changsha li gong da xue. III. American Society of Civil Engineers. Geo-Institute, IV. GeoHunan International Conference on Challenges and Recent Advances in Pavement Technologies and Transportation Geotechnics (2009 : Changsha, Hunan Sheng, China)

TE200.C45 2009

624.1'5136--dc22

2009022609

American Society of Civil Engineers  
1801 Alexander Bell Drive  
Reston, Virginia, 20191-4400

[www.pubs.asce.org](http://www.pubs.asce.org)

Any statements expressed in these materials are those of the individual authors and do not necessarily represent the views of ASCE, which takes no responsibility for any statement made herein. No reference made in this publication to any specific method, product, process, or service constitutes or implies an endorsement, recommendation, or warranty thereof by ASCE. The materials are for general information only and do not represent a standard of ASCE, nor are they intended as a reference in purchase specifications, contracts, regulations, statutes, or any other legal document. ASCE makes no representation or warranty of any kind, whether express or implied, concerning the accuracy, completeness, suitability, or utility of any information, apparatus, product, or process discussed in this publication, and assumes no liability therefore. This information should not be used without first securing competent advice with respect to its suitability for any general or specific application. Anyone utilizing this information assumes all liability arising from such use, including but not limited to infringement of any patent or patents.

ASCE and American Society of Civil Engineers—Registered in U.S. Patent and Trademark Office.

*Photocopies and reprints.*

You can obtain instant permission to photocopy ASCE publications by using ASCE's online permission service (<http://pubs.asce.org/permissions/requests/>). Requests for 100 copies or more should be submitted to the Reprints Department, Publications Division, ASCE, (address above); email: [permissions@asce.org](mailto:permissions@asce.org). A reprint order form can be found at <http://pubs.asce.org/support/reprints/>.

Copyright © 2009 by the American Society of Civil Engineers. All Rights Reserved.

ISBN 978-0-7844-1041-7

Manufactured in the United States of America.

## Geotechnical Special Publications

- 1 *Terzaghi Lectures*
- 2 *Geotechnical Aspects of Stiff and Hard Clays*
- 3 *Landslide Dams: Processes, Risk, and Mitigation*
- 7 *Timber Bulkheads*
- 9 *Foundations & Excavations in Decomposed Rock of the Piedmont Province*
- 11 *Dynamic Response of Pile Foundations - Experiment, Analysis and Observation*
- 14 *Geotechnical Aspects of Karst Terrains*
- 15 *Measured Performance Shallow Foundations*
- 16 *Special Topics in Foundations*
- 17 *Soil Properties Evaluation from Centrifugal Models*
- 18 *Geosynthetics for Soil Improvement*
- 19 *Mine Induced Subsidence: Effects on Engineered Structures*
- 21 *Hydraulic Fill Structures*
- 22 *Foundation Engineering*
- 23 *Predicted and Observed Axial Behavior of Piles*
- 24 *Resilient Moduli of Soils: Laboratory Conditions*
- 25 *Design and Performance of Earth Retaining Structures*
- 27 *Geotechnical Engineering Congress*
- 28 *Detection of and Construction at the Soil/Rock Interface*
- 29 *Recent Advances in Instrumentation, Data Acquisition and Testing in Soil Dynamics*
- 32 *Embankment of Dams - James L. Sherard Contributions*
- 33 *Excavation and Support for the Urban Infrastructure*
- 34 *Piles Under Dynamic Loads*
- 35 *Geotechnical Practice in Dam Rehabilitation*
- 37 *Advances in Site Characterization: Data Acquisition, Data Management and Data Interpretation*
- 39 *Unsaturated Soils*
- 40 *Vertical and Horizontal Deformations of Foundations and Embankments*
- 41 *Predicted and Measured Behavior of Five Spread Footings on Sand*
- 42 *Serviceability of Earth Retaining Structures*
- 43 *Fracture Mechanics Applied to Geotechnical Engineering*
- 44 *Ground Failures Under Seismic Conditions*
- 45 *In Situ Deep Soil Improvement*
- 46 *Geoenvironment 2000*
- 47 *Geo-Environmental Issues Facing the Americas*
- 48 *Soil Suction Applications in Geotechnical Engineering*
- 49 *Soil Improvement for Earthquake Hazard Mitigation*
- 50 *Foundation Upgrading and Repair for Infrastructure Improvement*
- 51 *Performance of Deep Foundations Under Seismic Loading*
- 52 *Landslides Under Static and Dynamic Conditions - Analysis, Monitoring, and Mitigation*
- 53 *Landfill Closures - Environmental Protection and Land Recovery*
- 54 *Earthquake Design and Performance of Solid Waste Landfills*
- 55 *Earthquake-Induced Movements and Seismic Remediation of Existing Foundations and Abutments*
- 56 *Static and Dynamic Properties of Gravelly Soils*
- 57 *Verification of Geotechnical Grouting*
- 58 *Uncertainty in the Geologic Environment*
- 59 *Engineered Contaminated Soils and Interaction of Soil Geomembranes*
- 60 *Analysis and Design of Retaining Structures Against Earthquakes*
- 61 *Measuring and Modeling Time Dependent Soil Behavior*
- 62 *Case Histories of Geophysics Applied to Civil Engineering and Public Policy*
- 63 *Design with Residual Materials: Geotechnical and Construction Considerations*
- 64 *Observation and Modeling in Numerical Analysis and Model Tests in Dynamic Soil-Structure Interaction Problems*
- 65 *Dredging and Management of Dredged Material*
- 66 *Grouting: Compaction, Remediation and Testing*
- 67 *Spatial Analysis in Soil Dynamics and Earthquake Engineering*
- 68 *Unsaturated Soil Engineering Practice*
- 69 *Ground Improvement, Ground Reinforcement, Ground Treatment: Developments 1987-1997*
- 70 *Seismic Analysis and Design for Soil-Pile-Structure Interactions*
- 71 *In Situ Remediation of the Geoenvironment*
- 72 *Degradation of Natural Building Stone*
- 73 *Innovative Design and Construction for Foundations and Substructures Subject to Freezing and Frost*

- 74 *Guidelines of Engineering Practice for Braced and Tied-Back Excavations*
- 75 *Geotechnical Earthquake Engineering and Soil Dynamics III*
- 76 *Geosynthetics in Foundation Reinforcement and Erosion Control Systems*
- 77 *Stability of Natural Slopes in the Coastal Plain*
- 78 *Filtration and Drainage in Geotechnical/Geoenvironmental Engineering*
- 79 *Recycled Materials in Geotechnical Applications*
- 80 *Grouts and Grouting: A Potpourri of Projects*
- 81 *Soil Improvement for Big Digs*
- 82 *Risk-Based Corrective Action and Brownfields Restorations*
- 83 *Design and Construction of Earth Retaining Systems*
- 84 *Effects of Construction on Structures*
- 85 *Application of Geotechnical Principles in Pavement Engineering*
- 86 *Big Digs Around the World*
- 87 *Jacked Tunnel Design and Construction*
- 88 *Analysis, Design, Construction, and Testing of Deep Foundations*
- 89 *Recent Advances in the Characterization of Transportation Geo-Materials*
- 90 *Geo-Engineering for Underground Facilities*
- 91 *Special Geotechnical Testing: Central Artery/Tunnel Project in Boston, Massachusetts*
- 94 *Performance Confirmation of Constructed Geotechnical Facilities*
- 95 *Soil-Cement and Other Construction Practices in Geotechnical Engineering*
- 96 *Numerical Methods in Geotechnical Engineering: Recent Developments*
- 97 *Innovations and Applications in Geotechnical Site Characterization*
- 98 *Pavement Subgrade, Unbound Materials, and Nondestructive Testing*
- 99 *Advances in Unsaturated Geotechnics*
- 100 *New Technological and Design Developments in Deep Foundations*
- 101 *Slope Stability 2000*
- 102 *Trends in Rock Mechanics*
- 103 *Advances in Transportation and Geoenvironmental Systems Using Geosynthetics*
- 104 *Advances in Grouting and Ground Modification*
- 105 *Environmental Geotechnics*
- 106 *Geotechnical Measurements: Lab & Field*
- 107 *Soil Dynamics and Liquefaction 2000*
- 108 *Use of Geophysical Methods in Construction*
- 109 *Educational Issues in Geotechnical Engineering*
- 110 *Computer Simulation of Earthquake Effects*
- 111 *Judgment and Innovation: The Heritage and Future of the Geotechnical Engineering Profession*
- 112 *Soft Ground Technology*
- 113 *Foundations and Ground Improvement*
- 114 *Soils Magic*
- 115 *Expansive Clay Soils and Vegetative Influence on Shallow Foundations*
- 116 *Deep Foundations 2002: An International Perspective on Theory, Design, Construction, and Performance*
- 117 *Discrete Element Methods: Numerical Modeling of Discontinua*
- 118 *A History of Progress: Selected U.S. Papers in Geotechnical Engineering*
- 119 *Soil Behavior and Soft Ground Construction*
- 120 *Grouting and Ground Treatment*
- 121 *Probabilistic Site Characterization at the National Geotechnical Experimentation Sites*
- 122 *Sinkholes and the Engineering and Environmental Impacts of Karst*
- 123 *Recent Advances in Materials Characterization and Modeling of Pavement Systems*
- 124 *GeoSupport 2004: Drilled Shafts, Micropiling, Deep Mixing, Remedial and Specialty Foundation Systems*
- 125 *Current Practices and Future Trends in Deep Foundations*
- 126 *Geotechnical Engineering for Transportation Projects*
- 127 *Recycled Materials in Geotechnics*
- 128 *Soil Constitutive Models: Evaluation, Selection, and Calibration*
- 129 *Advances in Designing and Testing Deep Foundations*
- 130 *Advances in Pavement Engineering*
- 131 *Contemporary Issues in Foundation Engineering*
- 132 *Advances in Deep Foundations: In Memory of Michael W. O'Neill*
- 133 *Earthquake Engineering and Soil Dynamics*
- 134 *Soil Dynamics Symposium in Honor of Professor Richard D. Woods*
- 135 *Erosion of Soils and Scour of Foundations*

- 136 *Innovations in Grouting and Soil Improvement*
- 137 *Legal and Liability Issues in Geotechnical Engineering*
- 138 *Site Characterization and Modeling*
- 139 *Calibration of Constitutive Models*
- 140 *Slopes and Retaining Structures under Seismic and Static Conditions*
- 141 *International Perspectives on Soil Reinforcement Applications*
- 142 *Waste Containment and Remediation*
- 143 *Geomechanics: Testing, Modeling, and Simulation*
- 144 *Sinkholes and the Engineering and Environmental Impacts of Karst*
- 145 *Seismic Performance and Simulation of Pile Foundations in Liquefied and Laterally Spreading Ground*
- 146 *Asphalt Concrete: Simulation, Modeling and Experimental Characterization*
- 147 *Unsaturated Soils 2006*
- 148 *Advances in Unsaturated Soil, Seepage, and Environmental Geotechnics*
- 149 *Site and Geomaterial Characterization*
- 150 *Soil and Rock Behavior and Modeling*
- 151 *Advances in Earth Structures: Research to Practice*
- 152 *Ground Modification and Seismic Mitigation*
- 153 *Foundation Analysis and Design: Innovative Methods*
- 154 *Pavement Mechanics and Performance*
- 155 *Underground Construction and Ground Movement*
- 156 *Geomechanics II: Testing, Modeling, and Simulation*
- 157 *Computer Applications in Geotechnical Engineering*
- 158 *Contemporary Issues in Deep Foundations*
- 159 *Case Studies in Earth Retaining Structures*
- 160 *Dynamic Response and Soil Properties*
- 161 *Embankments, Dams, and Slopes: Lessons from the New Orleans Levee Failures and Other Issues*
- 162 *Problematic Soils and Rocks and In Situ Characterization*
- 163 *Geoenvironmental Engineering*
- 164 *Innovative Applications of Geophysics in Civil Engineering*
- 165 *Geosynthetics in Reinforcement and Hydraulic Applications*
- 166 *Educational Activities in Geotechnical Engineering*
- 167 *Geotechnics of Soil Erosion*
- 168 *Grouting for Ground Improvement: Innovative Concepts and Applications*
- 169 *Soil and Material Inputs for Mechanistic-Empirical Pavement Design*
- 170 *Probabilistic Applications in Geotechnical Engineering*
- 171 *Advances in Shallow Foundations*
- 172 *Soil Improvement*
- 173 *Advances in Measurement and Modeling of Soil Behavior*
- 174 *Designing Our Underground Space*
- 175 *Field Measurements in Geomechanics 2007*
- 176 *Analysis of Asphalt Pavement Materials and Systems: Emerging Methods*
- 177 *GeoCongress 2008: Geotechnics of Waste Management and Remediation*
- 178 *GeoCongress 2008: Geosustainability and Geohazard Mitigation*
- 179 *GeoCongress 2008: Characterization, Monitoring, and Modeling of GeoSystems*
- 180 *From Research to Practice in Geotechnical Engineering*
- 181 *Geotechnical Earthquake Engineering and Soil Dynamics IV*
- 182 *Pavements and Materials: Characterization, Modeling, and Simulation*
- 183 *Sinkholes and the Engineering and Environmental Impacts of Karst*
- 184 *Pavements and Materials: Modeling, Testing, and Performance*
- 185 *Contemporary Topics in Deep Foundations*
- 186 *Contemporary Topics in In-Situ Testing, Analysis, and Reliability of Foundations*
- 187 *Contemporary Topics in Ground Modification, Problem Soils, and Geo-Support*
- 188 *Advances in Ground Improvement: Research to Practice in USA and China*

*This page intentionally left blank*

# Preface

This Geotechnical Special Publication (GSP), along with its eight companion volumes, contains selected papers from the GeoHunan International Conference: Challenges and Recent Advances in Pavement Technologies and Transportation Geotechnics held in Hunan, China on August 3 to 6, 2009. The conference was hosted by Changsa University of Science and Technology. This pavement and geotechnical conference was endorsed by a number of leading international professional organizations. This conference provided a showcase for recent developments and advancements in pavement and geotechnique and offered a forum to discuss and debate future directions for geo-engineering in the 21st century. Conference topics covered a broad array of contemporary issues and design and construction techniques for professionals involved in roadway pavement, geotechnical, geoenvironmental, and geomechanical disciplines.

The conference received 320 full papers from over 30 countries. All 320 full papers were peer-reviewed, and about 249 papers were accepted through a rigorous peer review process that were presented in 18 presentation sessions and six poster sessions, in addition to three invited keynote presentations. This GSP included 27 papers in the following five topics:

Advances in Unsaturated Soil, Seepage, and Environmental Geotechnics  
Geosynthetics  
Geo-environmental Engineering  
NDT Testing of Infrastructure Materials, and  
Bridge Approach Embankment

The editors would like to expression their appreciation for having been provided opportunity to be a part of the conferences' organization, and hope this proceeding will be useful to the geotechnical and pavement engineering community for many decades to come.

*This page intentionally left blank*

# Contents

## *Advances in Unsaturated Soil, Seepage, and Environmental Geotechnics*

<b>A Comparison of Total Suction Measurements with Thermocouple Psychrometer, Filter Paper Technique, and Chilled-Mirror Device.....</b>	<b>1</b>
Daniel Mabirizi and Rifat Bulut	
<b>Probabilistic Analysis of Finite Strain Consolidation with Stochastic Soil Compression Index and Hydraulic Conductivity.....</b>	<b>7</b>
Tong Qiu and Wei Chen	
<b>Remarks on Constitutive Modeling of Unsaturated Soils .....</b>	<b>13</b>
Xiong Zhang, Liangbiao Chen, and Lin Li	
<b>Swelling Behavior of Compacted Cohesive Soils—An Absorbed Energy Approach .....</b>	<b>20</b>
Zhongjie Zhang, Mingjiang Tao, and Mehmet T. Tumay	
<b>Gradient-Dependent Damage Constitutive: The Second-Order Gradient Damage Model.....</b>	<b>26</b>
Bing Zhao, Ying-ren Zheng, Ming-hua Zeng, Xue-song Tang, and Xiao-Qiang Yan	
<b>Analysis of Two-Dimensional Consolidation of Unsaturated Soils.....</b>	<b>33</b>
Xue-shan Cao and Zong-ze Yin	

## *Geosynthetics*

<b>Improving Bearing Capacity of Shallow Foundations on Weak Soils Utilizing Geosynthetic Reinforcing Technique.....</b>	<b>40</b>
Sao-Jeng Chao	
<b>Micromechanical Analysis of Soil Arching in Geosynthetic-Reinforced Pile-Supported Embankments .....</b>	<b>47</b>
Anil Bhandari, Jie Han, and Fei Wang	
<b>Large Physical Modeling to Optimize the Geometrical Conditions of Geotextile in Reinforced Loose Sand .....</b>	<b>53</b>
S. Shahaboddin Yasrobi, S. Mustapha Rahmaninezhad, and S. Farhad Eftekharzadeh	
<b>A Research on the Dynamical Characteristics of Road-Bridge Transition Sections Reinforced by Geogrid.....</b>	<b>60</b>
Guoyuan Chen	
<b>Numerical Modeling of a Reinforced Embankment Based on Centrifugal Test Dimensions.....</b>	<b>68</b>
Jian-Feng Chen, Song-Bo Yu, and Jie Han	
<b>Granular Lightweight Fill Composed of Sand and Tire Scrap.....</b>	<b>78</b>
An Deng and Jin-Rong Feng	

### *Geo-Environmental Engineering*

<b>Large Direct Shear Test Apparatus for In Situ Testing of Municipal Solid Waste Landfill Sites.....</b>	<b>86</b>
Liaqat Ali, Sarfraz Ali, and Ammar Maqbool	
<b>Feasibility Analysis for the Ecological Sustainability of Engineering Construction of the Express .....</b>	<b>92</b>
Tung-Tsan Chen, Yao T. Hsu, and Chun-Yuan Wang	
<b>Ant Colony Optimization Algorithm for Vertical Alignment of Highways.....</b>	<b>99</b>
Kun Miao, Liang Li, Xiao-Li Yang, and Yuan-Yuan Huo	
<b>Application of Analytic Hierarchy Process to Slope Greening Design .....</b>	<b>109</b>
Fang Wang, Fei Chen, and Yingying Cheng	

### *NDT Testing of Infrastructure Materials*

<b>Using Ground Penetration Radar Techniques for Roadway Structure Safety Evaluation .....</b>	<b>116</b>
Dar-Hao Chen, Andrew Wimsatt, and John Bilyeu	
<b>Visualizing 3-D Internal Soil Deformation Using Laser Speckle and Transparent Soil Techniques.....</b>	<b>123</b>
Jinyuan Liu	
<b>Experimental and Theoretical Studies on (Relative) Permittivity of the Tunnel Lining.....</b>	<b>129</b>
Yan-xi Gao and Xia Li	
<b>A Review on GPR Applications in Moisture Content Determination and Pavement Condition Assessment .....</b>	<b>138</b>
Can Chen and Jie Zhang	
<b>Non-Destructive Impedance Spectroscopy Measurement for Soil Characteristics .....</b>	<b>144</b>
Sarah E. Pluta and John W. Hewitt	
<b>Ultrasonic Pulse Velocity Tests on Compacted Soil.....</b>	<b>150</b>
David M. Weidinger, Louis Ge, and Richard W. Stephenson	
<b>Characterization of Early Stage Concrete by Ultrasonic Method.....</b>	<b>156</b>
Yan Liu, Bin Zhang, Xinbao Yu, and Xiong (Bill) Yu	
<b>Measuring Dielectric Constant in Highly Conductive Soils Based on Surface Reflection Coefficients.....</b>	<b>166</b>
Renpeng Chen, Wei Xu, Yunmin Chen, and Wei Chen	
<b>Comparison of Surface Wave Tests for Pavement System Thicknesses/Moduli .....</b>	<b>174</b>
Larry D. Olson and Patrick Miller	

### *Bridge Approach Embankment*

<b>Solving the Problems of Differential Settlement of Pavement Structures in the Bangkok Area.....</b>	<b>180</b>
Titi Paveenchana and Manoon Arayasiri	
<b>Contribution of Loamy Soil Treatment to Improve Embankments Performance.....</b>	<b>186</b>
Régis De Bel, Antonio Gomes Correia, and Jean-Claude Verbrugge	

*Indexes*

<b>Author Index.....</b>	<b>193</b>
<b>Subject Index.....</b>	<b>195</b>

*This page intentionally left blank*

# **A Comparison of Total Suction Measurements with Thermocouple Psychrometer, Filter Paper Technique and Chilled-Mirror Device**

Daniel Mabirizi<sup>1</sup> and Rifat Bulut<sup>2</sup>, M. ASCE

<sup>1</sup>Graduate Student, School of Civil and Environmental Engineering, Oklahoma State University, 207 Engineering South, Stillwater, OK 74078 USA

<sup>2</sup>Assistant Professor, School of Civil and Environmental Engineering, Oklahoma State University, 207 Engineering South, Stillwater, OK 74078 USA; rifat.bulut@okstate.edu

**ABSTRACT:** Soil suction is one of the most important parameters describing the moisture stress condition of unsaturated soils, and its measurement is equally important for realistic applications of unsaturated soil mechanics. The thermocouple psychrometers, filter paper method and chilled-mirror device are three soil suction measurement techniques that have found their places in describing the behavior of unsaturated soils in geotechnical engineering practice. However, as it is inherent with all the suction measurement methods there are still difficulties and uncertainties associated with these soil suction measurement techniques. In this paper, the filter paper, chilled-mirror psychrometer, and thermocouple psychrometer methods are evaluated and compared based on some recent observations and test results. These methods are used to measure total suctions of some high plasticity clay soils under very strict temperature control conditions. From the test results, the capabilities and limitations of the three methods are analyzed.

## **INTRODUCTION**

In general, soil suction refers to the measure of the free energy or negative stress in the pore water. The soil suction measured in terms of relative humidity is called total suction (Fredlund and Rahardjo 1993). This implies that total suction can only be measured indirectly by calibrating the suction devices against the relative humidity at thermodynamic equilibrium. In this paper, the calibration and characteristic curves for the filter paper, chilled-mirror psychrometer and thermocouple psychrometer methods are assessed, and used to describe the moisture-suction relationship in the soil sample. There are several devices available for measuring total suction. These devices vary widely in terms of range of measurement, accuracy, precision, and reliability. This paper makes a comparison of the filter paper, thermocouple psychrometer and chilled-mirror psychrometer for total suction measurements of various high plasticity clays. Since total suction measurements are highly temperature dependent, all soil testing was performed in a temperature controlled laboratory.

## MATERIALS AND METHODS

### Filter Paper Technique

The “non-contact” filter paper technique is used to measure total suction. The filter paper covers a wide range of suction measurements, as depicted in Figure 1. The filter paper discs estimate soil suction indirectly by measuring the amount of vapor moisture transferred from an unsaturated soil specimen to an initially dry filter paper. Basically, filter papers come to water vapor equilibrium with soil having a specific suction. Schleicher & Schuell No. 589–White Hard (WH) filter paper discs were used in this research study.

Prior to total suction measurements, filter papers are calibrated to determine the relationship between equilibrium water content and relative humidity using salt solutions of known osmotic potential, usually sodium chloride (NaCl) and potassium chloride (KCl). Filter papers in dry condition are suspended over known concentrations of salt solutions corresponding to the range of interest in sealed containers at constant temperature. The minimum equilibration period is generally at least two weeks. The equilibrium water content is measured and plotted against total suction for each salt concentration to define the wetting calibration curve. The calibration curve shown in Figure 1 developed by Bulut et al. (2002) for the Schleicher & Schuell No. 589–White Hard (WH) filter paper was employed in this study.

For the non-contact technique, a dry filter paper was suspended above a soil specimen in a sealed container for water vapor equilibrium between the filter paper and the soil specimen at a constant temperature. Equilibration period was at least seven days, but not more than ten days, for soil total suction measurements in this study. Having achieved equilibrium condition, the filter paper is removed and water content of the filter paper determined as quickly as possible. The calibration curve was thereafter used to determine total suction.

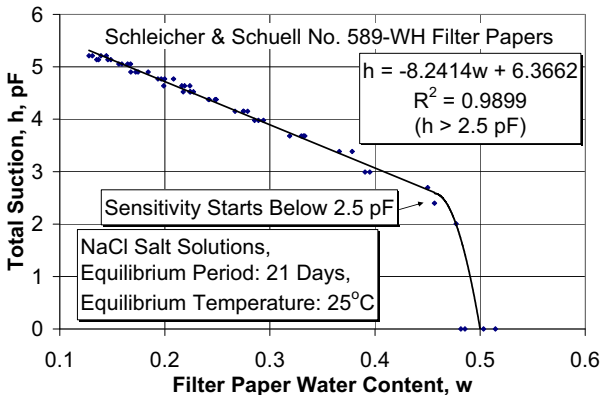
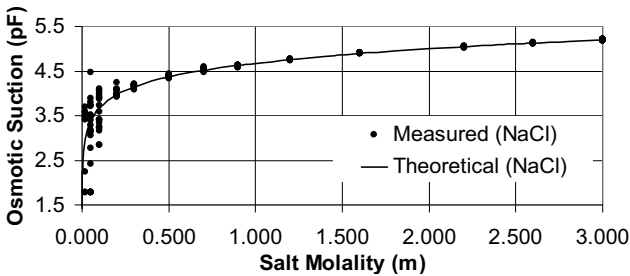


FIG. 1. Wetting filter paper calibration curve (Bulut et al. 2002).

**Chilled-Mirror Psychrometer**

In this study, the WP4 Dewpoint PotentiaMeter from Decagon Devices was adopted for the chilled-mirror technique total suction measurements. Basically, the instrument has an enclosed sample chamber which contains a mirror, a Peltier thermoelectric cooler, and a photodetector cell. The WP4 works on the premise that at equilibrium the water potential (total suction) of the air in the chamber is the same as the water potential (total suction) in the sample (WP4 Operator’s Manual – Version 4, 2003). Water vapor from the soil specimen is allowed to condense on the mirror and a photoelectric cell is used to detect the exact point at which condensation first appears on the mirror. The thermoelectric cooler is used to control temperature of the mirror. The WP4 then displays the final water potential and temperature of the sample.

The WP4 user manual suggests that a one point calibration (accuracy) check is performed prior to soil suction measurements using a potassium (or sodium) chloride salt solution at 4.36 pF suction. However, a full characteristic curve was developed for the WP4 device used in this research study, in order to assess the accuracy of the equipment over a very wide suction range, as shown in Figure 2. Figure 2(a) shows a very wide suction range, while Figure 2(b) depicts the sensitivity of the WP4 device at low suction levels. The characteristic curve was obtained using sodium chloride salt solutions from very low to very high concentrations. The water vapor equilibrium was reached within a few minutes during the development of the characteristic curve.



**FIG. 2(a). WP4 characteristic curve.**

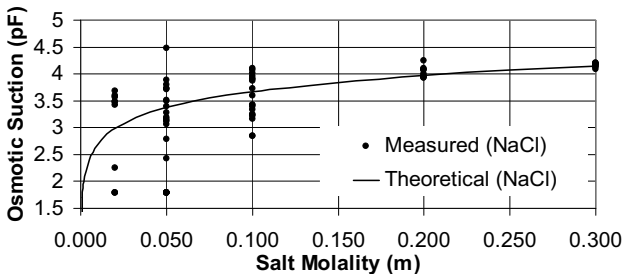


**FIG. 2(b). Lower portion of WP4 characteristic curve in Figure 2(a).**

Small pieces of soil specimens obtained from Shelby tube samples were employed for total suction measurements using the WP4 device. The soil samples and WP4 device were kept at the same location for at least several hours for temperature equilibrium prior to the testing. The sample cups were quickly filled approximately halfway with soil specimen and closed tightly with their lids to minimize drying of the specimen. The cups with the soil specimen inside were placed on top of the WP4 device for further temperature equilibrium for about 5 minutes. After that, the total suction measurements were performed immediately. Equilibration of soil specimens was achieved within 5 minutes within the WP4 device. In this study, four specimens were taken from each soil sample and each specimen was measured twice and the results obtained from each sample were averaged.

### Thermocouple Psychrometers

Thermocouple psychrometers measure the relative humidity in the air phase of the soil pores or the region near the soil (Fredlund and Rahardjo 1993). The thermocouple psychrometers used to measure soil suction in this research study were from Wescor Inc. and had stainless screen shields. The soil psychrometers were connected to a microvolt datalogger from Wescor Inc./Cambell Scientific Inc.

The psychrometers were calibrated at relative humidity values corresponding to total suctions of pF 3.67, 4.14, 4.37, 4.52, 4.63, and 4.68 by immersing the psychrometers in sodium chloride (NaCl) salt solution in a sealed container under controlled temperature conditions of  $25 \pm 0.1^\circ\text{C}$ . A calibration curve was developed for each psychrometer (Figure 3) defining the relationship between the thermocouple microvolt outputs and known total suction values of the NaCl solutions. Equilibration of soil psychrometers is achieved in one hour.

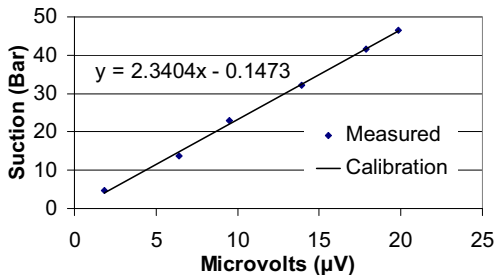


FIG. 3. Typical calibration curve for a single thermocouple psychrometer.

Thermocouple psychrometers were used in laboratory for unsaturated soil diffusion coefficient measurements. For each test, two small holes were drilled at specified locations into the side of a Shelby tube soil specimen and two psychrometers were buried in the drilled holes to measure total suction over a given period of time. These holes and the whole soil column were sealed to prevent loss or gain of moisture. The soil specimens were placed in a water bath to control temperature environment of the

sample. Typically, the test was run from four to about seven days. A detailed description of the unsaturated soil diffusion coefficient measurements can be found in Bulut et al. (2005).

**RESULTS AND DISCUSSIONS**

The comparisons of the three different suction measurement methods (i.e., the filter paper (FP), thermocouple psychrometer (TP), and chilled-mirror psychrometer (WP4)) were based on the suction results obtained from the unsaturated soil diffusion coefficient measurements. Soil suction measurements were performed on soil samples with physical properties summarized in Table 1. Table 2 shows the results obtained from total suction measurements obtained from the three total suction techniques being compared.

**Table 1. Physical Properties of Soil Samples**

Boring No.	Depth (ft)	Atterberg Limits		% Finer Than U.S. Sieve No.	
		LL (%)	PI (%)	4 (%)	200 (%)
1	4	52	32	100	97
2	1	91	46	100	93
3	8	93	57	100	94
4	6	77	48	100	94

**Table 2. Total Suction Test Results**

Boring No.	Sample Depth (ft)	*WP4 Total Suction (pF)	*FP Total Suction (pF)	*TP	
				Total Suction (pF)	Drying Time (min)
1	2-4	4.06	3.56	3.97	1370
	6-8	4.26	4.09	4.23	990
2	2-4	4.15	4.02	4.37	2300
	8-10	4.23	4.15	4.08	790
3	0-2	3.71	2.84	4.18	2560
	10-12	4.08	3.52	3.81	620
4	6-7	4.38	4.22	4.55	3450
	9-11	4.22	3.97	4.09	1150

**\*WP4, \*FP, and \*TP is chilled-mirror, filter paper, and thermocouple psychrometer respectively**

Results in Table 2 are evaluated based on the range and accuracy of the three suction measurement methods in Bulut and Leong 2008. Recent research studies on the filter paper method (i.e., Houston et al. 1994, Leong et al. 2002, Bulut and Wray 2005) demonstrates that if a consistent and well-maintained laboratory testing protocol is followed, the filter paper technique can be a very reliable method. The results in Table 2 are also in agreement with this statement, when the filter paper results are compared

with the results from the thermocouple and chilled-mirror techniques.

Total suction measurements were performed on the same Shelby tube soil specimens using the WP4 and FP methods. The WP4 measurements were performed before the specimen was setup with the FP and after the FP has reached suction equilibrium with the soil, which was at least one week. An average value of the two WP4 measurements was taken for comparison. There was no significant difference between the two measurements. As shown in Table 2, the FP results are consistently lower than the WP4 measurements. From the same Shelby tube, a soil specimen was prepared for diffusion coefficient measurements using thermocouple psychrometers. The diffusion test soil specimen was exposed to laboratory environment (relative humidity of about 60%) for drying under certain boundary conditions (Bulut et al. 2005). The last two columns in Table 2 depict the drying times and corresponding total suction results at the end of those drying periods. An evaluation of the results in Table 2 shows that suction measurements below 4 pF using the WP4 device should be very carefully scrutinized for their validity. For instance, the first row in Table 2 gives a TP reading of 3.97 pF after 1310 minutes of drying period, as compared to 3.56 pF from the FP and 4.06 from the WP4 device. When the FP results are used as a reference point, it is very likely that the soil specimen was at a suction of 3.56 pF. The TP measurement after 1310 minutes confirms that the soil was at a lower suction than 3.97 pF. However, the WP result of 4.06 pF is very high as compared to both the FP and TP measurements. This analysis can be carried out for other measurements in Table 2.

The difference in suctions was much less at high suction ranges providing more reliable total suction estimates. The filter paper technique is low cost and measures almost the entire range of total suction. If good laboratory protocol is established it provides very reliable total suction estimates compared to the WP4 and thermocouple psychrometer.

## REFERENCES

- Bulut, R. and Leong, E.C. (2008). "Indirect measurement of suction." *Geotechnical and Geological Engineering J.*, Vol. 26 (6): 633-644.
- Bulut, R. and Wray, W.K. (2005). "Free energy of water – suction – in filter papers." *Geotechnical Testing J.*, Vol. 28 (4): 355-364.
- Bulut, R., Aubeny, C.P. and Lytton, R.L. (2005). "Unsaturated soil diffusivity measurements." *International Symposium on Advanced Experimental Unsaturated Soil Mechanics (EXPERUS 2005)*, Trento, Italy: 281-286.
- Bulut, R., Hineidi, S.M. and Bailey, B. (2002). "Suction measurements – filter paper and chilled-mirror psychrometer." *Proceedings of ASCE Texas Section*, Waco, Texas: (CD-Rom).
- Fredlund, D.G. and Rahardjo, H. (1993). "Soil mechanics for unsaturated soils." *John Wiley and Sons*, New York, NY.
- Houston, S.L., Houston, W.R. and Wagner, A.M. (1994). "Laboratory filter paper measurements." *Geotechnical Testing J.*, Vol. 17 (2): 185-194.
- Leong, E.C., He, L. and Rahardjo, H. (2002). "Factors affecting the filter paper method for total and matric suction measurements." *Geotechnical Testing J.*, Vol. 25 (3): 322-333.

# Probabilistic Analysis of Finite Strain Consolidation with Stochastic Soil Compression Index and Hydraulic Conductivity

Tong Qiu<sup>1</sup> and Wei Chen<sup>2</sup>

<sup>1</sup>Assistant Professor, Department of Civil & Environmental Engineering, Clarkson University, Potsdam, NY 13699-5710; tqiu@clarkson.edu

<sup>2</sup>Graduate Student, Department of Civil & Environmental Engineering, Clarkson University, Potsdam, NY 13699-5710; chenwei@clarkson.edu

**ABSTRACT:** A probabilistic analysis of the effects of stochastic soil compression index and hydraulic conductivity on one-dimensional finite strain consolidation is presented. Random field simulation and finite strain consolidation are combined to perform Monte Carlo simulations. Parametric study on the effect of the standard deviation of the stochastic soil properties on output statistics relating to total settlement and consolidation time is conducted.

## INTRODUCTION

In geotechnical engineering practice, consolidation and settlement analysis for embankments on soft clay is generally deterministic in that the soil properties used are assumed to be average values determined from laboratory testing of soil samples. To account for soil variability in the field, engineers often make conservative assumptions regarding the soil properties based on their experience and engineering judgement. This practice may lead to unreliable and uneconomical designs. The objective of this paper is to provide more rational analysis for embankments on soft clay based on probabilistic analysis of finite strain consolidation.

In this paper, the effects of stochastic soil compression index and hydraulic conductivity on 1-D finite strain consolidation are presented. Karhunen-Loeve (K-L) expansion is used to generate the random fields in which spatial correlation is considered. The random field simulation and 1-D finite strain consolidation analysis are combined to perform Monte Carlo simulations. Parametric study on the effect of the standard deviation of the stochastic soil properties on output statistics relating to total settlement and consolidation time is conducted.

## FINITE STRAIN CONSOLIDATION MODEL

A 1-D finite strain consolidation code CS2 was used in this study (Fox and Berles 1997, Fox 1999). CS2 is a piecewise-linear numerical model for large strain

consolidation. The problem geometry is shown in Fig. 1. A saturated compressible clay layer has initial height  $H_o$  and is assumed to be in equilibrium under an effective overburden stress  $q_o$  and its own self-weight. The specific gravity of solids  $G_s$  is constant for the layer, and the initial distribution of pore water pressure is hydrostatic (i.e., zero excess pore pressure throughout). The compressible layer is modeled as a vertical column of  $R_j = 101$  elements, each having a central node and constant initial thickness. An instantaneous vertical total stress increment of  $\Delta q$  is applied to the layer at time  $t = 0$ . At some later time  $t$ , the height of the layer is  $H_t$ . Values of void ratio  $e$  and hydraulic conductivity  $k$  for the elements are updated at each time step, as are the positions of the nodes with respect to a fixed Eulerian coordinate system. Fig. 2 shows the log-linear constitutive relationships for the clay layer. Values of the initial void ratio and hydraulic conductivity at the midheight of the layer are  $e_o$  and  $k_o$ , respectively.

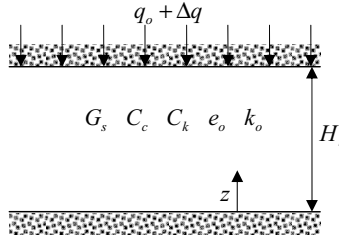


FIG. 1. Problem geometry

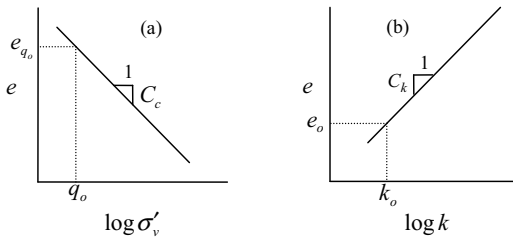


FIG. 2. Constitutive relationships for compressible layer:  
(a) compressibility; (b) hydraulic conductivity

The CS2 model is dimensionless such that solutions are independent of  $H_o$  and the absolute magnitude of  $k$ . For example,  $q_o$  is normalized as  $q_o^* = q_o / (H_o \gamma_w)$ ,  $\Delta q$  is normalized as  $\Delta q^* = \Delta q / (H_o \gamma_w)$ ,  $k$  is normalized as  $k^* = k / k_o$ , settlement  $S$  is normalized as  $S^* = S / H_o$ , and  $t$  is normalized as  $t^* = k_o t / H_o$ , where  $\gamma_w$  is the unit weight of water. A dimensionless solution for a given problem can be obtained once the boundary drainage conditions, soil properties, and loading conditions are specified.

## SIMULATION OF RANDOM FIELD

The spatial variation of soil properties can be decomposed into a smoothly varying trend (or mean) function  $T(z)$  and a fluctuating component  $w(z)$  as follows (Phoon and Kulhawy 1999):

$$Y(z) = T(z) + w(z) \quad (1)$$

where  $Y$  is the in situ soil property, and  $z$  is the depth. The fluctuating component  $w(z)$  represents the inherent soil variability. In this paper, the soil compression index  $C_c(z)$  and hydraulic conductivity  $k(z)$  are treated as stochastic with the trend function being deterministic while the fluctuating component being random. The trend function of  $C_c$  is assumed to be constant with depth and this assumption is generally valid for normally consolidated (NC) soft clay (see Fig. 2a). The trend function of  $k$  is assumed to have a log-linear relationship with void ratio (see Fig. 2b). Since the void ratio decreases with depth for NC clay, the trend function of  $k$  decreases with depth. The random fluctuating components of  $C_c$  and  $k$  are assumed to follow lognormal distributions (Gui *et al.* 2000, Baecher and Christian 2003). Thus, the detrended  $\ln C_c$  and  $\ln k$  are normally distributed.

To account for the spatial correlation of soil properties in  $z$  direction, the covariance function  $C(z_1, z_2)$  of the detrended  $\ln C_c$  or  $\ln k$  is assumed to be in the following form (Gui *et al.* 2000),

$$C_p(z_1, z_2) = \sigma_p^2 \exp(-|z_1 - z_2|/d_p) \quad (2)$$

where  $P$  denotes the spatially random functions  $\ln C_c$  or  $\ln k$ ,  $d_p$  is the correlation length  $d$  of  $P$  in  $z$  direction, and  $\sigma_p^2$  is the variance of  $P$ . The correlation lengths of  $\ln C_c$  and  $\ln k$  are assumed to be the same. The random fields of  $\ln C_c$  and  $\ln k$  are simulated using K-L expansion. The detailed procedures of K-L expansion for the simulation of stochastic processes are well documented in literature (e.g., Phoon *et al.* 2002) and are not presented herein.

## MONTE CARLO SIMULATION

Finite strain consolidation analysis (i.e., CS2) and random field simulation are combined to perform Monte Carlo simulations. One realization of the Monte Carlo simulation consists of the following four steps.

- (1) Random field of  $C_c$  in the soil column is first generated using K-L expansion.
- (2) Initial calculation in CS2 is performed to obtain the initial distribution of void ratio and effective stress.
- (3) Random field of initial  $k$  in the soil column is generated. The trend function of  $k$  is determined based on initial void ratio in step (2) and Fig. 2b. The

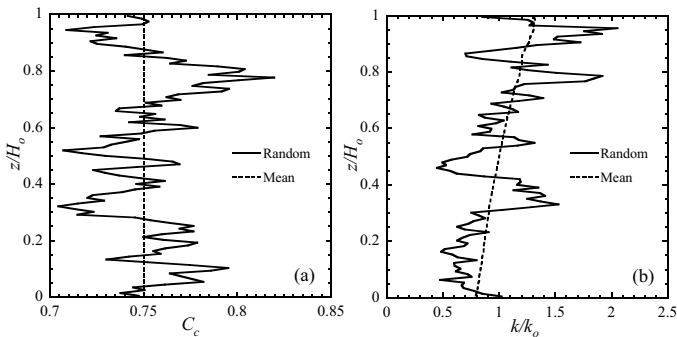
fluctuating component of  $k$  is obtained using K-L expansion.

- (4) Finite strain consolidation is performed using CS2. The compression index  $C_c$  for a given element remains unchanged after step (1) during the consolidation, while  $k$  is updated at each time step based on a constant  $C_k$  and Fig. 2b.

Five hundred realizations are generated by repeating steps (1) through (4). Output quantities of interest from these realizations are analyzed statistically.

## PARAMETERS AND SIMULATION RESULTS

Parameters used in the analyses are discussed in this section. For simplicity,  $G_s$  is assumed to be 2.7. This value is considered representative of most inorganic clays (Fox 1999). The initial void ratio (at midheight) of clay layer is assumed to be 1.5, which is representative of many soft clays. The value of  $C_k$  for many natural soft clay deposits is approximately equal to half of the initial void ratio (Mesri *et al.* 1994). Thus,  $C_k$  is calculated as  $C_k = e_o/2 = 0.75$ . The ratio of  $C_c/C_k$  falls between 0.5 and 1.0 for many natural clays (Fox 1999). Thus, the mean value of  $C_c$  is assumed to be equal to  $C_k$ . A normalized correlation length ( $d/H_o$ ) is assumed to be 0.1. Since the correlation length for many soil properties in vertical direction is on the order of 1 m (Phoon and Kulhawy 1999), the assumption of  $d/H_o = 0.1$  corresponds to an initial thickness of the clay layer on the order of 10 m. The normalized initial effective overburden stress  $q_o^*$  and total vertical stress increase  $\Delta q^*$  are assumed to be 1.0 and 5.0, respectively. For parametric study, 0.05, 0.1, and 0.2 are used for  $\sigma_{\ln C_c}$  (standard deviation of detrended  $\ln C_c$ ), and 0.2, 0.4, and 0.8 are used for  $\sigma_{\ln k}$  (standard deviation of detrended  $\ln k$ ).



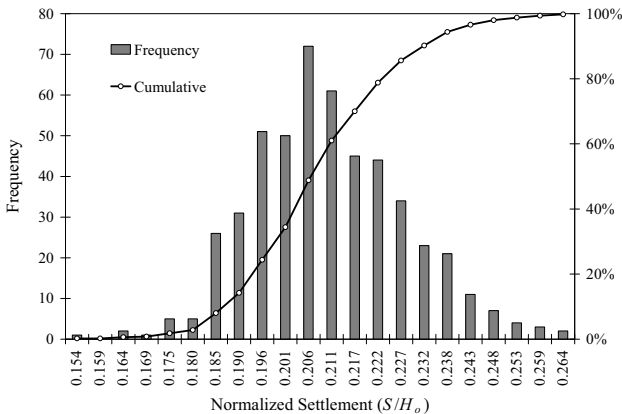
**FIG. 3. Profiles of random  $C_c$  and normalized  $k$  ( $\sigma_{\ln C_c} = 0.1$ ,  $\sigma_{\ln k} = 0.4$ )**

Fig. 3 shows the profile of  $C_c$  and normalized  $k$  for a realization based on  $\sigma_{\ln C_c} = 0.1$  and  $\sigma_{\ln k} = 0.4$ . The spatially correlated fluctuation of the random soil

properties around their mean/trend values (also shown in Fig. 3) is clearly demonstrated in Fig. 3. Table 1 shows the effect of variability of  $C_c$  on the statistics of final settlement  $S^*$ . Table 1 indicates that as the variability of  $C_c$  increases ( $\sigma_{\ln C_c}$  increases from 0.05 to 0.2), the coefficient of variation COV (i.e.,  $\sigma/\mu$ ) for the final settlement also increases. However, the mean values of the final settlement for the three cases considered are close to the deterministic value (i.e., 0.2037) based the average value of  $C_c$  (i.e., 0.75). Fig. 4 shows the histogram of final settlement for the case of  $\sigma_{\ln C_c} = 0.2$ . Table 2 demonstrates the effect of variability of  $C_c$  and  $k$  on the statistics of consolidation time. The deterministic values of  $t_{30}^*$ ,  $t_{60}^*$  and  $t_{90}^*$  based on the average values of  $C_c$  and  $k$  are 0.00148, 0.00600, and 0.01736, respectively. Table 2 indicates that COV for the consolidation time increases rapidly as uncertainty of  $k$  increase (i.e.,  $\sigma_{\ln k}$  increases), however, it is relatively insensitive of the uncertainty of  $C_c$ . The influence of uncertainties of  $C_c$  and  $k$  on consolidation time is more pronounced at early times than later times. The mean values of consolidation time deviates from the deterministic values as uncertainties of  $C_c$  and  $k$  increase.

**Table 1. Effect of Variability of  $C_c$  on Final Settlement**

$\sigma_{\ln C_c}$	Deterministic Value of $S^*$	Statistics of Probabilistic Values of $S^*$		
		$\mu$	$\sigma$	COV
0.05	0.2037	0.2040	0.0042	2.1%
0.1		0.2050	0.0088	4.3%
0.2		0.2076	0.0171	8.4%



**FIG. 4. Histogram of final settlement ( $\sigma_{\ln C_c} = 0.2$ )**

**Table 2. Effect of Variability of  $C_c$  and  $k$  on Consolidation Time  $t^*$** 

$t^*$	$\sigma_{\ln C_c}$	$\sigma_{\ln k} = 0.2$		$\sigma_{\ln k} = 0.4$		$\sigma_{\ln k} = 0.8$	
		$\mu$	COV	$\mu$	COV	$\mu$	COV
$t_{30}^*$	0.05	0.00150	12.0%	0.00155	23.6%	0.00174	48.8%
$t_{60}^*$		0.00612	10.5%	0.00635	20.3%	0.00741	42.9%
$t_{90}^*$		0.01777	10.2%	0.01852	19.3%	0.02215	41.2%
$t_{30}^*$	0.1	0.00152	14.0%	0.00157	24.3%	0.00178	53.8%
$t_{60}^*$		0.00620	12.7%	0.00646	21.2%	0.00751	44.2%
$t_{90}^*$		0.01802	12.8%	0.01890	20.5%	0.02233	41.3%
$t_{30}^*$	0.2	0.00157	19.6%	0.00162	28.5%	0.00183	51.6%
$t_{60}^*$		0.00641	18.9%	0.00667	26.2%	0.00780	45.9%
$t_{90}^*$		0.01879	19.9%	0.01966	26.4%	0.02354	44.8%

## CONCLUSIONS

The effect of spatially random compressibility index and hydraulic conductivity on final settlement and consolidation time has been investigated using a combination of finite strain consolidation, random field simulation, and Monte Carlo simulations. Research indicates that the proposed method is capable of generating realistic random field of soil properties, and may lead to more rational and reliable analysis of consolidation of soft clays.

## REFERENCES

- Baecher, G.B. and Christian, J.T. (2003). *Reliability and Statistics in Geotechnical Engineering*, John Wiley & Sons Ltd, England.
- Fox, P.J. (1999). "Solution charts for finite strain consolidation of normally consolidated clays." *J. Geotech. Geoenviron. Eng.*, ASCE, 125(10): 847-867.
- Fox, P.J. and Berles, J.D. (1997). "CS2: A piecewise-linear model for large strain consolidation." *Int. J. Numer. Anal. Meth. Geomech.*, 21: 453-475.
- Gui, S., Zhang, R., Turner, J.P., and Xue, X. (2000). "Probabilistic slope stability analysis with stochastic hydraulic conductivity." *J. Geotech. Geoenviron. Eng.*, ASCE, 126(1): 1-9.
- Mesri, G., Lo, D.O.K., and Feng, T.-W. (1994). "Settlement of embankments on soft clays." *Vertical and horizontal deformation of foundations and embankments, Geotech. Spec. Publ. No. 40*, A. T. Yeung and G.Y. Felio, eds., ASCE, New York, 1: 8-56.
- Phoon, K.K., Huang, S.P., and Quek, S.T. (2002). "Simulation of second-order processes using Karhunen-Loeve expansion." *Computers and Structures*, 80: 1049-1060.
- Phoon, K.K. and Kulhawy, F.H. (1999). "Characterization of geotechnical variability." *Can. Geotech. J.*, 36: 612-624.

## Remarks on Constitutive Modeling of Unsaturated Soils

Xiong Zhang<sup>1</sup>, A.M. ASCE, Liangbiao Chen<sup>2</sup>, and Lin Li<sup>2</sup>.

<sup>1</sup> Assistant professor, Alaska University Transportation Center, Department of Civil and Environmental Engineering, University of Alaska Fairbanks, Fairbanks, AK99775, USA(ffxz3@uaf.edu)

<sup>2</sup> Graduate student, Alaska University Transportation Center, Department of Civil and Environmental Engineering, University of Alaska Fairbanks, Fairbanks, AK99775, USA

**ABSTRACT:** More and more attention has been paid to account for the effects of hydraulic behavior including hydraulic hysteresis on the stress–strain behavior of unsaturated soils. Current trend is to have two elasto-plastic models for unsaturated soils, one is for the modeling of the mechanical behavior of the soil and the other is for the modeling of hydraulic behavior of the soil. However, few researchers have considered the consistency between these two models. In many existing constitutive models, main drying and wetting curves were assumed to be unique functions between degree of saturation and matric suction for the description of hydraulic hysteresis, in which the degree of saturation is a function of matric suction. In this paper, the Barcelona Basic Model (BBM) is selected to discuss problems associated with such an adoption.

### INTRODUCTION

One of the first constitutive models developed for partially saturated soils was the BBM (Alonso et al. 1990). This model was based upon the modified Cam clay model for fully saturated soils, and was extended for unsaturated states through the introduction of the concept of the loading-collapse yield surface. Since then there has been an increasing interest on unsaturated soils resulting in a large amount of theoretical developments (Wheeler and Sivakumar 1995, Cui and Delage 1996; Bolzon et al. 1996). A review of the early constitutive models can be found in Wheeler and Karube (1996), Delage and Graham (1996) and Gens (1996). Wheeler and Karube (1996) pointed out that in the BBM the models for the soil structure and the water phase were inconsistent and cannot be used for fully coupled hydro-mechanical

analyses. Since then many researchers developed elasto-plastic model for unsaturated soils in which special attention was paid to the modeling for the water phase (Vaunat et al. 2000; Gallipoli et al. 2003; Wheeler et al. 2003; Tamagnini 2004; Sheng et al. 2004; Tarantino and Tombolato 2005). Current trend is to have two elasto-plastic models for unsaturated soils, one is for the modeling of the mechanical behavior of the soil and the other is for the modeling of hydraulic behavior of the soil. However, few researchers have considered the consistency between these two models. In many existing constitutive models, main drying and wetting curves were assumed to be unique functions between degree of saturation and matric suction for the description of hydraulic hysteresis, in which the degree of saturation is a function of matric suction (Romero and Vaunat 2000; Tamagnini 2004; Wheeler et al. 2003; Sheng et al. 2004). In this paper, the BBM is selected to discuss problems associated with the constitutive modeling of unsaturated soils.

### MODIFIED STATE SURFACE APPROACH AND THE BBM

Sheng et al. (2004) considered that all the existing models are variants of the BBM and the BBM remains one of the fundamental models for unsaturated soils. Zhang and Lytton (2008a and 2008b) proposed a modified state surface approach (MSSA) to study volume change of unsaturated soils. In the MSSA, a conventional void ratio constitutive surface is divided into an elastic surface and a plastic hardening surface. It was found that the state surface used in the BBM consists of three surfaces as shown in Fig.1, an elastic surface AHIF, a plastic collapsible soil surface JIFGB, and a plastic expansive soil surface HCJI as shown in Fig.1. Their mathematical expressions are as follows:

$$e^e = C_1 - \kappa \ln p - \kappa_s \ln (s + p_{at}) \text{ (Elastic unloading/reloading surface)} \quad (1)$$

$$e = C_2 - \kappa_s \ln \left( \frac{s + p_{at}}{p_{at}} \right) - \lambda(s) \ln \left( \frac{p}{p^c} \right) \text{ (Plastic collapsible surface)} \quad (2)$$

$$e = C_3 - \kappa \ln p - \lambda_s \ln (s + p_{at}) \text{ (Plastic expansive surface)} \quad (3)$$

where  $e$  = void ratio,  $p$  = mean net stress,  $s$  = suction,  $\kappa$  = slope of the unloading-reloading line associated to the mean net stress,  $\kappa_s$  = slope of the unloading-reloading line associated to soil suction,  $p_{at}$  = atmospheric pressure. The superscripts “e” represents the elastic change in the specific volume.  $\lambda(s) = \lambda(0)[(1-r)\exp(-\beta s) + r]$ ;  $r$  = parameter controlling the slope of the virgin compression line,  $\beta$  parameter controlling the slope of the virgin compression line for

$s \neq 0, \lambda(0)$  = slope of the virgin compression line associated with the mean net stress at saturation ( $s=0$ );  $p_c$  = reference stress,  $\lambda_s$  = slope of the virgin compression line associated with soil suction, and  $C_1, C_2$  and  $C_3$  = constants. Note that Fig. 1 was plotted in scale based on the real data of Case 3 in Alonso et al. (1990).

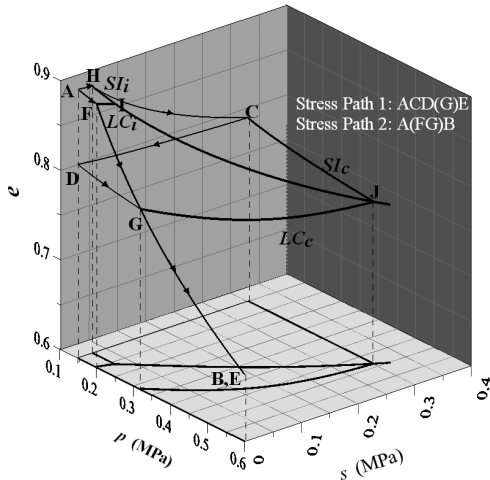


**FIG. 1. State surface used in the BBM (Zhang and Lytton 2006a).**

The plastic hardening surface is unique and remains stationary all the time in the  $e-p-s$  space, but the elastic surface is movable, depending on the occurrence of the plastic deformation. The proposed MSSA was successfully used to explain the BBM and many other unsaturated soil behaviors.

**SOIL RESPONSES UNDER UNDRAINED LOADING CONDITIONS**

An elasto-plastic model for unsaturated soil should be able to model any stress path including soil responses under undrained conditions. During undrained loadings, the stress path depends upon the internal coupling effect between the volumetric volume change and hydraulic behavior of the soil. Discussion of undrained conditions for an elasto-plastic model can provide some useful information regarding how the mechanical and hydraulic behaviors are coupled together in an unsaturated soil.

Let us consider the responses of a soil to isotropic loading and unloading under constant water content conditions as shown in Fig.2 in the BBM. Fig.2a presents the schematic plot of the stress path. The soil sample is initially in the elastic zone at an

arbitrary point A with an initial water content of  $(wG_s)_A$ . The corresponding saturated preconsolidation stress is labeled as  $P_0^*$  and the initial position of the LC yield curve is  $LC_0$ . An isotropic external load is applied to the soil and then immediately taken away from the sample and the corresponding stress path is ABC and CD, respectively. The LC yield curve is taken to a new position  $LC_1$  due to soil yielding. The whole process is so fast that there is no water drainage. For unsaturated soils, the following relationship is always valid:

$$S_r e = wG_s \tag{4}$$

The water content remains constant during the whole process. From points A to B, the soil is in the elastic region and the stress path falls on the elastic surface expressed by Eq. 1 according to the MSSA (Zhang and Lytton 2006a and b). The degree of saturation therefore can be calculated as follows:

$$S_r = \frac{(wG_s)_A}{e} = \frac{(wG_s)_A}{C_1 - \kappa \ln p - \kappa_s \ln (s + p_{at})} \tag{5}$$

From points B to C, the soil is in the elasto-plastic region and the stress path falls on the plastic hardening surface expressed by Eq.2. Correspondingly, the degree of saturation can be expressed as:

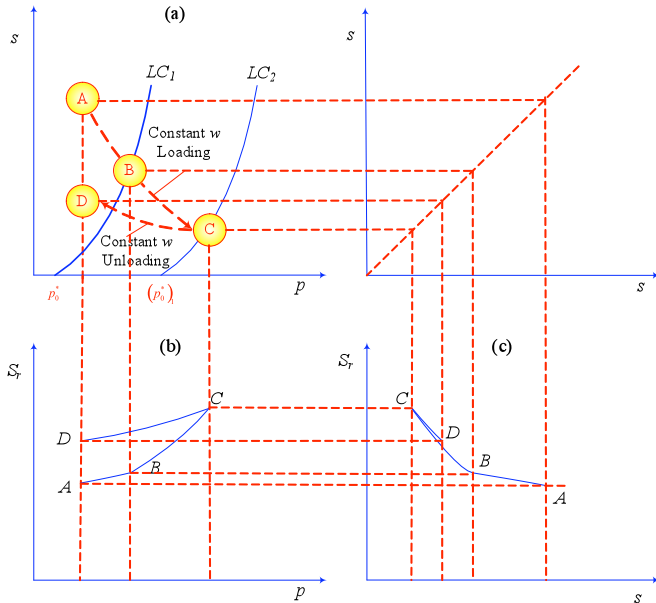


FIG. 2. Schematic soil response to undrained loading and unloading conditions.

$$S_r = \frac{(wG_s)_A}{e} = \frac{(wG_s)_A}{C_2 - \kappa_s \ln \left( \frac{s + p_{at}}{p_{at}} \right) - \lambda(s) \ln \left( \frac{p}{p^c} \right)} \quad (6)$$

From points C to D, it is an elastic unloading process according to the MSSA and BBM, and the stress path falls on a new elastic unloading surface parallel to the surface expressed by Eq. 1. The corresponding degree of saturation is as follows:

$$S_r = \frac{(wG_s)_A}{e} = \frac{(wG_s)_A}{C_1' - \kappa \ln p - \kappa_s \ln (s + p_{at})} \quad (7)$$

During this process, there is plastic deformation. As a results,  $C_1'$  in Eq.7 is less than  $C_1$  in Eq. 5, that is,  $C_1' < C_1$ . The changes in the degree of saturation during this process can be calculated from Eqs. 5 through 7. Figs.2b and 2c are the schematic plots of variations of degree of saturation versus the net normal stress and the matric suction during this process. Similarly, if the soil is loaded under constant water content conditions and the shear stress is not equal to zero, the degree of saturation should be a function of  $p$ ,  $q$ , and  $s$  according to the BBM.

$$S_r = \frac{(wG_s)_A}{e} = \frac{(wG_s)_A}{f(p, s, q)} \quad (8)$$

**PROBLEMS IN EXISTING CONSTITUTIVE MODELS**

The above discussion indicates that the degree of saturation should be a function of both mechanical stress (including normal stress  $p$  and shear stress  $q$ ) and suction  $s$ . However, in many existing constitutive models, main drying and wetting curves were assumed to be unique functions between degree of saturation and matric suction for the description of hydraulic hysteresis (Romero and Vaunat 2000; Tamagnini 2004; Wheeler et al. 2003; Sheng et al. 2004), the degree of saturation is a function of matric suction only. As a result, these constitutive models cannot correctly model the behavior of unsaturated soils under undrained conditions even under elastic conditions as illustrated by Eq.4. Gallipoli et al. (2003a and 2003b) attempted to incorporate the influence of changes of void ratio on the degree of saturation using a unique relationship between the degree of saturation, suction, and void ratio as follows:

$$S_r = \left\{ 1 + \left[ \phi (e)^{\nu} s \right]^n \right\}^{-m} \quad (9)$$

Where  $m$ ,  $n$ ,  $\phi$ , and  $\psi$  are soil constant. When Eq.4 is submitted into Eq.9, it is found that degree of saturation is still a function of suction only during undrained conditions.

## CONCLUSIONS

Based upon the discussion of soil responses under undrained loading and unloading process in the BBM, it is found that the assumption that main drying and wetting curves are unique functions between degree of saturation and matric suction for the description of hydraulic hysteresis is not consistent with the volumetric behavior of the soil. These models cannot simulate the behavior of unsaturated soils under undrained conditions even under elastic conditions.

## REFERENCES

- Bolzon, G., Schrefler, B. A. & Zienkiewicz, O. C. (1996). "Elastoplastic soil constitutive laws generalised to partially saturated states." *Geotechnique* 46, No. 2, 279–289.
- Cui, Y. J. and Delage, P. (1996). "Yielding and Plastic Behaviour of an Unsaturated Compacted Silt." *Geotechnique*, 46(2), pp. 291-311.
- Wheeler, S. J. and Sivakumar, V. (1995). "An Elasto-plastic Critical State Framework for Unsaturated Soil." *Geotechnique*, 45(1), pp. 35-53.
- Gens, A. (1996). "Constitutive Modelling: Application to Compacted Soil." *Proceedings of 1st International Conference on Unsaturated Soils*, Paris; 3, pp. 1179–1200.
- Delage, P. and Graham, I. (1996). "State of the Art Report-Understanding the Behavior of Unsaturated Soils Requires Reliable conceptual models." *Proceedings of 1st International Conference on Unsaturated Soils*, Paris; 3, pp.1223-1256.
- Wheeler, S. J. and Karube, D (1996). "State of the Art Report-Constitutive Modeling." *Proceedings of 1st International Conference on Unsaturated Soils*, Paris; 3, pp.1323-1356.
- Wheeler, S.J., Sharma, R.S. and Buisson, M.S.R. (2003). Coupling of hydraulic hysteresis and stress-strain behavior in unsaturated soils. *Geotechnique*, 53(1), 41-54.
- Vaunat, J. Romero, E. and Jommi, C. (2000). An Elasto-plastic hydro-mechanical model for unsaturated soils." *Experimental evidence and theoretic approaches in unsaturated soils* (Eds. Tarantino, A. and Mancuso, C.), pp. 121-138. Rotterdam: Balkema.
- Tarantino, A. and Tombolato, S. (2005). Coupling of hydraulic and mechanical behaviour in unsaturated compacted clay. *Geotechnique* 55, No.4, 307–317
- Tamagnini R., (2004). An extended Cam-clay model for unsaturated soils with hydraulic hysteresis. *Geotechnique* 54:223–228.
- Gallipoli D, Gens A, Sharma R, and Vaunat J. (2003). An elastoplastic model for unsaturated soil incorporating the effects of suction and degree of saturation on mechanical behaviour. *Geotechnique* 53:123–135
- Sheng D, Sloan SW, Gens A (2004) A constitutive model for unsaturated soils: thermomechanical and computational aspects. *Comput. Mech.* 33:453–465

- Zhang, X. and Lytton, R. L. (2007a). "A Modified State Surface Approach on Unsaturated Soil Behavior Study (I) Basic Concept." *Canadian Geotechnical Journal*. (Accepted pending final revision)
- Zhang, X. and Lytton, R. L. (2007b). "A Modified State Surface Approach on Unsaturated Soil Behavior Study (II) General Formulation." *Canadian Geotechnical Journal*. (Accepted pending final revision)

## Swelling Behavior of Compacted Cohesive Soils-an Absorbed Energy Approach

Zhongjie Zhang<sup>1</sup>, Mingjiang Tao<sup>2</sup>, and Mehmet T. Tumay<sup>3</sup>

<sup>1</sup> Pavement & Geotechnical Research Administrator, Louisiana Transportation Research Center, Baton Rouge, LA 70808, USA; [zzhang@dotd.louisiana.gov](mailto:zzhang@dotd.louisiana.gov)

<sup>2</sup> Assistant Professor, Department of Civil and Environmental Engineering, Worcester Polytechnic Institute, Worcester, MA 01609; [taomj@wpi.edu](mailto:taomj@wpi.edu)

<sup>3</sup> Georgia Gulf Distinguished Professor Emeritus, Department of Civil and Environmental Engineering, Louisiana State University, Baton Rouge, LA 70803, USA; Adjunct Professor, Department of Civil Engineering, Bogazici University, Istanbul, Turkey; [mtumay@eng.lsu.edu](mailto:mtumay@eng.lsu.edu)

**ABSTRACT:** Swelling characteristics of compacted cohesive soil were examined through laboratory tests from an absorbed energy perspective. A series of samples was prepared by a “compression procedure” in the laboratory, in which the energy or work absorbed by tested samples was derived from recorded forces and deformations. Swelling behavior of the compacted samples was found to correlate well with the absorbed energy of the samples. The testing results from this study also led to a correlation between swelling behavior and samples’ basic properties (dry unit weight and moisture content), which will provide a quick approximation for swelling susceptibility in the field. The factors that significantly affect swelling characteristics of the compacted soil were also identified. Good correlations among swelling behavior, the absorbed energy, dry unit weights and moisture contents confirmed the viability of the absorbed energy approach in characterizing swelling aspects of compacted cohesive soils.

### INTRODUCTION

Swelling phenomena of compacted cohesive soils have caused billions of dollars of damage to light weight structures around the world (Nelson and Miller 1997). Due to complex mechanisms of swelling, predicting swelling potential of a certain soil still presents a challenge to geotechnical practitioners. Many factors, such as the type and amount of clay, dry density, initial moisture content, and soils’ suction, have been recognized to significantly affect swelling behavior of cohesive soils. Numerous empirical correlations have been proposed by many researchers to predict swelling behavior. Seed et al. (1962) studied the swelling of artificial sand-clay mineral mixtures. They observed that swelling characteristics are well correlated with the type of clay and the amount of clay content, and an empirical relationship between swelling potential and soils’ plastic indices was proposed. Chen (1975) and Holtz and Gibbs

(1956) proposed their empirical correlations based on different soils and under different surcharges. The swelling of compacted soils is essentially the consequence of reduction in effective stress due to addition of water, thus correlating well with soils' suction values. However, measuring suction of soil samples is even more time-consuming than standard swelling tests in the laboratory. More research on swelling potential of compacted cohesive soils is still needed because a better understanding of swelling mechanism will help in seeking sound engineering measures to solve swelling-related problems.

Zhang et al. (2005a, 2005b, and 2005c) recently examined the properties of compacted soils through an absorbed energy approach, which is the work transferred to soil samples from mechanical compaction. Test results on three soils with different plastic indices indicated that good correlations exist among unconfined compression strength (UCS), the absorbed energy, soil's dry unit weights and moisture contents. These successful preliminary studies encourage the application of the absorbed energy concept to swelling behavior of compacted cohesive soils. A series of samples was molded by using a "compression procedure", and the standard odometer swelling tests were performed on these samples. The results from this study are presented herein, with an emphasis on the correlations among swelling behavior and the absorbed energy.

#### LABORATORY TESTS AND MATERIALS

The soil under investigation was gathered from pavement subgrade on US 190 in Louisiana. Soil's basic properties are summarized in Table 1, with its specific gravity equal to 2.69. Figure 1 shows the standard Proctor compaction curve of the soil. Its maximum dry unit weight was  $14.5 \text{ kN/m}^3$  (91.5 pcf) at an optimum moisture content of 26.1%. The soil is then classified as CL (low plasticity clay) and A-7-6 according to the Unified Soil Classification System and the AASHTO System, respectively.

Three sets of samples, as illustrated in Figure 1, were molded by using a "compression procedure". Among these samples, S-I had the same molding moisture content, S-II had the same dry unit weight, and S-III had the same degree of saturation. The "compression procedure" used to mold samples in this study is illustrated in Figure 2. Specifically, an odometer ring was placed at the bottom of a standard compaction mold. The mold was filled up to a height of 2 in. with predetermined amount of the soil-water mixture. Then, the soil-filled mold was placed in a load frame tester, and the soil sample is compressed to a predetermined density by a load cell. The forces applied to the soil sample and the sample's deformations during this compression process were recorded by a personal computer with a data acquisition card. A typical force-deformation curve is shown in Figure 2(d), with which the absorbed energy by the sample can readily be calculated.

**Table 1. Physical indices of tested soils**

Soil Type	Silt (%)	Clay (%)	LL (%)	PI (%)	$G_s$	Classification USCS/AASHTO
Clayey silt	60.7	28.4	46	18	2.69	CL/A-7-6

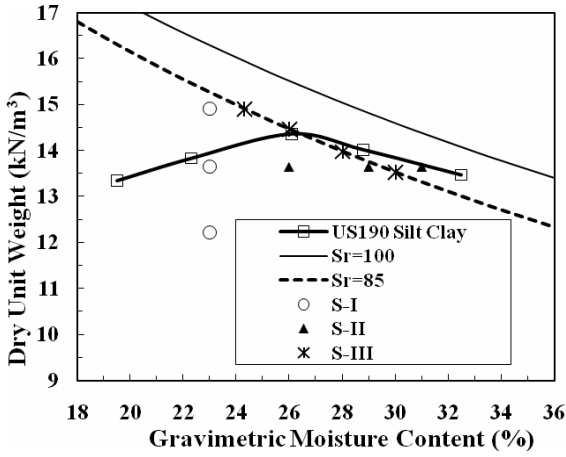


FIG. 1. Standard Proctor compaction curve of tested soil

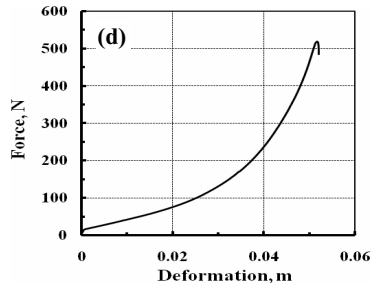


FIG. 2. “Compression procedure” for sample preparation: (a) compaction mold; (b) assemblage of compaction mold and odometer ring; (c) a load frame to compress samples; and (d) a typical force-deformation curve

After the samples were extruded from the compaction mold and trimmed, the standard odometer swelling test was performed by following ASTM D4546 method A. For each testing point shown in Figure 1, three duplicated samples were tested to assure the repeatability.

TEST RESULTS AND DISCUSSION

The swelling results are presented in terms of swelling pressures and swelling potential. Swelling pressure is the pressure value to return the specimen back its original state after swelling. Swelling potential is defined as the change in height in percentage of a sample’s initial height.

Linear correlations between swelling characteristics (swelling pressure and swelling potential) and the absorbed energy are shown in Figures 3(a) and 3(b). As expected, the more energy soil samples absorbed during the mechanical compaction process, the higher swelling potential the soil samples will possess.

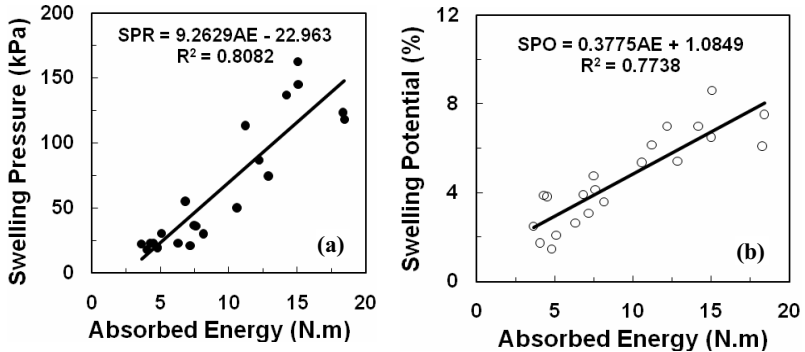


FIG. 3. (a) Swelling pressure versus absorbed energy (SPR–Swelling Pressure); and (b) swelling potential versus absorbed energy (SPO–Swelling Potential)

As suggested by Zhang et al. (2005a), the absorbed energy correlates well with soil state parameters (dry unit weight and moisture content). Such correlations make it possible to correlate swelling characteristics with soils’ state parameters. Based on the

results from this study, an absorbed energy-dry unit weight-moisture content correlation was obtained as:

$$AE = w^{-4.89}(0.0054\gamma_d - 0.0596) \quad R^2 = 0.838 \quad (1)$$

Where  $AE$  = absorbed energy in N.m;  $w$  = moisture content in decimal; and  $\gamma_d$  = dry unit weight in  $\text{kN/m}^3$ .

Then, good correlations among swelling characteristics, dry unit weight, and moisture content were also developed, which are given by Eqs. (2) and (3).

$$SPR = w^{-4.89}(0.0596\gamma_d - 0.7135) \quad R^2 = 0.720 \quad (2)$$

$$SPO = w^{-4.89}(0.002\gamma_d - 0.0225) + 1.085 \quad R^2 = 0.802 \quad (3)$$

Where  $SPR$  = swelling pressure in kPa; and  $SPO$  = swelling potential in percent. There correlations are also graphically illustrated in Figures 4(a) and 4(b).

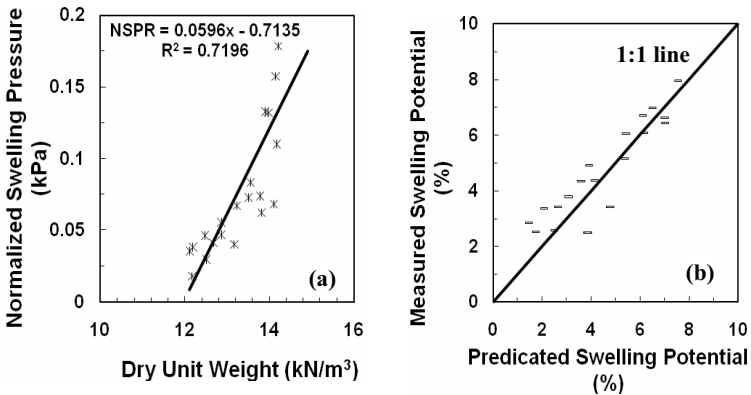


**FIG. 4. (a) Normalized swelling pressure versus dry unit weight (NSPR: normalized swelling pressure with respect to moisture content); and (b) measured swelling pressure versus predicted swelling pressure**

From Eqs. (2) and (3), it can be noted that  $SPR$  and  $SPO$  increase linearly with the increase in dry unit weight at a constant moisture content; while these two swelling parameters decrease nonlinearly with the increase in moisture content at a constant dry unit weight.

It is worth mentioning that swelling pressure and swelling potential values reported in this study were measured under a negligible amount of overburden pressures. Therefore, swelling characteristics as well as developed regression equations are relevant to the maximum swelling of the tested soil.

Figures 3(a) and (b) illustrate the relationships that swelling pressure and swelling potential increase linearly with absorbed energy of the soil. However, these relationships are constrained by an upper limit of absorbed energy or dry unit weight of the soil during mechanical compaction, which is bounded by the zero air void line as demonstrated in Figure 1.

## CONCLUSIONS

A series of laboratory tests were performed with respect to compacted soils' swelling characteristics. Some conclusions are drawn as follows:

- Swelling characteristics of compacted soils (swelling pressure and swelling potential) correlated well with the energy transferred into soils during the mechanical compaction pressure. The absorbed energy concept provides an alternative approach to understand swelling phenomena.
- Both dry unit weight and moisture content significantly affected swelling characteristics of compacted soils. By using regression equations (2) and (3), swelling characteristics can be reasonably and quickly approximated.
- The conclusions from this study are only valid for free swelling conditions since swelling pressures and swelling potentials were measured under negligible overburden pressures. Additional studies are under way with respect to the influence of overburden pressures.

## ACKNOWLEDGMENTS

The authors would like to thank Ryan Hedlund for conducting laboratory testing.

## REFERENCES

- Chen, F. H. (1975). *Foundations on expansive soils*, Elsevier Scientific Publishing Co., New York, 1<sup>st</sup> edition.
- Holtz, W. G., and Gibbs, H. J. (1956). "Engineering properties of expansive clays." *Transactions, ASCE*, Vol. 121, 641-677.
- Nelson, J. D., and Miller, D. J. (1997). *Expansive Soils: Problems and Practice in Foundation and Pavement Engineering*, John Wiley & Sons Inc., New Jersey.
- Seed, H. B., Woodward, R. J., and Lundgren, R. (1962). "Predication of swelling potential for compacted clays." *Journal of Soil Mechanics and Foundations Divisions, ASCE*, Vol. 88, No. SM 3, 53-87.
- Zhang, Z., Tao, M., and Tumay, M. T. (2005a). "Absorbed energy and soil performance." *Geotechnical Testing Journal*, ASTM, Vol.28, No.4, 404-409.
- Zhang, Z., Tao, M., and Tumay, M. T. (2005b). "Absorbed energy and compacted soil behavior," *Proceeding of the 16th International Conference on Soil Mechanics and Geotechnical Engineering*, Osaka, Japan.
- Zhang, Z., Tao, M., and Tumay, M.T. (2005c). "Behavior of unsaturated soils-an absorbed energy approach." *International Conference on Problematic Soils (Keynote paper)*, Famagusta, North Cyprus, ISBN 975-8401-22-X, Vol. 1, 47-57.

## Gradient-dependent Damage Constitutive: the Second-order Gradient Damage Model

ZHAO Bing<sup>1,2,\*</sup> ZHENG Ying-ren<sup>2</sup> ZENG Ming-hua<sup>1</sup> TANG Xue-song<sup>2</sup>  
YAN Xiao-Qiang<sup>3,1</sup>

<sup>1</sup>School of Civil Engineering and Architecture, Changsha University of Science and Technology, Changsha, China; \* Correspondence: zhaob\_m-y@163.com;

<sup>2</sup>Department of Architectural Engineering, Logistic Engineering University of PLA, Chongqing, China;

<sup>3</sup>School of Mathematics and Computer Science, Ningxia University, Yinchuan, China

**ABSTRACT:** When the strain tensor, the scalar damage quantity and the Laplacian thereof serve as the state variables of Helmholtz free energy, the general expressions of elasticity-gradient damage constitutive equations are derived directly from the basic law of irreversible thermodynamics by constitutive functional expansion method at the initial state. When damage variable equals to zero, the expressions can be simplified to linear elastic constitutive equations, when the damage gradient vanishes, the expressions can be simplified to the classical damage constitutive equations based on the strain equivalence hypothesis.

### INTRODUCTION

Since the pioneering works by *Kachanov*(1958) and *Rabotnov*(1963) for creep failure of metals, the damage mechanics has been greatly developed and has become a most active research area. Numerical analyses based on these local damage models, however, are often found to depend on the mesh size. The growth of damage tends to localize in the smallest band that can be captured by the spatial discretization. Upon mesh refinement, the solution converges to a localization zone of zero width (in the limit), which results in zero energy dissipation and hence the results become physically meaningless. This non-physical behavior is caused by the fact that the localization of damage is not consistent with the concept of a continuous damage field, which forms the basis of the continuum damage mechanics approach. Many solutions have been proposed to restore the objectivity of the numerical modeling and the physical reliability of the results. The most successful regularization techniques are based on the inclusion of the nonlocal effect. The idea of nonlocal theory, introduced during the 1960s, is to consider the field variables to be the mean of a spatial neighborhood of each point under consideration. Because the microstructure scale and the internal characteristic which indicate the interaction of the microstructure are

introduced, the nonlocal theory has unique advantage in solving strain localization and softening. If all of the field variables in equations are treated as nonlocal, the problem will be too complex to solve, so lots of models were improved by some scholars. A nonlocal damage theory in which the damage energy release rate were dealt with nonlocal average, was first proposed by Pijaudie and Bazant in 1987. An elastic-plastic nonlocal constitutive model was proposed by Bazant and Lin in 1987; In 1988, the variable local strain in damage parameters has been dealt through nonlocal average by Bazant; the nonlocal stress has been dealt through spatial average, which has been proposed by Bazant in 1994. The essential idea of above nonlocal damage model is to subject to nonlocal treatment only those variables that control softening, and treat the other variables as local. Because all above nonlocal damage theory depended on empirical hypotheses, to construct a nonlocal damage model is lack of the unity in methodology and the tightness in theory. An overall review has been given by M Jirasek, and a successful nonlocal model should satisfy the two fallows: the one is that the calculation results under elastics should be consistent with the nonlocal model; the other is the solution of pole units in tension should be consistent with actual solution.

The paper is organized in three sections. After a brief review of literatures in the first section, the Helmholtz free energy function  $\Psi$ , with state variables of strain tensor, scalar damage variable and damage gradient are introduced, based on this introduction, a general forms of gradient anisotropic damage model is derived in the second section. In the third section, the degenerated forms of general gradient anisotropic damage model were discussed.

## ELASTICITY-GRADIENT DAMAGE BASIC EQUATION

### Thermodynamics Equation

For an isothermal and infinitesimal deformation process, the Clausius-Duhem inequtation is

$$\sigma_{ij} \cdot \dot{\varepsilon}_{ij} - \dot{\Psi} \geq 0 \quad (1)$$

where  $\sigma_{ij}$  is Cauchy stress tensor,  $\varepsilon_{ij}$  is infinitesimal strain tensor,  $\Psi$  is the Helmholtz free energy (specific free energy) of per unit volume.

For isotropic elastic damage problem, strain tensor and damage quantity are served as state quantities of free energy in classical damage theory. But in fact, the damage quantity represents nothing more than statistical average microscopic breakage on a representative element volume (REV). When damage is not very sharp in space, it is appropriate to use the statistical average quantity instead of the reality quantity. But damage gradient will always take place along with the inhomogeneity which always existent. When damage is high nonlinear in REV (for example, localization occur), the free energy state of REV will be changed with the damage gradient  $\nabla^2 D$ . Therefore, in the paper, it is natural to assume that the free energy depends on the damage gradient  $\nabla^2 D$ , as well as depends on damage quantity  $D$  and strain tensor  $\varepsilon_{ij}$ . Then,  $\Psi$  can denote as

$$\Psi = \Psi(\varepsilon_{ij}, D, \nabla^2 D) \quad (2)$$

$$\dot{\Psi} = \frac{\partial \Psi}{\partial \varepsilon_{ij}} \dot{\varepsilon}_{ij} + \frac{\partial \Psi}{\partial D} \dot{D} + \frac{\partial \Psi}{\partial \nabla^2 D} \nabla^2 \dot{D} \quad (3)$$

The substitution of Eq. (3) into Eq. (1) yields:

$$\left( \sigma_{ij} - \frac{\partial \Psi}{\partial \varepsilon_{ij}} \right) \dot{\varepsilon}_{ij} - \left( \frac{\partial \Psi}{\partial D} \dot{D} + \frac{\partial \Psi}{\partial \nabla^2 D} \nabla^2 \dot{D} \right) \geq 0 \quad (4)$$

The inequality (4) holds for an arbitrary value of  $\dot{\varepsilon}_{ij}$ , which require

$$\sigma_{ij} = \frac{\partial \Psi}{\partial \varepsilon_{ij}} \quad (5)$$

$$- \left( \frac{\partial \Psi}{\partial D} \dot{D} + \frac{\partial \Psi}{\partial \nabla^2 D} \nabla^2 \dot{D} \right) \geq 0 \quad (6)$$

Defining damage energy release rate as

$$Y = - \frac{\partial \Psi}{\partial D} \quad (7)$$

then the inequality (6) becomes

$$Y \left( \dot{D} - \frac{\partial D}{\partial \nabla^2 D} \nabla^2 \dot{D} \right) \geq 0 \quad (8)$$

where,  $\frac{\partial D}{\partial \nabla^2 D}$  has dimension of length, and it reflects microstructure interactive of material.

Let:

$$l^2 = \frac{\partial D}{\partial \nabla^2 D} \quad (9)$$

where,  $l^2$  is internal characteristic length parameters . Then Eq. (8) is written as:

$$Y \left( \dot{D} - l^2 \nabla^2 \dot{D} \right) \geq 0 \quad (8a)$$

### Elasticity-gradient Damage Basic Equation

The initial damage state of a material is assumed to be  $\varepsilon_{ij} = (\varepsilon_{ij})_0$ ,  $c_{ij} = (c_{ij})_0$ ,  $Y = Y_0$ , where  $D=0$  and  $\nabla^2 D=0$ . The Helmholtz free energy  $\Psi$  is expanded to Taylor's series with respect to  $\varepsilon_{ij}$ ,  $D$  and  $\nabla^2 D$ . The series is truncated at the second power of  $\varepsilon_{ij}$ , the  $N$ \_th power of  $D$  and the first power of  $\nabla^2 D$ , since  $\varepsilon_{ij}$  is an infinitesimal variable and  $D$  is a variable with finite values ( $0 \leq D \leq 1$ ). For elastic isotropic damage, the expansion of  $\Psi$  is:

$$\begin{aligned} \Psi = & \Psi_0 + \sum_{r=1}^N C^{(r)} D^r + \left( \frac{\partial \Psi}{\partial \nabla^2 D} \right)_0 \nabla^2 D + \sum_{r=0}^N F_{ij}^{(r)} D^r \varepsilon_{ij} + \left( \frac{\partial \Psi}{\partial \nabla^2 D} \right)_0 \nabla^2 D M_{ij} \varepsilon_{ij} \\ & + \left( \frac{\partial \Psi}{\partial \nabla^2 D} \right)_0 \nabla^2 D \sum_{r=1}^N H_{ij}^{(r)} D^r \varepsilon_{ij} + \frac{1}{2} C_{ijkl} \varepsilon_{ij} \varepsilon_{kl} + \frac{1}{2} \sum_{r=1}^N A_{ijkl}^{(r)} D^r \varepsilon_{ij} \varepsilon_{kl} \end{aligned}$$

$$\begin{aligned}
 & + \frac{1}{2} \left( \frac{\partial \Psi}{\partial \nabla^2 \mathbf{D}} \right)_0 \nabla^2 \mathbf{D} \sum_{r=1}^N \mathbf{B}_{ijkl}^{(r)} \mathbf{D}^r \varepsilon_{ij} \varepsilon_{kl} + \frac{1}{2} \left( \frac{\partial \Psi}{\partial \nabla^2 \mathbf{D}} \right)_0 \nabla^2 \mathbf{D} N_{ijkl} \varepsilon_{ij} \varepsilon_{kl} \\
 & + \left( \frac{\partial \Psi}{\partial \nabla^2 \mathbf{D}} \right)_0 \nabla^2 \mathbf{D} \sum_{r=1}^N \mathbf{P}^{(r)} \mathbf{D}^r
 \end{aligned} \tag{10}$$

where,  $C^{(r)}$  and  $\mathbf{P}^{(r)}$  are scalar coefficient,  $F_{ij}^{(r)}$ ,  $M_{ij}$  and  $H_{ij}^{(r)}$  are two order tensor coefficient,  $C_{ijkl}$ ,  $A_{ijkl}^{(r)}$ ,  $B_{ijkl}^{(r)}$  and  $N_{ijkl}$  are four order tensor coefficient.  $\Psi_0$  denote Helmholtz free energy of initial damage state,

Let  $Y_0$  the damage energy release rate of initial damage state

$$Y_0 = - \left( \frac{\partial \Psi}{\partial \mathbf{D}} \right)_0 \tag{11}$$

it denote the threshold value of damage energy release rate when damage take place, then  $\left( \frac{\partial \Psi}{\partial \nabla^2 \mathbf{D}} \right)_0 = \left( \frac{\partial \Psi}{\partial \mathbf{D}} \right)_0 \frac{\partial \mathbf{D}}{\partial \nabla^2 \mathbf{D}} = - Y_0 I^2$ . The substitution of  $\left( \frac{\partial \Psi}{\partial \nabla^2 \mathbf{D}} \right)_0$  into Eqs. (10) yields:

$$\begin{aligned}
 \Psi = & \Psi_0 + \sum_{r=1}^N C^{(r)} \mathbf{D}^r - Y_0 I^2 \nabla^2 \mathbf{D} + \sum_{r=0}^N F_{ij}^{(r)} \mathbf{D}^r \varepsilon_{ij} - Y_0 I^2 \nabla^2 \mathbf{D} M_{ij} \varepsilon_{ij} \\
 & - Y_0 I^2 \nabla^2 \mathbf{D} \sum_{r=1}^N H_{ij}^{(r)} \mathbf{D}^r \varepsilon_{ij} + \frac{1}{2} C_{ijkl} \varepsilon_{ij} \varepsilon_{kl} + \frac{1}{2} \sum_{r=1}^N A_{ijkl}^{(r)} \mathbf{D}^r \varepsilon_{ij} \varepsilon_{kl} \\
 & - \frac{1}{2} Y_0 I^2 \nabla^2 \mathbf{D} \sum_{r=1}^N B_{ijkl}^{(r)} \mathbf{D}^r \varepsilon_{ij} \varepsilon_{kl} - \frac{1}{2} Y_0 I^2 \nabla^2 \mathbf{D} N_{ijkl} \varepsilon_{ij} \varepsilon_{kl} \\
 & - Y_0 I^2 \nabla^2 \mathbf{D} \sum_{r=1}^N \mathbf{P}^{(r)} \mathbf{D}^r
 \end{aligned} \tag{12}$$

Eq. (12) is the general expressions of Helmholtz free energy. The substitution of Eq. (12) into Eq. (5) and Eq. (7) yields:

$$\begin{aligned}
 \sigma_{ij} = & \left\{ C_{ijkl} + \sum_{r=1}^N A_{ijkl}^{(r)} \mathbf{D}^r - Y_0 I^2 \nabla^2 \mathbf{D} \sum_{r=1}^N B_{ijkl}^{(r)} \mathbf{D}^r - Y_0 I^2 \nabla^2 \mathbf{D} N_{ijkl} \right\} \varepsilon_{kl} \\
 & + \sum_{r=0}^N F_{ij}^{(r)} \mathbf{D}^r - Y_0 I^2 \nabla^2 \mathbf{D} M_{ij} - Y_0 I^2 \nabla^2 \mathbf{D} \sum_{r=1}^N H_{ij}^{(r)} \mathbf{D}^r
 \end{aligned} \tag{13}$$

$$\begin{aligned}
 \mathbf{Y} = & Y_0 - \sum_{r=1}^N r C^{(r)} \mathbf{D}^{r-1} - \sum_{r=0}^N F_{ij}^{(r)} r \mathbf{D}^{r-1} \varepsilon_{ij} + Y_0 M_{ij} \varepsilon_{ij} + Y_0 I^2 \nabla^2 \mathbf{D} \sum_{r=1}^N H_{ij}^{(r)} r \mathbf{D}^{r-1} \varepsilon_{ij} \\
 & + Y_0 \sum_{r=1}^N H_{ij}^{(r)} \mathbf{D}^r \varepsilon_{ij} - \frac{1}{2} \sum_{r=1}^N A_{ijkl}^{(r)} r \mathbf{D}^{r-1} \varepsilon_{ij} \varepsilon_{kl} + \frac{1}{2} Y_0 I^2 \nabla^2 \mathbf{D} \sum_{r=1}^N B_{ijkl}^{(r)} r \mathbf{D}^{r-1} \varepsilon_{ij} \varepsilon_{kl} \\
 & + \frac{1}{2} Y_0 \sum_{r=1}^N B_{ijkl}^{(r)} \mathbf{D}^r \varepsilon_{ij} \varepsilon_{kl} + \frac{1}{2} Y_0 N_{ijkl} \varepsilon_{ij} \varepsilon_{kl} + Y_0 I^2 \nabla^2 \mathbf{D} \sum_{r=1}^N \mathbf{P}^{(r)} r \mathbf{D}^{r-1} \\
 & + Y_0 \sum_{r=1}^N \mathbf{P}^{(r)} \mathbf{D}^r
 \end{aligned} \tag{14}$$

where the higher order terms of  $\varepsilon_{kl}$  in Eq. (13) were ignored.

Considering the irreversibility of damage, when the damaged material is unloaded completely to initial damaged state, it is seen that  $\sigma_{ij} = (\sigma_{ij})_0$ ,  $\varepsilon_{ij} = (\varepsilon_{ij})_0$ ,  $(\sigma_{ij})_0 = C_{ijkl} (\varepsilon_{kl})_0$ ,  $Y = Y_0$  and  $D \neq 0$ ,  $\nabla^2 D \neq 0$ . ( $D$  may be an arbitrary positive value in its allowable range). From Eq. (13) and Eq. (14), it is found that:

$$\left\{ C_{ijkl} + \sum_{r=1}^N A_{ijkl}^{(r)} D^r - Y_0 l^2 \nabla^2 D \sum_{r=1}^N B_{ijkl}^{(r)} D^r - Y_0 l^2 \nabla^2 D N_{ijkl} \right\} (\varepsilon_{kl})_0 + \sum_{r=0}^N F_{ij}^{(r)} D^r - Y_0 l^2 \nabla^2 D M_{ij} - Y_0 l^2 \nabla^2 D \sum_{r=1}^N H_{ij}^{(r)} D^r = 0 \quad (15)$$

and

$$\begin{aligned} & - \sum_{r=1}^N r C^{(r)} D^{r-1} - \sum_{r=0}^N F_{ij}^{(r)} r D^{r-1} (\varepsilon_{ij})_0 + Y_0 M_{ij} (\varepsilon_{ij})_0 \\ & + Y_0 l^2 \nabla^2 D \sum_{r=1}^N H_{ij}^{(r)} r D^{r-1} (\varepsilon_{ij})_0 + Y_0 \sum_{r=1}^N H_{ij}^{(r)} D^r (\varepsilon_{ij})_0 \\ & - \frac{1}{2} \sum_{r=1}^N A_{ijkl}^{(r)} r D^{r-1} (\varepsilon_{ij})_0 (\varepsilon_{kl})_0 + \frac{1}{2} Y_0 l^2 \nabla^2 D \sum_{r=1}^N B_{ijkl}^{(r)} r D^{r-1} (\varepsilon_{ij})_0 (\varepsilon_{kl})_0 \\ & + \frac{1}{2} Y_0 \sum_{r=1}^N B_{ijkl}^{(r)} D^r (\varepsilon_{ij})_0 (\varepsilon_{kl})_0 + \frac{1}{2} Y_0 N_{ijkl} (\varepsilon_{ij})_0 (\varepsilon_{kl})_0 \\ & + Y_0 l^2 \nabla^2 D \sum_{r=1}^N P^{(r)} r D^{r-1} + Y_0 \sum_{r=1}^N P^{(r)} D^r = 0 \end{aligned} \quad (16)$$

In a arbitrary damage state, there is

$$\varepsilon_{ij} = (\varepsilon_{ij})_0 + d\varepsilon_{ij}, \quad \sigma_{ij} = (\sigma_{ij})_0 + d\sigma_{ij}, \quad (\sigma_{ij})_0 = C_{ijkl} (\varepsilon_{ij})_0 \quad (17)$$

Ignoring the higher order term of  $d\varepsilon_{ij}$ , the substitution of Eqs.(15)-(17) into Eqs.(13)-(14) yields

$$\begin{aligned} d\sigma_{ij} & = \left\{ C_{ijkl} + \sum_{r=1}^N A_{ijkl}^{(r)} D^r - Y_0 l^2 \nabla^2 D \sum_{r=1}^N B_{ijkl}^{(r)} D^r - Y_0 l^2 \nabla^2 D N_{ijkl} \right\} d\varepsilon_{kl} \quad (18) \\ Y & = Y_0 - \sum_{r=0}^N F_{ij}^{(r)} r D^{r-1} d\varepsilon_{ij} + Y_0 M_{ij} d\varepsilon_{ij} + Y_0 l^2 \nabla^2 D \sum_{r=1}^N H_{ij}^{(r)} r D^{r-1} d\varepsilon_{ij} \\ & + Y_0 \sum_{r=1}^N H_{ij}^{(r)} D^r d\varepsilon_{ij} + \left\{ -\frac{1}{2} \sum_{r=1}^N A_{ijkl}^{(r)} r D^{r-1} + \frac{1}{2} Y_0 l^2 \nabla^2 D \sum_{r=1}^N B_{ijkl}^{(r)} r D^{r-1} \right. \\ & \left. + \frac{1}{2} Y_0 \sum_{r=1}^N B_{ijkl}^{(r)} D^r + \frac{1}{2} Y_0 N_{ijkl} \right\} \left\{ d\varepsilon_{kl} (\varepsilon_{ij})_0 + d\varepsilon_{ij} (\varepsilon_{kl})_0 \right\} \end{aligned} \quad (19)$$

Eq. (18) and Eq. (19) are the general forms of gradient anisotropic damage model.

## DISCUSSION

(1) When  $D=0$ ,  $\nabla^2 D=0$ , Eq.(18) is degenerated into linear elastic stress-strain constitutive equations, where  $C_{ijkl}$  is elastic tensor.

$$d\sigma_{ij} = C_{ijkl} d\varepsilon_{kl} \quad (20)$$

(2) When  $D \neq 0$ ,  $\nabla^2 D = 0$  and  $N = 1$ ,  $A_{ijkl}^{(1)} = -C_{ijkl}$ ,  $B_{ijkl}^{(1)} = 0$ ,  $N_{ijkl} = 0$ ,  $F_{ij}^{(1)} = 0$ ,  $M_{ij} = 0$ ,  $H_{ij}^{(1)} = 0$ , Eqs.(18)-(19) are degenerated into the classical damage constitutive equations based on the strain equivalence hypothesis:

$$d\sigma_{ij} = (1-D) C_{ijkl} d\epsilon_{kl} \quad (21)$$

$$Y = Y_0 + \frac{1}{2} C_{ijkl} \left\{ d\epsilon_{kl}(\epsilon_{ij})_0 + d\epsilon_{ij}(\epsilon_{kl})_0 \right\} \quad (22)$$

(3) When  $D \neq 0$ ,  $\nabla^2 D \neq 0$  and  $N = 1$ ,  $A_{ijkl}^{(1)} = -C_{ijkl}$ ,  $B_{ijkl}^{(1)} = -C_{ijkl}$ ,  $N_{ijkl} = C_{ijkl}$ ,  $F_{ij}^{(1)} = 0$ ,  $M_{ij} = 0$ ,  $H_{ij}^{(1)} = 0$ , the simplified gradient damage equation are obtained from Eqs. (18)-(19):

$$d\sigma_{ij} = C_{ijkl} d\epsilon_{kl} (1-D) \left\{ 1 - Y_0 l^2 \nabla^2 D \right\} \quad (23)$$

$$Y = Y_0 + \frac{1}{2} C_{ijkl} \left\{ d\epsilon_{kl}(\epsilon_{ij})_0 + d\epsilon_{ij}(\epsilon_{kl})_0 \right\} \left\{ 1 + Y_0 (1-D - l^2 \nabla^2 D) \right\} \quad (24)$$

## CONCLUSIONS

(1) When damage gradient serve as the state variables of Helmholtz free energy, the general expressions of elasticity-II order gradient damage constitutive equations are derived directly by constitutive functional expansion method at the initial damage state.

(2) When damage variable equals to zero, the elasticity-II order gradient damage constitutive equations can be simplified to linear elastic constitutive equations, when the damage gradient vanishes, the expressions can be simplified to the classical damage constitutive equations based on the strain equivalence hypothesis.

## ACKNOWLEDGMENTS

The authors appreciate the support of the Scientific Research Fund of Hunan Provincial Education Department (07B004), and the support of the project of Hunan Provincial science and technology Department (2008FJ3013).

## REFERENCES

- Kachanov, L. M.. (1958). "Time of the rupture process under creep conditions". *Izv Akad Nauk USSR, Otd. Techn. Nauk.*, 8: 26~31.
- Rabotnov Y N. (1963). "On the equations of state for creep". *Prog. in Appl. Mech.*, 307~315.
- Tang, X. S., Jiang, C. P., Zheng, J. L.. (2002). "Anisotropic elastic constitutive relations for damaged materials by application of irreversible thermodynamics". *Theoretical and Applied Fracture Mechanics*, Vol. 38(3):211~220.
- Belytschko, T.. (1986). "Strain-softening materials and finite-element solutions" *.Int. J. Solids Struct.* Vol. 23:163-180.
- Bazant, Z. P., Ta-peng, Chang. (1987). "Nonlocal finite element analysis of strain-softening solids". *Journal of Engineering Mechanics*, Vol.113:89-105.
- Zhao, Bing., Li, Ning, Sheng, Guo-gang.(2005). "Recent development of strain localization of softening geo-materials". *Rock and Soil Mechanics*, Vol.26(3): 111-118. (in Chinese)

- Eringen, A. C.. (1972). "Nonlocal polar elastic continua" *Int. J. Solids Struct.* Vol. 10: 233-248.
- Ellen, K., Ekkehard, R., de Borst, R.. (2000). "An anisotropic gradient damage model for quasi-brittle materials". *Computer Methods of Applied Mechanical and Engineering*, Vol. 183(1): 87-103.
- Pijaudier, G., Bazant, Z. P.. (1987). "Nonlocal damage theory". *Journal of Engineering Mechanics*, Vol.113: 1512-1533.
- Bazant, Z. P., Peng-Bao, Lin. (1987). "Nonlocal yield limit degradation" . *Int. J. for Num. Methods in Engineering*, Vol. 26: 1805-1823.
- Bazant Z P, Feng-Bao Lin. (1988). "Nonlocal smeared cracking model for concrete fracture". *Journal of Engineer- ing Mechanics*, Vol. 114: 2493-2511.
- Bazant, Z. P., Pijaudier, G.(1988)."Nonlocal continuum damage, localization, instability and convergence" . *Journal of Applied Mechanics*, Vol. 55:287-293.
- Bazant, Z. P.. (1994). "Nonlocal damage theory based on micro-mechanics of crack interactions". *Journal of Engineering Mechanics*, Vol. 120:593-617.
- Milan, J. (1998). "Nonlocal models for damage and fracture: comparison of approaches". *Int. J. Solids Structures*, Vol. 35: 4133-4145.
- Tang, X. S., Jiang C.P., Zheng J. L.. (2001)."General Expressions of Constitutive Equations for Isotropic Elastic Damaged Materials". *Applied Mathematics and Mechanic*, Vol. 22(12):1468-1475.

## Analysis of Two-Dimensional Consolidation of Unsaturated Soils

Xue-shan CAO<sup>1</sup>, Zong-ze YIN<sup>2</sup>

<sup>1</sup>Associate Professor, Hohai University, Nanjing 210098, China, Caoxueshan\_7712@hhu.edu.cn

<sup>2</sup>Professor, Hohai University, Nanjing 210098, China, yinzz@hhu.edu.cn

**ABSTRACT:** It is essential to study the practicality of consolidation and simplified approach of unsaturated soils with high degree of saturation. The water and air in the pores can be regarded as a mixed fluid in unsaturated soils when degree of saturation is between 70% and 95%. Mass balance, mixed fluid continuity, modified water continuity equations are then established regarding the compressibility of the mixed fluid in the pores. The influence of permeability and initial degree of saturation of soils are analyzed with the new method. The conclusions are: there is a strong interaction between the pore-air and pore-water in the consolidation of unsaturated soils with low permeability; the degree of pore-air pressure influence on consolidation of unsaturated soils is related to initial degree of saturation of soils.

### INTRODUCTION

Infrastructure construction in China has increased tremendously as a result of the high speed economic development since 1980s. There are many problems related to the consolidation of unsaturated soils, such as the problems with slope stability of expansive soils in the south to north water transfer canal and the hydraulic fracturing in core wall of a high rock-fill dam. Therefore, it is essential to study a practical approach for the consolidation of unsaturated soils under the influence of permeability and initial degree of saturation.

### METHODS OF CONSOLIDATION OF UNSATURATED SOILS.

The consolidation of unsaturated soils is very complex, because of the interaction between pore-air and pore-water. The two-phase fluid, as put forwards by Fredlund and Rahardjo(1993), established employing the pore-air and pore-water continuity equations, can be applied for any degree of saturation. However, it has too many variables and equations which are difficult to solve in a two-dimensional problem(Dakshanamurthy et al.1984), making it very difficult for applications. In fact, the consolidation method of unsaturated soils can be simplified under some degree of saturation.

(1) unsaturated soils with  $S_r < 40\%$ . The pore-water is absorbed in soil skeleton, and the pore-air is connected with outside. In this case, the pore-air can move freely and the increase of the pore-water pressure is very small, and the deformation can take place quickly under loading. Therefore, the finite element method using total stresses could be applied to calculate the soil deformation.

(2) unsaturated soils with  $S_r > 95\%$ . The compressibility of pore-fluid could be ignored because there is less amount of air in the pores or the air is dissolved in water. Therefore, the Biot consolidation theory of saturated soils could be used for deformations.

(3) unsaturated soils with  $40\% < S_r < 70\%$ . The pore-water is adsorbed on the soil particles in the pore space, and the pore-air occupies the center portion of the pore space. The pore-air has very high coefficient of permeability. Therefore, the continuity equation is established and the pore-air pressure is dissipated quickly (Yin 2007; Ling et al. 2005).

(4) unsaturated soils with  $70\% < S_r < 95\%$ . The pore-water could move freely. The pore-air is occluded in the water and moves with the pore-water. Then, the water and air in the pores are regarded as a mixed fluid with a single compressibility value, and the fluid continuity equation is established to simplify the consolidation problem (Chang et al. 1983; Yin et al. 1998, 2007; Cao et al. 2008). The method with simple consolidation equations could be applied in engineering with a few parameters. It was originally put forward by Chang & Duncan (1983), and was improved by Yin et al. in 1998. Although there are many achievements on the method, some assumptions are unreasonable, and the suction measurements are difficult. Fortunately, it is an important development that water continuity equation (Yin et al. 2007; Cao et al. 2008), put forward by Yin et al., is added to calculate pore-water pressure. Then the pore-air pressure, and suction could be obtained. But there are still some defects. Therefore, a more reasonable and simplified method of fluid consolidation needs to be developed by improving the water continuity equation.

## ESTABLISHING CONSOLIDATION EQUATIONS FOR UNSATURATED SOILS

When the degree of saturation is high, the pore-water and pore-air are assumed as a mixed fluid moving together. Continuity equation of the mixed fluid is established using the coefficient of mixed fluid and the compressibility of mixed fluid.

### Fluid pressure

The mixed fluid pressure  $u_m$  is a weighted average of the pore-water pressure  $u_w$  and pore-air pressure  $u_a$  through the parameter  $\chi$ :

$$u_m = (1 - \chi)u_a + \chi u_w = u_a - \chi u_s \quad (1)$$

Then the effective stress equation can be modified as follows:

$$\{\sigma\} = \{\sigma'\} + \{M\}u_m \quad (2)$$

Equation (2) shows that the total stress is the sum of the mixed fluid pressure and the soil skeleton stress.

**Pore fluid continuity equation**

Considering the pore-fluid continuity equation and mass balance equation, the displacement and mixed fluid pressure  $u_m$  can be obtained:

$$\begin{cases} -[\partial][D][\partial]\{w\} + [\partial]\{M\}u_m = \{f\} \\ \frac{\partial}{\partial t}\{M\}[\partial]\{w\} - \frac{k_m}{\gamma_m}\nabla^2 u_m + \frac{1}{B_m} \cdot \frac{\partial u_m}{\partial t} = 0 \end{cases} \quad (3)$$

where  $\{f\}$  is the volume force,  $\{w\}$  is the displacement variable,  $\gamma_m$  is the mixed fluid unit weight and  $k_m$  is the mixed fluid permeability coefficient,  $B_m$  is the volume compressed modulus of mixed fluid.

There is an extra item in the above equations, comparing Biot consolidation equations. Then the equations are solved by modifying Biot consolidation equation program.

**Water continuity equation**

It is essential to add the water continuity equation to improve the simplified method of fluid consolidation. This was not a reasonable assumption in the past that (1) volume change of pore-water is only related to the change of pore-water pressure; (2) the coefficient of pore-fluid is (2-5) times larger. In fact, the volume change of the pore-water caused by drained water volume, is related to the volume change of the pore and the change of degree of saturation in the process of consolidation of unsaturated soils. Thus, the pore-water pressure is calculated and the interaction between the pore-water and pore-air is avoided. This is another improvement in the simplified method of unsaturated soils consolidation.

Considering the water and mixed fluid continuity equations, the new water continuity equation is:

$$-\frac{k_w}{\gamma_w}\nabla^2 u_w = S_r \left( -\frac{k_m}{\gamma_m}\nabla^2 u_m \right) \quad (4)$$

where  $\gamma_w$  is the water unit weight,  $k_w$  is the water permeability coefficient. Equation (4) expresses that the volume change of the pore-water caused by drained water volume equals the product of the drained volume change of the pore-fluid and degree of saturation.

Combining  $u_m$  and  $u_w$ , the suction can be obtained:

$$u_s = \frac{u_m - u_w}{1 - \chi} \quad (5)$$

**ANALYSIS OF UNSATURATED SOILS CONSOLIDATION**

**Numerical example and influence factors**

Figure 1 shows an embankment 7.5 m high, constructed on an unsaturated soil depth

of 7 m. The fill load is applied in two stages. The fill height and period for the first and second stage are 4.5 m, 20 days, 3 m, 20 days, respectively. The computed model is symmetric. The groundwater table is located at 5 m below the bottom of the unsaturated soil layer (i.e.  $z=-5\text{m}$ ). The embankment is drained at the grade surface and undrained at the bottom. The top of the embankment is drained in the process of construction, and undrained 20 days after the completion of construction. On the drainage boundaries, the pore-air pressure is  $-150\text{kPa}$ , and suction is  $150\text{kPa}$ . The parameters of the fill are the same as that of the foundation soil.  $\gamma=20\text{kN/m}^3$ , the other Duncan-Chang model parameters of E-B are summarized in Table 1. The initial pore-air pressure equals the atmospheric pressure. The initial pore-water pressure depends on its location from the ground water table, i.e.  $-\gamma_w z$ .

The node number 90 (as given in Figure 1), below the ground surface (2.5–3.0 m), far from the boundaries of water and air pressure, is selected to observe the change of mechanical properties.

**Table 1: Parameter of E-B of embankment**

$C$ /kPa	$\Phi$ /( $^\circ$ )	$R_f$	$K$	$N$	$K_B$	$M$	$K_{ur}$	$e_0$	$K_w$ /cm/s	$S_{r0}$ /%	$S_1$ /%	$\lambda$	$u_{sb}$ /kPa
30	35	0.7	150	0.3	300	0.2	300	0.8	$10^{-7}$	80	15	2	40

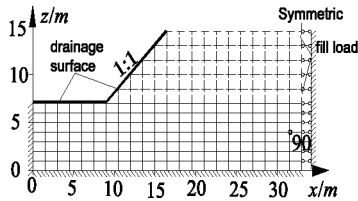


**Fig. 1 Computed mesh of embankment**

### Influence of permeability of soils

The coefficient of permeability is an important parameter to influence the pore-water pressure and rate of dissipation in the process of consolidation of unsaturated soils. The results of  $u_a$ ,  $u_w$ ,  $\sigma_z$  of unsaturated soils with different permeability of  $k_{ws}=10^{-5}\text{cm/s}$ ,  $k_{ws}=10^{-6}\text{cm/s}$ ,  $k_{ws}=10^{-7}\text{cm/s}$  in the period of construction and consolidation are shown in Figure 2.

Figure 2(a) shows the result of  $u_a$  of unsaturated soils with different permeability in the period of construction and consolidation. The increase of pore-air pressure caused by compression under loading is related to the coefficient of permeability. When  $k_{ws}=10^{-5}\text{cm/s}$ , the pore-air pressure is always zero, because the pore-water moves very quickly, and the pore-air pressure is dissipated very quickly. When  $k_{ws}=10^{-6}\text{cm/s}$ , the

pore-air pressure increases, and the pore-air pressure is dissipated quickly. When  $k_{ws}=10^{-6}$  cm/s, the pore-air pressure increases to large values, and the pore-air pressure is dissipated slowly.

Figure 2(b) shows the result of  $u_w$  of unsaturated soils with different permeability in the period of construction and consolidation. The increment of pore-water pressure, raised by compression under loading, is related to the coefficient of permeability. When  $k_{ws}=10^{-5}$  cm/s, the pore-water pressure increases very quickly under loading, and dissipates with time in the process of consolidation. Thus, the pore-air pressure is zero and have no influence on the increase and dissipation of pore-water pressure. When  $k_{ws}=10^{-6}$  cm/s, the pore-water pressure increases quickly under loading, and continues to increase to highest in the process of consolidation. The pore-water pressure is dissipated slower, and the time of consolidation is prolonged. Thus, the pore-air pressure has some influence on the change of pore-water pressure. When  $k_{ws}=10^{-7}$  cm/s, the pore-water pressure increases small under loading, and continues to increase to highest in the process of consolidation. And the pore-water pressure is dissipated slowest, and the time of consolidation is longest. Thus, the pore-air pressure has great influence on the change of pore-water pressure.

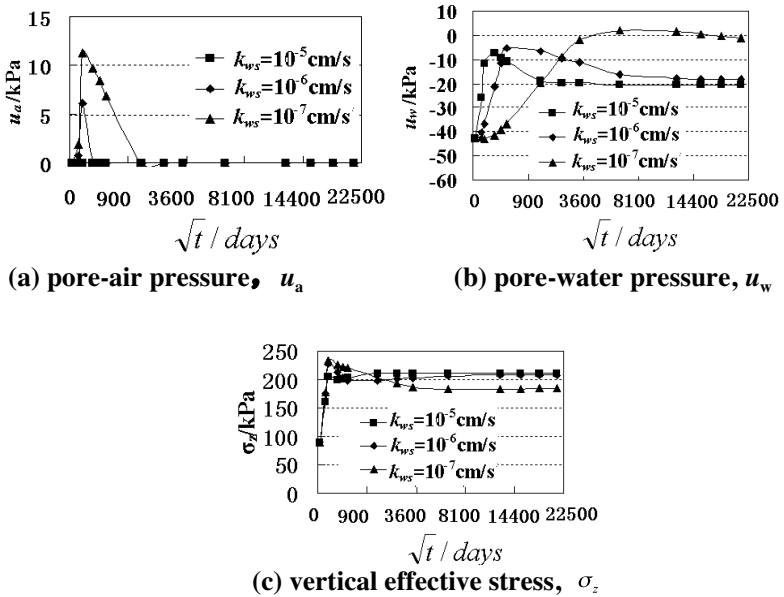


Fig. 2 Result of  $u_w$ ,  $u_a$ ,  $\sigma_z$ , of unsaturated soils in different permeability in the period of construction and consolidation

Figure 2(c) shows the result of  $\sigma_z$  of unsaturated soils with different permeability in

the period of construction and consolidation. When  $k_{ws}=10^{-5}$ cm/s, the vertical effective stress increases under loading and continues to increase in the time of consolidation. When  $k_{ws}=10^{-6}$ cm/s, the vertical effective stress increases more under loading and decrease quickly in the first and increase in the latter time of consolidation, because some suction before loading turns into the new increment of vertical effective stress. When  $k_{ws}=10^{-7}$ cm/s, the vertical effective stress increases more under loading and decrease in the first and increase in the latter time of consolidation, because some suction before loading turns into the new increment of vertical effective stress.

Therefore, the lower the coefficient permeability is, the bigger the pore-air pressure increases more, and the pore-air pressure has greater influence on the change of pore-water pressure.

### Influence of initial degree of saturation of soils

The degree of saturation of soils is related to the water content and ratio of soil pore (Fredlund et al.1993). And the degree of saturation of soils depends on the the water content when the ratio of soil pore is defined. Result of  $u_a$ ,  $u_w$  of unsaturated soils with different initial degree of saturation 85%, 90%, 93% in the period of construction and consolidation are showed in Figure 3.

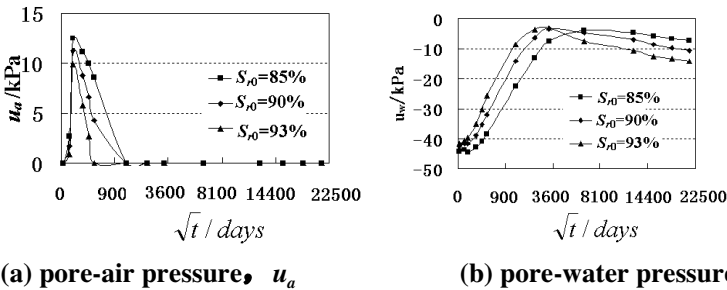


**Fig. 3 Result of  $u_a$ ,  $u_w$  of unsaturated soils in different initial degree of saturation in the period of construction and consolidation**

Figure 3(a) shows the result of  $u_a$  of unsaturated soils with different initial degree of saturation  $S_{r0}$  in the period of construction and consolidation. When  $S_{r0}=85\%$ , the volume of pore-air is most, and the pore-air pressure increases to the highest. When  $S_{r0}=90\%$ , the volume of pore-air is more, and the pore-air pressure increases to the higher. When  $S_{r0}=93\%$ , the volume of pore-air is much, and the pore-air pressure increases to the high.

Figure 3(b) shows the result of  $u_w$  of unsaturated soils with different initial degree of saturation in the period of construction and consolidation. When  $S_{r0}=85\%$ , the pore-air pressure is highest, thus, the extremum of pore-water pressure is smallest and the time of dissipation is longest. When  $S_{r0}=93\%$ , the extremum of pore-water pressure is high,

but the speed of dissipation is quickest.

## CONCLUSIONS

(1) It is essential to study practicality of unsaturated soils consolidation method to be simplified by degree of saturation.

(2) The pore-water and pore-air can be regarded as a mixed fluid with high degree of saturation, then the simplified method of consolidation equations is established.

(3) the influence of soil permeability on consolidation for the interaction between pore-air and pore-water is intensified in the unsaturated soils with low permeability.

(4) the degree of pore-air pressure influence on consolidation of unsaturated soils is related to initial degree of saturation of soils.

## ACKNOWLEDGMENTS

The authors appreciate the support of the International Engineering Foundation.

## REFERENCES

- Cao X S., Yin Z. Z., Ling H.(2008). "Deformation and simplified computation of unsaturated soils under compression loads." *Chinese Journal of Geotechnical Engineering*, Vol.30(1): 61-65(in Chinese).
- Cao X. S., Yin Z. Z., "Simplified Computation of Two-dimensional Consolidation of Unsaturated Soils." *Soil and Rock Mechanics* (waiting).
- Chang C. S., Duncan J. M.(1983), "Consolidation analysis for partly saturated clay by using an elastic-plastic effective stress-sating model." *International Journal for numerical and analytical methods in geomechanics*, Vol.17(7):39-55.
- Dakshanamurthy V., Fredlund D G., Rahardjo H.(1984), "Coupled three-dimensional consolidation theory of unsaturated porous Media." *Preprint of papers: 5th Int. Conf. Expansive soils, Institute of engineers, Australia, May :99-104.*
- Fredlund D G, Rahardjo H(1993), *Soil mechanics for unsaturated soils*. John Wiley & Sons, INC.
- Ling H., Yin Z. Z.(2005). "Two- or three- dimensional simplified consolidation calculation of unsaturated soil." *Advances in Science and Technology of Water Resources*, Vol. 27(2). (in Chinese).
- Yin Z. Z.(2007). "Principle of soil engineering", *Water Press of China* (in Chinese)
- Yin Z Z, Sun C L, Miao L C.(1998). "Consolidation of unsaturated expansive soils."//*2nd International Conference on Unsaturated Soils*. China, :494-500.
- Yin Z Z, Ling H.(2007). "Simplified computation of 1D consolidation for partially saturated soil." *Chinese Journal of Geotechnical Engineering*, Vol. 29(5): 633-637(in Chinese).

## **Improving Bearing Capacity of Shallow Foundations on Weak Soils Utilizing Geosynthetic Reinforcing Technique**

Sao-Jeng Chao<sup>1</sup>

<sup>1</sup>Associate Professor and Chairman, Department of Civil Engineering, Ilan University, Taiwan, chao@niu.edu.tw

**ABSTRACT:** The purpose of this paper is to propose the geosynthetic soil reinforcing technique as a simple and cost-effective alternative of improving the bearing capacity of shallow foundations. It is also expected that the geosynthetic soil reinforcing technique presented herein can help prevent those buildings built on shallow foundations from excessive settlements. Over the last few decades, many pilot and full-scale tests have been conducted, and it has been confirmed that the geosynthetic soil reinforcing technique can improve the bearing capacity of shallow foundations. This paper summarizes the processes of the theoretical development, experimental work, and numerical simulation on the bearing capacities of shallow foundations built on soils reinforced utilizing the geosynthetic reinforcing technique.

### **INTRODUCTION**

The inadequate bearing capacities of the shallow foundations of buildings result in many practical problems during construction work (Chao, 2006). The issues of inadequate bearing capacity of shallow foundations due to weak soil conditions may be solved by employing the geosynthetic reinforcing technique to strengthen the properties of the weak soil (Wu, 2003; Chao, 2008). Studies on the geosynthetic soil reinforcing technique started around 1980s. In the past 30 years, many pilot and full-scale tests have been conducted. Based on those study results, it has been widely accepted that the geosynthetic reinforcing technique can improve the bearing capacity as well as reduce the settlement of shallow foundations (Holtz et al, 1997).

The purpose of this paper is to propose the geosynthetic soil reinforcing technique as a simple and cost-effective alternative of improving the bearing capacity of shallow foundations. This paper summarizes the theoretical development, experimental work, and numerical simulation on the bearing capacities of the shallow foundations built on reinforced soils. It is also expected that the geosynthetic soil reinforcing technique presented herein can help prevent those buildings built on shallow foundations from excessive settlements.

**THEORETICAL DEVELOPMENT**

The geosynthetic reinforcement placed under the shallow foundation is illustrated in Fig. 1. The failure mechanism of the reinforcement can be classified into 2 categories as follows (Michalowski, 2004):

1. The loading from the shallow foundation tends to drive the soil underneath outward. Since the stiffness of the reinforcement is larger than the soil, the driving force is handled by the reinforcement. As a result, the reinforcement may reach the tensile strength and break down. This kind of failure happens at location 1 in Fig. 1.
2. The active zone under the shallow foundation tends to move downward. The initial mobilizing plane resists to slide with the help of soil shear strength and the reinforcement. When the movement achieves certain amount, the reinforcement may fail in shear direction. This kind of failure happens at location 2 in Fig. 1.

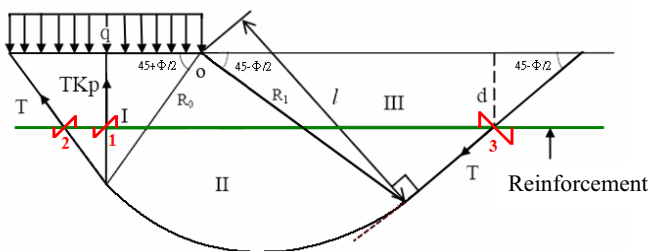


**FIG. 1. Illustration of the stress distribution under the shallow foundation**

In addition, the passive zone far away from the shallow foundation would also fail when the reinforcement reaches its shear strength, which happens simultaneously with aforementioned failure mechanism. This kind of failure happens at location 3 in Fig. 1.

**Bearing Capacity Under Tensile Failure**

For developing the value of the tensile stress in the reinforcement, we can assume that the tensile stress in the reinforcement increasing with the depth because the length is reduced down along the active zone as shown in Fig. 1. We set up the equilibrium condition by proportioning the triangle as shown in Fig. 2, given by

$$\frac{\left( q_{nr} + \frac{q_{nr} \cdot B}{B \cdot K_s} \right) \cdot d}{2} = T \cdot K_p \Rightarrow q_{nr} = 2T \cdot K_p \frac{1}{\left( 1 + \frac{1}{K_s} \right) d} \tag{1}$$

where  $K_s = \frac{\frac{1}{2} \cdot B \cdot \tan(45 + \frac{\phi}{2}) - d}{\frac{1}{2} \cdot B \cdot \tan(45 + \frac{\phi}{2})}$  and  $K_p = \tan^2(45 + \frac{\phi}{2})$

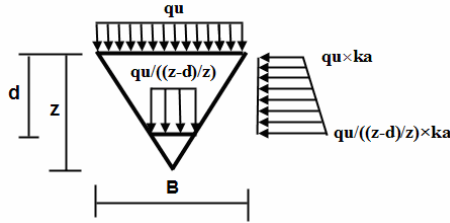


**FIG. 2. Reinforcement under tensile failure mechanism**

Using Equation (1) and considering the tensile strength provided from the reinforcement at location 3 all together, we finally can reach a compact form as follows:

$$q_{nr} = T \left[ \frac{\tan^2(45 + \frac{\phi}{2}) \cdot B \cdot \tan(45 + \frac{\phi}{2}) - 2d}{d \cdot B \cdot \tan(45 + \frac{\phi}{2}) - d} + \frac{4}{B} \cdot \sin(45 + \frac{\phi}{2}) \cdot e^{\frac{\pi}{2} \tan \phi} \right] \tag{2}$$

Equation (2) is the supplementary bearing capacity comes from the reinforcement which is failed under tensile condition both at the location 1 and location 3.

**Bearing Capacity Under Shear Failure**

The initial mobilizing plane resists to slide with the help of soil shear strength and the reinforcement. When the movement of the active zone is large enough to shear the reinforcement as shown in Fig. 3, the relation can be written as

$$q_{ng} \cdot B \cdot \sin(45 + \frac{\phi}{2}) = 2T \Rightarrow q_{ng} = \frac{2T}{B \cdot \sin(45 + \frac{\phi}{2})} \tag{3}$$

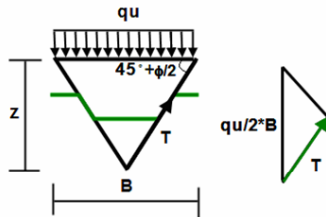


**FIG. 3. Reinforcement under shear failure mechanism**

For the purpose of simplicity, we directly highlight the final form here as follows:

$$q_{ug} = \frac{2T \left( 1 + 4e^{\theta \tan \phi} \cdot \sin^2 \left( 45 + \frac{\phi}{2} \right) \right)}{B \cdot \sin \left( 45 + \frac{\phi}{2} \right)} \tag{4}$$

Equation (4) is the supplementary bearing capacity comes from the reinforcement which is failed under shear condition at the location 1 and tensile condition at location 3.

**EXPERIMENTAL WORK**

Sandy and clayey soils were used in the laboratory tests to determine the reinforcement efficiency. The efficient ratio of reinforcing was defined as the bearing capacity of shallow foundation with reinforcement over that without reinforcement.

The sandy soil used in the laboratory test was classified as SP. The friction angle  $\phi$  was about  $45^\circ$  while no cohesion was considered. The geosynthetic reinforcement was placed at the depth of  $0.5B$  from the surface. A round footing was used for this test. The relationship of bearing capacities and settlements of the shallow foundations with and without reinforcement for sandy soil is shown in Fig. 4.

As shown Fig. 4, the ultimate loading of shallow foundation without reinforcement is only 738 kgf, while the ultimate loading of the shallow foundation with reinforcement can reach 1158 kgf. Based on the results of the laboratory tests for sandy soil, the efficient ratio of reinforcing is 1.6.

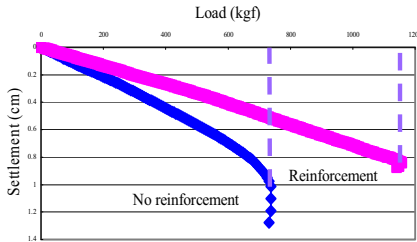


**FIG. 4. Test results of sandy soil with and without reinforcement**

The clayey soil used in the test was classified as CL with the property of PI ranging from 12 to 40 and LL from 16 to 58 from the investigation report. The unconfined compression strength  $c_u$  was in the range of  $36\text{--}51 \text{ kN/m}^2$ . The geosynthetic reinforcement was also placed at the depth of  $0.5B$  from the surface. The relationship between bearing capacities and settlements of shallow foundations with and without reinforcement for clayey soil are shown in Fig. 5.

As shown in Fig. 5, the ultimate loading of shallow foundation without reinforcement is just 483 kgf, while the ultimate loading of the shallow foundation with

reinforcement can reach 1036 kg. Based on the results of the laboratory tests for clayey soil, the efficient ratio of reinforcing is 2.2. It can be found that the efficient ratio of reinforcing for clayey soil is better than that for sandy soil.

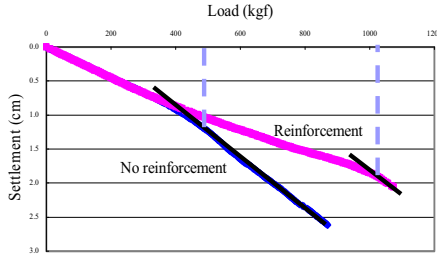


**FIG. 5 Test results of clayey soil with and without reinforcement**

**NUMERICAL SIMULATION**

In order to further understand the performance of the geosynthetic reinforced soil, a finite element program PLAXIS was utilized. The geosynthetic reinforcement and the soil can be easily simulated using PLAXIS to predict the bearing capacities and settlements of the laboratory tests.

The soil model employed the Mohr-Coulomb failure criteria while the reinforcement simply used the elastic tensile model. The boundary conditions were chosen to be fixed on the bottom for both directions and on the lateral boundary for horizontal direction. The mesh generated for FEM simulation is shown in Fig. 6.

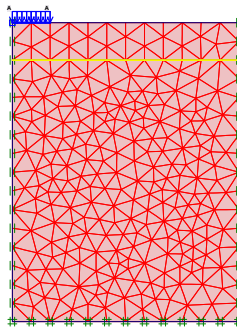


**FIG. 6 FEM mesh for the laboratory tests**

The properties of the sandy soil and clayey soil are summarized as follows:

	Sandy Soil	Clayey Soil
Unit Weight ( $g/cm^3$ )	2.1	1.94
Elastic Modulus $E$ ( $g/cm^2$ )	448,500	124,000

Poisson Ratio	0.3	0.35
Friction Angle (degree)	45	0
Apparent Cohesion ( $\text{g}/\text{cm}^2$ )	50	300

The material property of the geosynthetic reinforcement  $E_A = 300,000 \text{ g}/\text{cm}$ . The predicted ultimate bearing capacity obtained from FEM for sandy soil is  $1930 \text{ g}/\text{cm}^2$  without reinforcement. Furthermore, the predicted result is  $2877 \text{ g}/\text{cm}^2$  with reinforcement. The value of efficient ratio of reinforcing for sandy soil in the laboratory condition is 1.5 in Fig. 7. On the other hand, based on the predicted result obtained from FEM for clayey soil, the ultimate bearing capacity is  $744 \text{ g}/\text{cm}^2$  without reinforcement. In addition, the predicted result is  $1834 \text{ g}/\text{cm}^2$  with reinforcement. The value of efficient ratio of reinforcing for clay in the laboratory condition is 2.5 in Fig. 8.



**FIG. 7 The predicted results from FEM for sandy soil**

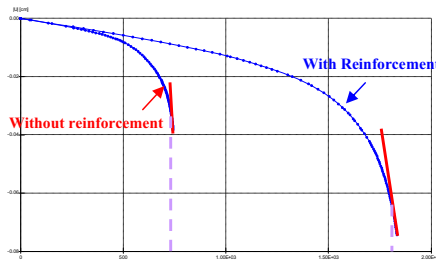


**FIG. 8 The predicted results from FEM for clayey soil**

**CONCLUSIONS**

The inadequate bearing capacity and the excessive settlement problems of shallow foundations due to weak soil conditions may be solved by employing the geosynthetic reinforcing technique to strengthen the weak soil. The geosynthetic reinforcement placed under the shallow foundation can be derived by classifying into 2 categories and obtained the close-form solutions. Based on the results of laboratory tests, it is found that the efficient ratio of reinforcing is 1.6 for sandy soil and 2.5 for clayey soil. On the

other hand, based on the predicted result obtained from FEM, the value of the efficient ratio of reinforcing is 1.5 for sandy soil and 2.5 for clayey soil, which agree with experimental results. Finally, it is notable that the worse condition provides the better efficient ratio for reinforcing.

## REFERENCES

- Chao, S.J. (2006). "Study of geosynthetic reinforced subgrade expressway in Taiwan." Fourth International Conference on Soft Soil Engineering (4th ICSSE), Vancouver, Canada: 237-243.
- Chao, S.J. (2008). "Performance study on geosynthetic reinforced shallow foundations." Sixth International Conference on Case Histories in Geotechnical Engineering, Arlington, VA.: 7.35a.
- Holtz, R.D., Christopher, B.R. and Berg, R.R. (1997). *Geosynthetic Engineering*, Bitech Publishers Ltd., Canada.
- Michalowski R. L. (2004). "Limit loads on reinforced foundation soils." Journal of Geotechnical and Geoenvironmental Engineering, ASCE: 381-390.
- Wu, L.L. (2003). *Design and Performance Analysis of Geosynthetic Applications in Railroad Track Mitigation*, Ph. D. Dissertation, National Cheng-Kung University, Taiwan.

# Micromechanical analysis of soil arching in geosynthetic-reinforced pile-supported embankments

Anil Bhandari<sup>1</sup>, Jie Han<sup>2</sup>, and Fei Wang<sup>3</sup>

<sup>1</sup>Graduate Research Assistant, Civil, Environmental, and Architectural Engineering (CEAE) Department, the University of Kansas, USA. banil@ku.edu

<sup>2</sup>Associate Professor, Civil, Environmental, and Architectural Engineering (CEAE) Department, the University of Kansas, USA. jiehan@ku.edu

<sup>3</sup>Ph. D. Candidate, Institute of Geotechnical Engineering, Southeast University, Nanjing, 210096, China; Currently Visiting Scholar at the University of Kansas, USA. feiwangseu@gmail.com

**ABSTRACT:** Geosynthetic-reinforced pile-supported embankments have been used as an economic and rapid construction technique for earth structures, such as embankments and retaining walls over soft soil. They have limited total and differential settlements and increase load transfer from soft soil to piles thereby leaving less load to the soil. Two key mechanisms of this technique are: soil arching within the embankment fills when a differential settlement occurs to mobilize the fill shear strength and tension membrane effects of geosynthetic reinforcement when it deforms. This study focuses on understanding the complex load transfer mechanisms by performing a numerical study using the Discrete Element Method (DEM). The granular backfill material was modeled using cylindrical rods. The geogrid reinforcement was modeled using bonded particles. At the end of the simulation, the displacements of granular particles were plotted for the illustration of soil arching.

## INTRODUCTION

Geosynthetic-reinforced pile-supported embankment is an economic solution to combat total and differential settlement problems encountered in the construction of earth structures over the soft soil (Han and Gabr 2002). This construction technique is equally useful to address the challenges posed by an existing sinkhole under a proposed highway alignment (Wang et al. 2008). Soil arching is a key mechanism to transfer the load due to the embankment weight and external loadings to the piles from the soft soil or a void area. The details of soil arching and the governing factors can be found in Giroud et al. (1990), McKelvey (1994), Han and Gabr (2002), Jenck et al. (2007), and Chen et al. (2008). For an unreinforced embankment, the height of soil arching is generally taken as 1.5 to 2.5 times the width of voids or clear spacing between the piles / pile caps (Terzaghi, 1943). This height should be less for a geosynthetic reinforced embankment. However, the equal height of soil arching is assumed in the reinforced embankment as in the unreinforced embankment and the

strength of the geosynthetic is designed based on this assumption (Giroud et al. 1990). In the present study, discrete element method (DEM) modeling of unreinforced and geogrid-reinforced embankments supported on piles is presented to show the differences in the height of soil arching. The DEM modeling treats soil as a particulate medium. Therefore, the DEM modeling is a suitable tool to study the behavior of granular materials used in the construction of the embankment.

## NUMERICAL SIMULATION

A 1.6 m high and 1.5 m long rectangular box was created using four walls (FIG. 1). A 15 mm diameter particles were generated at a porosity of 0.16 using a radial expansion technique as described in Itasca (2004). A model created using the radial expansion technique generates high stress which should be brought to an initial stress condition. The details of achieving the initial stress condition can be found in the authors' previous research (Bhandari and Han 2009; Bhandari et al. 2009). After achieving the initial stress condition, a geogrid sheet was placed by generating the bonded particles (large particles of diameter 2.6 mm on the nodes and small particles of diameter 1.0 mm between nodes) inside the guided walls (created at 1.3 m below the top wall), which were optional depending on whether an unreinforced or reinforced case was studied. A 0.3m X 0.3 m pile cap was placed on either side of the model using walls and the particles inside the pile caps were deleted because they do not interact with particles outside the walls and there is a need for the calculation of the unbalanced force on the walls from the particles outside. Furthermore, the porosity of the assembly below 1.3 m (i.e., between the pile caps) was increased to 0.3 from an initial porosity of 0.16 by randomly deleting the particles within this zone. The high porosity within this zone was to simulate the compressible soil. Because of this compressible soil in the lower part, the geogrid would deform and a soil arching would develop. At the top of the model, a vertical stress of 15 kPa was applied to simulate the traffic load of an embankment. Nine measurement circles were installed in the model as shown in FIG. 1 to measure the stresses.

The micromechanical properties of the soil were evaluated using the biaxial test simulation while those of the geogrid were evaluated using a tensile test simulation. The micromechanical properties used in this study are shown in Table 1. This soil had a friction angle of 41°. The details of these simulations can be found in Bhandari and Han (2009) and Bhandari et al. (2009).

**Table 1. Micromechanical Properties for DEM Analysis.**

Material	Parameters	
Soil	Young's modulus of the particle-particle contact, $E(\text{MPa}^2)$	85
	Ratio of normal to shear stiffness of particles, $k_n/k_s$	1.2
	Friction coefficient ( $\mu$ )	0.55
Geogrid	Young's modulus of the particle-particle contact, $E(\text{MPa}^2)$	351
	Ratio of normal to shear stiffness of particles, $k_n/k_s$	1.0
	Friction coefficient ( $\mu$ )	0.44
	Contact bond strength (kN/m)	20.4

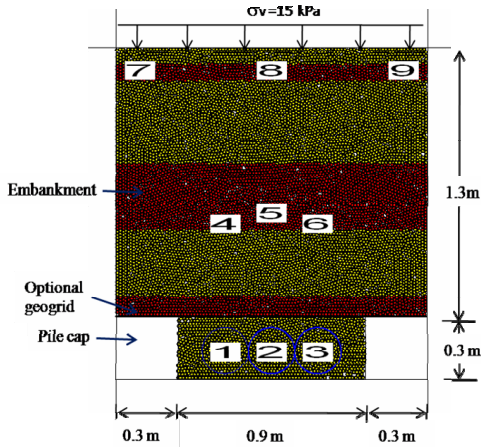


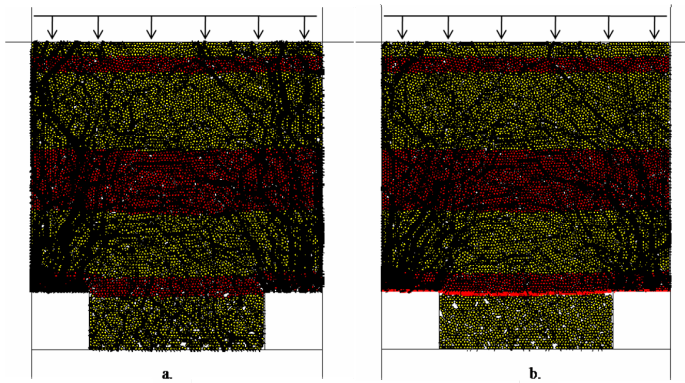
**FIG. 1 DEM Model of a Geosynthetic-reinforced Pile-supported Embankment**

**ANALYSIS OF RESULTS**

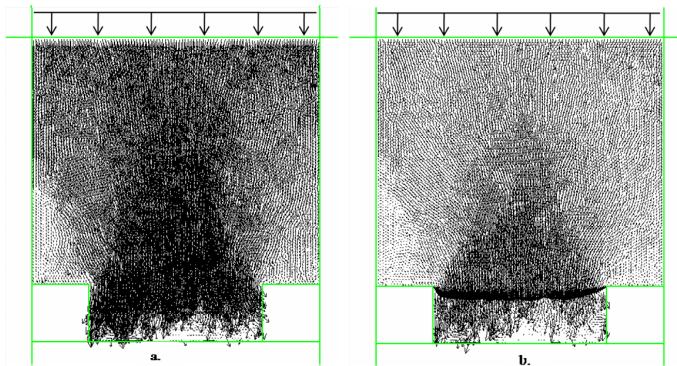
**Influence of geogrid on soil arching**

In this simulation, the soil between the pile caps had a tendency to settle as the soil between the pile caps had a higher porosity. The movement of the soil caused the mobilization of the shear strength of the embankment soil adjacent to the yielding area and transferred the load from the yielded soil to the adjacent soil. This phenomenon increased the pressure on the pile cap and reduced the pressure on the soil between the pile caps. The contact force distribution of the unreinforced model in FIG. 2a shows higher contact forces over the pile caps compared to the soil between the pile caps, which is as an evidence of soil arching. It is noteworthy to mention that the thickness of the contact force chains indicates its relative magnitude. FIG. 2b also illustrates the similar soil arching phenomenon in the reinforced model. However, the geogrid reduced the contact forces transmitted to the soil below the geogrid. Tensile forces developed in the geogrid, which acted as a tensioned membrane.

The displacement vectors of the soil particles for the unreinforced and the reinforced models are shown in FIG. 3. The same magnitude of the maximum displacement was used for these two figures for the comparison purpose. For the unreinforced model, FIG 3a shows that the differential settlement extended to the top of the embankment. It can be concluded that the ratio of the embankment height (h) to the clear spacing between the pile caps (s) at 1.44 used in this model was insufficient to alleviate the differential settlement at the top of the embankment. Similar findings were reported by Chen et al. (2008) in an experimental investigation of the soil arching.



**FIG. 2 Contact Force Distribution (a) Unreinforced Embankment (b) Geosynthetic-reinforced Pile-supported Embankment**



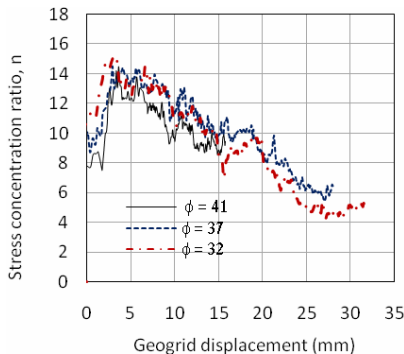
**FIG. 3 Displacement Vector Distribution (a) Unreinforced Embankment (b) Geosynthetic-reinforced Pile-supported Embankment**

FIGURE 3b shows the displacement vectors of the geogrid-reinforced model. The geogrid reduced the displacement of the embankment fill compared to the unreinforced model. The reduced displacement would transfer less force to the adjacent soil in the embankment and would reduce the stress on the pile caps. On the other hand, the tensioned geogrid would transfer the vertical component of the geogrid stress to the pile caps and the stress on the pile caps would increase. In the unreinforced model, the pressure on the pile caps was 66.4 kPa while that in the reinforced model was 65.9 kPa. The similar pressure on the pile caps indicated that the presence of the geogrid reinforcement did not change the contribution of the pile caps on the total load sharing in this study.

The displacement vectors of the geogrid-reinforced model show that the height ( $h_c$ ) of an equal settlement plane is same as the clear spacing between the pile caps ( $s$ ) for the given soil properties in Table 1. Furthermore, Fig 3b shows a triangular shape of the soil arching with a shear angle of  $63.5^\circ$ , where the shear angle is defined as the angle formed by the shear plane relative to the horizontal plane (Van Eekelen et al. 2003). This angle is close to the active angle of  $65.5^\circ$  (i.e.,  $45^\circ + 41^\circ/2$ ). The triangular shape of the shear plane was observed in an experimental study of piled embankments by Van Eekelen et al. (2003).

**Development of soil arching with pile-subsoil relative displacement**

FIGURE 4 shows the change in the stress concentration ratio ( $n$ ) with the maximum geogrid deformation. Stress concentration ratio ( $n$ ) is often used to characterize the degree of soil arching and defined as a ratio of the stress on the pile cap,  $\sigma_p$ , to the stress on the soil,  $\sigma_s$  (Han and Gabr 2002). The stress concentration ratio increased with the maximum geogrid deformation up to a maximum value, and then decreased with a further increase in the maximum geogrid deformation. Similar behavior was observed for soils with different friction angles ( $\phi$ ). FIGURE 4 also shows that more deformation of the geogrid was required for the soil of a low friction angle compared to the soil of a high friction angle to achieve a stable soil arching as characterized by the constant  $n$ . However, the peak stress concentration ratio was similar for all three soils with different friction angles, which is attributed to the tension membrane effect of the geogrid. A geogrid reinforcement used in an embankment with the soil of a low friction angle would be subjected to a higher vertical stress than that used in an embankment with the soil of a high friction angle. Though there was less stress transfer to the pile caps due to soil arching in the soil of a low friction angle, the vertical component of the higher tensile stress in the geogrid would be transferred to the pile caps. As a result, the net stress on the pile cap would remain close.



**FIG. 4 Stress concentration ratio (n) versus maximum geogrid displacement.**

## CONCLUSIONS

This study focused on the different aspects of soil arching for a geosynthetic-reinforced piled-supported embankment using DEM modeling. The modeling results showed that the height ( $h_c$ ) of an equal settlement plane was lower for the geogrid-reinforced embankment than the unreinforced embankment. A triangular shape of the soil arching was observed in the geogrid-reinforced embankment. For an embankment soil of a low friction angle, larger geogrid deformation was required to achieve a stable soil arching compared to the soil of a high friction angle.

## REFERENCES

- Bhandari, A. and Han, J. (2009). "DEM study of a shallow foundation under vertical loading." Submitted to *International Foundation Congress and Equipment Expo '09*, ASCE, Orlando, Florida.
- Bhandari, A., Han, J., and Parsons, R. L. (2009). "Discrete element method investigation of geogrid-aggregate interaction under a cyclic wheel load." Submitted to *Transportation Research Record*.
- Chen, Y. M., Cao, W. P., and Chen, R. P. (2008). "An experimental investigation of soil arching within basal reinforced and unreinforced piled embankments." *Geotextiles and Geomembranes*, 26(2), 164-174.
- Giroud, J. P., Bonaparte, R., Beech, J. F., and Gross, B. A. (1990). "Design of soil layer-geosynthetic systems overlying voids." *Geotextiles and Geomembranes*, 9(1), 11-50.
- Han, J. and Gabr, M. A. (2002). "Numerical analysis of geosynthetic-reinforced and pile-supported earth platforms over soft soil." *Journal of Geotechnical and Geoenvironmental Engineering*, 128(1), 44-53.
- Itasca. (2004). *Patice Flow Code in Two Dimensions*, Itasca Consulting Group, Inc., Minnesota.
- Jenck, O., Dias, D., and Kastner, R. (2007). "Two-dimensional physical and numerical modeling of a pile-supported earth platform over soft soil." *Journal of Geotechnical and Geoenvironmental Engineering*, 133(3), 295-305.
- McKelvey, J. A., III. (1994). "Anatomy of soil arching." *Geotextiles and Geomembranes*, 13(5), 317-329.
- Terzaghi, K. (1943). *Theoretical Soil Mechanics*, Wiley, New York, 66-75.
- Van Eekelen, S. J. M., Bezuijen, A., and Oung, O. (2003). "Arching in piled embankments; experiments and design calculations." *Proceedings, BGA International Conference on Foundations, Innovations, Observations, Design and Practice*, Dundee, United Kingdom. Thomas Telford, London, 885-894.
- Wang, F., Han, J., Miao, L. C., and Bhandari, A. (2008). "Numerical analysis of geosynthetic-bridged and drilled shaft-supported embankments over large sinkholes." Submitted to *Geosynthetics International*.

## **Large Physical Modeling to Optimize the Geometrical Conditions of Geotextile in Reinforced Loose Sand**

S. Shahaboddin Yasrobi<sup>1</sup>, S. Mustapha Rahmaninezhad<sup>2</sup> and S. Farhad Eftekharzadeh<sup>3</sup>

<sup>1</sup>Assoc. Professor of Tarbiat Modares University, Tehran, Iran; [yasrobis@modares.ac.ir](mailto:yasrobis@modares.ac.ir)

<sup>2</sup>MSc. Student, Tarbiat Modares University, Tehran, Iran; [rahmaninezhad@modares.ac.ir](mailto:rahmaninezhad@modares.ac.ir)

<sup>3</sup>Assis. Professor, Transportation Research Institute, Tehran, Iran, [eftekarzadehir@yahoo.com](mailto:eftekarzadehir@yahoo.com)

**ABSTRACT:** Laboratory large scale model tests for optimizing the geometrical conditions of geotextile in reinforced standard dry sand 161 (patterned in Iran) were carried out. Based on the results of the model tests, the number of reinforcement layers, critical depth of reinforcement and the dimensions of the geotextile layers for mobilizing the maximum bearing capacity were determined and the results were compared with the Plate Load Tests (ASTM-D1194). The total number of tests in this study was 45. The models dimensions were with 100 cm × 100 cm × 80 cm (length × width × depth) and the circular foundation had a diameter of 200 mm.

### **INTRODUCTION**

Geosynthetic soil reinforcements such as geotextiles, geogrids and geocomposites have beneficial effects on the bearing capacity and settlement of shallow foundations (Koerner, 1997 and Shukla and Yin, 2006). Several researches have shown the effects of geosynthetic soil reinforcements on ultimate bearing capacity (e.g. Giudo et. al. 1985, Omar et. al. 1993 and Boushehrian and Hataf, 2003). Most of the laboratory model tests available have been conducted with square and strip foundations. This study presents the results of laboratory model tests on the circular foundation supported by loose sand reinforced with geotextile layers in order to reduce the stress concentrations occurring in the corners of square and strip foundations.

### **LABORATORY MODEL TESTS**

Bearing capacity tests were conducted in a box with 100cm × 100cm × 80cm (length × width × depth) dimensions. This box was made of wood supported by steel profiles. The inner side of the box was covered by plastics to reduce friction. It was filled with special sand patterned in Iran (Standard Sand 161). Its specifications are given in Table 1. The circular foundation had a diameter of 200mm. It was made of iron plate.

**Table 1. Specifications of Standard Sand161**

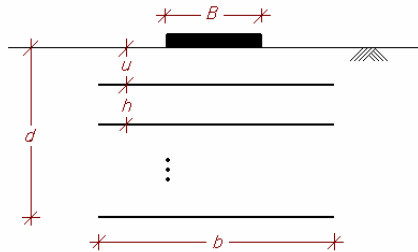
Parameter	Value
GS	2.66
$e_{max}$	0.928
$e_{min}$	0.583
D 50	0.26
F %	0
Cu	1.8
Cc	1.19

Figure 1 shows a circular foundation (diameter  $B$ ) supported by sand, which is reinforced with  $N$  number of geotextile layers. The vertical space between the geotextile layers is  $h$ . The top layer of geotextile is located at the depth ( $u$ ) measured from the bottom of the foundation. The width and the length of the geotextile layers is  $b$ . The depth ( $d$ ) of reinforcement below the bottom foundation is:

$$d = u + (N - 1) h. \quad [1]$$

For shallow foundation on dry sand without reinforcement, the bearing capacity at the allowable settlement is called  $q$ . When the sand is reinforced with geotextile layers, the bearing capacity at the allowable settlement  $q^{(R)}$  will increase. The increase in the bearing capacity can be expressed in a non-dimensional form as the Bearing Capacity Ratio (BCR):

$$BCR = q^{(R)} / q \quad [2]$$

**FIG. 1. Circular foundation supported by sand reinforced with geotextile.**

For all tests, the average the unit weight ( $\gamma_d$ ) and the Relative Density of Compaction ( $D_r$ ) were kept at  $14.4\text{kN/m}^3$  and 35%, respectively. The range of variation for the  $D_r$  was  $\pm 5\%$  of the average value. An Iranian nonwoven geotextile was used for the present tests (2N400). The physical properties of the geotextile are given in Table 2.

**Table 2. Physical properties of the used geotextile (2N400)**

Fabric Properties	Test Method (ASTM)	Unit	
Polymer Type			PET
Unit Weight	D-5261	$\text{gr/m}^2$	400
Thickness	D-5199	mm	1.60
Grab Tensile Strength	D-4632	N	1750
Grab Elongation	D-4632	%	>50
Trapezoidal Tear	D-4833	N	595
Puncture Strength	D-4533	N	930
Wide with Tensile	D-4595	$\text{kN/m}$	23.1

In conducting the model tests, the box was filled with 138.7 kg dry sand, which is then compacted per 10cm thickness. The geotextile layers were placed at the desired values of  $u/B$  and  $h/B$  in the sand. The foundation was placed on the surface of the sand bed. Loading was applied by a hydraulic jack. The loads and the corresponding settlement ( $s$ ) were measured by a proving ring and three digital gauges. Figure 2 shows the arrangements of jack and gauges on the foundation.



**FIG. 2. The arrangements of jack and gauges on the foundation.**

## MODEL TESTS RESULTS

The first test was conducted on the unreinforced sand. The load ( $q$ ) per unit area versus  $s$  plot was obtained from the Plate Load Tests (PLT). The experimental ultimate bearing capacity at the allowable settlement of 25.1mm (ASTM-D1194) was determined to be 8.4kN/m<sup>2</sup>.

In the second test series, the number of geotextile layers ( $N$ ) was taken as variable. The constant parameters were:  $u/B=h/B=0.5$  and  $b/B=4$ . Figure 3 shows the plot of experimental  $q$  versus  $s$  plot obtained from the tests with the circular foundation.

It is inferred from this plot that, for these foundations, the magnitude of  $q$  increases with an increase in  $N$  at the allowable settlement. The load at the allowable settlement almost increased when  $N$  increased to 3. For  $N \geq 3$ , the allowable load remained constant.

Figure 4 shows the plot of the variation of BCR with  $d/B$ . For the given foundation, the magnitude of BCR increases with  $d/B$  up to maximum value and thereafter remains constant. The critical value of  $d/B$  is about 1.5-2 for circular foundations. Guido et. al. (1985) determined the critical value of  $d/B$  for square foundations as 1-1.25 while Omar et. al. (1993) determined it as 1.4-2.

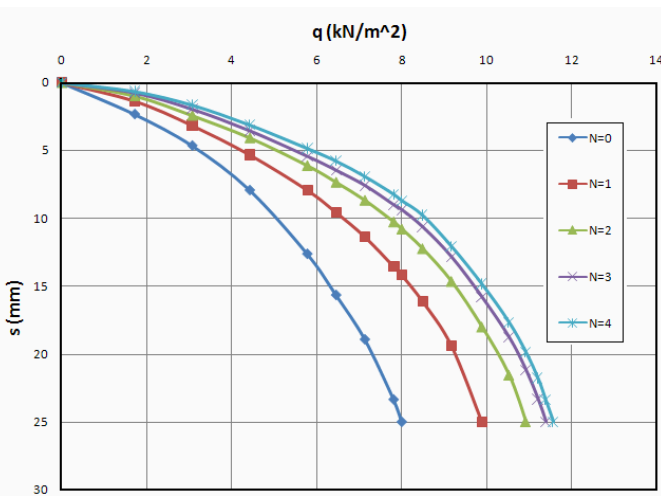


**FIG. 3. The effect of number of layers on the bearing capacity and settlement ( $u/B=h/B=0.5$ ,  $b/B=4$ )**

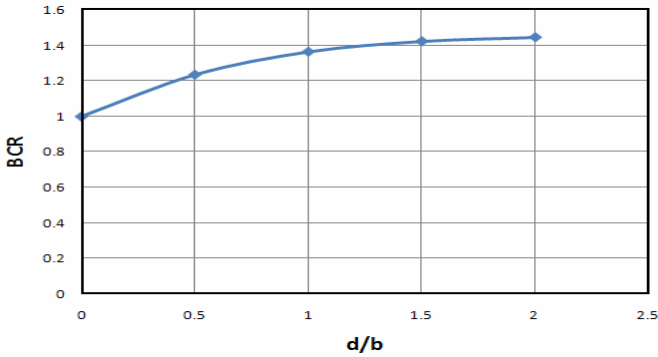


**FIG. 4. The effect of depth of layers ( $d/B$ ) on BCR**  
 ( $u/B=h/B=0.5, b/B=4$ )

The third test series were conducted to determine the optimum dimensions of the geotextile layers. The depth of the reinforcement was kept at about the same level as  $d/B=1$  determined from the second test series. The BCR obtained from these tests are plotted against  $b/B$  in Figure 5.

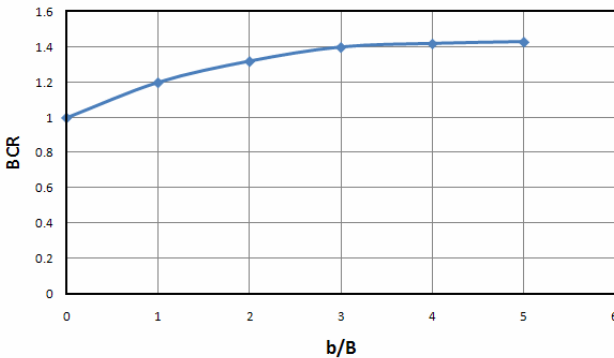


**FIG. 5. The effect of dimensions of geotextile layers ( $b/B$ ) on BCR**  
 ( $u/B=h/B=0.5, d/B=1$ )

It can be seen from this figure that the BCR attained maximums at about  $b/B = 3$  for circular foundations. The magnitude of the critical  $d/B$  for square foundations was determined by Guido et. al. (1985) as 2.5-3 and by Omar and Dos (1993) as 4.5.

To obtain the maximum benefit of  $u/B$  ratio, the fourth test series were conducted. The results obtained from these tests are plotted in Figure 6. In larger  $u/B$  ratios, the

failure surface in sand at ultimate load will be fully located above the top layer of reinforcement. In these tests,  $N=1$  was constant. It appears from the plot (fig. 6) that the maximum BCR for circular foundation occurs at around  $u/B = 0.25$ .

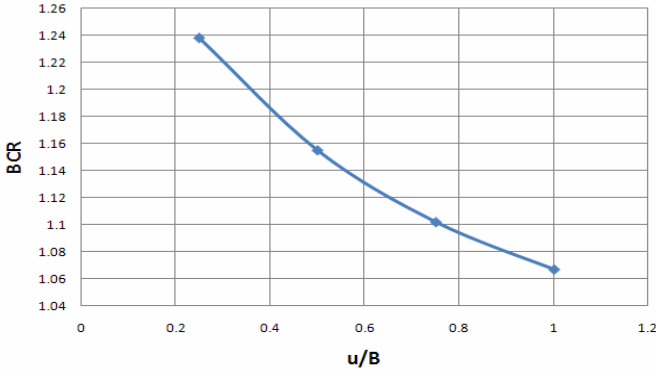


**FIG. 6. The effect of depth of the first layer ( $u/B$ ) on BCR**

As Binquet and Lee (1975) observed in order to obtain maximum benefit from the reinforcement for square foundations, it is desirable that  $u/B$  be less than 0.67 while Guido et. al. (1985) and Omar et. al. (1993) determined  $u/B$  as approximately 0.75 about 1 for square and strip foundations, respectively.

## CONCLUSIONS

Large physical modeling results of circular foundations to optimize the geometrical conditions of geotextile in reinforced loose sand include:

1. The effective depth of geotextile reinforcement is about  $B$ .
2. The maximum width of reinforcement required for mobilization of maximum bearing capacity is about  $3B$ .
3. The maximum depth of placement of the first layer of geotextile is about  $0.25B$ .

## ACKNOWLEDGMENTS

The authors here by appreciate the Transportation Research Institute (affiliated to the Ministry of Road and Transportation) of Iran and Tarbiat Modares in Iran for their support of this research.

## REFERENCES

Koerner, R.M. (1997). "Designing with Geosynthetics." Prentice Hall.

- Shukla, S.K. and Yin, J.H. (2006). "Fundamentals of Geosynthetic Engineering." *Taylor & Francis*.
- Boushehrian, J.V. and Hataf, N. (2003). "Experimental and numerical investigation of the bearing capacity of model circular and ring footings on reinforced sand." *Geotextiles and Geomembranes* 21:241-256.
- Guido, V.A., Biesiadecki, G.L. and Sullivan, M.L. (1985). "Bearing capacity of a geotextile reinforced foundation." *The 1th International Conference on Soil Mechanics and Foundation Engineering, San Francisco*, Vol. 3: pp. 1777-1780.
- Binquet, J. and Lee, K.L. (1975). "Bearing capacity analysis on reinforced earth slabs." *ASCE Journal of the Geotechnical Engineering Division*, 101: 1257-1276.
- Omar, M.T., Das, B.M., Puri, V.K. and Yen, S.C. (1993). "Ultimate bearing capacity of shallow foundations on sand with geogrid reinforcement." *Can. Geotech. J.* 30: 545-549.

## **A Research on the Dynamical Characteristics of Road-bridge Transition Sections Reinforced by Geogrid**

Guoyuan Chen

Associate Professor, College of Civil Engineering and Mechanics, Central South University of Forestry and Technology, Changsha, 410004, Hunan China; guojiao373737@126.com

**ABSTRACT:** The dynamic response of Guanjiazhuang Bridge of Qinghuangdao-Shenyang passenger rail line was tested. The relations among dynamic stress and dynamic acceleration of road-bridge transition sections reinforced by geogrid, and the velocity of the train were studied, as well as the attenuation rule of the dynamic response versus the depth of the roadbed. Based on those test results, a dynamic model of the track-roadbed is built to numerically simulate the dynamic response of road-bridge transition sections. The simulation results are consistent with the obtained test results, which show that the road-bridge transition sections reinforced by the geogrid can effectively prevent the propagations of dynamic stress and dynamic acceleration in the roadbed, and reduce the dynamic load effects on the roadbed.

### **INTRODUCTION**

Conditions of foundation, stuffing material of the roadbed behind the bridge abutment, design, construction, and so on will all cause differences between the sedimentation of the abutment and the roadbed (Cunlin 1999). When the train passed with a high speed, additional dynamic stress will be generated to the roadbed, which further increases the differences between sedimentation of the abutment and the roadbed and causes dangers to the train. Thus, the research on road-bridge transition reinforced by geogrid is of great significance. Based on the research sponsored by the Ministry of Railway of China, this paper analyzes the dynamic features of the road-bridge transition when high speed trains travel on, and the effect of the

road-bridge transition reinforced by geogrid, which will provide theoretical and practical guidance for similar projects.

**INTRODUCTION TO THE PROJECT**

The place is covered by quaternary alluvial-new deposit, which is supported by the metamorphic rock of the Archean group. The groundwater, the fourth porosity groundwater with a 0.2~1.9m burial depth is recharged by rainfall. The road-bridge transition section of the Guanjiazuang Bridge is reinforced by geogrid, and the roadbed of the transition shapes like an inversed trapezium. Its vertical and cross-section is demonstrated in Fig 1.

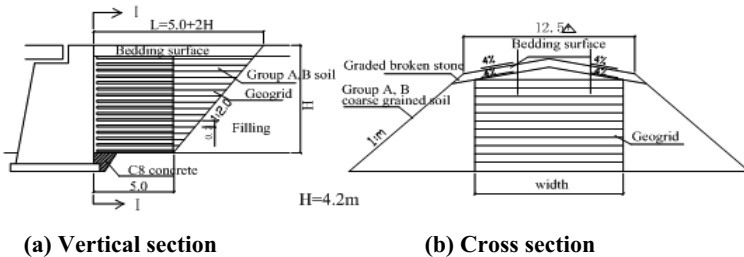


**Fig.1. Design figure of road-bridge transition sections**

**ANALYSIS OF MEASURED RESULTS IN THE FIELD**

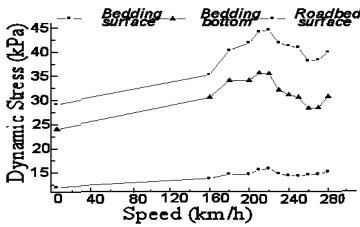
**1. Arrangement of the testing components and testing organization**

In order to find how the dynamic response of the roadbed in the road-bridge transition sections will change along the lengthwise direction and depth of the railway, three testing cross-sections are set up along the lengthwise direction of the road-bridge transition section. The distances from those cross sections to the abutment back are respectively 3m, 10m and 15m. On the testing cross-section, acceleration sensor is put on the bedding surface, and soil pressure boxes are put on the bedding surface, the bedding bottom and the roadbed body surface. The train under test is “Pioneer” EMU, and the testing speeds are 160 km/h, 200 km/h, 220 km/h, 240 km/h and 250km/h. The train travels at each stated speed for 3 rounds to satisfy the demands of the engineering point measurement.

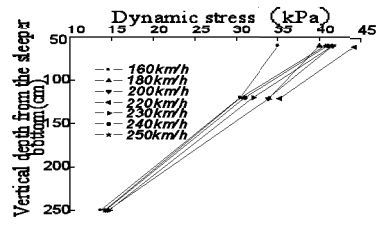
**2. Analysis of testing results**

With the increase of speed, the dynamic stress and acceleration of the roadbed tend to increase first and then decrease. In addition, the dynamic stress decreases when the depth of roadbed increases. The variation curve of dynamic response of the road-bridge transition section reinforced by geogrid can be generated based on the experiment data, which is shown in Fig. 2.

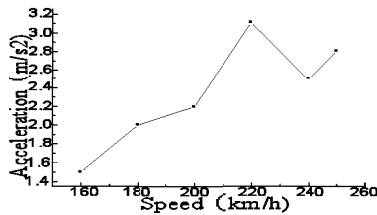
From Fig.2, the dynamic loading effect is gradually shown when train speed increases. Moreover, the sensitivities of dynamic stress of the measuring points in the depth direction to train speed are different: the shallower the measuring point, the more the dynamic stress influenced by the train speed. The dynamic stress linearly attenuates with the depth. The peak value of the bedding acceleration relates to the train speed. The bedding vibration is aggravated with the train speed increases, demonstrating a law similar to that of the dynamic stress. Therefore, the use of geogrid can add rigidity to the entire bedding, and reduce the influence that dynamic stress brings to the bedding.



(a) Dynamic stress vs. speed



(b) Dynamic stress attenuating in the depth direction



(c) Vibration acceleration varying with speed

**Fig.2. Curves of dynamic response**

## SIMULATED CALCULATION OF DYNAMIC RESPONSE

### 1. Calculation model

#### (1) Computational domain

A finite difference method was built in this paper with the FLAC (Fast Lagrangian Analysis of Continua in 2-Dimensions). This method is according to the practical conditions of the tested road-bridge transition and the characteristics of the experimental train load. Indexes like the vibration acceleration of the train body, the wheel-rail contact force will all gradually decrease with the increase of the transition length (Yu, Wang et al. 1999; Qiang Luo et al. 2000). When the transition length becomes greater than 15~20m, each index changes slightly. Therefore, we took 15m as the calculation length: the bridge length, transition length and the roadbed length is 3m, 7m, 5m respectively. The calculation depth is set as 7.2m below the rail.

#### (2) The initial condition and boundary conditions

When calculation is in the initial balance status, the model bottom adopts fixed boundary condition. Given the infinite length of the roadbed, the longitudinal displacement of fixed line is adopted and each point has zero displacement under its initial condition.

#### (3) The structural unit of geogrid roadbed

The Geogrid is modeled by the anchor-rope unit in FLAC. At the Geogrid unit node, spring-slide is used to model the mechanical behavior of geogrid's tangential plane. The shearing force between the geogrid and the geotechnical interface is controlled by the characteristics of connection friction (Yegian et al. 1998). And the effective side-stresses of the geogrid are assumed to be equal. According to the node connected unit's displacement field, the grid displacement is calculated with the interpolation method.

#### (4) The simulation of the train load

This paper simulates the interactive acting force with exciting force which reflects the wave friction effect of the rail surface. Taking into account cyclical features of the train load, the paper simulates the train load by the function of exciting force (Yaozhuang Li 2005), as shown below:

$$F(t) = p_0 + p \sin \omega t$$

where:  $F(t)$  is the train vibration load;  $p_0$  is the wheel static-load;  $p$  is the exciting force;  $\omega$  is the circular frequency.

### 2. Calculation parameters

The calculation parameters of the geogrid, the roadbed and roadbed body are chosen according to the geogrid's characteristics, train load, the boundary condition and initial conditions (Jun Liu 2006; Wei Liu 2005). Table 1 and Table 2 give these parameters in detail.

**Table 1. The calculation parameters of geogrid**

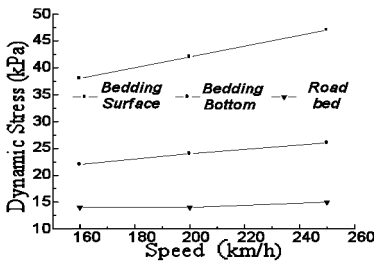
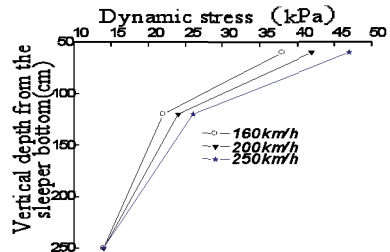
Elasticity modulus(Pa)	Grid width(m)	Yield strength(N)	Normal rigidity(N/m3)	Thickn ess(m)	Interface cohesion(N)
2.0E11	0.04	225000.0	2.0E7	0.0125	100000.0

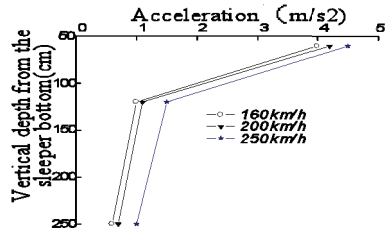
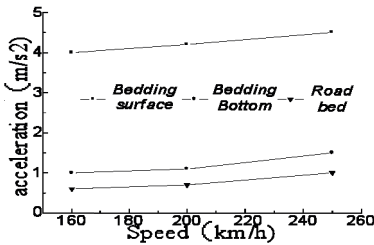
**Table 2. The calculation parameters of bedding and roadbed**

Parameters	K	G	$\mu$	Density(kN/m <sup>3</sup> )	Damping ratio
Roadbed	210	0.092	0.25	24.0	0.030
Bedding surface	190	0.094	0.25	21.4	0.028
Bedding bottom	110	0.120	0.30	19.0	0.035
Roadbed body	90	0.135	0.35	18.0	0.035

### 3. Analysis of dynamic calculation results

According to the dynamic analysis model and the calculation parameters above, a simulation analysis have been done. This simulation primarily focuses on the analysis of the dynamic stress and dynamic acceleration of rail roadbed under different train speeds. The calculation points distribute on bedding surface, bedding bottom and the superface of roadbed body. Then the relationship between the dynamic response and the train speed is obtained, as shown in Fig.3.

**(a) Dynamic stress vs. speed****(b) Dynamic stress attenuation with depth**



(c) Acceleration variation with speed

(d) Acceleration attenuation with depth

**Fig3. Numerical simulations of dynamic analysis.**

Fig. 3 shows that the dynamic stresses of the bedding surface and bedding bottom in the transition section reinforced by geogrid tend to be linearly proportional to the train speed. The linearity between the dynamic stress of the bedding surface and the speed is most prominent while that of the bedding bottom takes the second, and that of the roadbed body isn't prominently influenced by the speed variation. Therefore, the dynamic stress generated by the train mainly influences the bedding. The dynamic stress attenuation speed is not only proportional to the roadbed depth but also to the train speed. Also the vibration accelerations of the bedding surface, bedding bottom and the roadbed body are proportional to the train speed. When train speed exceeds 200km/h, the rising tendency of the vibration acceleration attenuation becomes faster, which shows up the same law of dynamic stress except a faster attenuation. This indicates that the vibration effect of the train load to the roadbed exerts mainly on the bedding surface.

**COMPARATIVE ANALYSIS OF MEASURED RESULTS AND NUMERICAL CALCULATIONS**

In order to verify the correctness of the proposed calculation model and the calculation parameters, this paper compared the calculated results with the test data, as shown in Table 3.

**Table 3. Comparisons between the test data and calculated results**

Speed (km/h)	Items	Dynamic stress of the superface			Acceleration of superface of bedding surface
		Bedding surface	Bedding bottom	Roadbed body	

		(kPa)	(kPa)	(kPa)	(m/s <sup>2</sup> )
160	<b>Tested values</b>	35.6	30.1	13.7	1.5
	<b>Calculated values</b>	38.1	22.9	14.3	3.8
	<b>Relative errors(%)</b>	7.0	23.9	4.3	153.3
200	<b>Tested values</b>	41.6	33.9	14.6	2.2
	<b>Calculated values</b>	42.9	24.8	14.9	4.1
	<b>Relative errors(%)</b>	3.1	26.8	2.1	86.4
250	<b>Tested values</b>	40.7	30.5	13.7	2.8
	<b>Calculated values</b>	47.1	26.8	15.3	4.5
	<b>Relative errors(%)</b>	15.7	12.1	11.7	60.7

According to table 3, the proposed model is almost in good agreement with field measurement data except the value for the acceleration on the top side of bedding surface at the speed of 160km/h. The complexity and indeterminacy of the experimental condition in the field test may produce such non-conformity data, but overall, the field test data are fundamentally in conformity with the numeric simulation results, which proves that the proposed model can be applied to analyze the vibration characteristics of the road-bridge transition section.

## CONCLUSIONS

In line with the test data and the simulation results, the research concludes that:

- (1) The train's kinetic action to the roadbed increases with the rise of the train speed, and then the dynamic response of the roadbed goes up.
- (2) The dynamic response of the train to the bedding surface is much greater than that of the train to the top surface of the roadbed body. Therefore, the surface stratum should be reinforced during the road-bridge transition section design.
- (3) The roadbed dynamic stress and vibration acceleration attenuates faster with the rise of the depth value. And the attenuation rate is related to the train speed. When the roadbed depth reaches a certain value, the dynamic influence of the train will not be prominent, which indicates that the road-bridge transition section reinforced by geogrid can better prevent the dynamic stress and vibration acceleration from spreading in the roadbed. It can also diminish the live loading to the roadbed. Therefore, it is a relatively reasonable road-bridge transition section form.

## REFERENCES

- Cunlin, Shi. (1999). "Technological Measures of Road-bridge Transitions Section".

*Subgrade Engineering*, (5):27-31.

- Jun, Liu. (2006). "A Research into the Numeric Simulation of the Reinforced Wall by Geogrid and Its Characteristics". *Master Theses of He Hai University*.
- Qiang,Luo and Ying, Cai. "A Research into the Deformation Restriction and Reasonable Length of Road-bridge Transitions section of High-speed Railway." *Standard Design of Railroad*, 20 (6-7) : 2-4.
- Wei Liu. (2005). "The Numeric Experimental Research into the Side Slope Reinforced by Geogrid.", *Master Theses of Beijing University of Technology*.
- Yaozhuang, Li; Pingwu, Guan. (2005). "Structural Dynamics and its Application." *Anhui Scientific Press*.
- Yegian, Harb and Kadakal. (1998). "Dynamic Response Analysis Procedure for Landfills with Geosynthetic Liners." *J. Geotech. Engr. ASCE*, 1027-1033
- Yu,Wang; Wangming, Zhai; Qichang, Wang; etal. (1999). "A New Approach to Determine the Length of Railway Transitions section ." , *Railway Engineering Journal*, (4):25-28

## Numerical Modeling of a Reinforced Embankment Based on Centrifuge Test Dimensions

Jian-Feng Chen<sup>1</sup>, Song-Bo Yu<sup>2</sup>, Jie Han<sup>3</sup>

<sup>1</sup> Associate Professor, Department of Geotechnical Engineering and Key Laboratory of Geotechnical and Underground Engineering of Ministry of Education, Tongji University, 1239 Siping Road, Shanghai 200092, People's Republic of China; jf\_chen@tongji.edu.cn

<sup>2</sup> Ph.D student, Department of Geotechnical Engineering, Tongji University, 1239 Siping Road, Shanghai 200092, People's Republic of China; yusongbo@gmail.com

<sup>3</sup> Associate Professor, Department of Civil, Environmental, and Architectural Engineering, The University of Kansas, 2150 Learned Hall. 1530 W, 15th Street, Lawrence, KS 660045, USA; jiehan@ku.edu

**ABSTRACT:** A centrifugal test of a geogrid reinforced embankment with lime-stabilized soil as backfill on soft clay was conducted to investigate the reinforcement mechanisms. A finite element model was developed to simulate the centrifugal test based on the test dimensions. Verifications of the numerical model were taken by comparing the numerical results with the measurements obtained from the centrifugal test, and it was found that both were in good agreement.

### INTRODUCTION

Although geosynthetics have been widely used in practice to improve the stability of various geotechnical projects, the reinforcement mechanisms are still far from clear. In recent years, there have been a series of centrifugal tests conducted on scaled-down geosynthetics-reinforced structures to investigate the reinforcement mechanisms and some were simulated in combination of numerical methods (Bolton and Sharma 1994; Xie et al. 1995; Mandal and Joshi 1996; Sharma and Bolton 1996; Ding and Bao 1999; Sharma and Bolton 2001; Hu et al. 2003; Viswanadham and Mahajan 2004; Yu et al. 2005).

Ding and Bao (1999) developed a plane finite element model to simulate geosynthetics-reinforced embankments on soft hydraulic fill and compared the numerical results with the centrifugal test measurements. A non-linear hyperbolic constitutive model and two-dimensional (2D) solid elements were used to characterize the behavior of the hydraulic fill and the geosynthetics, respectively.

Sharma and Bolton (2001) simulated geotextile-reinforced embankments on soft clay with or without wick drains using a 2D finite element program CRISP in combination of centrifuge tests. The Cam-clay model, the Mohr-Coulomb criterion,

and the liner elastic bar elements were employed to model the foundation, the embankment and the geotextile, respectively.

Hu et al. (2003) and Yu et al. (2005) used a 2D finite element model to verify the results of centrifugal tests conducted on a scaled-down geotextile-reinforced levee. They chose an elasto-brittle model and a complex model with a united water-drop shape yield surface to characterize the geotextile and the soils, respectively. However, these numerical simulations were performed on the prototypes which were modeled by the centrifugal tests.

The staged-construction processes of embankments are usually simulated in centrifugal tests by increasing accelerations. According to the law of similarity, the dimensions of a centrifugal model vary with increasing centrifugal accelerations, which is different from actual conditions in prototype. Consequently, numerical simulation based on the dimensions of a centrifugal test model in a changing acceleration field is reasonable and significant. However, such documentations are very limited so far.

In this paper, a numerical model was developed based on the dimensions of a centrifugal test conducted on a geogrid-reinforced embankment with lime-stabilized soil as backfill using a 2D finite element program PLAXIS. Verifications of the numerical model were carried out by comparing the numerical results with the measurements obtained from the centrifugal test.

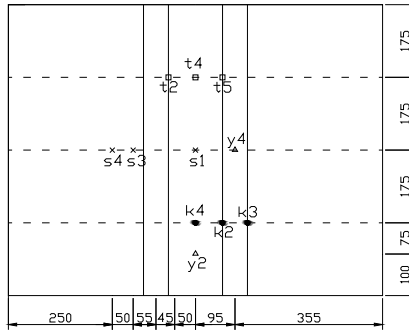
## NUMERICAL MODELING

### *Centrifugal Test*

As shown in Figure 1, the scaled-down centrifugal lime-stabilized embankment had a height of 60 mm, a crest width of 130 mm, and a 1:1 slope, underlain by a soft silty clay foundation of 250 mm thickness. A 5 mm thick sand cushion was placed between the foundation and the embankment. A model geogrid made of high-density polyethylene plastics (HDPE) was placed in the middle of the cushion. Model sand drains of 5 mm diameter were installed in a triangular pattern at a center-to-center spacing of 32 mm. The water table was set at the ground surface elevation.

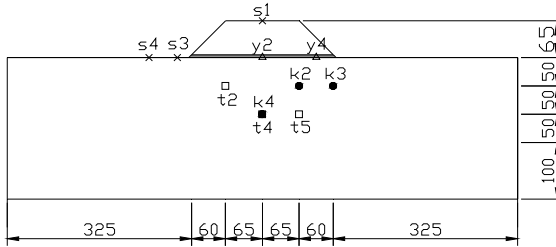
Six pore pressure transducers and six earth pressure cells were installed at various locations in the clay foundation. Four displacement sensors were placed on the surface of the model. Four strain gauges were glued onto the surface of the model geogrid with epoxy resin. Detailed description of instrumentations can be found in Chen et al. (2008). As some of the instruments did not work well, Figure 1 only illustrates the arrangement of functional ones.

Figure 2 presents an acceleration-time curve. A three-staged construction of the embankment was simulated by increasing the acceleration up to three levels of 33.3g, 66.7g, and 100g. The three level accelerations corresponded to the construction heights of 2, 4, and 6 m, respectively, according to the similarity law of centrifugal test. After each staged construction, there was one month waiting period in the prototype; that is, 39.0, 9.7, and 4.3 min waiting periods in the model.



x Displacement sensor      □ Earth pressure cell  
 ● Pore pressure transducer      △ Strain gauge

(a) Plane view



(b) Cross view

FIG. 1. Model dimensions and instrumental arrangements (unit: mm).

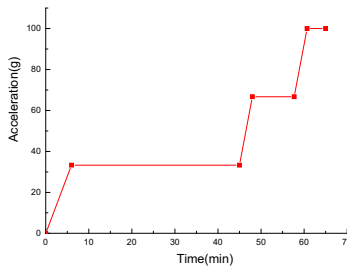


FIG. 2. Relationship curve between acceleration and time.

**Matching Procedure in Axisymmetry and Plane Strain**

The actual field consolidation of soil around each drain is close to an axial symmetry, which should be converted into a plane strain condition for 2D finite element program. Hansbo (1981) deduced a simple equation to solve the

consolidation of foundation with sand drains considering the factors of smear and well resistance. Hird et al. (1992) then converted Hansbo's equation to an equivalent plane-strain consolidation equation, that is

$$k_{hp} = \frac{B^2}{R^2} \frac{\mu_p}{\mu} k_h \tag{1}$$

where  $k_h$  is the horizontal permeability of the clay foundation; the subscript p denotes plane-strain condition; B is the half width of the plane-strain unit cell; R is the radius of the axisymmetric unit cell;  $\mu$  and  $\mu_p$  are dimensionless factors defined as

$$\mu = \ln(n/s) + (k_h/k'_h) \ln s - 0.75 + \pi z(2l-z)k_h/q_w \tag{2}$$

$$\mu_p = \frac{2}{3} + \frac{2k_{hp}}{BQ_w}(2lz - z^2) \tag{3}$$

where  $q_w$  and  $Q_w$  are the discharge capacities of the plane strain and axisymmetric drains, respectively;  $k'_h$  is the horizontal permeability in the smeared zone; l is the drain length; z is the depth of the calculated point;  $n = R/r_w$ ,  $s = r_s/r_w$ ,  $r_s$  and  $r_w$  stand for the radii of the smeared zone and the vertical drain, respectively.

If both smear and well resistance effects are ignored, the following relationships can be obtained:  $s = 1$ ,  $k_h/q_w \rightarrow 0$ ,  $k_{hp}/Q_w \rightarrow 0$ . Replace these relationships into Eqs. (2) and (3) and assume B is equal to R, thus Eq. (1) can be simplified as

$$k_{hp} = \frac{0.67}{\ln n - 0.75} k_h \quad (n > 2.12) \tag{4}$$

Effort was taken to control the disturbance to the clay foundation when the model sand drains were installed. The discharge capacity of the drains was found high during the centrifugal test. Therefore, well resistance and smear effect were ignored in the numerical analysis.

For triangular pattern installation, the relationship between the radius of the axisymmetric unit cell (R) and the center-to-center spacing of sand drains (S) can be expressed as

$$R = 0.525 \cdot S \tag{5}$$

Assuming  $B=R$  (i.e.,  $B=16.8$  mm), the relationship  $k_{hp} = 0.6k_h$  can be obtained using Eqs. (4) and (5) with  $S=32$  mm.

### Finite Element Model and Constitutive Parameters

Due to the inherent symmetry of the embankment, only one half of the embankment was modeled. Figure 3 shows the model developed by 2D finite element program PLAXIS. The model had the same dimensions as that in the centrifugal test as shown in Figure 1(b) except the spacing of drains (2B) at 33.6 mm. Full fixity was assumed along the bottom of the model. The vertical boundaries of the model were fixed in the horizontal direction. The ground surface was fully drained and the water table was set at the ground surface. An unstructured FE mesh that consists of 15-node, triangular elements was used.

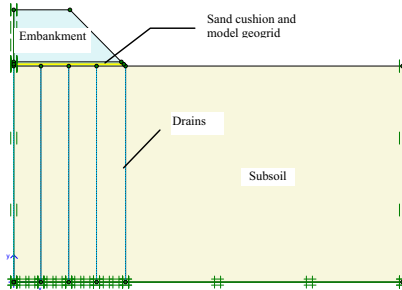


FIG. 3. Geometry of numerical model.

The Mohr-Coulomb model was used to characterize the constitutive behavior of the embankment and the sand cushion. The geogrid element inherent in PLAXIS was used to simulate the model geogrid. Sand drains were modeled as drainage boundaries with a zero-excess pore pressure condition. The hardening-soil model developed by Schanz et al. (1999) was used to model the foundation clay. The hardening-soil model is essentially nonlinear and elastoplastic, in which the yield surface in the principle stress space consists of a hardening hexagonal yield surface enclosed by a hardening cap. Failure of the model is defined in accordance with the Mohr-Coulomb criterion. Constitutive model parameters of the hardening-soil model can be readily determined from consolidated drained triaxial and oedometer tests based on the methods suggested by Schanz et al. (1999). Table 1 summarizes the values of the constitutive parameters for the FE analysis.

Table 1. Constitutive Model Parameters for the FE Analysis

Material	Model	$\gamma_{unsat}$	$\gamma_{sat}$	$k_h$	$E_{ref}$	$\nu$	$c$	$\phi$	$\psi$	$E_{50}^{ref}$	$E_{oed}^{ref}$	$E_w^{ref}$	$m$
Clay	Hardening-Soil	13.0	17.3	0.235 <sup>b</sup>	--	--	8	23	0	4.70	4.70	14.1	1
Lime-stabilized soil	Mohr-Coulomb	19.1	22.0	--	425	0.2	109	35	0	--	--	--	--
Sand	Mohr-Coulomb	16.0	20.0	11570	3	0.3	1	30	0	--	--	--	--

<sup>a</sup>  $\gamma_{unsat}$  — unit weight above water table ( $\text{kN}\cdot\text{m}^{-3}$ );  $\gamma_{sat}$  — unit weight below water table ( $\text{kN}\cdot\text{m}^{-3}$ );  $k_h$  — horizontal permeability ( $10^{-9}\text{m/s}$ );  $E_{ref}$  — Young's modulus (MPa);  $\nu$  — Poisson's ratio;  $c$  — cohesion (kPa);  $\varphi$  — friction angle (degree);  $\psi$  — dilation angle (degree);  $E_{sc}^{st}$  — secant stiffness in standard drained triaxial test (MPa);  $E_{sc}^{st}$  — tangent stiffness for primary oedometer loading (MPa);  $E_{un}^{st}$  — Young's modulus for unloading and reloading (MPa);  $m$  — power for stress-level dependency of stiffness.

<sup>b</sup> horizontal permeability in the plane-strain condition  $k_{hp} = 0.6 \times k_h = 0.141 \times 10^{-9} \text{m}\cdot\text{s}^{-1}$ ; vertical permeability was assumed to be equal to the horizontal permeability.

Geogrid cannot sustain compressive loading. Two parameters needed for FE analysis are the elastic axial stiffness (EA) and the tensile strength ( $N_p$ ). EA can be determined from the curve of the elongation of the geogrid plotted against the applied force and is the ratio of the axial force per unit width to the axial strain. Through tensile tests conducted on the model geogrid, 0.71 kN/m of the axial force per unit width at 5% elongation and 1.32 kN/m of tensile strength were obtained (Chen et al. 2008). Thus, for the model geogrid,  $EA=0.71/5\%=14.2 \text{ kN/m}$  and  $N_p=1.32 \text{ kN/m}$ .

### **Modeling Procedure**

The process of increasing centrifugal accelerations was achieved by setting the multiplier  $\sum Mweight$  in PLAXIS as three acceleration stages (33.3g, 66.7g, and 100g) as illustrated by Figure 2. Following each acceleration stage, a consolidation computation for the waiting period was carried out. As significant deformations were found in the centrifuge test, the options of Updated Mesh and Updated water pressures were selected to account for large deformations.

## **NUMERICAL RESULTS AND ANALYSES**

Figure 4 shows the contours of resultant deformations, vertical total stresses and pore pressures at an acceleration of 100.0 g.

Significant vertical and horizontal displacements occurred under the center and toe of the embankment, respectively, while slight heave occurred at the ground surface beyond the toe as shown in Figure 4(a). The vertical stresses were higher but the pore pressures were lower close to the drains compared to those between two neighboring drains as shown in Figures 4 (b) and 4 (c).

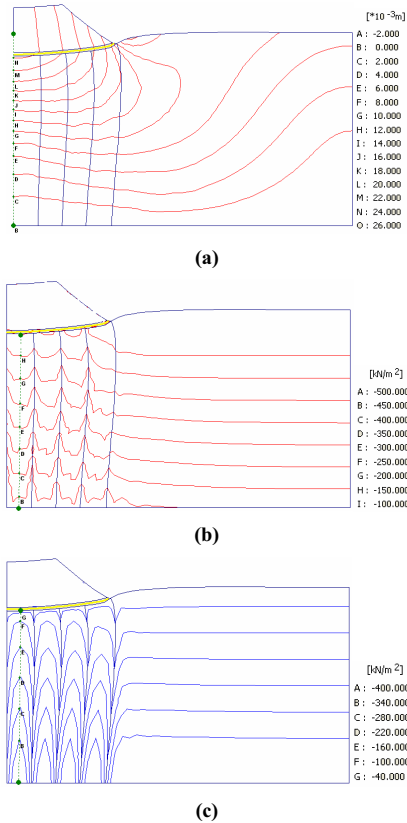


**FIG. 4. Contours of: (a) resultant deformations; (b) vertical total stresses; and (c) pore pressures.**

Figures 5 to 8 present the comparisons of the computed and measured settlements, earth pressures, pore pressures and reinforcement forces, respectively.

As shown in Figure 5, the computed and measured settlements at s1 (located at the embankment center) and s3 (150 mm away from the center) in general are in good agreement. The computed heave at s4 (200 mm away from the center) was approximately 2 mm larger than the measurement while both varied with time in a similar.

The computed earth pressures were slightly higher than the measured ones as shown in Figure 6. Comparison of the computed and measured pore pressures shows good agreement as shown in Figure 7. It can be also seen that both computed and measured pore pressures dissipated rapidly during the waiting periods.

As shown in Figure 8, the computed reinforcement force at y2 was approximately

30% higher than the measured value. The computed reinforcement force at y4 was higher than the measured value at the stage of 33.3 g; whereas both were close when the acceleration was increased. Note that the measurement point y2 was adjacent to the front Plexiglas window. The friction from the window surface might be attributed to an underestimation of the measured reinforcement force at y2. However, both the numerical and experimental results show that the reinforcement force at the embankment center (y2) was larger than that below the slope (y4).

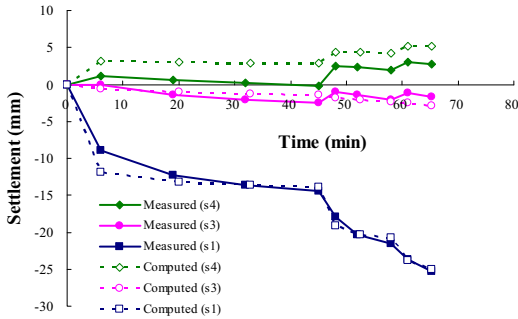


FIG. 5. Comparison of the computed and measured settlements.

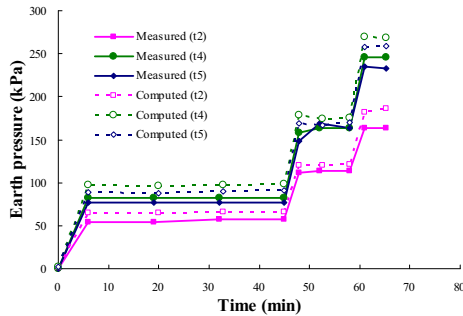


FIG. 6. Comparison of the computed and measured earth pressures.

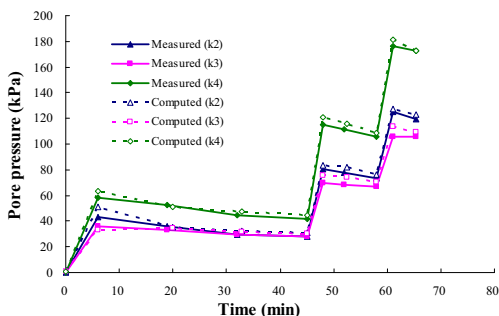


FIG. 7. Comparison of the computed and measured pore pressures.

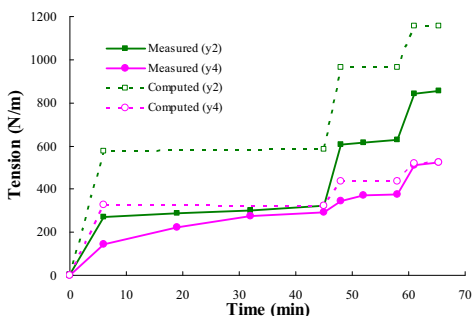


FIG. 8. Comparison of computed and measured tensile forces of reinforcements.

## CONCLUSIONS

A finite element model was developed based on a centrifuge test performed on a geogrid-reinforced embankment with lime-stabilized soil as backfill on soft clay. Verifications of the numerical model were carried out by comparing the numerical results with the experimental ones from the centrifugal test.

Comparisons of the computed and measured settlements, earth pressures, pore pressures and reinforcement forces show good agreement in general.

## ACKNOWLEDGMENTS

The financial support from the Natural Science Foundation of China under grant No. 50508030 is gratefully acknowledged. The authors also would like to thank the staff of Key Laboratory of Geotechnical and Underground Engineering of Ministry of Education in Tongji University for their help in centrifugal testing.

## REFERENCES

- Bolton, M. D., Sharma, J. S. (1994). "Embankments with base reinforcement on soft clay." *Proceedings of International Conference on Centrifugal* 94, A. A. Balkema, Rotterdam, 587-592.
- Chen, J. F., YU, S. B., Ye, T. F., et al. (2008). "Centrifuge modeling of reinforced embankment with lime-stabilized soil as backfill on soft clay." *Chinese Journal of Rock Mechanics and Engineering*, 27(2), 287-293 (in Chinese).
- Ding, J. H., Bao, C. G. (1999). "Centrifugal model test and finite element analysis of geosynthetic-reinforced embankments on soft ground and dredger fill." *China Civil Engineering Journal*, 32(1), 21-25 (in Chinese).
- Hansbo, S. (1981). "Consolidation of fine-grained soils by prefabricated drains." *Proceedings of International Conference on Soil Mechanics and Foundation Engineering*, A. A. Balkema, Rotterdam, 677-682.
- Hird, C. C., Pyrah, I. C., Russell, D. (1992). "Finite element modelling of vertical drains beneath embankments on soft ground." *Geotechnique*, 42(3), 499-511.
- Hu, H. R., Chen, S. L., Shen, Z. J. (2003). "Centrifugal and numerical modeling of geosynthetic reinforced embankments on soft clay." *Rock and Soil Mechanics*, 24(3), 389-394 (in Chinese).
- Mandal, J. N., Joshi, A. A. (1996). "Centrifuge modelling of geosynthetic reinforced embankments on soft ground." *Geotextiles and Geomembranes*, 14(2), 147-155.
- Schanz, T., Vermeer, P. A., Bonnier, P. G. (1999). "Formulation and verification of the hardening-soil model." *Beyond 2000 in Computational Geotechnics*, A. A. Balkema, Rotterdam, 281-290.
- Sharma, J. S., Bolton, M. D. (1996). "Centrifuge modeling of an embankment on soft clay reinforced with a geogrid." *Geotextiles and Geomembranes*, 14(1), 1-17.
- Sharma, J. S., Bolton, M. D. (1996). "Finite element analysis of centrifugal tests on reinforced embankments on soft clay." *Computers and Geotechnics*, 19(1), 1-22.
- Sharma, J. S., Bolton, M. D. (2001). "Centrifugal and numerical modelling of reinforced embankments on soft clay installed with wick drains." *Geotextiles and Geomembranes*, 19(1), 23-44.
- Xie, Y. L., Pan, Q. Y., Zeng G. X. (1995). "Study on deformation behavior of soft clay ground with centrifugal model test." *Chinese Journal of Geotechnical Engineering*, 17(4), 45-50 (in Chinese).
- Yu, Y. Z., Zhang, B. Y., Zhang, J. M. (2005). "Action mechanism of geotextile-reinforced cushion under breakwater on soft ground." *Ocean Engineering*, 32(14/15), 1679-1708.
- Viswanadham, B. V. S., Mahajan, R. (2004). "Modeling of geotextile reinforced highway slopes in a geotechnical centrifuge." *Geotechnical Engineering for Transportation Projects: Proceedings of Geo-Trans, ASCE, Reston, Va.*, 637-646.

## Granular Lightweight Fill Composed of Sand and Tire Scrap

An Deng<sup>1</sup> and Jin-Rong Feng<sup>2</sup>

<sup>1</sup> Associate Professor, Key Laboratory of Ministry of Education for Geomechanics and Embankment Engineering, Hohai University, Nanjing 210098, China;  
Geotechnical Research Institute, Hohai University, Nanjing 210098, China; a\_deng@hhu.edu.cn  
<sup>2</sup> ditto

**ABSTRACT:** A granular geomaterial, known as sand-tire lightweight fill, was proposed by blending sand with disposed tire scrap in proportions. The geomaterial can be used as alternative backfill in many infrastructure works, where less overburdens and lateral loads are expected. The reuse of tire scraps may not only address growing environmental and economic concerns, but also help solve geotechnical problems associated with low soil shear strength. In this study, an experimental testing program was undertaken with the goal of evaluating the compression and shear behavior of the materials. Three tests were implemented, i.e., 1-D compression tests, direct shear tests and consolidated drained triaxial compression tests. A compression strain-load model was proposed to describe its compression behavior. Rebound-reload tests revealed that materials' plastic deformation was associated with the mixing ratios. The tire scrap content was found to influence the stress-strain and volumetric strain behavior of the mixtures. Mixtures underwent shear contraction during shearing processes, which is different from the shear dilation of compact sands. Effects of mixing ratios and stress conditions on shear deformation behaviors were also discussed.

### INTRODUCTION

Along with the escalating development of global auto industry, disposed tires are becoming one of overwhelming solid byproducts. According to the statistics (CRIA 2006), over 100 million tires are manufactured in China annually, close to the generations of the U.S. and Japan; around 50 million tires are disposed in a year. Disposals of such vast volume byproducts not only occupy large-scale stack yards or landfills; improper or unsafe handling (e.g. irrational combustion) may pose adverse impact to the environments. To beneficially reuse disposed tires is thought to be the ultimate solution to this concern. Such efforts have initiated worldwide, for instance, as substantial energy sources via safe combustion, to be used into embankments and vibration isolation or mitigation facilities (CRIA 2006, Humphrey 1999). With the rapid advance of chipping and grinding techniques, more and more researchers have focused

on the reuses of tires in the form of scraps, particularly as construction granular materials owning special properties. For instance, the tire scraps can be proportioned into asphalt concrete to mitigate vibration and noise, and thermal gradients (Huang and Zhang 2006, 2007, Cao and Ren 2007). The tire scraps can be concreted into pavement bricks, providing walk-comfortable effect. The scraps are also technically suitable for the uses of absorbing pollutants and preventing soil piping in filter systems (Waritha and Rao 2006). Recently, tire scraps were mixed with soils and pozzolanic materials to make structural geomaterials (Pierce and Blackwell 2003, Tweedie et al. 1998, Edil and Bosscher 1994, Foose et al. 1996). There are few publicly accessible sources focusing on the nonstructural geomaterials without addition of pozzolanic materials.

In this paper, tire scraps and construction sands were mixed into a matrix at certain mass ratios. Such formed geomaterials, known as sand-tire lightweight fills, have advantages over general fills by being lightweight. The property of low unit weight enables the lightweight fills suitable for various infrastructure works where less overburdens and lateral loads are expected, e.g., embankments rested on difficult ground, embankments under broadening, bridge abutments, slope and retaining structures, and utilities trench backfilling works. To research the mechanical behavior, especially deformation characteristics of sand-tire lightweight fills, helps predict the settlement and deformation of the field applications. A laboratory study was conducted to discover the compression and shear deformation behaviors through 1-D compression tests, direct shear tests and triaxial compression tests. Factors affecting the deformation behaviors were analyzed. The work can be regarded as an initiative for further addressing the constitutive laws of such granular lightweight geomaterials.

## EXPERIMENTAL PROGRAM

### Materials and Specimens

Materials consisted of construction sands and tire scraps. The water content of sand was around 5%. Sand specific gravity was 2.62. Figure 1 shows the sand gradation curves. The sand was well graded. Tires are made of rubber, a polymer with elastic and frictional property. The tires were chipped into even scraps by the manufacturers, as shown in Figure 2. The size of scraps fell within 4-5 mm. The tire specific gravity was 1.33, a half of typical soils, contributive to reducing the unit weight of mixtures.

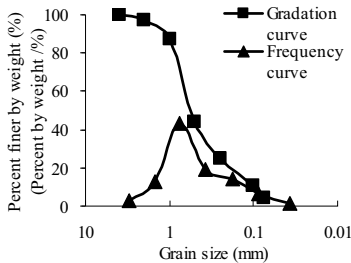


FIG. 1. Gradation curves of sands.



FIG. 2. Scrap tire beads.

The sands and tire scraps were mixed together according to the mass ratio of sand versus tire, known as sand-tire ratio  $\eta$ . The ratios included 10:0, 9:1, 8:2, 7:3, 6:4 and 0:10. Scaled materials were mixed homogeneously via air-mixing methods. The mixing ratios and unit weights of mixtures are presented in Table 1. It is seen that one tenth increment in tire leads to 10% decrement in unit weight of mixtures.

**Table 1. Mixing Ratios and Densities of Specimens.**

Sand-Tire Ratios $\eta$	Relative Densities, $D_r$	Densities, $\rho$ (g/cm <sup>3</sup> )
10 : 0	0.7	1.784
9 : 1	0.7	1.617
8 : 2	0.7	1.466
7 : 3	0.7	1.325
6 : 4	0.7	1.257
0 : 10	0.7	0.701

### Test Methods

Test methods included 1-D compression tests, fast direct shear tests and consolidation-drained (CD) triaxial compression tests. The test procedures were implemented in accordance with Standard for Soil Test Method (GB/T50123-1999). In 1-D compression test, the loads  $P$  were 12.5, 25, 50, 100, 200, 400, 800, 1600 and 3200 kPa. The normal stresses  $\sigma$  in direct shear tests included 100, 200, 300 and 400 kPa. The confining pressures  $\sigma_3$  in CD tests included 100, 200, 300 and 400 kPa. The axial compression rate in CD tests was 0.015 mm/min (i.e. 0.018% strain per min).

## RESULTS AND DISCUSSION

### Compression Characteristics

Terzaghi's 1-D consolidation model assumes that the volumetric strain of soils comes solely from void decrease, and that contraction of soil particles and pore water are neglectable. In sand-tire mixtures, however, the rubber tire scrap, as an elastic polymer material, is relatively less rigid compared to the sand. As a result, tire scraps are prone to exhibiting non-neglectable volumetric strain if exposed to high isotropic pressures. As such, the void ratio  $e$  is better to be replaced with an alternative parameter to predict the settlement or deformation of the mixture in 1-D compression tests. To quantify the compression deformation, compression strain  $\epsilon_c$  (representing vertical deformation divided by the specimen initial thickness), was used to account for both the void and tire scrap compression. The relationship between  $\epsilon_c$  and vertical loads  $P$  may reflect the compression characteristics of lightweight fills under 1-D loading conditions, and be used to calculate the compression modulus  $E_s$ .

Figure 3 presents the  $\epsilon_c$  -  $\log P$  curves of specimens at varied ratios. It is shown that the curves develop hyperbolically without clear yield or jump points, which is thought

ascribed to the elastic and frictional property of tire scraps. The curve developments are clearly associated with the sand-tire ratios. With ratio  $\eta$  transiting from 10:0 to 0:10, sand component decreases and tire scrap component increases; the specimen's compression deformation intensifies. When the mixture consists solely of tire scraps ( $\eta=0:10$ ),  $\epsilon_c$  -  $\log P$  curve is isolated from the other curves, presenting substantial deformation. It is inferred that sand particles efficiently fill the voids of tire scraps and thus offset partial compressions.

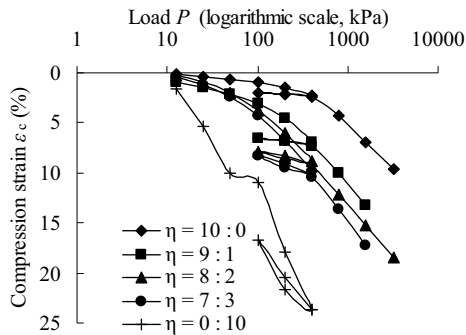


FIG. 3.  $\epsilon_c$  -  $\log P$  curves of sand-scrap tire fills.

Rebound-reloading procedures were also conducted in the 1-D compression tests. The loading  $P$  followed the path of 400-100-400 kPa. Resilient index  $C_{s1-4}$  was defined as the slope of the rebound curves shown in Figure 3. A high  $C_{s1-4}$  value indicates a high elasticity and low plasticity of mixtures. It is shown that  $C_{s1-4}$  increases with the increase of tire scrap (decrease of  $\eta$ ), which means that tire scrap is able to convert the mixture into an elastic body. It is also seen that the compression of sand-tire mixture is composed of two parts, i.e., plastic deformation and elastic deformation. Both of them increases with decrease of  $\eta$ .

Simulation of the  $\epsilon_c$  -  $\log P$  curves results in a quantified estimation of deformation or settlements of practical works using the sand-tire fills. The curves may be simulated using Eq. 1, where,  $a_1, b_1$  representing curve fitting parameters (see Table 2).

$$\log(P) = \epsilon_c / (a_1 + b_1 \epsilon_c) \tag{1}$$

Table 2. Parameters for  $\epsilon_c$  -  $\log P$  Hyperbolic Simulations.

$\eta$	$a_1$	$b_1$	$R^2$
10 : 0	0.21	0.27	0.99
9 : 1	0.71	0.27	0.99
8 : 2	0.63	0.27	0.97
7 : 3	0.67	0.29	0.98
0 : 10	1.77	0.33	0.95

### Direct Shear Deformation Characteristics

Figs. 4 and 5 depict the shear stress-shear displacement curves of specimens under normal stresses  $\sigma$  of 100 and 300 kPa. The curves develop hyperbolically. It is seen that there is a clear difference between curve of pure sand and curves of mixed materials. The curves are basically divided into two groups. For pure sand specimens, the stress is constant after the peak value is reached, being a strain-soften style of compact sand; for sand-tire mixtures, the curves are strain-hardening styles, similar to loose sands. It is interpreted that not only elastic tire scraps decrease the rigidity of whole mixtures, but also the volumetric contraction of the scraps offsets sand dilation, similar to the shear deformation of loose sands.

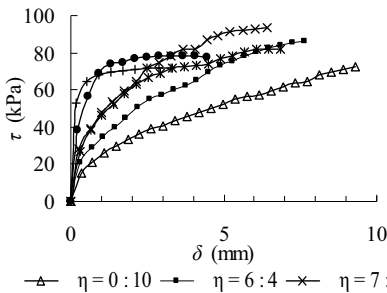


FIG. 4.  $\tau$ - $\delta$  curves ( $\sigma=100\text{kPa}$ )

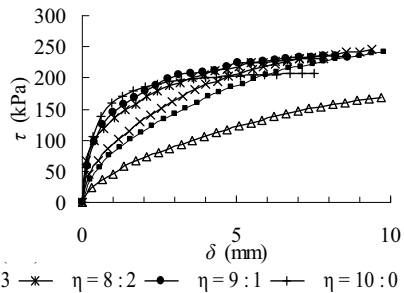


FIG. 5.  $\tau$ - $\delta$  curves ( $\sigma=300\text{kPa}$ )

It is also shown in Figs. 4 and 5 that shear resistances decrease with the increase of tire scraps (decrease of  $\eta$ ). With the increase of tire scrap contents, the stress-harden level intensifies. This can be interpreted in terms of the shear strength mechanism (Qu 1987, Lu et al. 2006). It is pointed out that internal friction angle  $\varphi$  of granular materials is related to three components, as shown in Eq. 2.

$$\varphi = \varphi_{\mu} + \varphi_d + \varphi_b \quad (2)$$

Where,  $\varphi$  representing internal friction angle of granular soils,  $\varphi_{\mu}$  representing component of sliding friction,  $\varphi_d$  representing component of dilation,  $\varphi_b$  representing component of breakage and rearrangement.

In the case of sand-tire mixtures, contractible tire scraps offset the sand dilation. The mixture is lagged in particle breakage and rearrangement compared to pure sands (leading to decreased  $\varphi_b$ ). Furthermore, the interlock force is offset (leading to decreased  $\varphi_d$ ). While tire scraps are able to slightly increase skin friction, such resultant increase of  $\varphi_{\mu}$  is less than the decrease of  $\varphi_b$  and  $\varphi_d$ . As a result, the shear resistance is reduced on the whole.

**Triaxial Shear Deformation Characteristics**

Figs. 6-9 depict the deviator stress-volumetric strain-axial strain curves of specimens at sand-tire ratios of 10:0, 9:1 and 7:3, respectively. Under the conditions of same mixing ratio and different confining pressure  $\sigma_3$ , hardening levels of deviator stress-axial strain curves increase with  $\sigma_3$ . With the increase of  $\sigma_3$ , relative densities of mixtures increase. The interlock force and shear resistance increase. As a result, the higher the  $\sigma_3$ , the higher shear resistance and elastic modulus.

Distinct from the shear dilation of compact sand, all mixtures underwent shear contract. Under the same axial strain  $\epsilon_a$ , the higher the  $\sigma_3$ , the more the volumetric strain  $\epsilon_v$ . If the portion of tire scrap increases (Fig. 9), the influence of confining pressures on volumetric strain is clearer. It is thought that high  $\sigma_3$  effectively “consolidates” the scrape before shearing. The major volumetric strain of tire scraps was accomplished in the consolidation processes. On the other side, such highly “consolidated” scraps yield relatively less volumetric strain.

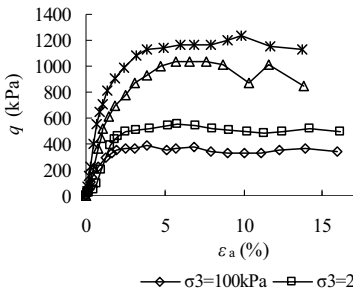


**FIG. 6.**  $q-\epsilon_a$  curves ( $\eta=10:0$ )

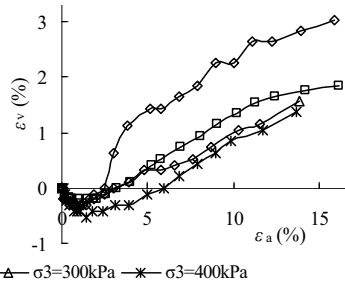


**FIG. 7.**  $\epsilon_v-\epsilon_a$  curves ( $\eta=10:0$ )

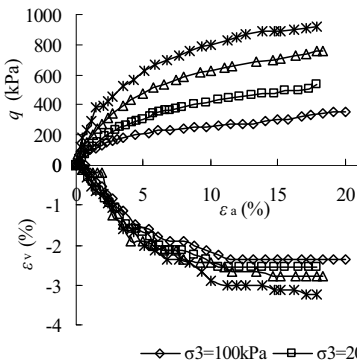


**FIG. 8.**  $q-\epsilon_v-\epsilon_a$  curves ( $\eta=9:1$ )

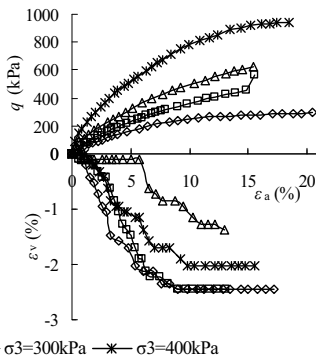


**FIG. 9.**  $q-\epsilon_v-\epsilon_a$  curves ( $\eta=7:3$ )

The shear strength parameters ( $c$  and  $\varphi$ ) for sand-tire mixtures are shown in Table 3. It is shown that internal friction angle  $\varphi$  ranges between  $28^\circ$  and  $32^\circ$  for sand-tire mixtures, slightly less than that of pure sands ( $33^\circ$ - $35^\circ$ ) and substantially more than that of pure tire scraps ( $18.1^\circ$ ). It is meant that inclusion of a volume of sand helps maintain the internal friction and interlock effect of mixtures. It is also shown that inclusion of tire scraps trigger cohesion in the mixtures, with  $c$  being on average 30 kPa for sand-tire mixtures. It is seen that the inclusion of tire scrap enhances the shear strength, in particular the cohesion, and that mixtures of  $\eta = 8:2$  and  $7:3$  are technically advantageous over the others, providing a balanced combination of  $c$  and  $\varphi$ .

**Table 3. Direct Shear Strength Parameters Sand-Tire Mixtures.**

$\eta$	Direct Shear Tests		CD Shear Tests	
	$c$ (kPa)	$\varphi$ ( $^\circ$ )	$c$ (kPa)	$\varphi$ ( $^\circ$ )
10 : 0	0	32.9	0	34.8
9 : 1	15	32.2	29.1	29.7
8 : 2	30	29.4	31.1	28.9
7 : 3	31	28.3	28.3	28.5
0 : 10	15.5	18.1	-	-

## CONCLUSIONS

This work was conducted to research the compression and shear deformation characteristics of granular sand-tire lightweight fills. It was found that the relationship between compression and load develops hyperbolically. The compression included two parts, e.g., elastic and plastic deformation, which increased with decrease of  $\eta$ . The compression summation can be used for predicting the settlement of practical works. Mixtures underwent shear contraction in triaxial tests. Hardening levels of stress-strain curves increased with confining pressures. The contents of tire scraps were able to influence the relationship between confining pressures and volumetric strains.

## ACKNOWLEDGEMENTS

The work was supported by National Natural Science Foundation of China (50708031) and Scientific Research Foundation for the Returned Overseas Chinese Scholars, SEM.

## REFERENCES

- Cao, H.H. and Ren, F.T. (2007). "Traffic noise reduction properties of asphalt rubber pavement." *J. Beijing Univ. Technol.*, Vol. 33 (5): 455-458. (in Chinese)
- CRIA. (2006). "Report on the reuse of environmental protection of disposed rubber." *China Rubber*, Vol. 22 (17): 4-9. (in Chinese)
- Edil, T.B. and Bosscher, P.J. (1994). "Engineering properties of tire chips and soil mixtures." *Geotech. Test. J.*, Vol. 17 (4): 452-464.
- Foose, G.J., Benson, C.H., and Bosscher, P.J. (1996). "Sand reinforced with shredded

- waste tires." *J. Geotechnical & Geoenv. Engrg.*, Vol. 122 (9): 760-767.
- Huang, W.Y., and Zhang, Y.X. (2006). "Mechanism and process control of road-use asphalt rubber reaction procedure." *J. Highway Transport. Res. Dev.*, (11): 5-9. (in Chinese)
- Huang, W.Y., and Zhang, Y.X. (2007). "The technical criteria frame of pavement used asphalt rubber in China." *Cent. S. Highway Eng.*, (1): 111-114. (in Chinese)
- Humphrey, D.N. (1999). "Civil engineering applications of tire shreds." *P. Tire Ind. C.*, Clemson University, 1999, pp. 1-16.
- Lu, T.H., Liu Z.D., and Chen G.X. (2006). *Advanced Soil Mechanics*. China Machine Press, Beijing. (in Chinese)
- Pierce, C.E. and Blackwell, M.C. (2003). "Potential of scrap tire rubber as lightweight aggregate in flowable fill." *Waste Manage.*, Vol. 23 (3): 197-208.
- Qu, Z.J. (1987). *Soil Plasticity Mechanics*. Publishing House of Chengdu University of Science and Technology, Chengdu, 1987. (in Chinese)
- Tweedie, J.J., Humphrey, D.N., and Sandford, T.C. (1998). "Tire shreds as lightweight retaining wall backfill: active conditions." *J. Geotechnical & Geoenv. Engrg.*, Vol. 124 (11): 1061-1070.
- Waritha, M.A. and Rao, S.M. (2006). "Predicting the compressibility behaviour of tire shred samples for landfill applications." *Waste Manage.*, Vol. 26 (3): 268-276.

## Large Direct Shear Test Apparatus for Insitu Testing of Municipal Solid Waste Landfill Sites

Dr Liaqat Ali<sup>1</sup>, Sarfraz Ali<sup>2</sup>, and Ammar Maqbool<sup>3</sup>

<sup>1</sup>National University of Science and Technology (NUST), Pakistan, liaqatnit@yahoo.com

<sup>2</sup>National University of Science and Technology (NUST), Pakistan, sarfrazengr@yahoo.com

<sup>3</sup>National University of Science and Technology (NUST), Pakistan, aammermaqbool@yahoo.com

**ABSTRACT.** To optimize utilization of the closed municipal solid waste (MSW) sites, there is a dire need to establish simple, reliable and cost effective testing methodologies. Characterization of MSW sites is difficult due to non availability of standard procedures and limited worldwide experience. The shear strength is probably the most important parameter for the design of any structure on the closed MSW sites. Direct Shear Test has been widely used for the evaluation of the shear strength of MSW. Because of the obvious limitations of lab testing of MSW samples, a Field Large Size Direct Shear Apparatus was designed. Numerous insitu direct shear tests were performed in a closed MSW sites with the designed apparatus and very encouraging results were obtained. While maintaining simplicity, the apparatus allows strict load and deformation control. This paper highlights the salient design features of the apparatus.

**Keywords:** MSW, Insitu Shear Strength of MSW, Field Direct Shear Test Apparatus

### INTRODUCTION

For safe and stable design of intended structures, MSW sites necessitate a comprehensive geotechnical investigation. Shear strength parameters are the most important geotechnical properties. Due to large variation in composition and difficulty of extraction of undisturbed samples for laboratory investigation, large direct shear apparatus is required for in-situ testing. It was therefore decided to design and manufacture a direct shear test apparatus for insitu testing of large representative samples of MSW. The design and testing procedure of the new apparatus is based on number of factors peculiar to un-controlled and non-engineered MSW sites.

### DESIGN FEATURES OF LARGE DIRECT SHEAR TEST APPARATUS

**Specimen Size and Shape.** Through visual observation, horizontal and vertical profiling using various techniques and physical segregation of solid waste at six pits

at different MSW sites in Pakistan, it was concluded that the size of representative sample should not be less than 1 m x 1 m x 0.65 m. Therefore direct shear box measuring 1.22 m x 1.22 m x 0.75 m was manufactured to ensure testing of representative specimen.

**Method of Loading.** The apparatus was designed to allow strain-controlled shear tests. The box is strong and rugged to allow application of normal stress in the form of concrete blocks, steel panels, etc. Horizontal shearing force is applied with the help of a motorized jack via push beam connected to the upper shear box.

**Drainage Conditions.** The size of particles of the MSW are very large with a very high permeability, therefore the apparatus is designed to allow drainage from bottom of apparatus during the shear test.

**Robust.** The apparatus is very robust; suitable for soft and medium soils also.

**Simplicity and Practicality.** The apparatus can easily be manufactured using the guide lines given in this paper. The apparatus is simple to use and easy to transport.

**Friction Between Components.** Owing to the large size of the apparatus vis-à-vis the weight, it was obvious that the upper and lower box will develop very high friction between them. Therefore steel wheels have been provided under the upper shear box which rolls on guide-rails provided longitudinally on the lower shear box.

**Light Weight - Manual Transportation.** It will mostly not be possible to transport the apparatus to the test site on a vehicle because of the low strength of the MSW. The heaviest component of the apparatus is designed in such a way that it could be conveniently carried by two persons across the MSW site and quickly assembled on the test site.

## CONSTRUCTION DETAILS OF THE APPARATUS

The apparatus is fabricated with steel and wood that include a number of innovative elements. Various dimensions of the apparatus are shown in Table 1; plan and side views of the major components of the apparatus are shown in Figure 1 and 2.

**The Shear Box.** It consists of an Upper Shear Box and a Lower Shear Box. The shear box has the capability of sustaining lateral shearing force of upto 100 kN.

**Upper Shear Box.** It is made of steel angle iron (L-sections) and rectangular steel pipe fitted with detachable wooden planks. Details of different components are labeled in Figures 3 through 6. Joints between various steel parts are welded and the detachable wooden planks are fixed to the steel frame with steel bolts. The steel frame is provided with two pairs of 7 cm diameter low friction steel wheels at the bottom on both sides to minimize friction between the upper and lower boxes.

**Lower shear box.** It is made of 10 mm thick steel sheet welded to 5 cm x 5 cm x 6 mm L-section H-frame. The 2.1 m long H-frame act as sliding rail for the top shear box and is capable of facilitating maximum shear displacement of 60 cm. Chisel edge at the bottom, is flushed into the ground surface to hold the specimen and provide a reference. A small gap, created by the low friction steel wheels, separates the two boxes. 9 mm dia steel bars are welded on each side rail, as shown in Figure 7, to prevent derailment of the upper shear box during application of the shearing force.

**Normal Load Bearing Steel Plate.** A detachable steel load bearing is provided with the upper shear box for uniform distribution of normal stress as shown in Figure 11

and Figure 12. Normal load can be placed in the form of curb stones, concrete blocks and even sand bags. The size of the bearing plate is 3 cm lesser than the internal width of the shear box to prevent friction with the side walls of upper shear box.

**Table 1. Dimensions of the Large Direct Shear Test Apparatus**

Dimensions	Complete Box	Upper Box	Lower Box	Push Beam	Bearing Plate
Height (cm)	75	60	13	-	-
Length x Width (cm)	122 x 122	122 x 122	122 x 122	18 x 18	119 x 119
Weight (kg)	327	140	100	50	37

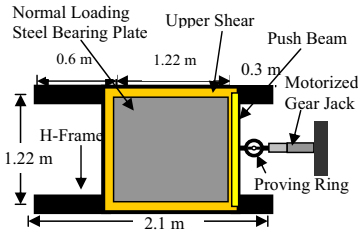


**FIG. 1: Plan view of Large Direct Shear Test Apparatus.**

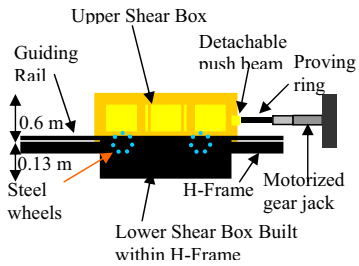


**FIG. 2: Side view of Large Direct Shear Test Apparatus.**



**FIG. 3. Panoramic view of Upper Shear Box.**

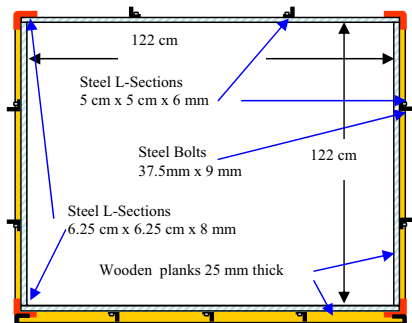


**FIG. 4. Plan of Upper Shear Box at mid height.**

**Proving Ring.** A 100 kN proving ring is used with the large direct shear apparatus for measuring the shear stress as shown in Figure 10. The proving ring is provided with a dial gauge having a least count of 0.002 mm. Load cell along with the data acquisition system can also be used instead of the proving ring.

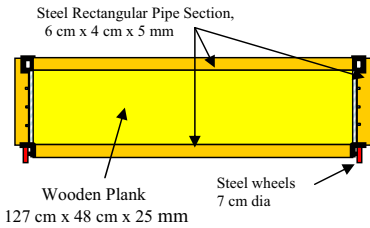


**FIG. 5. Front elevation of Upper Shear Box at mid axis.**

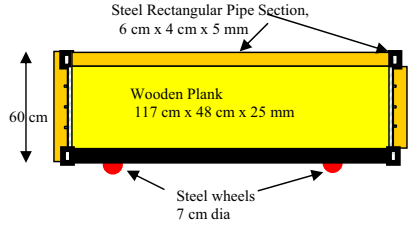


**FIG. 6. Side elevation of Upper Shear Box at mid axis.**

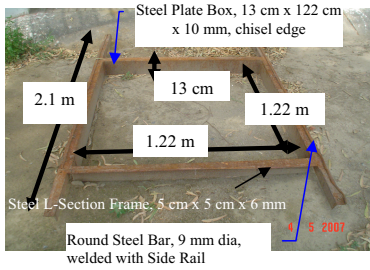


**FIG. 7. Panoramic View of Lower Shear Box.**

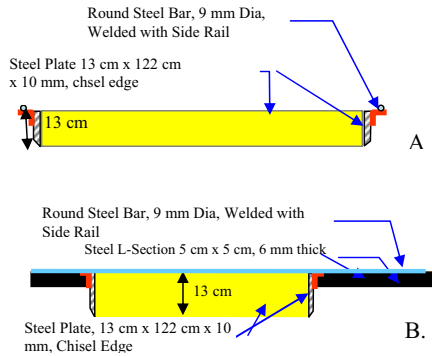


**FIG. 8. A. Front elevation of Lower Shear Box at mid axis. B. Side elevation of Lower Shear Box at mid axis.**

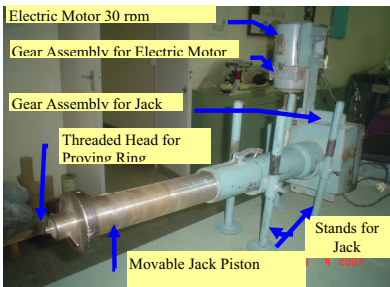


**FIG. 9. Panoramic View of Specially Fabricated Motorized**

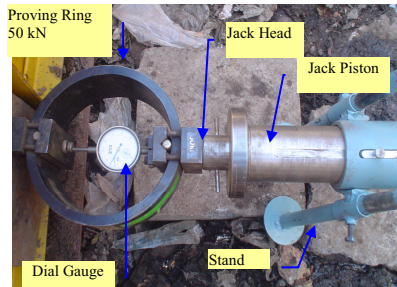


**FIG. 10. Proving Ring 50 kN attached with Jack Threaded Head. Gear Jack.**

**Motorized Jack.** A 220 volts electric motor with a speed of 30 rpm is attached to the jack to move piston of the jack at the rate of 4 mm/min to a maximum distance of 30 cm. The electric motor with gear can be used at different speeds depending on the required rate of shear and shearing stress. The jack piston has a threaded male head which is screwed into the 100 kN proving ring. The jack is provided with a two way control switch which controls the inward and outward movements of the jack piston; Figure 9 shows different components of the motorized jack. The jack can also be operated manually with a detachable handle.

**Push Beam.** A high strength detachable steel push beam is provided for uniform distribution of the shearing stress across the entire width of the upper shear box as shown in Figure 11. This push beam is made of 8 mm thick mild steel plate bent to make a C-channel and three 8 mm thick steel plates welded on the hollow side.

## TESTING PROCEDURE

**Excavation of Pit.** Mark an area measuring 1.2 m x 1.2 m on the ground at the test site and excavate a trench around this area to the desired depth ensuring minimum possible disturbance to the sample in the centre.

**Placement of the Shear Box.** The lower shear box is placed around the sample in a way that it penetrates approximately 13 cm into the solid waste such that collar is flushed to the ground. The upper box is then placed over lower box; steel wheels provided at the bottom of upper shear box maintain space for the shear plane to occur. Thereafter the normal bearing plate is placed on top of specimen for application of normal load as shown in Figure 12.

**Application of Normal Stress.** The required normal stresses can be achieved with any suitable material which can be easily carried to test site such as concrete blocks, sand bags, etc. Each specimen should be tested for three progressive normal stresses by ‘staged direct shear test’ to avoid preparation of new samples and to eliminate effect of sample variability.

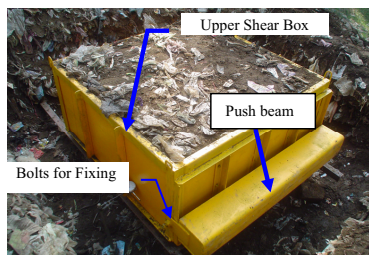


**FIG. 11.** Boxes fixed on the test specimen.



**FIG. 12.** Normal Load Bearing Plate placed over the specimen.

**Application of Shearing Stress.** The lateral load is applied to the upper shear box by means of a 100 kN motorized jack at a constant rate. Different strain rates are

possible through appropriate gear installation; gear with a speed of 4 mm/ min was used with the jacks in our test program.

### SAMPLE TEST RESULTS

The apparatus was used for measuring direct shear strength of MSW in a closed MSW site near Islamabad, Pakistan. To avoid preparation of new specimens and to eliminate effects of sample variability, specimen were sheared repeatedly under increasing normal stresses of 6 kPa, 13 kPa, and 20 kPa at relative displacements of 2%, 3%, and 4% strains. Sample test results are shown in Figure 13 and 14.

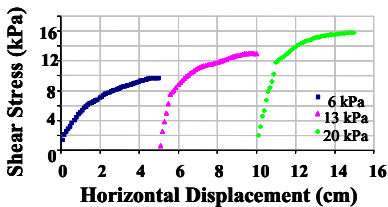


FIG. 13. Shear Stress vs. Horizontal Displacement.

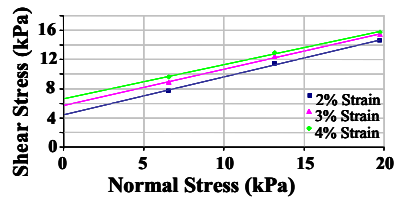


FIG. 14. Shear Stress vs. Normal Stress ( $C = 6.63$  kPa,  $\Phi = 25.07^\circ$ ).

### CONCLUSION

Presently construction of structures over closed MSW sites is very rare because of the lack of understanding of the geotechnical behavior of MSW sites and absence of suitable apparatus to evaluate their strength and settlement characteristics. The apparatus proposed in this paper can be manufactured with little technical skill. The results obtained from the apparatus are real representative of the shear strength of MSW at the particular site.

### REFERENCES

- Pakistan Environmental Protection Agency and Japan International Corporation Agency (2005). "Guidelines for Solid Waste Management."
- Aamir Maqbool (2007). "Evaluation of in-situ strength and settlement characteristics of MSW." *MS Thesis*, National University of Sciences and Technology, Pakistan.
- Zeccos, D.P. (2005). "Evaluation of Static and Dynamic Properties of Municipal Solid Waste". *PhD Thesis*, University of California, Berkeley.
- ASTM (2004). "Standard Test Method for Direct Shear Test of Soils Under Consolidated Drained Conditions." D3080-03, West Conshohoken, PA 19428-2959.
- Houston et al., (1995). "Insitu Testing Methods for Dynamic Properties of MSW Landfills." *Proceedings of the session sponsored by the Soil Mechanics Committee of the Geotechnical Engineering Division of ASCE*, Vol 54, pp73-82.

## **Feasibility Analysis for the Ecological Sustainability of Engineering Construction of the Express**

Tung-Tsan Chen<sup>1</sup>, Yao T. Hsu<sup>2</sup>, Chun-Yuan Wang<sup>3</sup>

<sup>1</sup> Assistant Professor, Department of Construction Engineering, National Kinmen Institute of Technology, No.1 University Rd., Kinmen County, 892, Taiwan, Email: tungtsan@kmit.edu.tw

<sup>2</sup> Associate Professor, Department of Transportation Technology and Management, Fung Chia University, Taiwan, R.O.C., Email: hsuyt@fcu.edu.tw

<sup>3</sup> Professor, Dean and Vice President, Department of Business Administration, Nanya Institute of Technology, Taiwan, R.O.C., Email: banking4303@yahoo.com.tw

**ABSTRACT :** This research is based on three different views of the industry, academic and government. Our assessment criterion goals were five dimensions of “the utility aspect”, “the economic aspect”, “the adoption principle”, “the working-method characteristic” and “the environmental condition”. Using each representative detailed item from the experts’ interviews and literature reviews, and utilizing Fuzzy Delphi Method (FDM) and Fuzzy Analytic Hierarchy Process (FAHP), we get the comprehensive performance with relative weighted index. Applying the Matrix Law of Value, we compare the comprehensive performance value of traditional method and ecological method which are applied to construct national roads. We find that the ecological method of building national roads is feasible and is better than the traditional method.

### **INTRODUCTION**

The frequent economic development activity in Taiwan, have caused the destruction of the ecological environment. The great killer to the environmental ecology is that the road is frequently excavated and filled out. Using the ecological method on the national road, we should assess slope protection, drainage, case content, bridge, tunnel, retaining wall, bar, illumination, serving area, overpass, ecological corridor, ecological buffering area and the management of construction. The main purpose is to reduce the negative impact upon the ecological environment of the road construction, and to keep environmental sustainability. This research is from the view of road construction and environmental protection. Basing on ecological knowledge and ecological engineering, we compare the relative advantages of the traditional method and ecological method applied to the feasibility of the national road construction.

**Construction of fuzzy AHP hierarchy**

We approached the key dimensions of the evaluation criteria of ecological sustainability through comprehensive investigation and consultation with several experts, including two professors in civil engineering, two professors in construction engineering, three experienced ecologists and five experienced staffs in professional procurement of the government department. These individuals were asked to rate the accuracy, adequacy and relevance of the criteria and to verify their “content validity” in terms of ecological sustainability assessment. Synthesizing the literature review such as Chiou and Tzeng( 2001 ); Bergen et al.( 2001 ); Forman( 1998 ); we develop the hierarchical structure used in this study.

There are five dimensions of evaluation, including Economy, Utility, Adoption Principle, Method and Environment. From these, 20 evaluation criteria for the hierarchical structure were used in this study. (See 1,2<sup>nd</sup> column in table 1)

**Table 1. Fuzzy triangular membership function of evaluation criteria**

Dimensions	Criteria	Min.	Geo. mean	Max.	State
Economy	Unit building cost	6	8.51149	10	
	Maintenance cost	3	8.00825	10	
	Amount of the budget	5	8.22011	10	
Utility	Durable service life	2	5.43613	10	Delete
	Improvement of efficiency	2	6.58376	9	Delete
	Reduction of maintenance cost	1	3.56975	9	Delete
	Function of the landscape road	5	8.00792	10	
Adoption Principle	Effect of construction method	7	8.00932	9	
	Practicability	5	7.05083	10	Delete
Method	Security	3	6.11813	9	Delete
	Gracefulness	6	8.41042	10	
	Economy	6	8.00294	10	
Environment	Concept of ecology	8	9.53102	10	
	Artistic vision	7	8.70345	10	
	Future major trend	6	8.01244	10	
	Compare with the tradition	4	6.37751	9	Delete
	Difficult degree of construction	3	6.53467	9	Delete
Environment	Geometry conditions of the road	8	9.27172	10	
	Cooperate with other environment	7	8.64017	10	
	Natural weather conditions	4	7.01487	9	Delete

**Selection of evaluation criteria**

This research is to investigate face-to-face interview with 6 scholars, 7 industry professionals and 7 government experts of Highway Administration Bureau.

According to the definition of Laarhoven and Pedrycz ( 1983 ) , a triangular fuzzy number (TFN) should possess the following basic features. A fuzzy number A on R will be a TFN if its membership function,  $\mu_{\tilde{A}}(x): R - [0,1]$  is equal to

$$\mu_{\tilde{A}}(x) = \begin{cases} (x - L)/(M - L), & \dots\dots\dots L \leq x \leq M \\ (U - x)/(U - M), & \dots\dots\dots M \leq x \leq U \\ 0, & \dots\dots\dots \text{otherwise} \end{cases} \quad (1)$$

Where, L and U stand for the lower and upper bounds of the fuzzy number  $\tilde{A}$  respectively, and M for the modal value (geometric mean).

- (1) If  $M_A \geq S$ , Accept influence factor A which is an evaluation criterion.
- (2) If  $M_A < S$ , Reject influence factor A.

Where  $M_A$  is a decision group to the influence factor A, S is a threshold value whose size will influence the choice numbers of assessment criteria. General research mostly takes  $S = 0.8$ , that is the most important assessment criterion.

After passing through Fuzzy Delphi Method, numbers of the overall criteria were reduced originally from 20 into 12, deleting 8 criteria which did not have the representative appraisal. The structure of the evaluation criteria after deleting is shown in Fig.1.

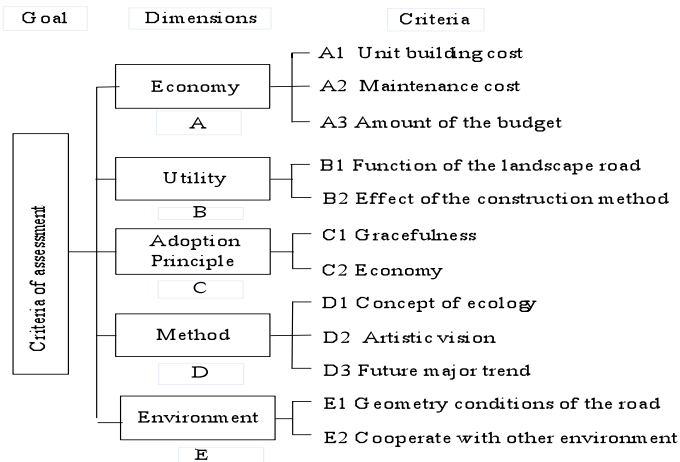


**Fig. 1. The structure of AHP for ecological sustainability applied to road**

**ANALYSIS, FINDINGS, AND DISCUSSION**

**Ranking the fuzzy number**

It is necessary to nonfuzzify ranking for fuzzy numbers in table 3 for comparison of each criterion (Hsieh et al. 2004) . The procedure of defuzzification (DF) is to locate the Best Nonfuzzy Performance value (BNP) by equation (1):

$$DF_i = [(UR_i - LR_i) + (MR_i - LR_i)]/3 + LR_i \quad \forall i \dots\dots\dots (1) \quad A$$

According to the value of the derived DF or BNP for each criterion, the ranking of each criterion can then proceed as shown in table 2.

**Table 2. Ranking fuzzy weight of assessment dimensions**

Dimensions	Min.	Geo. mean	Max.	DF.	Rank
A Economy	0.0711	0.1706	0.4207	<b>0.2208</b>	2
B Utility	0.1042	0.1407	0.3107	<b>0.1852</b>	5
C Adoption Principle	0.0992	0.1774	0.3487	<b>0.2085</b>	4
D Method	0.1150	0.2317	0.4246	<b>0.2571</b>	1
E Environment	0.0785	0.1773	0.3730	<b>0.2096</b>	3

**Comparing comprehensive performance**

Five kinds of different facilities are the research object that enumerated respectively to the traditional method and the ecological method, as table 3 shows. Experts and scholars interviewed give subjective evaluation in 5 grades to facilities as shown in table 3. Normalizing the sample data, we carry on the calculation of performance value (Zadeh 1973) . The result is shown in table 4 and table 5.

**Table 3. The sample data of the third stage questionnaire**

Facilities \ Criteria	Economy	Utility	Adoption Principle	Method	Environ.
:Pavement of traditional method (T1)	2	2	3	2	2
●:Pavement of permeability (E1)	(4)	(4)	(4)	(4)	(4)
:Retaining wall of anchor (T2)	1	2	1	1	2
●:Retaining wall of frame (E2)	(5)	(4)	(5)	(4)	(3)
:Slope protection of spray (T3)	3	2	2	2	2
●:Slope protection of grille (E3)	(4)	(4)	(4)	(5)	(3)
:Cutting of excavation (T4)	2	2	3	3	2
●:Tunnel (E4)	(3)	(4)	(4)	(4)	(4)
:Pavement of asphalt concrete (T5)	2	1	2	1	2
●:Pavement of chain brick (E5)	(4)	(5)	(5)	(5)	(4)

Note: : Traditional method; ●: Ecological method

Retracing the data to an expert's questionnaire, we calculate:

$$\text{Scoring.value} = X_i \times 100 / \sum_{i=1}^n X_i = Q_i \dots \dots \dots (2)$$

1. Traditional method: Pavement of traditional method

$$2 \times 100 / (2 + 1 + 3 + 2 + 2 + 4 + 5 + 4 + 3 + 4) = 6.67$$

2. Ecological method: Pavement of permeability

$$4 \times 100 / (2 + 1 + 3 + 2 + 2 + 4 + 5 + 4 + 3 + 4) = 13.33$$

**Table 4. Scoring value of satisfying degree in selection samples**

Facilities \ Criteria	Economy	Utility	Adoption Principle	Method	Environ.
:Pavement of traditional (T1)	6.67	3.45	9.38	6.45	7.14
●:Pavement of permeability (E1)	(13.33)	(13.79)	(12.50)	(12.90)	(14.29)
:Retaining wall of anchor (T2)	3.33	6.90	3.13	3.23	7.14
●:Retaining wall of frame (E2)	(16.67)	(13.79)	(15.63)	(12.90)	(10.71)
:Slope protection of spray (T3)	10.00	6.90	6.25	6.45	7.14
●:Slope protection of grille (E3)	(13.33)	(13.79)	(12.50)	(16.13)	(10.71)
:Cutting of excavation (T4)	6.67	6.90	9.38	9.68	7.14
●:Tunnel (E4)	(10.00)	(13.79)	(9.38)	(12.90)	(14.29)
:Pavement of asphalt concrete (T5)	6.67	3.45	6.25	3.23	7.14
●:Pavement of chain brick (E5)	(13.33)	(13.79)	(15.63)	(16.13)	(14.29)

$$\text{Performance.value} = \sum_{i=1}^5 DF_i \times Q_i \dots \dots \dots (3)$$

Pavement of traditional method:

$$(0.2208 \times 6.67) + (0.1852 \times 3.45) + (0.2085 \times 9.38) + \dots + (0.2096 \times 7.14) = 7.22$$

Pavement of permeability:

$$(0.2208 \times 13.33) + (0.1852 \times 13.79) + (0.2085 \times 12.50) + \dots + (0.2096 \times 14.29) = 14.22$$

**Table 5 Comprehensive performance value of different methods**

Traditional method	Pavement of traditional	Retaining wall of anchor	Slope protection of spray	Cutting of excavation	Pavement of asphalt concrete	Average
	Ecological method	Pavement of permeability	Retaining wall of frame	Slope protection of grille	Tunnel	
<b>Performance Value</b>	7.22 (14.42)	4.99 (15.05)	7.94 (14.50)	8.69 (13.03)	5.74 (16.57)	6.92 (14.71)

**Feasibility analysis of ecological method**

Fig. 2 shows the comprehensive performance value that the traditional method and ecological method are used to assess five kinds of different project facilities of national road. We find the superiority of ecological method basing on the following:

1. Three kinds of experts such as government department, scholar and industry reflect that the ecological method maps to the higher performance value of engineering construction of national road unanimously.
2. The average performance value shows that “pavement of permeability” is higher than “pavement of traditional method”, “retaining wall of frame” is higher than “retaining wall of anchor”, “slope protection of grille” is higher than “slope protection of spray”, “tunnel” is higher than “cutting of excavation” and “pavement of chain brick” is higher than “pavement of asphalt concrete”. This shows the ecological method is superior to the traditional method in the engineering construction of national road.

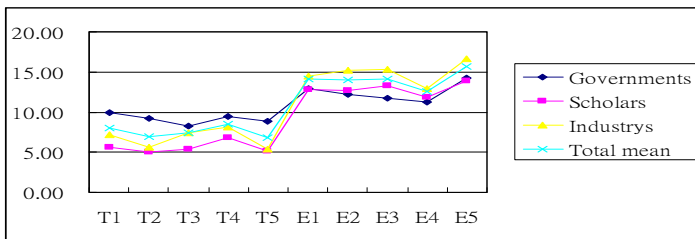


**Fig. 2 Performance value of different experts' group**

**CONCLUSIONS**

In recent years, advanced countries advocate that the ecological method, could maintain the structure and function of the natural ecosystem to ensure the human security and to reach the ideal sustainability at the same time. We find that the ecological method of “the slope protection”, “retaining wall “, “drainage facilities”, ”tunnel “and “serving area” of national road can offer better satisfaction than the traditional method . The comprehensive performance value of the ecological method is 14.71 which is superior to the traditional method of 6.92. This implies that the ecological method on the road construction deserves extensive adoption.

**REFERENCES**

- Bergen S. D., Bolton S. M., Fridley J. L. (2001). "Design principles for ecological engineering".
- Chiou H.K., Tzeng G.H. (2001). "Fuzzy hierarchical evaluation with grey relation model of green engineering for industry." *Int J Fuzzy Syst*, 3(3): 466-475.
- Forman, R. T.T., (1998). "Road and Their Major Ecological Effects." *Annual Review. Ecol.syst.*, 29: 207-231.
- Hsieh T.Y., Lu S.T., Tzeng G.H. (2004). "Fuzzy MCDM approach for planning and design tenders selection in public office buildings" *Int J Project Manage*, 22(7):573-584.
- Laarhoven P.J.M., Pedrycz W.(1983). "A fuzzy extension of Saaty's priority theory" *Fuzzy Sets Syst*, 11(3): 229-241.
- Zadeh L.A. (1973). "The concept of a linguistic variable and its application to approximate reasoning." *ERL-M 411*, Berkeley, Calif.

## Ant Colony Optimization Algorithm for Vertical Alignment of Highways

Miao Kun, Li Liang, Yang Xiao-Li , HuoYuan-Yuan

School of Civil and Architectural Engineering, Central South University, Changsha  
410075, China

Email: miao98004@126.com

**ABSTRACT:** Based on discrete theory, this article tries to develop an optimization methodology to produce an optimum vertical highway profile for a pre-selected horizontal alignment. The aim of the program was to establish an initial vertical alignment according to discreet ground elevation of station. Considering the discreet characteristic of the ground elevation and the intersection point of grade line, a discrete model is presented. The automatic design problem is set to select the number, location and elevation of the intersection point of the grade line after considering several designing constraints. To solve the constrained nonlinear problem, an ant colony optimization algorithm is adopted to select the roadway grades that minimize the earthwork cost and satisfy the geometric specification. A numerical example is presented to illustrate the application of the program.

### 1. INTRODUCTION

The alignment design of roadway normally involves the vicissitudinary applications of two elements: the horizontal design and the vertical design. The two parts would be employed by turn for many times before the final alignment of the roadway could be established. Usually, the vertical alignment design is based on a pre-selected horizontal alignment. The horizontal alignment could provide the related data of road centerline and some necessary parameters to the automatic design of vertical alignment. Following a certain algorithm we could turn to the vertical alignment automatically with the help of computer by using the ground data and parameter provided by the horizontal alignment. To realize this idea, many scholars devoted to researches involving the following algorithm: enumeration, dynamic programming, linear programming, and genetic algorithms.

Enumeration has been employed by Easa (1988). The searching process is exhaustive. the dynamic programming (Goh et al., 1988; Fwa, 1989) is more effective and better than before. The method makes it possible to optimize the grade change point and the position of the elevation, obtaining the best railroad vertical section design. However, when it comes to three-or-more-dimension cases, the model could not cope with problems caused by the advanced time and space complexity. For the

two-dimensional problem, the memory requirement for it is approximately of  $O(n \cdot m)$ , while the computational times is of  $O(n \cdot m^2)$ . If applying it in a higher dimension situation, computation is not able to be carried out

Another alternative approach for the problem is to regard the road profile as a continuous function, such as a spline function to simulate alignments and turn it into a constrained nonlinear programming problem. After all, the function curve is quite different from the alignment of roadway.

The linear programming approaches (ReVelle et al., 1997; Chapra and Canale, 1988; Fwa, 1989) were used for vertical alignment optimization. The approaches employed much more simplified assumptions to establish a model which was adapted to linear programming approaches. However the computing ability was limited.

Numerical Search (Goh et al., 1988; Fwa, 1989) is effective, but there exist some local optimal in the search space.

Genetic Algorithms: Jong (1998) employed genetic algorithms for vertical alignment optimization. Only in the condition that the preliminary design is given and the number of intersection points (grade change points) is determined, the algorithm could carry on. But actually, the computer, not given by an engineer, should calculate the number of intersection point out.

Ant colony optimization algorithm is a kind of important intellectual colony optimization algorithm, ant colony optimization algorithm was established initially by Dorigo (1997, 1999), an Italian scholar. Its basic idea is that ant individuals deliver the information by the pheromone. When an ant is crawling, it will not only release its own pheromone which would gradually disappear at a certain velocity on its route, but also detect the circumstance nearby to figure out whether the pheromone exists or not. An ant adopts a kind of positive feedback mechanism, if more ants had chosen this route, there will be more pheromone left on the route, and this route also will lead more ants to select it, creating a higher pheromone. So the final result is that ants form an optimum route.

Ant colony optimization algorithm can provide solution to many intractable NP-hard optimization problems. It has its own advantage in solving the complicated combination optimization, with huge parallelism, positive feedback and robustness. A great deal of literature shows that the ant colony optimization algorithm had successfully worked out the following combination optimization problem: Traveling salesman (TSP), Vehicle routing (VRP), Job shop scheduling (JSP) and so on.

If the vertical alignment automatic optimization is built into a model with discrete idea, it could be seen as the problem of combinational optimization essentially. Thus, we could use the ant colony optimization algorithm to seek a route effectively. This paper is set to solve the problem of vertical alignment automatic optimization with the help and development of ant colony optimization algorithm.

2. THE MODEL

The design parameter of road alignment includes the position and elevation of intersection points, the radius of vertical curve. Among the parameters, the earthwork coast is mainly determined by the position and elevation of intersection points. Therefore this paper only considers the position and elevation of intersection points as the parameter of optimization to illustrate this algorithm.

Once the centerline of the road is established, the elevation of every intermediate station is going to be given to decide the ground profile. This is a discrete procedure which also corresponds with the basic requirement of ant colony algorithm.

If we make a grid for the model, and along with the ground profile, we draw a vertical parallel line at each intermediate station with a certain horizontal space. The line is going to be equally divided in the bilateral direction. Thus, scattered grid points are formed along the ground profile, as shown in Figure 1.

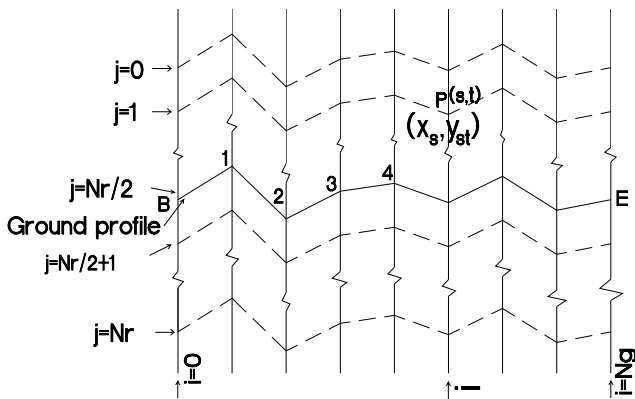


Figure 1. Form of Grid

The lines are indexed by 0,1,2, ...,Ng (middle stick station), the horizontal lateral lines are indexed by 0,1,2, ..., Nr (from up to down).

Grid points  $G_{ij} \in G = \{ (i, j) \mid i \in [0, Ng], j \in [0, Nr] \}$ ; The horizontal and vertical coordinate of  $P_{ij}$  is  $(x_{ij}, y_{ij})$  (i.e. intermediate stations and the elevation); The problem can be expressed by seeking the serial set of all the grade change points, to make the objective functions minimum,  $route = \{ P_0, P_1, P_2, \dots, P_t, \dots, P_{Np} \}$ ,  $P_t = \{ (i, j) \mid i \in Hroute, j \in Vroute \}$ ,  $Np+1$  is the total number of the grade change points.

$$Z = \min C(P_0, P_1, P_2, \dots, P_t, \dots, P_{N_p}) \quad (1)$$

$$\begin{aligned} \text{s.t. } \sum_{j=0}^{N_r} w_{ij} &= 1, \quad i \in \text{Hroute}^k \\ \sum_{j=0}^{N_r} w_{ij} &= 0, \quad i \notin \text{Hroute}^k \\ \sum_{i=0}^{N_d} w_{ij} &< N_d, \quad j = 0, 1, \dots, N_r \\ w_{ij} &\in \{0, 1\}, \quad (i, j) \in G \end{aligned}$$

$$L_{\min} \leq x_{i+1} - x_i \leq L_{\max}, \quad i \in \text{Hroute}^k,$$

$$I_{\min} \leq \frac{y_{i+1} - y_i}{x_{i+1} - x_i} \leq I_{\max}, \quad (i, j) \in \text{route}^k$$

$$j = Nb, \quad i = 0$$

$$j = Ne, \quad i = Nd.$$

Hroute is a subset of the horizontal number in route set, while Vroute is a subset of the vertical number in the route set. The decision variant  $w_{ij}$  shows whether the ant passes the grid point;  $G_{ij}$ ,  $w_{ij}=1$  shows that the route includes the grid point  $G_{ij}$ , and  $w_{ij}=0$  shows that the route does not include the grid point  $G_{ij}$ .

(0,Nb) is the starting number, (Ng,Ne) is the ending number of the profile;

$$\text{generally: } Nb = \frac{N_r}{2}, \quad Ne = \frac{N_r}{2}.$$

$L_{\min}$  is the allowed minimum slope length.  $L_{\max}$  is the allowed maximum slope length.  $I_{\min}$  is the allowed minimum roadway grades.  $I_{\max}$  is the allowed maximum roadway grades.

### 3. ANT ALGORITHM TO THE PROBLEM

#### 3.1 The way of choosing intersection point:

Placing the ants at point B, ants will then start from point B, and step toward the destination E, every ant can select only one point at one step, and which point would be chosen as the next step depends on the transition probability. " $p_{ij,uv}^k$ " is the transition probability that an ant steps from point  $G_{ij}^k$  to point  $G_{uv}^k$ ,  $k=\{0,1, 2, \dots, m\}$ , and it could be worked out by eqn (2). There are two factors: the pheromone ants have left behind on the route and the heuristic information between the two points, which are affecting the transition probability. Respectively, " $\tau_{ij,uv}$ " and " $\eta_{ij,uv}$ " represent the two factors. The parameter " $\alpha$ " and " $\beta$ " are used to show the level of relative influence on an

ant's choice between point “G<sup>k</sup><sub>ij</sub>” and point “G<sup>k</sup><sub>uv</sub>”. “α” is the pheromone transition factor that reflects the relative importance of pheromone. “β” is expectation transition factor that reflects the importance of “visibility”.

$$P^k_{ij,uv}(t) = \frac{[\tau_{ij,uv}(t)]^\alpha \cdot [\eta_{ij,uv}(t)]^\beta}{\sum_{(u,v) \in \text{arrived}^k} [\tau_{ij,uv}(t)]^\alpha \cdot [\tau_{ij,uv}(t)]^\beta}, \text{ if } (u,v) \in \text{arrived}(i,j)^k \tag{2}$$

3.2 The construction of “set arrived”

The present point of ant “k” is assumed as P<sub>t</sub>(i,j) (the ant k reaches a grade change point at the moment T). According to the usual way of dealing with TSP problems, the total number of visiting point is (Ng-i) × Nr should start from column i+1 to column Ng. If the length of the road increases, the number of the grid points will also increase, which will make the calculation impossible. Therefore an arrived set of the visiting points should be chosen according to the current point to minimize the storage and searching range. The set is named “set arrived” (denoted by arrived (i,j)) includes all the possible points that an ant may reach at point P<sub>t</sub>(i,j).

As the design of the vertical alignment, from a grade change point to the next point, the next grade change point must be restricted in the space within the minimum roadway grades and the maximum roadway grades and the minimum slope length and the maximum roadway length. Therefore all the grid points in the space form a set Arrived. If an arbitrary point Q (u,v) is assumed to belong to the set Arrived (i,j), then the choice possibility P<sup>k</sup><sub>ij,uv</sub> between the point P<sub>t</sub>(i,j) and the points within the set Arrived should be calculated in order. Using the method of roulette wheel selection according to the possibility, the next point P<sub>t+1</sub> to be visited should be selected. And when the ant visits this grade change point, P<sub>t+1</sub> should be stored in the set Route<sup>k</sup> of this cycle. In order to ensure that the ant goes from the start point to the ending point and each grid column is visited only once, the points visited should be stored in the set Route<sup>k</sup> immediately. Actually the set Route<sup>k</sup> is a kind of tabu set, and the points in the set Route<sup>k</sup> will not be chosen again. If the ant chooses to visit the next point, then actually a grade section is formed between this point and the next point. The route that the ant goes from the starting point to the ending point is the grade change point set which is a way of the vertical alignment, as shown in Figure 2.

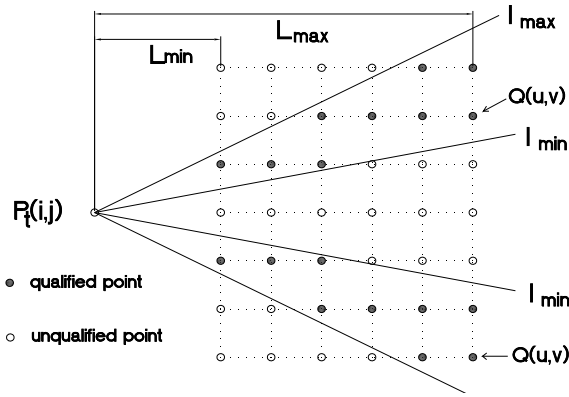


Figure 2. Set Arrived of Point Pt

3.3 The update of pheromone:

There are two aspects in the update of pheromone on each grade line. On one hand the pheromone will be increased if the ant selects to pass through that line, on the other hand, the pheromone is a kind of material of volatility, it could gradually disappear at a certain time. So the amount of pheromone changing at the moment “t+n” could be calculated as follow:

$$\tau_{ij,uv}^k(t+n) = (1-\rho) \cdot \tau_{ij,uv}^k(t) + \Delta\tau_{ij,uv}^k(t) \tag{3}$$

$$\Delta\tau_{ij,uv}^k(t) = \sum_{k=1}^m \Delta\tau_{ij,uv}^k(t) \tag{4}$$

$\Delta\tau_{ij,uv}(t)$  is the increment of pheromone between the points “ $P_i$ ” and “ $P_{t+1}$ ” in a cycle. (at the original moment,  $\Delta\tau_{ij,uv}(t) = 0$ ).  $\tau_{ij,uv}^k(t)$  is the pheromone which is left by the ant “k” between the points “ $P_i$ ” and “ $P_{t+1}$ ” in a cycle. “ $\rho$ ” is the volatile coefficient of pheromone, so “ $1-\rho$ ” shows the remainder level of pheromone.

Ant colony algorithm could divide into ant-cycle algorithm, ant-quantity algorithm and ant-density algorithm according to the renew way of pheromone. Ant-cycle algorithm is the one that the feedback information used in searching process is overall, but the feedback information used in ant-quantity algorithm and ant-density algorithm is local. So the ant-cycle algorithm is more discreet than the other two algorithms, and

$\Delta\tau_{ij,uv}^k(t)$  can be worked out by the following function:

$$\Delta\tau_{ij,uv}^k(t) = \frac{Q}{\sum_{s=1}^{Ng} (yg_s - yd_s)^2} \tag{5}$$

where  $yg_s$  = The ground elevation of the intermediate station “k”.  $s \in \{0,1, 2, \dots, Ng\}$ ;  $yd_s$  = The design elevation of the intermediate station “k”.  $s \in \{0,1, 2, \dots, Ng\}$ ;  $Q$  = The intensity of pheromone, affecting the convergence velocity to a certain extent.

### 3.4 The usage of heuristic function

The heuristic function is used to work out the visibility that could show the influence of guidance factor between the two points. So the function should be the total cost of all the roadway cost, including earthwork cost, vehicle operating cost, land cost and pavement cost. But this report is purposed to illustrate the application of ant colony algorithm in vertical alignment design, so it only regard the earthwork cost as the target of optimization in the objective function. The other three kinds of roadway cost are assumed to be excluded from the objective function. The earthwork cost  $C$  is mainly due to the relative difference between grade and ground elevations. The computation of the cutting and filling cost is summarized below according to C. J. GoH and E. P. CHEW and T. F. Fwa (1988) .Let “ $\mu$ ” and “ $\nu$ ” denote the filling and cutting cost per unit cross sectional area that may be location dependent. Let

$\Delta_i = yd_i - yg_i, \Delta_{i+1} = yd_{i+1} - yg_{i+1}$ , where  $h$  = the vertical distance of a grid;  $C_i$  = the earthwork cost between the station “ $i$ ” and “ $i+1$ ”,  $i \in \{0,1, 2, \dots, Ng\}$ .

(i) Cutting, no crossing of ground profile and road profile

$$\text{If } \Delta_i < 0 \text{ and } \Delta_i \cdot \Delta_{i+1} \geq 0 \text{ then } C_i = -\frac{\nu h}{2} (\Delta_i + \Delta_{i+1}). \tag{6}$$

(ii) Fitting, no crossing

$$\text{If } \Delta_i \geq 0 \text{ and } \Delta_i \cdot \Delta_{i+1} \geq 0 \text{ then } C_i = \frac{\mu h}{2} (\Delta_i + \Delta_{i+1}). \tag{7}$$

(iii) Crossing, cutting, and filling

$$\text{If } \Delta_i \geq 0 \text{ and } \Delta_i \cdot \Delta_{i+1} < 0 \text{ then } C_i = \frac{h}{2} \cdot \frac{\mu\Delta_i^2 + \nu\Delta_{i+1}^2}{\Delta_i - \Delta_{i+1}}. \tag{8}$$

(iv) Crossing, cutting, and filling

$$\text{If } \Delta_i < 0 \text{ and } \Delta_i \cdot \Delta_{i+1} < 0 \text{ then } C_i = \frac{h}{2} \cdot \frac{\nu\Delta_i^2 + \mu\Delta_{i+1}^2}{-\Delta_i + \Delta_{i+1}}. \tag{9}$$

So the heuristic function between point “G<sub>ij</sub>”and “G<sub>uv</sub>” is  $\eta_{ij,uv} = \frac{1}{\sum_{s=i}^u C_s}$  .

3.5 The processing of fixed points constrain

As for the constraints, we had set a set arrived which is made up of all optional points to make sure that the route is under our control. But actually we might have to set another kind of constraint. It is that we need some intermediate stations keeping a certain elevation fixed to satisfy the requirement. For example, the elevation of a bridge or a tunnel is not allowed to be modified. Supposed elevation of  $G_{ij}$  is  $yg_i$ , let

$H_1 = yg_i - \varepsilon, H_2 = yg_i + \varepsilon$  ( $\varepsilon$  is a quite small real number). If we divide the space between “H<sub>1</sub>”and “H<sub>2</sub>”more accurately to obtain a finer grid, that we will force ants to select those accurate grid points to keep the elevation of this point change in a small range, as shown in Figure 3.

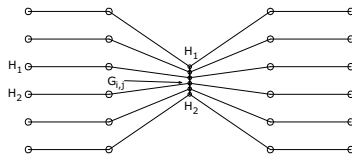


Figure 3. Fixed Point Constrain

3.6 A numerical example

The length of a highway in Hunan Province is 4360m. We set parameter as follows:

$$\alpha = 0.2, \beta = 4.0, \rho = 0.4, Q = 100, I_{\min} = 0.3\%, I_{\max} = 6.0\%, L_{\min} = 120, L_{\max} = 900,$$

Nr=20, Nc=219. The vertical space distance is 0.6m, the horizontal space distance is 20m. The whole region is divided by 219×20 grids in our experiment. The iteration number of ants is 60. The result alignment shows in Figure 4 (only a part of the alignment). The total running time is 6.72s on a computer with Intel(R) core(TM)2 Duo CPU T7250, 1G memory.

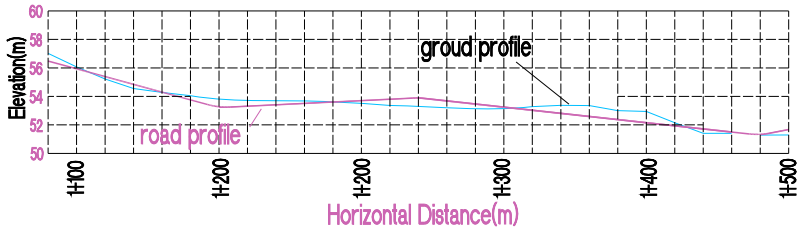


**Figure 4. A numerical example**

3.7 The selection of parameter

Ant colony algorithm is a kind of stochastic algorithm. The accuracy of the result has something to do with the optimum parameter. For instance, “m”(the total number of ants) exercises a power influence upon the result. Table 1 shows that the more the ants are, the better the result is.

**Table 1. Cost about the Total Number of Ants**

m	Worst	Average	Best
2	180.72	137.5764	110.562
12	146.491	120.8007	92.5396
100	110.37	100.8759	84.5539

The classic ant colony algorithm cannot supply the parameter. So only by a lot of experiments can we get more suitable parameters. We run the program 100 times in the case of changing a parameter to get some experimental results:

$$0 \leq \alpha \leq 5, 0 \leq \beta \leq 5, 0.1 \leq \rho \leq 0.9, 10 \leq Q \leq 10000.$$

**4.CONCLUSIONS**

According to the ant colony algorithm, we designed a program to carry out automatic design of roadway vertical section. This program has the following advantage:

- (1) Creating the grade change point automatically: the program can automatically select the number, location and elevation of the grade change points considering several design constraints, while some other methodology can only select the elevation of the grade change points.
- (2) Computing efficiently a large number unknown parameter, just as our experiment, the program is able to compute a long distance roadway with a large quantity of parameters in a high speed.

**ACKNOWLEDGMENTS**

Support was provided by the China National Science Fund through grant 50578160 .

**REFERENCES**

- Easa, S. M. (1988), "Selection of Roadway that Minimize Earthwork Cost using Linear Programming," *Transportation Research*, Part-A, Vol. 22A, No. 2, pp.121-136.
- Goh, C.J., E.P. Chew, and T.F. Fwa (1988), "Discrete and Continuous Model for Computation of Optimal Vertical Highway Alignment," *Transportation Research*, Part-B, Vol. 22B, No. 9, pp. 399-409.
- Goh, C.J. and K.L. Teo (1988), "Control Parametrization: A Unified Approach to Optimal Control Problems with General Constraints," *Automatica*, Vol. 24, No. 1, pp. 3-18.
- Fwa, T.F. (1989), "Highway Vertical Alignment Analysis by Dynamic Programming," *Transportation Research Record* 1239, TRB, National Research Council, Washington, D.C., pp. 1-9.
- ReVelle, C.S., E.E. Whitlatch, and J.R. Wright (1997), "Civil and Environmental Systems Engineering," Prentice Hall, New Jersey.
- Jong, Jyh-Cherng (1998), "Optimizing Highway Alignment with Genetic Algorithms," Ph.D. Dissertation, Department of Civil Engineering, University of Maryland, College Park, 1998.
- M. Dorigo & L. M. Gambardella, 1997. "Ant Colony System: A Cooperative Learning Approach to the Traveling Salesman Problem". *IEEE Transactions on Evolutionary Computation*, 1 (1): 53-66.
- M. Dorigo, G. Di Caro & L. M. Gambardella, 1999. "Ant Algorithms for Discrete Optimization". *Artificial Life*, 5 (2): 137-172.

## Application of Analytic Hierarchy Process to Slope Greening Design

WANG Fang<sup>1</sup>, CHEN Fei<sup>2</sup>, CHENG Yingying<sup>3</sup>

<sup>1,3</sup>Ph.D. candidate in Transportation Engineering, Transportation College, Southeast University, NO.2, Sipailou, 210096, Nanjing, P.R China. PH: 86-25-83795856, E-mail: [wawf-122673@126.com](mailto:wawf-122673@126.com)

<sup>2</sup>Associate professor of the Transportation College, Southeast University, NO.2, Sipailou, 210096, Nanjing, P.R China, PH: 86-25-83795856, E-mail: [cf@seu.edu.cn](mailto:cf@seu.edu.cn)

**ABSTRACT:** With the rapid development of highway construction in China, the importance of slope greening design is gradually increasing. This paper applied Analytic Hierarchy Process (AHP) into the design of slope greening and respectively analyzed the weight of engineering effect, investment, ecologic function, aesthetics, visual safety for drivers and cultural connotation for a slope greening design. Through the analysis, this paper discussed the methods and principle for slope greening design using AHP. Finally, the paper obtained the result that the effectiveness and the reliability of engineering technology environments are the most key considered factors for slope greening design and also consider the act of protecting original ecological environment, hindering the noise and beautifying the environment for a slope greening design. The method and principle in this paper can provide theoretical method for slope greening design.

### INTRODUCTION

The construction of highway started relatively late in China, which started in the beginning of 80's. The protection design of side slope usually used engineering protection in the first stage of highway construction. After 1990's, with the *Specifications for Environmental Impact Assessment of Highways (JTJ 005- 96)* and *Specifications for Environmental Protection of Highways (JTJ/T 006- 98)* were

implemented, engineering protection of slope replaced by plant protection gradually. Different from the traditional engineering protection technology, the objective of side-slope greening and protection are not only ensuring slope stability, but also beautifying environment, protecting environment, displaying humanistic spirits, representing urban characteristic and satisfying drivers psychic demands, and so on. Reviewing the development milestones of highway construction in China, the author found that highway slope greening has some problems, such as serious grasses degradation, poor effect of landscape, single tree species, and so on. By comparing and analyzing, AHP is considered to be a suitable method for highway slope greening design. Above all, this paper discussed the methods and principle for slope greening design using AHP, which can provide theoretical method for slope greening design.

## THE ESTABLISHMENT OF HIERARCHY STRUCTURE

### Mathematical foundation of AHP

A thorough treatment of the basic mathematical concepts of AHP is found in the literatures (Gass 1985; Harker and Vargas 1987; and Saaty 1977). Based on define of AHP, the author putted forward the process of analysis system of slope greening design as follows:

- 1) Establishing hierarchy structure model of slope greening design to make all elements to be decomposed, which were shown in figure 1;
- 2) According to formula 1, determining relative weight of all elements based on the questionnaire investigation to five experts in ecology, plant landscaping, garden art and highway construction;
- 3) Establishing analysis matrix and calculating the every elements weight coefficient  $w = (W_1, W_2 \dots, W_n)$  and maximum eigenvalue  $\lambda_{\max}$ ;
- 4) Judging the consistency of the matrix and checking the effectiveness and the reliability of results. the method is firstly calculating every vector of weights or priorities  $w = (W_1, W_2 \dots, W_n)$  and the maximum eigenvalue  $\lambda_{\max}$ ; And secondly obtaining consistency index for every judgment matrix "CI" according to formula (2);
- 5) Finally, comparing the "CI" to the mean random consistency index "RI" showing in table 1 to show the effectiveness and the reliability of results when CI/RI being less than 0.1.

Therefore, the primary task in the AHP involves the estimation of weights of a set of objects from a positive and reciprocal matrix of pairwise comparison  $A = (a_{ij})$ , which is

$$A = \begin{bmatrix} a_{11} & a_{12} & \dots & a_{1n} \\ a_{21} & a_{22} & \dots & a_{2n} \\ \cdot & \cdot & \dots & \cdot \\ a_{n1} & a_{n2} & \dots & a_{nn} \end{bmatrix} \tag{1}$$

$$CI = \frac{\lambda_{\max} - n}{n - 1} \tag{2}$$

Where for all  $i, j = 1, 2, \dots, n$  it would be necessary to develop a vector of weights or priorities  $W = (W_1, W_2, \dots, W_n)$ , which can reflect the weight of every elements.

**Table 1 The Mean Random Consistency Index “RI”**

Order Number	1	2	3	4	5	6	7	8	9
RI	0.00	0.00	0.58	0.90	1.12	1.24	1.32	1.41	1.45

**Elements analysis and system establishment of slope greening design**

By comparing and analyzing, the experts considered the most important factors for slope greening design should being engineering technology  $B_1$ , economic benefit  $B_2$ , ecological function  $B_3$ , landscape function  $B_4$ , driving safety  $B_5$ , humanities and sociological evaluation  $B_6$  for slope greening design. As figure 1 showing, the paper established the analysis system of slope greening design, which contains object hierarchy, rule hierarchy and index hierarchy.

**The evaluation system of engineering technology**

Slope greening plays a role of preventing erosion and stabilizing side slope, therefore, whose first purpose is ensuring the effective and safe of engineering technology. Moreover, it is necessary that considering working security and simplicity. Therefore, the author established evaluation system of engineering technology based on four aspects, which are the effectiveness of engineering technology  $C_{11}$ , the reliability of engineering technology  $C_{12}$ , working simplicity of engineering technology  $C_{13}$  and working security of engineering technology  $C_{14}$ .

**The evaluation system of economic benefit**

With the development of highway construction, the economic benefit for an special highway construction not only consider the construction cost during construction period, but also consider maintenance cost during operation period. For a slope greening design, the author analyzed the construction cost saving  $C_{21}$ , the maintenance cost saving  $C_{22}$ , the economic saving for reducing traffic accidents  $C_{23}$ , and the benefit for traffic volume increasing  $C_{24}$ .

**The evaluation system of ecological function**

It is generally held by highway workers that slope greening not only plays a role of

preventing erosion and stabilizing side slope, but also plays key roles of improving environment structure, reducing pollution, and hindering the noise. From the ecological view, some fundamental ecological function are given out in this paper, such as soil and water conservation  $C_{31}$ , water purification  $C_{32}$ , air purification  $C_{33}$ , hindering the noise  $C_{34}$ , protecting animal  $C_{35}$ , windbreak and sand fixation  $C_{36}$  and protecting original ecological environment  $C_{37}$ .

#### **The evaluation system of landscape function**

“Landscape” has two meanings in geography. The first meaning is “scenery”, which is a visual object from the aesthetic aspect, and the second meaning is “natural land area or water area”. Therefore, the paper established the evaluation system of landscape function based on the six elements, which are abundance and contrast of color  $C_{41}$ , comparison of space  $C_{42}$ , landscape diversity index  $C_{43}$ , connectivity index of green space  $C_{44}$ , landscape heterogeneity index  $C_{45}$ , landscape fragmentation index  $C_{46}$ ,

#### **The evaluation system of driving safety**

Slope greening affects the traffic safety to some extent. Slope greening play key roles in reducing the dull sense, directing the line of sight, preventing crashing, and so on. It is important to exert the safety character of the slope greening model and provide the graceful, comfort and harmonious safety traffic condition. Thus, the author established the evaluation system of driving safety based on the six elements, which are directing the line of sight  $C_{51}$ , ensuring visual comfort  $C_{52}$ , and delaying appearance of fatigue  $C_{53}$ .

#### **The evaluation system of humanities and sociological evaluation**

Slope greening, a part of basic highway construction, firstly should satisfy users' demand. Furthermore, slope greening, as a special visual object, should have social connotation, cultural connotation and aesthetic value. Therefore, the paper established the evaluation system of humanities and sociological evaluation from drivers' spiritual demand  $C_{61}$ , regional culture embodiment  $C_{62}$ , economic and civilization symbol  $C_{63}$ .

## **THE CALCULATION OF HIERARCHY STRUCTURE**

#### **The calculation of the factors of rule hierarchy**

As table 1 showing, the paper established the judgment matrix of every hierarchy of the slope greening design and determined the pairwise comparison of all elements by the questionnaire investigation to the experts.

According to the AHP, it is necessary to develop every vector of weights or priorities  $W = (W_1, W_2, \dots, W_n)$ , judge the consistency of the matrix and check the effectiveness and reliability of results. As table 2 shows, the paper obtain every vector of weights or priorities  $w = (W_1, W_2, \dots, W_n)$ , the maximum eigenvalue and consistency index for every judgment matrix “CI”, which were compared to the Mean random consistency index “RI” based on the table 1.

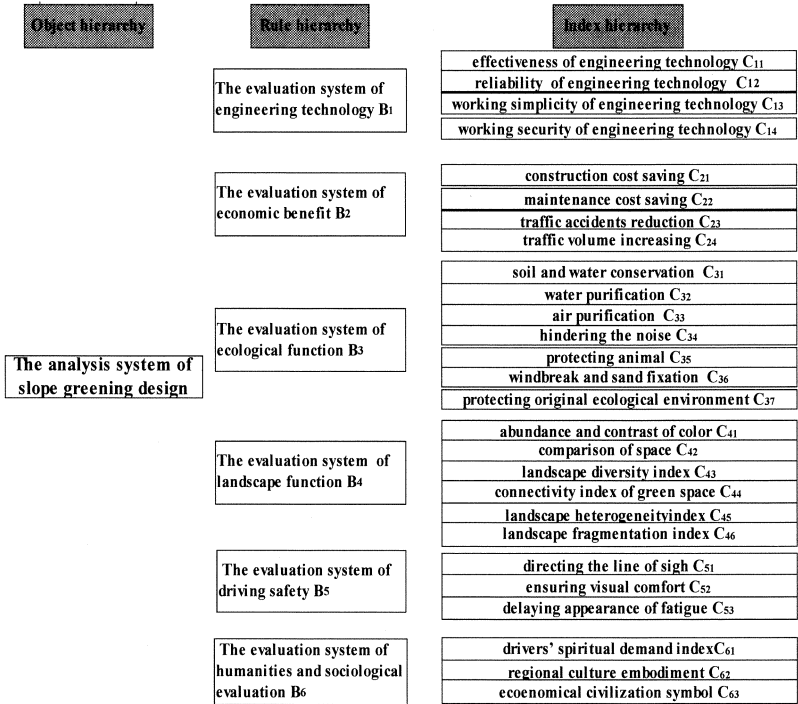


FIG 1.The system of slope greening design

Table 1. Judgment Matrix of Every Hierarchy

A: Rule hierarchy

A	B <sub>1</sub>	B <sub>2</sub>	B <sub>3</sub>	B <sub>4</sub>	B <sub>5</sub>	B <sub>6</sub>
B <sub>1</sub>	1	7	1/2	2	4	5
B <sub>2</sub>	1/7	1	1/7	1/5	1/3	1/3
B <sub>3</sub>	2	7	1	2	3	3
B <sub>4</sub>	1/2	5	1/2	1	2	3
B <sub>5</sub>	1/4	3	1/3	1/2	1	2
B <sub>6</sub>	1/5	3	1/3	1/3	1/2	1

B: Index hierarchy **B<sub>1</sub>** and **B<sub>2</sub>**

<b>B<sub>1</sub></b>	<b>C<sub>11</sub></b>	<b>C<sub>12</sub></b>	<b>C<sub>13</sub></b>	<b>C<sub>14</sub></b>	<b>B<sub>2</sub></b>	<b>C<sub>21</sub></b>	<b>C<sub>22</sub></b>	<b>C<sub>23</sub></b>	<b>C<sub>24</sub></b>
<b>C<sub>11</sub></b>	1	2	5	2	<b>C<sub>21</sub></b>	1	1/3	1/5	1/2
<b>C<sub>12</sub></b>	1/2	1	4	2	<b>C<sub>22</sub></b>	3	1	1/2	2
<b>C<sub>13</sub></b>	1/5	1/4	1	1/3	<b>C<sub>23</sub></b>	5	2	1	3
<b>C<sub>14</sub></b>	1/2	1/2	3	1	<b>C<sub>24</sub></b>	2	1/2	1/3	1

C: Index hierarchy **B<sub>3</sub>**

<b>B<sub>3</sub></b>	<b>C<sub>31</sub></b>	<b>C<sub>32</sub></b>	<b>C<sub>33</sub></b>	<b>C<sub>34</sub></b>	<b>C<sub>35</sub></b>	<b>C<sub>36</sub></b>	<b>C<sub>37</sub></b>
<b>C<sub>31</sub></b>	1	1	2	1/2	3	5	1/2
<b>C<sub>32</sub></b>	1	1	2	1/2	3	5	1/2
<b>C<sub>33</sub></b>	1/2	1/2	1	1/3	3	3	1
<b>C<sub>34</sub></b>	2	2	3	1	3	3	1
<b>C<sub>35</sub></b>	1/3	1/3	1/3	1/3	1	1	1/3
<b>C<sub>36</sub></b>	1/5	1/5	1/3	1/3	1	1	1/3
<b>C<sub>37</sub></b>	2	2	1	1	3	3	1

D: Index hierarchy **B<sub>4</sub>**

<b>B<sub>4</sub></b>	<b>C<sub>41</sub></b>	<b>C<sub>42</sub></b>	<b>C<sub>43</sub></b>	<b>C<sub>44</sub></b>	<b>C<sub>45</sub></b>	<b>C<sub>46</sub></b>
<b>C<sub>41</sub></b>	1	2	3	3	5	7
<b>C<sub>42</sub></b>	1/2	1	1	1	5	5
<b>C<sub>43</sub></b>	1/3	1	1	1	3	5
<b>C<sub>44</sub></b>	1/3	1	1	1	2	5
<b>C<sub>45</sub></b>	1/5	1/5	1/3	1/2	1	2
<b>C<sub>46</sub></b>	1/7	1/5	1/5	1/5	1/2	1

E: Index hierarchy **B<sub>5</sub>** and **B<sub>6</sub>**

<b>B<sub>5</sub></b>	<b>C<sub>51</sub></b>	<b>C<sub>52</sub></b>	<b>C<sub>53</sub></b>	<b>B<sub>6</sub></b>	<b>C<sub>61</sub></b>	<b>C<sub>62</sub></b>	<b>C<sub>63</sub></b>
<b>C<sub>51</sub></b>	1	3	3	<b>C<sub>61</sub></b>	1	1/5	2
<b>C<sub>52</sub></b>	1/3	1	1/3	<b>C<sub>62</sub></b>	5	1	3
<b>C<sub>53</sub></b>	1/3	3	1	<b>C<sub>63</sub></b>	1/2	1/3	1

**Table 2. Single-level Sequencing and Consistency Check**

	<b>W=(W<sub>1</sub>, W<sub>2</sub> . . . . ,W<sub>n</sub>)</b>	<b>λ<sub>max</sub></b>	<b>CI</b>	<b>CI/RI</b>
A	(0.291,0.035,0.323,0.176,0.094,0.081)	6.21	0.042	0.033
B <sub>1</sub>	0.291 (0.437,0.294,0.074,0.194)	4.23	0.073	0.081
B <sub>2</sub>	0.035 (0.088,0.272,0.483,0.157)	4.01	0.003	0.005
B <sub>3</sub>	0.323 (0.180,0.180,0.127,0.198,0.051,0.048,0.216)	7.42	0.07	0.053
B <sub>4</sub>	0.176 (0.373,0.196,0.165,0.155,0.073,0.037)	6.14	0.028	0.023
B <sub>5</sub>	0.094 (0.630,0.107,0.203)	3.04	0.02	0.034
B <sub>6</sub>	0.081 (0.252,0.589,0.160)	3.05	0.025	0.043

**Hierarchy general ranking**

By calculating and analyzing, this paper obtained the hierarchy general ranking is as follows:

**Table 3. The Hierarchy General Ranking of Slope Greening Design**

<b>C<sub>11</sub></b>	<b>C<sub>12</sub></b>	<b>C<sub>37</sub></b>	<b>C<sub>41</sub></b>	<b>C<sub>34</sub></b>	<b>C<sub>51</sub></b>	<b>C<sub>31</sub></b>	<b>C<sub>32</sub></b>	<b>C<sub>14</sub></b>
0.13	0.09	0.07	0.07	0.07	0.06	0.06	0.06	0.06
<b>C<sub>62</sub></b>	<b>C<sub>33</sub></b>	<b>C<sub>42</sub></b>	<b>C<sub>43</sub></b>	<b>C<sub>44</sub></b>	<b>C<sub>53</sub></b>	<b>C<sub>13</sub></b>	<b>C<sub>61</sub></b>	<b>C<sub>23</sub></b>
0.05	0.04	0.03	0.03	0.03	0.02	0.02	0.02	0.02
<b>C<sub>35</sub></b>	<b>C<sub>36</sub></b>	<b>C<sub>63</sub></b>	<b>C<sub>45</sub></b>	<b>C<sub>52</sub></b>	<b>C<sub>22</sub></b>	<b>C<sub>46</sub></b>	<b>C<sub>24</sub></b>	<b>C<sub>21</sub></b>
0.02	0.02	0.01	0.01	0.01	0.01	0.01	0.01	0

**CONCLUSION**

According the results showing table 3, the considered factors for slope greening were divided into six groups. Firstly, the effectiveness and the reliability of engineering technology environments are the most key considered factors. Secondly, it is necessary to consider the act of protecting original ecological environment, hindering the noise and beautifying the environment for a slope greening design. Thirdly, slope greening plays key roles in directing the line of drive sight, and protecting soil and water.

**REFERENCES**

Liu Chunxia, and Han Liebao.(2007) “Evaluation of integrated benefits of freeway greening ” Urban environment and urban ecology, Vol 20,No3,6,38-44

"The analytic hierarchy process: theoretical developments and some applications."(1987). Int. J. Mathematical Modelling. 9(3-5), 161-395

Ouyang Eede, He Huiqin, Li Qian(2008)”The application of AHP into the choice of plants for road slope greening ”. Technical,67-68

Q. Q. Liu and V. P. Singh, F.ASCE(2004). “Effect of Microtopography, Slope Length and Gradient, and Vegetative Cover on Overland Flow through Simulation”. Journal of hydrologic engineering, Vol 9,No5,375-382

Liu Huaixiang, Zeng Sheng,Zhu Gang(2007). “The choice of slope scheme using AHP”. Journal of China & Foreign Highway, Vol 27,No5,27-31.

## Using Ground Penetration Radar Techniques for Roadway Structure Safety Evaluation

Dar-Hao Chen<sup>1</sup>, Ph.D., P.E., Andrew Wimsatt<sup>2</sup>, Ph.D., P.E., and John Bilyeu<sup>3</sup>, P.E.

<sup>1</sup> School of Highway Engineering, Changsha University of Science & Technology, Chiling Road 45#, Changsha, Hunan, 410076 and Texas Department of Transportation 4203 Bull Creek #39, Austin, TX 78731. Email: [dchen@dot.state.tx.us](mailto:dchen@dot.state.tx.us)

<sup>2</sup> Texas Transportation Institute. Email: [A-Wimsatt@ttimail.tamu.edu](mailto:A-Wimsatt@ttimail.tamu.edu)

<sup>3</sup> Texas Department of Transportation. Email: [jbilyeu@dot.state.tx.us](mailto:jbilyeu@dot.state.tx.us)

### ABSTRACT

Early identification of voids under a roadway structure is critical on preventing major failures from occurring. In this study, a 400MHz Ground Coupled Penetrating Radar (GCPR) was utilized to characterize the subsurface conditions of two roadway pavements (US290 and 34<sup>th</sup> Street). A huge (1.8m\*4.6m\*3.7 m=30.6 m<sup>3</sup>) void under US290's reinforced concrete pavement was successfully identified by GCPR. Video inspection indicated that a disjointed storm pipe had caused washout and void. Fortunately, the disjointed storm pipe was identified in time. Otherwise, the 30.6 m<sup>3</sup> void would have continued to grow in size until the pavement collapsed, which may have caused human casualties and property loss. This study has successfully demonstrated that the GCPR is able to identify void locations. Despite leaking sand from a Mechanically Stabilized Earth (MSE) wall, no voids were detected by the GCPR surveys near the MSE wall on 34<sup>th</sup> street. It is concluded that the erosion of the fill behind the MSE wall is in a very early stage, so that voids are not large enough to be detected by the GCPR. Therefore, it was recommended that regular inspections should be performed.

### INTRODUCTION

Detecting concealed subsurface voids under a roadway is critical for preventing tragedies from occurring. The development of voids beneath roadways is a serious hazard, making their early detection an important aspect of infrastructure maintenance and remediation. Leaks or pipe breaks allow for fine aggregate to be carried away, resulting in local base erosion, the formation of weak areas, and eventually voids. In addition, the subsurface voids tend to increase in size with time, due to additional erosion and/or washout [Wilson and Garman 2007]. Thus, there is a critical need to develop non-destructive and in-situ characterization techniques to evaluate structural safety to prevent the occurrence of severe consequences such as a collapsed roadway. In modern roadway engineering, one of the most useful noninvasive methods is Ground Penetrating Radar (GPR), which transmits and records the passage of electromagnetic waves through the roadway structure.

GPR operates by transmitting an electromagnetic pulse from an antenna into the ground and then recording properties of the reflections of this pulse, such as time

taken for the reflected signals to return to the antenna and the amplitude and phase of the reflected signal [Evans et al. 2007]. The reflected energy contains a record of the properties and thickness of the layers within the roadway structure. Reflected waves are converted into voltage, and the pattern of voltage versus time is recorded [Maser and Scullion 1992]. GPR technology is very effective for identifying areas where physical properties have changed, and there may be potentially hazardous voids. The Texas Department of Transportation and the Texas Transportation Institute have utilized the GPR technology with success in locating voids under roadway pavements [Chen and Scullion 2008]. The methodologies presented in this study for detecting subsurface voids are applicable to any other projects.

In general, air voids and water-filled voids are both detectable using GPR because the dielectric constants of both air (1) and water (81) are substantially different than most pavement materials (from 5 to 8) [Chen and Scullion 2008]. If the void is air-filled, a large negative peak will appear in the waveform, since the dielectric constant of air is much less than pavement material. Conversely, a large positive peak in the waveform will appear at the surface of a water-filled void, because that is where the dielectric increases substantially.

The potential of nondestructive testing is presented, with special focus on technical advances in GPR applications for void detection. This paper presents two case studies (US290 and 34<sup>th</sup> Street) where a 400 MHz Ground Coupled Penetrating Radar (GCPR) was used to identify subsurface voids. The GCPR surveys were performed at walking speed, approximately 5km/hr.

### **Case Study 1 - A 1.8m x 4.6m x 3.7m Void Under US290**

Austin District maintenance personnel of the Texas Department of Transportation (TxDOT) observed that a section of a longitudinal joint in continuously reinforced concrete pavement (CRCP) had faulted and separated in a Mechanically Stabilized Earth (MSE) retaining structure of US290 in Southwest Austin. The fault and lane drop-off measured up to 75mm and the joint had separated up to 25mm. A narrow asphalt patch in the faulted area was applied by the Maintenance personnel. The lane drop-off and longitudinal cracks near the MSE wall prompted district personnel to request an investigation to assess the safety of the structure and to determine if there were significant voids under the CRCP.

The main concern was that the lane drop-off and longitudinal cracks near the inlet and storm drainpipe may be associated with voids in the MSE structure, making it unsafe. A 400MHz GCPR antenna was used to survey and map the subsurface condition. GCPR data was collected in the longitudinal direction parallel to the faulted joint and at selected transverse locations. The reflections from the rebar are readily visible as a series of hyperbolas (refer to Fig. 1). The reason that a transverse bar appears as a hyperbola is because the metal is imaged not only when the GCPR antenna is directly above, but also when the antenna is approaching and leaving the target [Daniels 1996]. The apex of the hyperbola represents the top of the steel rebar, and its measured depth correlates well with what was given in the design plan.

A significant anomaly adjacent to the drainpipe was found, as shown in Fig. 1. There is a clear change in the GCPR image at this location. The anomaly starts directly under

the CRCP. The anomaly shows a significant drop in material dielectrics, and based on the reflection pattern, it was a suspected void. The indication of the voids was an inversion of the GPR voltage, indicating a change in dielectric (high to low), as shown in Fig. 2. Normally, the dielectric increases with pavement layers at greater depth, yielding a positive reflection at the depth of each layer interface. There are inversions and significant negative reflections in the GPR image where the anomaly is. Based on the image, the size of the suspected void was estimated to be significant.

The design plan indicated that a transverse storm drain was placed underneath the concrete pavement near the end of the faulted joint, so GCPR data was collected in this area, as indicated in Fig. 2. The GCPR data indicated an anomaly over the transverse storm drain as shown in Fig. 1. Note that when the amplitude and travel time of the GPR return signals are continuous, this indicates areas in good condition. However, when there are amplitude and signal travel time variations, the deteriorated area can be easily identified. The GPR method, as many other nondestructive techniques, has advantages and limitations. One limitation is the need for trained personnel to interpret GPR data. Also, in almost all cases, destructive testing is required for validation.

A pavement core was taken, and a void approximately 1.8m (6ft) deep, 4.6m (15ft) long, and 3.7 m (12ft) wide was found, as shown in Fig. 2. The estimated void is approximately 30.6 m<sup>3</sup>. As can be seen in Fig. 2, the transverse storm drain had separated. This separation caused water to erode the area around the drain. The resulting moisture intrusion in this area and moisture flow from the grassy median through the embankment into the void may have resulted in the embankment settling where the longitudinal joint faulted.

Fortunately, the disjointed storm pipe was identified in time. Otherwise, the 30.6 m<sup>3</sup> void would have grown in size and probably caused the pavement to collapse, which may have caused human casualties and property loss. Augering is planned in the area of the longitudinal joint failure to see if there are other problems with the underlying embankment material such as deeper voids that cannot be detected by the GCPR. District personnel are planning to let a project to repair this area.



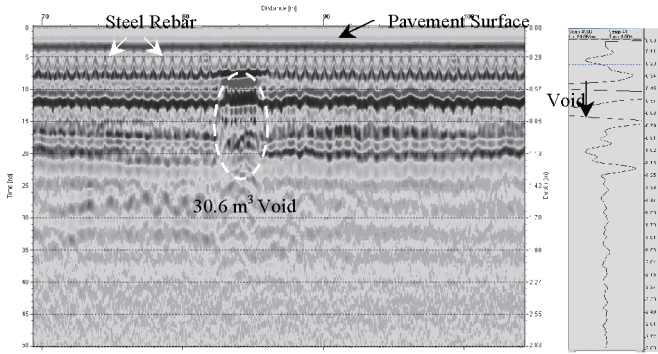


**Fig. 1 Conditions of US290 Showing 75mm Drop-Off on Top of a Mechanically Stabilized Earth (MSE) Retaining Structure and GPR Images Showing Voids**

**Case Study 2 - Loss of Backfill Sand on 34<sup>th</sup> Street**

Amarillo District personnel have been concerned with the loss of backfill sand in a MSE retaining structure, as shown in Fig. 3. There are medium to severe transverse cracks on the pavement surface, as shown in Fig. 3. In general, depressions in asphalt pavements, as well as excessive cracking are early indicators of base and subgrade deterioration. The deposits of leaking sand near the MSE wall and the surface cracks prompted district personnel to request an investigation to assess the safety of the structure and to determine if there are significant voids under the pavement.

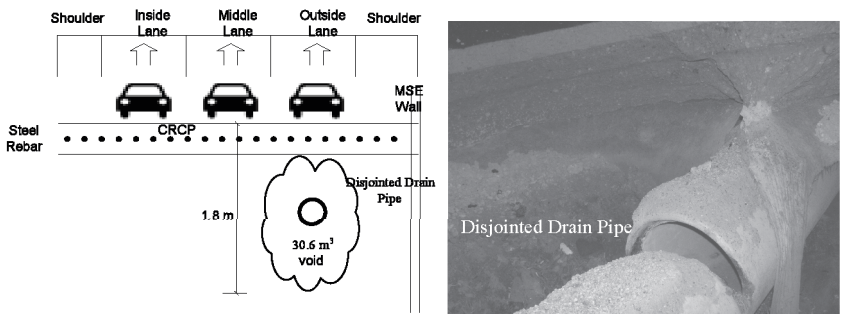


**Fig. 2 Confirmed 30.6 m<sup>3</sup> (4.6\*3.7\*1.8 m) Void Under CRCP With Disjointed Pipe**

**Case Study 2 - Loss of Backfill Sand on 34<sup>th</sup> Street**

Amarillo District personnel have been concerned with the loss of backfill sand in a MSE retaining structure, as shown in Fig. 3. There are medium to severe transverse

cracks on the pavement surface, as shown in Fig. 3. In general, depressions in asphalt pavements, as well as excessive cracking are early indicators of base and subgrade deterioration. The deposits of leaking sand near the MSE wall and the surface cracks prompted district personnel to request an investigation to assess the safety of the structure and to determine if there are significant voids under the pavement.

Previous TxDOT specifications allowed for fine sand to be used in MSE walls for backfill. Field observations indicate that many MSE projects have similar leaking sand problems. TxDOT's in-house study revealed that the loss of sand is normally associated with significant amounts of water that enters the embankment through joints, ruptured drainage pipes, approach slabs, or in the vicinity of bridge abutments [Chen et al 2007].

Normally, if water enters the top of the wall in any appreciable quantity, it will seek a path out through any breach in the filter fabric covering inside of the wall panels. Once this process begins, piping will occur, carrying out the fine sand backfill with the water. Note that once the fabric is broken, it is difficult to patch the outside of the MSE panel, because the hydrostatic pressure would exceed the adhesion of the patch material, or eventually tear the patch itself [Chen et al 2007]. The structure was about 12 years old when the leaking sand was noticed and the investigation started. The typical pavement section consists of 38mm (1.5 inches) of HMA, 200mm (8 inches) of cement-treated base (7% cement), and 150mm (6 inches) of lime treated subgrade. The main concern was the loss of backfill sand that may lead to voids in the MSE structure, making the embankment unsafe. Four parallel GCPR tests were conducted, among others, to determine the extent of voids under the pavement. Fig. 3 shows the GCPR testing near the edge of the MSE wall. Typically, the voids were found close to the MSE wall, and then gradually would extend into the travel lane.

Fortunately, no significant signal inversion (indicating voids) can be found in the GCPR images in any tested areas. There are obvious changes in the middle section because of the changes in material and design. It is concluded that the leaking of sand deposits near the MSE wall is in a very early stage. Thus, any voids are not large enough to be detected by the GCPR. In addition, unlike the concrete pavement (that would bridge over the void until it got very large) the asphalt pavement would settle gradually into the voids. Therefore, it was recommended that regular inspection should be performed to monitor the MSE.

## CONCLUSIONS

It is one of the main functions of transportation agencies to provide safe transportation facilities for effective and efficient movement of people and goods. The development of voids beneath roadways is a serious hazard, making their early detection an important aspect of preventing major failures from occurring. A 400MHz GCPR was used in two projects to identify voids beneath roadway structures in Texas. The presence of air filled voids beneath roadway structures are clearly identified in GCPR images, as they generate a signature that is relatively easy to identify. A huge void (30.6 m<sup>3</sup>) under US290's reinforced concrete pavements was successfully identified by GCPR. It was found from the video inspection that the disjointed storm pipe caused erosion and a large void. Fortunately, this was found in time, or it may have caused the

roadway to collapse. This study has successfully demonstrated that the GCPR is able to identify void locations.

Despite leaking sand from the MSE wall on 34<sup>th</sup> street, no significant voids were detected. It is concluded that the erosion of the fill behind the MSE wall is in the very early stage, so voids are not large enough to be detected by the GCPR. Therefore, it was recommended that regular inspection should be performed to monitor the MSE wall.

**ACKNOWLEDGEMENTS**

The supports and assistances from Miguel Arellano, and Mike Taylor of Texas Department of Transportation and Tom Scullion and Lee Gustavus of Texas Transportation Institute are much appreciated.

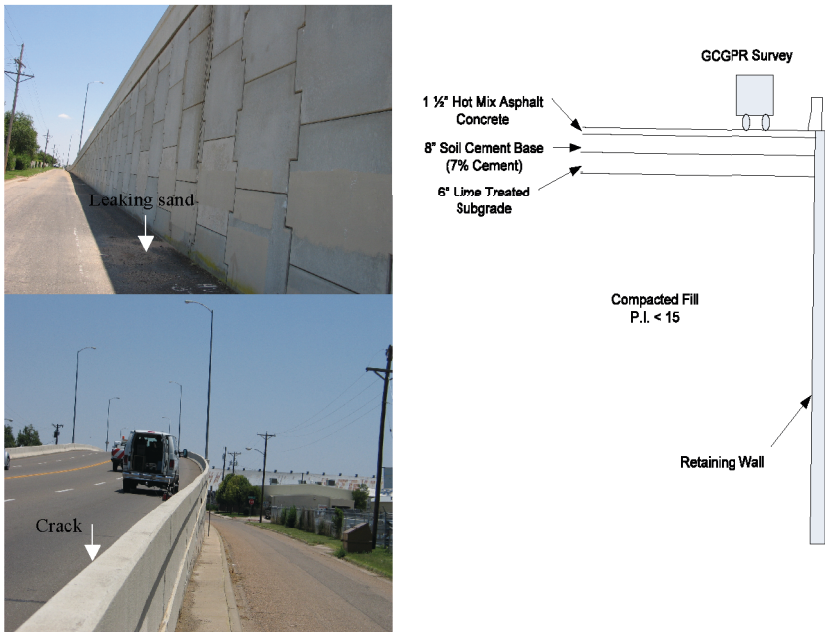


**Fig. 3 Deposit of the Leaking Sand at the MSE Wall, GCPR Testing Near the MSE Wall and Transverse Cracks on the Pavement Surface, and Schematic of the MSE Wall**

**REFERENCES**

- Chen, Dar-Hao, Nazarian, S. and Bilyeu, J. (2007) “Failure Analysis of a Bridge Embankment With Cracked Approach Slabs and Leaking Sand”. *Journal of Performance of Constructed Facilities, ASCE*. Vol. 21. Number 5. pp 375-381. October 2007.
- Chen, Dar-Hao, and Scullion, T. (2008) “Detecting Subsurface Voids Using Ground Coupled Penetrating Radar” *Geotechnical Testing Journal, ASTM*. Vol. 31. Number 3. pp. 217-224. May 2008.
- Daniels, D.J. (1996). *Subsurface-Penetrating Radar*, The Institute of Electrical Engineers, pp. 1 – 62.
- Evans, R., Frost, M., Stonecliffe, M. and Dixon, N. (2007) “Assessment of In Situ Dielectric Constant of Pavement Materials”. *Transportation Research Record: Journal of the Transportation Research Board*. Number 2037 . pp128-135.
- NCHRP (1998) *National Cooperative Highway Research Program(NCHRP) Synthesis of Highway Practice 255: Ground Penetrating Radar for Evaluating Subsurface Conditions for Transportation Facilities*. TRB, National Research Council, Washington, D.C., 1998.
- Maser, K. R., and T. Scullion (1992). *Automated Pavement Subsurface Profiling Using Radar: Case Studies of Four Experimental Field Sites*. In *Transportation Research Record 1344*, TRB, National Research Council, Washington, D.C., 1992, pp. 148–154.
- Wilson, W. and Garman, K. M (2007) “Identification and Delineation of Sinkhole Collapse Hazards in Florida Using Ground Penetration Radar and Electrical Resistivity Imaging”  
[http://www.dot.ca.gov/hq/esc/geotech/gg/geophysics2002/114garman\\_sinkhole4.pdf](http://www.dot.ca.gov/hq/esc/geotech/gg/geophysics2002/114garman_sinkhole4.pdf)

## **Visualizing 3-D Internal Soil Deformation Using Laser Speckle and Transparent Soil Techniques**

Jinyuan Liu, P.E., P.Eng., M. ASCE

Assistant Professor, Dept of Civil Engineering, Ryerson University, Canada; Jinyuan.liu@ryerson.ca

**ABSTRACT:** This paper addresses the needs for non-intrusively measuring 3-D internal soil deformation in geotechnical engineering. In this research transparent soil is used to measure internal soil deformation under a model footing. Transparent soil is made of either amorphous silica gel or powder with a pore fluid having the same refractive index to model either sand or clay. An optical system consisting of a laser light, a CCD camera, a frame grabber, and a computer was developed to optically slice a transparent soil model. A distinctive laser speckle pattern is generated by the interaction of the laser light and transparent soil. Digital image cross-correlation was used to calculate 2-D displacement fields between two speckle images captured consecutively during footing settlement. A 3-D displacement field was obtained in Matlab<sup>®</sup> by combining multiple slices of 2-D displacement fields. The results showed that the developed optical system and transparent soil are suitable for more advanced 3-D soil deformation measurements.

### **INTRODUCTION**

Visualization of three-dimensional (3D) internal soil deformation or strain field can significantly improve the interpretation and understanding of geotechnical engineering problems and help in solving these problems more efficiently. Many techniques and methods have been utilized to obtain internal soil deformation and strains, including radiography, computerized axial tomography, and magnetic resonance imaging (Roscoe et al. 1963). However, all the investigations above are either intrusive or limited by the high cost and technical difficulties.

Transparent materials including photoelastic material and glass have been used in model studies to investigate stress and flow fields inside natural soil. However, these studies are limited by the fact that these materials cannot model soil behaviour and have poor quality of transparency. This paper presents the development of a transparent material and measurement of internal soil deformation under a model footing using image processing and laser speckle techniques.

## TRANSPARENT SOIL

Mannheimer and Oswald (1993) and Iskander et al. (1994) demonstrated that a material made of silica powder and a pore fluid with the same refractive index exhibits similar stress-strain behaviour as natural clay. Later another kind of transparent soil was developed to model sand, which is made of silica gel. Transparent soil mentioned in this paper has been used by other researchers in their model studies (Welker et al. 1999; Gill and Lehane 2001).

### **Amorphous Silica Powder for Modeling Clay**

Amorphous silica powder used in this study was a commercial product of PPG, Inc. used without further processing. It has a two-pore system inside. It consists of ultrafine particles with individual diameters on the order of 0.02  $\mu\text{m}$ . These particles combine to form larger porous aggregates. Four different kinds of silica ranging in aggregate size from 1.4 to 175  $\mu\text{m}$  were used for modelling clay. Amorphous silica powders exhibited typical stress-strain behavior in conventional triaxial compression tests. The measured behaviors of amorphous silica powder appear to represent a generic clay whose properties depend on the size of silica and consolidation history. The deformation mechanism and magnitudes were consistent with those of natural clays at strains less than 15%, which permits modeling deformational problems, since the strength corresponding to the strain of interest is comparable to that of natural soils. More details can be found in Iskander et al (2002a).

### **Amorphous Silica Gel for Modeling Sand**

Silica gel is a colloidal form of silica. It is inert and porous, and is available in sizes ranging from 0.5 mm to 5 mm. The most common shapes are rounded bead and angular particle. Typical stress-strain behaviors for both fine and coarse silica gel are consistent with those of natural sands. Dense specimens of fine silica gel exhibited typical shear dilate behavior, particularly at low confining pressures. The residual strength of dense samples approaches the peak strength of loose samples at the same normal pressure. The angles of friction from triaxial tests were 30°–36° for fine silica gel and 31°–34° for coarse silica gel. Young's Modulus ranged between 24-84 MPa depending on density and size. More details can be found in Iskander et al (2002b).

### **Pore Fluids**

Two liquids resulted in sufficiently clear samples. The first is a blend of mineral oil and a normal paraffinic solvent by one-to-one weight ratio, which has a refractive index of 1.447 at 25°C. The second is a brine mixture blended from calcium bromide and water to have a refractive index of 1.448 at 25°C. These two fluids are not miscible which permits studying multiphase flow problems.

## DIGITAL IMAGE PROCESSING AND LASER SPECKLE TECHNIQUES

### **Digital Image Correlation**

Digital image cross-correlation (DIC) is a classic pattern recognition technique where two images are compared to obtain the relative displacement between them. DIC is widely used in many engineering fields to obtain spatial deformation patterns, albeit with several names. The discrete form of standard cross-correlation function is as follows:

$$C(\Delta x, \Delta y) = \frac{1}{MN} \sum_{m=0}^{M-1} \sum_{n=0}^{N-1} f(m, n) g(m + \Delta x, n + \Delta y) \quad (1)$$

where M and N are the dimensions of the interrogated images, f and g are the intensities of two images being interrogated. The correlation function given above is sensitive to the average intensity of images. Therefore, the zero normalized cross-correlation function is normally used in the analysis.

### Laser Speckle in Transparent Soil

A laser light sheet was used to target a region of interest inside a transparent soil model. The laser light sheet was generated by passing a laser beam through a line generator lens. The interaction between transparent soil and the laser light sheet produced a distinctive speckle pattern. The speckle pattern created by a laser beam scattered from a rough surface or from particles in a liquid, has a well-defined spatial structure (Goodman 1975). The speckle properties typically depend on both the roughness and reflectance of the surface. Laser speckle technique used here has been applied intensively in many engineering fields (Erf 1978).

## AN OPTICAL SYSTEM FOR SOIL DEFORMATION MEASUREMENTS

### An Optical Test Set-up

An optical test set-up, shown in Fig. 1, was developed to consist of a CCD camera, a laser, a loading frame, a test table, and a computer for image processing. The camera with a resolution of 640×480 pixels was set 20 cm away from the model. It is controlled by the computer through a frame grabber. The used laser was 35mW He-Ne laser with a wavelength of 632.8 nm. A Plexiglas mould with dimensions of 50×150×300 mm was used in the tests. A model footing with a plan dimension of 50×25 mm was used to simulate a continuous footing with a width of 25 mm. Load was applied vertically through a screw mechanism. A load cell and an LVDT were connected to a loadframe to measure load and deformation during the test. A precise linear stage with a resolution of 0.01 mm was used to move the transparent soil mould, which allows for slicing the model.

### Sample Preparation

A strong "sand" overlying soft "clay" case was simulated in this study. Silica gel with a diameter of 0.5 to 1.5 mm, obtained from *Multisorb Technologies Inc.*, was used without further processing in this study. Flo-Gard SP with its average aggregate size of 1.4 μm, obtained from *PPG Inc.*, was used to model clay. A blend of mineral oil and paraffinic solvent was used to make transparent soil model.

For the sample preparation, first, a silica slurry was made of silica powder and the pore fluid and a separated specimen was made of silica gel. Second, a vacuum was applied to de-air both specimens until they turned transparent. Third, silica slurry was poured into the Plexiglas mould and consolidated using a plate with a filter paper attached to its bottom. Forth, de-aired silica gel was poured on top of silica powder sample after its consolidation.

After that, the model was placed and adjusted on the linear stage platform. A loading mechanism was designed to push down the model footing vertically onto the soil. The sample was then sliced at specific cross-sections by controlling the movement of the sample through a linear stage.

The load-settlement curve of the model footing is shown in Fig. 2 with the deformation steps labeled inside. The curve represented a punching or a local shear failure, which was reasonable considering the low strength of the “clay” layer relative to the strength of top “sand” layer.

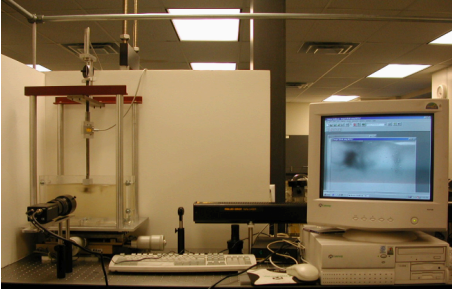


**Fig. 1. An optical test set-up for measuring internal soil deformation**

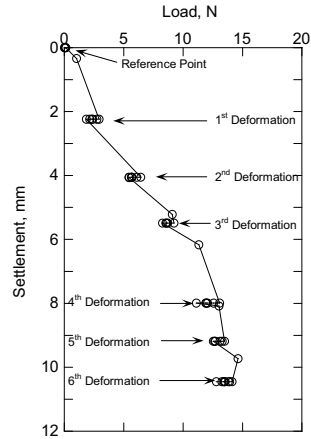


**Fig. 2. Load-settlement curve of the model footing**

## INTERNAL DEFORMATION MEASUREMENT

### Displacement Field Analyses

A typical 2-D displacement field was calculated by cross-correlating two images on the same cross-section at different loading stages, shown in Fig. 3. 2-D displacement magnitude fields from four different cross-sections were combined into a 3-D displacement magnitude field. Slicing this 3-D displacement magnitude field details the distribution of displacements inside the field, as shown in Fig. 4. The consistent distribution of displacement along the depth coincides with the plain strain problem investigated in this study.

### Strain Field Analysis

Strains can be calculated using the predicted displacement field. Green's strains were used regardless of the magnitude of the displacement. The maximum shear strain was then calculated based on Green's strains. The failure envelope was assumed to coincide with the peak maximum shear strain. The failure development was then studied by locating the peak maximum shear strain. The out-of-plane displacement component was not obtained by the optical system. It was assumed that the influence on the strain field from out-of-plane displacement component was insignificant in this study because of a plain strain problem studied here.

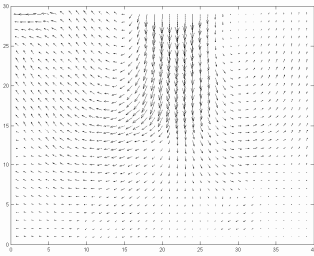


**Fig. 3. A typical 2-D displacement field inside transparent soil**

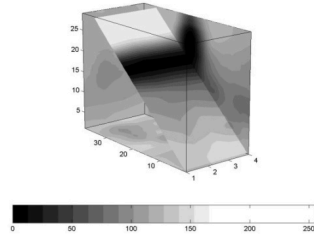


**Fig. 4. Distribution of displacement field along the depth**

The maximum shear strain on a section 10 mm inside the transparent soil model is shown in Fig. 5 for the first loading stage, where the peak shear strain regions were shaded. A punching shear failure mode occurred in the top “sand” layer. The failure plane extended along the footing edge downward to the surface of the lower clay layer and then spread outward. The triangular zone assumed by Terzaghi (1943) was appreciable even at the early loading stage. The failure model was similar to that reported by Meyerhof (1974) for a footing on thin sand layer overlying a clay layer, which is the problem being simulated in this study.

No continuous failure plane was developed in both the first and sixth loading stages. However, the failure envelopes developed on the sixth loading stages were more appreciable than earlier loading stages. The distributions of maximum shear strain in different cross sections agreed with each other at the same deformation steps. It shows that the maximum shear strain is mainly located around the footing. It punches into clay layer below and spreads to both sides, which again agrees with the failure envelope proposed by Meyerhof (1974).

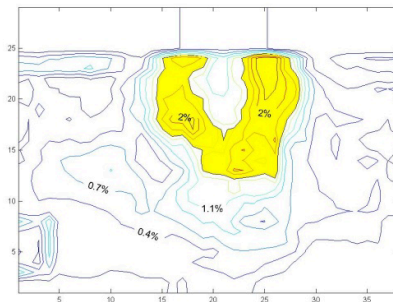


**Fig. 5. Typical maximum shear strain field**

## CONCLUSIONS

3-D displacement fields under a model footing inside a transparent soil model were obtained and measured non-intrusively using digital image processing and laser speckle techniques. Transparent soil is made of amorphous silica with a pore fluid having the same refractive index. The distinctive laser speckle images generated by the interaction between the laser light and transparent soil were used to calculate the displacement between two images using digital image correlation. A soil profile consisting of "sand" overlying soft "clay" was simulated in the model test. The deformation and strain fields under the model footing were similar to those published. The results show that transparent soil and the developed optical system are capable for more advanced 3-D deformation measurements in geotechnical engineering.

## ACKNOWLEDGEMENTS

This research is funded by the National Science Foundation through NSF Grant No. CMS 9733064: CAREER: Modeling 3-D Flow & Soil Structure Interaction Using Optical Tomography. The supports from Dr. Magued Iskander of Polytechnic University and the help from Mr. Chratien Mak of Ryerson University are greatly appreciated.

## REFERENCES

- Erf, R.K. ed. (1978). *Speckle Metrology*, Academic Press, New York.
- Gill, D. and Lehane, B. (2001). "An optical technique for investigating soil displacement patterns." *GTJ*, 24(3): 324-329.
- Goodman, J. W. (1975). "Statistical properties of laser speckle patterns." In: *Laser speckle and related phenomena*, Dainty (ed.), 9-75.
- Iskander, M. Lai, J., Oswald, C., Mannheimer, R. (1994). "Development of a transparent material to model the geotechnical properties of soils." *GTJ*, 17(4): 425-433.
- Iskander, M., J. Liu, & Sadek, S. (2002a). "Transparent amorphous silica to model clay." *JGGE*, 128(3): 262-273.
- Iskander, M., Sadek, S., and Liu, J. (2002b). "Optical measurement of deformation using transparent silica gel to model sand." *IJPMG*, 2(4):13-26.
- Mannheimer, R. and Oswald, C. (1993). "Development of Transparent Porous Media with Permeabilities and Porosities Comparable to Soils, Aquifers, and Petroleum Reservoirs," *Ground Water*, 31(5): 781-788
- Meyerhof, G. (1974). "Ultimate bearing capacity of footings on sand layer overlying clay." *CGJ*, 11(2): 224-229.
- Roscoe, K., Arthur, J., & James, R. (1963). "The determination of strains in soils by an X-ray method." *CE & PWR*, 58: 873-876 and 1009-1012.
- Terzaghi, K.(1943). *Theoretical Soil Mechanics*, Wiley, New York.
- Welker, A., Bowders, J., and Gilbert R. (1999). "Applied research using transparent material with hydraulic properties similar to soil." *GTJ*, 22(3): 266-270.

## Experimental and Theoretical Studies on (Relative) Permittivity of the Tunnel Lining

GAO Yan-xi<sup>1</sup>, LI Xia<sup>2</sup>

<sup>1</sup>Professor, Department of Communications and Transportation Engineering, Changsha University of Science & Technology, Changsha, 410076, Hunan, P. R. China; [gaoyanxigeo@sina.com](mailto:gaoyanxigeo@sina.com)

<sup>2</sup>Senior Engineer, Department of Communications and Transportation Engineering, Changsha University of Science & Technology, Changsha, 410076, Hunan, P. R. China; [sunny819@163.com](mailto:sunny819@163.com)

**ABSTRACT:** In the paper, for two cases of different ages and different depths, the speed of radar wave transmitted in the testing concrete lining is measured by using the ground penetrating radar (GPR), and corresponding data of permittivity of the concrete lining are therefore obtained. An abnormal phenomenon of the permittivity is observed which shows that the value of permittivity will increase linearly with the depth of the concrete lining. Combined with the characteristics of tunnel lining and taken the free water distribution into account, a new dielectric model of the concrete lining is put forward. Results show that this model can be used to explain the experimental results and provide correct reference for the GPR use in measuring the depth of the concrete lining with good accuracy.

**Key words:** (relative) permittivity, ground penetrating radar; concrete lining in tunnel; free water distribution

### I. INTRODUCTION

The use of ground penetrating radar (GPR), especially subsurface radar, has grown rapidly in recent years as a valuable tool for nondestructive surveys of structural concrete. Applications range from determination of major construction element thickness and location of metallic reinforcing bars and ducts, to location of voids, honeycombing, delamination, cracking and moisture ingress. Such applications have been reported in many technical papers and are reviewed and illustrated in Concrete Society Technical Report No. 48[Concrete1997]. To achieve these goals, we need to

know the accurate propagation speed of electromagnetic wave in the concrete. According to the electromagnetic wave theory, this speed depends on the relative permittivity of the medium. However, solid component, water content and porosity will affect the value of the relative permittivity of the concrete [Soutsos, *et.al.*2001]. So, the determination of accurate permittivity of the concrete is crucial to these applications.

For mature concrete, the paper [TsuiMatthews1997] discussed a number of dielectric models to estimate the effective dielectric properties. Such materials are classified as heterogeneous mixtures and are typically composed of two or more constituents having different dielectric properties. This paper focuses on premature concrete which is often the case in tunnel constructions when nondestructive surveys of structural concrete are required. For premature concrete there is an ageing process in which quite different features will be presented. For example, the effective permittivity of the concrete will change with the depth, contrary to the general theory, according to which the permittivity is regarded as a constant. Therefore, it would be useful for an inspecting engineer to know the variations and to correct the measurement data.

The paper is organized as follows: in Sec. 2 we present the experiment scheme and sample preparation process. Experimental results are also given in this section. In Sec.3 we give a theoretical explanation to the experimental phenomenon and put forward a simple formula for practical correct use in the nondestructive surveys of structural concrete. We conclude our discussion in Sec.4.

## II. SCHEME OF EXPERIMENT AND PREPARATION OF THE SPECIMEN

The primary purpose of the experiment is through GPR to measure the permittivity of the lining in tunnels. For nonferromagnetic materials, the permeability approaches to unit i.e.  $\mu_r \approx 1$ , so the index of refraction  $n$  reduces to  $n = \sqrt{\epsilon_r \mu_r} \approx \sqrt{\epsilon_r}$ , where  $\epsilon_r$  is the (relative) permittivity of the material. Thus we have:

$$\epsilon_r = n^2 = \left(\frac{c}{v}\right)^2 = \left(\frac{ct}{2l}\right)^2 \quad (1)$$

here  $c$  is the propagating speed of the radio wave in vacuum, and  $v$  is the propagating speed in medium. The  $t$  represents the time during which the radio wave goes a forth-and-return route,  $l$  is the depth of the lining. Thus, based on this formula, our experiment is conducted as follows: we record the time of double route with the GPR and measure the depth of lining, then, finally get the permittivity of the lining.

First, we prepare a designed specimen to mimic the tunnel lining structure. The strength of the specimen is C25 and the mix proportion of water/cement/sand/broken stone is 195:465:550:1170. The diameter of the broken stone is about 20.0mm. The

side and bottom of the specimen are wrapped with resin so that the water can only evaporate through the top surface, which is very close to the practical situation where a large area concrete is present. In the specimen, we also bury in advance six round steel bars of 16mm in diameter to locate the different depth of the concrete by reflection of electromagnetic wave from these steel bars. The specimen is shown in Fig. 1. and its size in Fig. 2.



**FIG. 1. Picture of the specimen.**

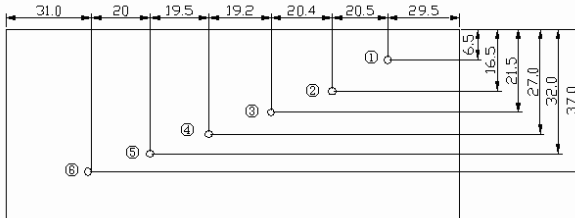


**FIG. 2. Sectional drawing of the specimen (the unit is centimeter).**

In the experiment, from corrugated shape pattern of radar’s single channel we read the double-route time. Then we measure the actual distance which represents the depth of the specimen. By the speed formula  $v = 2l/t$ , we could obtain the speeds of the radar waves. Since there are six steel bars, we can get six wave speeds which are designated by  $v_1, v_2, v_3, v_4, v_5$  and  $v_6$ . We also set the time of measurement into groups of 10 to 40 days to check the ageing properties of the testing concrete.

The experimental results are shown with figures. The Fig. 3 is the graph of the radar speed versus concrete age, and Fig. 4 is the graph of the radar speed versus the depth of the specimen.

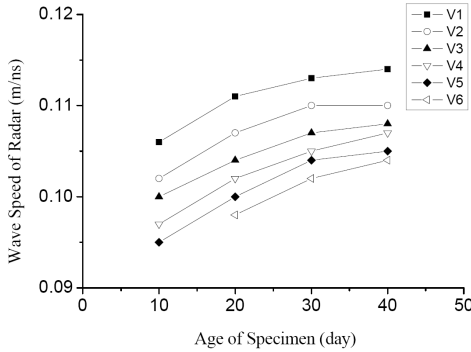


**FIG. 3. The graph of the radar speed versus concrete age specimen.**

From Fig. 3 we can see that the speed of the radar wave is connected with the age. The measured wave speeds  $v_1 \sim v_6$  are all increased with the age. The wave speeds within age of 10~20 days are increased more appreciably than the wave speeds within age of 30~40 days. Especially for age over 40 days, the wave speeds will change very little and tend to stable values. This is because the amount of water contained in the specimen eventually becomes less due to the evaporation. This result is consistent with the related studies [Zhou2006].

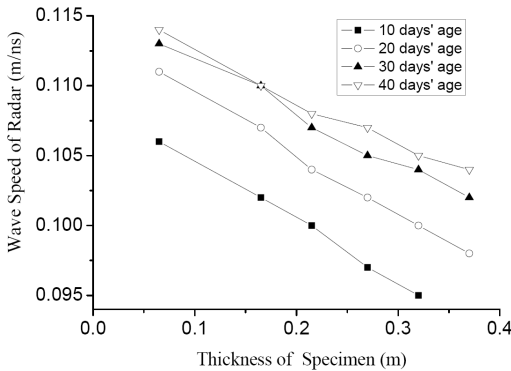


**FIG. 4. The graph of the radar speed versus the depth of the specimen.**

In addition, from this figure we see that even in the same age the wave speeds are

different for different depths. This feature can be seen more clearly in Fig. 4: the radar wave speed decreases for deeper depth. The speed-depth relation is almost linear. This is an abnormal result: because for certain material the permittivity should be a constant! Although there are some variations for mixtures, there is certainly not any linear relation between the speed and depth. To our knowledge few reports have been found on this problem. But it is a problem for accurate nondestructive detection in real engineering projects and deserves a further investigation.

In fact, this abnormal phenomenon can be settled down by considering the existence of water in the specimen. Not only can the amount of water contained in the concrete affect the wave speed, but also the water distribution in the concrete can cause the change in speed. This is the subject of the next section.

### III. THE THEORETICAL EXPLANATION OF THE EXPERIMENTAL RESULTS

Let us check the relationship between the permittivity of the concrete and the depth of the specimen. We note that the propagating speed of the radar wave is determined by the permittivity of the medium. Therefore, the change of speed of the radar wave with the depth of the concrete can be expressed with the change of the permittivity with the depth. Substituting data obtained from the experiment into the wave speed formula, we can get the average permittivity at depth  $l$ . We can then draw the graph of the permittivity of the concrete versus the depth of the specimen shown as in Fig. 5.

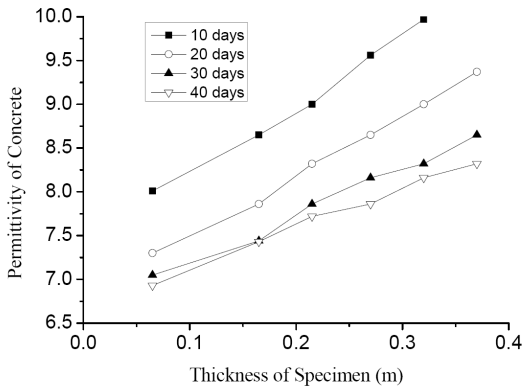


**FIG. 5. The graph of the permittivity of the concrete versus the depth of the specimen.**

It can be seen from Fig. 5 that the permittivity is getting large with the increase in

depth, taking on roughly a linear relation. The amount of water contained in the concrete will play a main role in determining the value of the permittivity, i.e. for different moisture capacity it will exhibit different permittivity. The value of the permittivity for common concrete is about 6~18, while the permittivity of water is around 80. Because of this, the permittivity of the concrete is mainly determined by the water contained in it. Furthermore, for concrete containing water, there are two factors which will lead to the change in permittivity: one is the moisture capacity; the other is the inhomogeneous distribution of water in the concrete. The effect of the first factor can be seen from our experiment where the speed of the radar wave becomes large as the age is getting older, which is a process of water loss. As for the second factor, it will also change the radar wave. In fact, the free water will take on a certain distribution along the vertical direction due to the effect of gravitation. Although such change is very small and can be totally neglected from mechanics or material's function point of view, it can be registered by the radar (the accuracy of GPR is about 0.01 ns). It is the free water distribution that accounts for the cause of the abnormal phenomenon in which the permittivity would increase as the lining gets thicker.

According to volumetric model which considers only the volume fraction of the constituents, the effective dielectric constant of the mixture is [TsuiMatthews1997]

$$\varepsilon^* = \varepsilon_h + \sum_{i=1}^N \tau_i (\varepsilon_i - \varepsilon_h) \quad (2)$$

where the subscripts  $h$  and  $i$  denote the permittivity of the host and inclusions.  $\tau_i$  is the volume fraction of the  $i$ th component. In general case,  $\tau_i$  is a constant due to the conservation of all components in the mixture. As a result, the final effective dielectric also assumes a constant as we usually used in the normal case. However, if the amount of component varies, the volume fraction  $\tau_i$  will no longer be a constant. For example, the water in the mixture undergoes evaporation. As a result, the final effective dielectric becomes a variable quantity.

We suppose that the concrete is composed of three different components, i.e. solid, water and air. Regarding the solid component as a host we can rewrite Eq.(2) as

$$\varepsilon^* = \varepsilon_h + \tau_w (\varepsilon_w - \varepsilon_h) + \tau_a (\varepsilon_a - \varepsilon_h) \quad (3)$$

where  $\tau_w$ 、 $\tau_a$  are the volume fractions of water and air respectively. Generally speaking, the volume fraction of solid component keeps unchanged, while volume fractions of water and air do change as the age time becomes longer. We write the volume fraction  $\tau_a$  as

$$\tau_a = (\tau - \tau_h) - \tau_w = C - \tau_w \quad (4)$$

where  $\tau$  is the total volume fraction, and  $\tau_h$  is the volume fraction of solid

component. Because  $\tau$  and  $\tau_h$  take on fixed values, their difference is also a constant which will be denoted as  $C$ . By eliminating the volume fraction  $\tau_a$ , the Eq.(3) becomes

$$\varepsilon^* = \varepsilon_h + C(\varepsilon_a - \varepsilon_h) + \tau_w(\varepsilon_w - \varepsilon_a) \tag{5}$$

Next, we consider  $\tau_w$  as a function of the altitude  $z$ . We assume that the free water in the gravitational field satisfies the Boltzmann distribution as air molecular does in the same field. Therefore, we can get similarly the water molecular number per volume at altitude  $z$  [Wang1965]

$$n(z) = n_0 e^{-mgz/kT} \tag{6}$$

where  $n_0$  is the density of water molecular at  $z=0$ ,  $m$  is the mass of a molecular of water,  $g$  is the gravity acceleration,  $k$  is the Boltzmann constant and  $T$  is the absolute thermodynamic temperature.

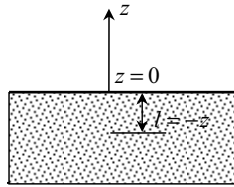


**FIG. 6. The relationship between the depth of the concrete and the coordinate  $z$  .**

According to Eq.(6), we can get the volume fraction of water at  $l = -z$  (see Fig. 6)

$$\tau_w(l) = D e^{mg|l/kT} \tag{7}$$

where  $D$  is a constant which is proportional to  $n_0$ . Substituting Eq.(7) into Eq.(5), We finally arrive at

$$\varepsilon^* = \varepsilon_h + C(\varepsilon_a - \varepsilon_h) + D e^{mg|l/kT} (\varepsilon_w - \varepsilon_a) \tag{8}$$

It can be seen from this equation that the change in effective permittivity comes from two aspects: one is from the second term  $C(\varepsilon_a - \varepsilon_h)$  (negative) in the above equation, which represents the change of effective permittivity with the increase of the age. It reflects the influence of the moisture on the effective permittivity. The other comes from the third term which reflects the influence of free water on the effective permittivity. People often consider the first factor and totally ignore the second. However, Eq.(8) makes up the deficiency and could be used to explain the abnormal phenomenon of permittivity.

At the room temperature, the term  $mg/kT$  is comparatively small, being about  $2 \times 10^{-3}$ . Besides, the thickness of concrete is about one meter. In this case, Eq.(8) can be expanded in Taylor power series. By neglecting terms of order  $(mgl/kT)^2$ ,  $(mgl/kT)^3$ , and so forth, we get

$$\epsilon^* = \epsilon_n + C(\epsilon_a - \epsilon_n) + D(\epsilon_w - \epsilon_a) + D \frac{mgl}{kT} (\epsilon_w - \epsilon_a) \quad (9)$$

Apparently, the above equation can now be used to explain our experimental results: in addition to the first three terms which are constant, there is an extra term which is linearly dependent on the depth  $l$ . This term shows the fact that the effective permittivity will increase linearly as the depth is increased.

Besides, it can be seen from the experimental results that the tendency become slow down of increasing linearly with the depth's increase when the age is getting longer. This feature illustrates the fact that the influence of free water distribution will become lessened when the amount of free water in the concrete is reduced, which means that the concrete approaches to mature state and the permittivity will eventually turn into a constant.

#### IV. CONCLUSIONS

We summarize our main results as follows:

1, Companied with the age extension, the actually measured wave speed in the concrete is increased. The increment of the wave speed is large in the early age, and eventually becomes small in the later age, which is in accordance with the supposed theory that the amount of water in concrete will play a major role in determining the speed of the radar wave traveling in it. Besides, we have also found that within the same age the wave speed will be inversely dependent on the depth of the specimen. By relation between waves and permittivity, we then obtain the permittivity of the testing concrete. The results so obtained show an abnormal feature: the permittivity is not a constant for the testing concrete, but is linearly dependent on the depth of the testing concrete, contrary to the general assumption at first sight.

2, By assuming that the abnormal feature of permittivity results from the distribution of the free water, also combining the Boltzmann distribution theory of thermodynamics, we have put forward a new volumetric model which can explain well the thickness-dependence of the permittivity. In the shallow condition, we have obtained a simple expression for the refined volumetric model which is convenient for the engineering use.

#### ACKNOWLEDGEMENTS:

We thank Prof. Jiang, Y.M. for many discussions. This work was supported by the National Science Foundation of China under the Grant No. 10674181.

## REFERENCES

- Concrete Society, (1997). "Guidance on radar testing of concrete structure." *Tech.Rep.* 48, 88.
- Soutsos, M.N. Bungey, J.H. Millard, S.G. Shaw, M.R. and Patterson, A. (2001), "Dielectric properties of concrete and their influence on radar testing." *NDT&E International*, 34(6), 419-425.
- Tsui, F. and Matthews, S.L. (1997). "Analytical modeling of the dielectric properties of concrete for subsurface radar applications." *Construction and Building Materials*, 11(3), 149-161.
- Wang, Z.X. (1965) "An introduction to statistical physics (in Chinese)." *People's Education Publisher*.
- Zhou, D.C. (2006). "Application and testing research on concrete structure performance by the ground penetrating radar." Master Thesis, *Zhengzhou University*.

## **A Review on GPR Applications in Moisture Content Determination and Pavement Condition Assessment**

Can Chen<sup>1</sup>, S.M. ASCE and Jie Zhang<sup>2</sup>, M. ASCE, Ph.D., P.E.

<sup>1</sup> Graduate Student, Department of Civil Engineering, New Mexico State University, P.O. Box 30001, MSC-3CE, Las Cruces, NM 88003-8001; can@nmsu.edu

<sup>2</sup> Assistant Professor, Department of Civil Engineering, New Mexico State University, P.O. Box 30001, MSC-3CE, Las Cruces, NM 88003-8001; jzhang@nmsu.edu

**Abstract:** In highway engineering, GPR is a nondestructive tool for measuring pavement layer thickness, moisture content of subgrade soils, and assessing other pavement conditions, such as moisture-related pavement damage. From the reflected GPR wave information, dielectric properties of the materials, which are highly dependent on soil or aggregate-water-air systems, can be estimated. An increase in dielectric constant may indicate an increase in water content of dielectric materials. However, the relationship between dielectric value and moisture content is complex and controlled by many factors. GPR studies, which consider both real and imaginary parts of dielectric value and its frequency-dependent behavior, have shown potentials for developing more robust model to predict moisture content. This paper presents an overview of GPR applications in estimating water content and assessing pavement condition. Further investigation of GPR is also discussed.

### **INTRODUCTION**

GPR is a powerful, reliable, and high performance nondestructive testing tool for solving various engineering problems related to highway applications such as determining pavement layer thickness, detecting subsurface distresses and voids, estimating moisture content of subgrade soils, rebar locations and reinforcement cover depth, etc. Identification of pavement damage due to anomalous moisture content is problematic because damages are frequently hidden in subgrade and pavement layers. Current core sampling method involves physical damages to pavement and gives only point measurement data. Furthermore, uncertainties are introduced during in-situ sampling and lab testing. Therefore, GPR as a continuous and non-destructive method for assessing pavement condition is of great importance. This paper first reviews the basic principles of GPR and describes its application in moisture content assessment. Then the development of GPR in pavement condition and damage detecting are discussed.

## BASIC PRINCIPLES OF GPR

### *Dielectric Property*

Dielectrics include any non-metallic materials that cannot conduct electricity efficiently, such as soils, concrete and water. Relative dielectric permittivity characterizes the response of a dielectric to a traveling electromagnetic (EM) wave. As shown in Eq. (1), it is a complex number,  $\epsilon$  with the real part being called dielectric constant,  $\epsilon'$ , and the imaginary part,  $\epsilon''$ , being called dielectric loss.

$$\epsilon = \epsilon' - j\epsilon'' \quad (1)$$

Since dielectric constant is frequency-dependent, GPR measurement is also frequency-dependent. However, at low frequencies ( $f \leq 1\text{GHz}$ ) it is possible to assume that the dielectric loss is low and dielectric constant is almost equal to the relative dielectric permittivity. Since the dielectric constant of water below 1GHz is about 81, comparing to soils, asphalt, and concrete materials with dielectric constant around 3 to 8 as well as air with dielectric constant of 1, dielectric constant measurement can successfully assess water intrusion and air voids in construction materials. GPR is one of the equipment using dielectric contrast between different materials to investigate the internal material conditions. The larger the dielectric constant contrast, the higher the amplitude of the reflection would be shown on GPR waveform. In addition, reflections from a low dielectric constant material beneath a high dielectric constant one would result in a negative peak in the waveform. Correspondingly, a positive peak in the waveform indicates a material with high dielectric constant.

### *GPR Resolution and Penetration Depth*

The resolution of GPR depends on the frequency bandwidth of the antenna and the polarization of EM waves. Antenna with higher frequencies would produce a better image resolution and higher detectability to small voids but at the same time decrease the EM wave penetration depth. In addition to frequency, penetration depth would also be influenced by water content, salt content and wave polarization. The term wave polarization refers to the trajectory of the electric field as being viewed in the direction of wave propagation. If the electric field of the wave is perpendicular to the plane of incidence, it refers to perpendicular polarization. Similarly, if the electric field is parallel to the plane of incidence, it refers to parallel polarization. It is beneficial to have different polarizations because any anomalies inside materials oriented parallel to the polarized direction of the electric field would show strong reflection and can be detected easier (Hong and Oral, 1998).

## MODELS TO ESTIMATE PAVEMENT WATER CONTENT

GPR surveys on pavement moisture content can be divided into two parts: the first considers water content in subgrade soils and unbound base, the other concerns the water content within pavement construction materials. Since time-domain reflectometry (TDR) has already been accepted as a reliable method for soil water

content measurement for many years and GPR has been conceived as the natural intermediate-scale counterpart of TDR, research findings in TDR can be used in GPR for measuring soil water. Currently, there are two methods are used in TDR to relate water content and dielectric constant. The first one focuses on establishing empirical relationships between volumetric water content and dielectric constant of soil without considering the physical justification. The most commonly used model was developed by Topp et al. (1980), which is a third-order polynomial relationship. Although Topp's model has been used with fairly good results in a wide range of soils, it is not suitable for organic soils, clays and fine-textured soils due to the distinct dielectric loss with the increase of wave frequency. For the second method in TDR measurement, the relationship between soil water content and dielectric constant is based on dielectric mixing models, in which soils are divided into three components: solid matter, air and water. The bulk dielectric constant of the solid particle-water-air system proposed by Dobson et al. (1985) can be expressed in the complex refractive index model (CRIM) with the form:

$$\epsilon'_b = \left[ \theta \epsilon'_w{}^\alpha + (1-n) \epsilon'_s{}^\alpha + (n-\theta) \epsilon'_a{}^\alpha \right]^{1/\alpha} \quad (1)$$

where  $\epsilon'_b$  is the bulk dielectric constant of soil,  $\theta$  is the volumetric water content,  $n$  is the soil porosity,  $\epsilon'_a$ ,  $\epsilon'_s$  and  $\epsilon'_w$  are the dielectric constants of air, solid, and water components, respectively. Roth et al. (1990) later found that in Eq. (2)  $\alpha = 0.5$  can best describe the relationship between soil water content and dielectric constant. Further research on dielectric mixing model for soil water content measurement can be found in Friedman (1998), Klemunes (1998), and Huisman et al. (2003).

GPR and TDR water content measurement for pavement materials have been applied in pavement cement-treated base (Chen et al. 2006, Staab et al. 2004), concrete slabs (van Beek et al. 1999, Laurens et al. 2003) and HMA surface course (Liu 2007). However, no quantitative or conclusive results relating the water content and EM wave changes have been reported in cement-treated base. Similar to soils, concrete materials can be treated as three-phase materials and the CRIM model was proved to be successful in concrete water content prediction (Laurens et al. 2003). For HMA materials, by applying Topp model Liu (2007) found that a 2-5% change in wave velocity through HMA materials implies a moisture content change of 0.8-1.4% which corresponds to a saturation change of 10-20% in HMA.

## PAVEMENT CONDITION ASSESSMENT

### *Pavement Thickness Evaluation*

The principles of using GPR reflections to compute the pavement layer thickness was given in Maser and Scullion (1992). EM waves would reflect at pavement layer interfaces due to the variation of dielectric constant in different layer materials. Therefore, pavement thickness can be measured by the time difference between layer reflections and the radar wave velocity in each layer. The time difference can be directly obtained from the waveform and the wave velocity is related to the dielectric constant through:

$$v = c / \sqrt{\epsilon'} \quad (3)$$

where  $v$  is the velocity of the wave propagating in materials and  $c$  is the velocity of light in free space.

Studies of GPR application in determining both flexible and rigid pavement thickness have been carried out (Maser and Scullion 1992, Saarenketo and Scullion 1994, Amara 2001, Al-Qadi, et al. 2004, Willett et al. 2006). Based on evaluation of over 150 pavement sections, Maser and Scullion (1992) pointed out that using GPR yields accuracies around  $\pm 5\%$  for asphalt layer thickness and  $\pm 9\%$  for base thickness. Later, Al-Qadi et al. (2006) proposed an algorithm which requires a two air-coupled antennae system in order to improve measurement accuracy. However, cautions must be paid in GPR applications in rigid pavements as the concrete thickness determination by GPR was proved to be much less accurate compared to asphalt pavements. Willett et al. (2001) reported a  $\pm 14\%$  to  $42\%$  error in rigid pavement thickness measurement. The reasons are (1) concrete has a much greater electromagnetic attenuation than asphalt due to its moisture content and dissolved salts; (2) concrete has similar dielectric constant as granular base material so that it is not easy to obtain a detectable reflection from concrete/base interface; (3) EM waves cannot penetrate through steel reinforcement (Scullion et al. 1994).

### ***Pavement Defects Evaluation***

Pavement damage is usually associated with the changes of voids in pavement materials. However, such void changes cannot be predicted due to the lack of historical records and the presence of overlays.

For asphalt pavement, GPR is widely used in detecting void changes caused stripping and rutting (Rmell and Scullion 1997, Morey 1998). However, most researches are experience-based. The experience of the Texas Transportation Institute indicated that intermittent negative peaks between the first peak (air-surface) and second peak (surface-base) in asphalt pavements can indicate the occurrence of stripping (Rmell and Scullion 1997). However, Saarenketo and Scullion (2000) pointed out that similar peaks can also be received from an internal asphalt layer with different electrical properties. Thus drill cores and FWD data should always be used to confirm the GPR interpretation. Similar to stripping detection, Chen et al. (2003, 2006) showed that GPR can supply some clues in determining the rutting layer by measuring layer thickness and relative moisture content in pavements with other parameters obtained by FWD, seismic, cone penetrometer as well as other methods. However, the requirements for precise measurement and interpretation are still the major problem associated with this application.

For rigid pavement, void changes are mainly due to faulting, pumping and delamination cracking. Alongi (1992) divided the delamination cracking into dry and wet conditions and indicated that in dry conditions cracking can be detected from the air gap size and in wet conditions it can be determined by signal attenuation. In dry conditions, Maser (1996) indicated that such delamination cracking (always around 2-3mm) had little influence on GPR waveform. Scullion (1994) further concluded that only voids bigger than 15mm can be detected. Thus, GPR detectability decreases

with decreasing void size. In wet conditions, rebar steel corrosion is the dominant cause for delamination cracking, which can cause an increase in water conductivity and a significant attenuation in EM waves. The relationship between wave attenuation and water conductivity was studied by Algongi (1992) and Daniels (2004).

In composite pavements, Maser (2002) used GPR for reflective cracking detection. He concluded that if obvious negative or positive peaks were shown on the waveform around the asphalt/concrete interface, it would indicate the occurrence of reflective cracking with high air voids or high water content. However, no follow-up field study was reported.

### ***Location and Orientation of Steel in Rigid Pavements***

The location, orientation and cover depth of reinforcing steel have a great influence on rigid pavement conditions. The principle of GPR in locating reinforcement is the fact that steel is highly conductive and will reflect almost all the incident energy. In addition, the polarization of the electromagnetic field must be considered. In order to obtain distinctive image of the reinforcement on the waveforms, parallel polarization should be chosen (Hong and Oral 1998). Based on experiments, Maierhofer (2003) found that for both polarizations, the horizontal position as well as the varying depth of each dowel can be determined very clearly from the waveform. However, to detect structures behind reinforcement, Maierhofer (2003) indicated that the relative polarization which can suppress reflections from rebars should be selected. In addition, Pérez-Gracia et al. (2007) indicated that the migration post-processing technique can greatly enhance the discrimination of rebars in concrete. When several reinforcement grids are placed inside concrete slab, Bungey et al. (1994) concluded that steel bars of any size can be detected when they are spaced at 200 mm or more but for closer spacing, cover depth will be the primary factor for detecting rebars.

## **CONCLUSIONS**

This paper provides a review on GPR applications in evaluating moisture content and assessing related pavement conditions. It shows that GPR can serve as a useful diagnostic tool to identify pavement condition. However its limitations are also obvious. It is not suitable for rigid pavement thickness measurement, and for materials containing more salt and clayey soils. In addition, current GPR measurements are still experience and qualitative based, further development in GPR technique and application is needed.

## **REFERENCES**

- Algongi, A.J., Clemena, G.G., and Cady, P.D. (1992). "Condition evaluation of concrete bridges relative to reinforcement corrosion." SHRP-S-325.
- Al-Qadi, I.L., Jiang, K., and Lahouar, S. (2006). "Analysis tool for determining flexible pavement layer thickness at highway speed". 85th Annual Meeting of Transportation Research Board.
- Amara, L., Al-Qadi, I. L. and Samer, L. (2003). "Optimization of ground-penetrating radar data to predict layer thickness in flexible pavements." *Journal of Transportation Engineering*, 129(1), pp. 93-99.
- Bungey, J. H., Millard, S. G., and Shaw, M. R. (1994), "The influence of reinforcing steel on radar surveys of concrete structures." *Construction and building materials*, 8(2), pp. 119-126.

- Chen, D. H., Bilyeu, J., Scullion, T., and Zhou, F. (2003) "Forensic evaluation of premature failure of Texas specific pavement study--1 sections." *J. of Perf. Cons. Fac.*, ASCE, 17(2), pp. 67-73.
- Chen, D. H., Bilyeu, J., Scullion, T., Nazarian, S. and Chiu, C., (2006) "Failure investigation of a foamed-asphalt highway project." *J. of Infra. Sys.*, ASCE, 12(1), pp. 33-40.
- Chen, R. P., Chen, Y. M., Wang, J. X. and Drnevich, V. P. (2006). "Application of TDR on LKD and Cement-treated soil." *Proc. TDR 2006*.
- Daniels, D. J. (2004). "Ground penetrating radar, 2nd edition." Institution of Electrical Engineers, London.
- Dobson, M. C., Ulaby, F. T., Hallikainen, M. T. and El-Rayes, M. A. (1985). "Microwave dielectric behavior of wet soil, Dielectric mixing models." *IEEE Trans. Geosci. Remote Sens.*, GE-23(1), pp. 35-46.
- Friedman, S. P. (1998). "A saturation degree-dependent composite spheres model for describing the effective dielectric constant of unsaturated porous media." *Water Resour. Res.*, 34, pp. 2949-2961.
- Hong, C.R. and Oral, B. (1998). "Electromagnetic properties of concrete at microwave frequency range." *ACI Materials Journal*, 95(3), pp. 262-271.
- Huisman, J. A., Hubbard, S. S., Redman, J. D. and Annan, A. P. (2003). "Measuring soil water content with ground penetrating radar: a review." *Vadose Zone J.*, 2, pp. 476-491.
- Klemunes, J. K. (1998). "Determining soil volumetric content using time domain reflectometry." Federal Highway Administration, McLean, VA.
- Laurens, S., Balayssac, J. P., Rhazi, J., Klysz, G., and Arliguie, G. (2003). "Non destructive evaluation of concrete moisture by GPR technique: experimental study and direct modeling." *International Symposium (NDT-CE)*.
- Liu, L.B. (2007) "GPR for fast pavement assessment." Report No. JHR 07-310.
- Maierhofer, C. (2003). "Nondestructive evaluation of concrete infrastructure with ground penetrating radar." *J. of Mat. In Civil Engrg.*, ASCE, 15(3), pp. 287-297.
- Maser, K. R. and Scullion, T. (1992). "Influence of asphalt layering and surface treatments on asphalt and base layer thickness computations using radar." Texas DOTPD Rep. TX-92-1923-1, Texas.
- Maser, K. R. (1996) "Condition assessment of transportation Infrastructure using ground-penetrating radar." *Journal of Infrastructure Systems*, 2(2), pp. 94-101.
- Maser, K. R. (2002). "Use of ground-penetrating radar data for rehabilitation of composite pavements on high-volume roads." *Transportation Research Record*, 1568, pp.122-126.
- Morey, R. (1998). "Ground penetrating radar for evaluating subsurface conditions for transportation facilities." NCHRP Synthesis of Highway Practice 255, TRB.
- Pérez-Gracia, V. et al. (2007). "Experimental analysis of the resolution in shallow GPR survey." *Proc. of the SPIE*, 6749, pp. 67492M.
- Roth, K., Schulin, R., Fluhler, H. and Attinger, W. (1990). "Calibration of time domain reflectometry for water content measurements using composite dielectric approach." *Water Resour. Res.*, 26 (10), 2267-2273.
- Rmell, E. and Scullion, T. (1997). "Detecting stripping in asphalt concrete layers using ground penetrating radar." *Transportation Research Record*, 1568, pp.165-174.
- Saarenketo, T. (1998). "Electrical properties of water in clay and silty soils." *Journal of Applied Geophysics*, 40, pp. 73-88.
- Saarenketo, T. and Scullion, T. (1994). "Ground penetrating radar applications on roads and highways." Res. Rep. 1923-2F, Texas Transp. Inst., College Station, Texas.
- Saarenketo, T. and Scullion, T. (2000). "Road evaluation with ground penetrating radar." *Journal of Applied Geophysics*, 43, pp. 119-138.
- Staab, D.A., Tuncer B. E. and Alumbaugh, D. A. (2004). "Non-destructive evaluation of cement-mixed soil." *Geosupport 2004, Proc. of Sessions of the GeoSup*, pp. 838-849.
- Topp, G. C., Davis, J. L. and Annan, A. P. (1980). "Electromagnetic determination of soil water content: measurements in coaxial transmission lines." *Water Resour. Res.*, 16(3), pp. 574-582.
- Saarenketo, T. and Scullion, T. (1994). "Ground penetrating radar applications on roads and highways." Research Rep. 1923-2F, Texas Transportation Institute, College Station, Texas.
- van Beek, A., van Breugel, K. and Hilhorst, M. A. (1999). "Monitoring system for hardening concrete based on dielectric properties." *Utilizing ready-mixed concrete and mortar*, pp. 303 - 312.
- Willett, D.A., Mahboub, K.C., and Rister, B. (2001). "Accuracy of ground-penetrating radar for pavement-layer thickness analysis." *J. Trans. Engrg.*, ASCE, 132(1), pp. 96-103.

## Non-Destructive Impedance Spectroscopy Measurement for Soil Characteristics

Sarah E. Pluta<sup>1</sup> and John W. Hewitt<sup>2</sup>

<sup>1</sup>Project Engineer, TransTech Systems, Inc., 1594 State Street, Schenectady, NY 12304;  
spluta@transtechsys.com

<sup>2</sup>Project Manager, TransTech Systems, Inc., 1594 State Street, Schenectady, NY 12304;  
jhewitt@transtechsys.com

**ABSTRACT:** A non-nuclear, non-invasive instrument capable of measuring density and moisture content of soil using electromagnetic impedance spectroscopy (EIS) is currently being developed. During the development of the empirical soil model, it was found that the model was sensitive to the specific surface area of the material being measured. With the material's specific surface area being accounted for, in six test compactions a 119% increase in accuracy was seen by the soil density gauge's (SDG) wet density calculation when compared to the Nuclear Density Gauge's wet density calculation.

### INTRODUCTION

Because of the growing effort to develop a non-nuclear alternative to the Nuclear Density Gauge (NDG), the investigators are currently working on the development of a non-nuclear, non-invasive instrument capable of measuring density and moisture content of soil during road and other civil infrastructure construction using electromagnetic impedance spectroscopy (EIS). Using EIS and a parametric approach, an empirical model was developed to calculate wet density and moisture of soil, specifically, a run-of-cruiser poorly-graded gravel with silt and sand (ASTM USCS classification GP-GM), during a Department of Homeland Security (DHS) contract. The empirical model was then tested on four controlled gradations within the ASTM USCS classifications of 1) well-graded gravel with sand (GW), 2) well-graded sand (SW), 3) well-graded gravel with silt and sand (GW-GM), and 4) sandy silt (ML). The test compactions were completed with controlled moisture levels within a 36-inch by 36-inch by 15-inch wooden frame using an electric vibrator plate compactor, VIBCO/Heinrich Plate compactor Model TP-1830, which had an 18-inch by 18-inch plate area. Holding the moisture constant in four of the test samples and varying the gradation allowed for the investigation of the effect of changing gradations on the EIS frequency response, without the added complication of moisture influences. Next, moisture was varied to allow for a secondary test to be completed on the effect of gradation on the calculation of moisture.

A practical, real-world, real-time model to transform the impedance data into soil density and moisture does not exist for the sensor setup currently being using, i.e., a surface, non-invasive, concentric ring setup, shown in Figure 1. Therefore, experimental data was collected for the development of an empirical soil model to be used in the SDG via a parametric approach. The SDG's sensor operates by the transmission of a constant voltage from the center electrode to the receiving electrode, passing through the material under test (MUT) and utilizing 86 frequencies between 300kHz and 40MHz.

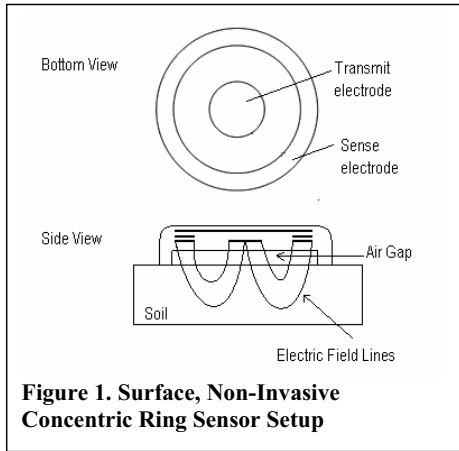


**Figure 1. Surface, Non-Invasive Concentric Ring Sensor Setup**

## TECHNOLOGY BACKGROUND

EIS is the measurement of a material's dielectric properties (permittivity) based on the interaction of an external field with the electric dipole moment of the MUT, over a known frequency range. Typically, soil is a mixture of stone, water and air. Since the water molecule has a permanent dipole, its dielectric constant (approximately 80) is higher than that of dry soil, which is only polarizable by atomic and electronic polarization. Therefore, dry soil has a low dielectric constant (approximately 5). The dielectric constant of the soil matrix is not constant, but varies with frequency and 'depends on physical parameters such as soil texture, soil water content and type and concentration of ions in the soil solution' [1]. For these reasons, the investigators used both the real and imaginary parts of the measured permittivity. To take advantage of the fact that the permittivity of soil is dominated by the soil water content at low frequencies, an EIS measurement is taken from 300kHz to 40MHz.

The development of models to measure soil properties, like moisture and density, has been investigated and summarized by several researchers [1,5,6,7]. The use of dispersions seen in soil to develop these models is common. One such dispersion, commonly called the Maxwell-Wagner dispersion, is caused by the applied electric field on the bonds between the water and soil particles, which have different dielectric values [1,5,7]. Within the SDG's measurement frequency range, the investigators are able to make use of this information and the empirically derived soil dielectric mixing equation [1,8] to aid in the development of the empirical soil model. The investigators used second order parametric curve fitting and regression analysis on the frequency data to develop the empirical soil model. A second order curve was fitted to the frequency spectra (i.e.,  $y = Ax^2 + Bx + C$ ). Then, by completing a regression analysis on the second order fitted coefficients/parameters (i.e.,  $A$ ,  $B$  and  $C$ ), a pattern was identified that was related to wet density and moisture content. Another benefit of using the curve fitting approach was the reduction in noise

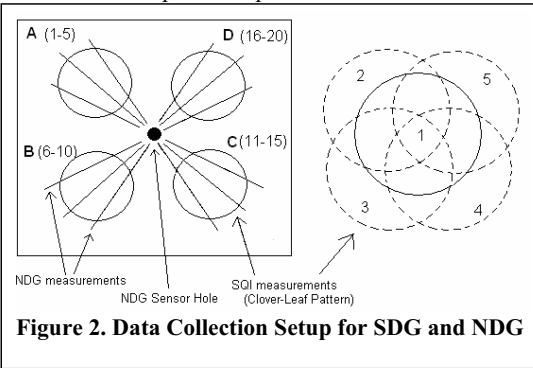
associated with the surface measurements and single point analysis. Using the spectra enabled the extraction of physical meaning from the fitted coefficients, thereby allowing the investigators to draw conclusions about the soil compaction data and enabling the development of an empirical linear inversion model for wet density and moisture. The empirical inversion model for the current sensor setup is proprietary information.

## EXPERIMENTAL SETUP

Starting with a run-of-crusher GP-GM soil, the material was broken down for the gradation testing into twelve sieve sizes and reassembled into three predetermined gradation mixtures, GW, SW and GW-GM. The fourth gradation, ML, a sandy silt, was used as is from a quarry in New York State. Below, Tables 1 and 2, are the gradation breakdowns in terms of percent gravel, percent sand and percent fines as defined by ASTM D 2487 specification and Proctor test results as defined by ASTM D 698, respectively.

After each soil was assembled, GW, SW, GW-GM(1), GW-GM(2), and ML, de-ionized water was added to moisturize the soil to 7.09%, 7.14%, 7.30%, 5.61% and 8.25%, respectively. The GP-GM soil had a test moisture level of 7.12%. After the water was added, the soil was thoroughly mixed and allowed to sit covered overnight before testing began. The moisture levels were determined by pulling samples at the beginning and end of each compaction, as defined by ASTM D 2216.

The compaction of each material was completed in the wooden frame, using the VIBCO electric plate compactor. Data was collected with four SDGs and a NDG, a



CPN MC3 Portaprobe with a 12-inch rod and with a current factory calibration, following the pattern shown in Figure 2, after one, two, four and eight compactor passes. In Figure 2, the four circles, labeled A, B, C and D, represent the centers of the SDG measurements and the three lines over the SDG circles represent the

placement of the NDG for its three measurements. The SDG's measurement pattern is shown to the right as a clover-leaf pattern of five.

**Table 1. Tested Soil Gradation Summary**

	GP-GM*	GW	SW	GW-GM(1)	GW-GM(2)	ML
<b>% Gravel</b>	48.21	65.04	10.03	53.63	40.77	2.90
<b>% Sand</b>	41.35	29.93	82.14	36.05	49.82	32.70
<b>% Fine</b>	10.44	5.03	7.83	10.32	9.41	64.40

**Table 2. Tested Soil Proctor Information**

	GP-GM*	GW	SW	GW-GM (1)	GW-GM (2)	ML
<b>Proctor Peak (lb/ft<sup>3</sup>)</b>	137.27	136.65	135.22	141.5	141.5	125.02
<b>Proctor Optimum Moisture (%)</b>	8.50	9.50	8.13	7.63	7.63	10.13

\* GP-GM soil was the material used for the break down and reassembly process.

## EXPERIMENTAL RESULTS

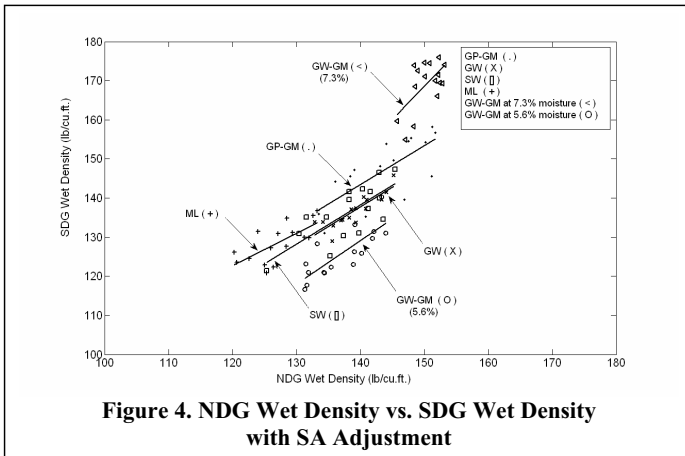
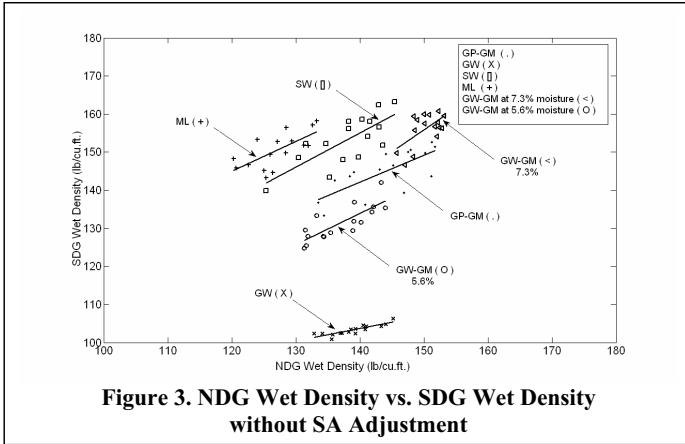
Since the EIS response of soil using the SDG sensor could not be estimated in advance, several controlled compactions were completed, varying the moisture level, density level and gradation separately. Then, working with the soil responses of the collected compaction data, the form of the soil response was estimated with a second order equation. The equation's parameters that best fit the data were identified. Afterwards, the parameters were further interpreted such that statistically significant patterns were revealed expressing the soil's density and moisture properties. Using the identified patterns, a system model was developed to calculate the soil's wet density and moisture content. Applying this model to the gradation data, Figure 3, it can be seen that changing the soil type alters the response from the original model such that the original model for one soil type is not robust enough for all soil types in terms of wet density. In order to make the original model more robust, thus enabling use on handling several soil types, adjustment were made.

### Model Enhancement

It was found that by using the MUT's specific surface area (SA), linear adjustments could be made to the soil model's calculation of wet density and moisture. Bulk SA adjustments were developed using the SA of idealized particles found in soil for gravel, sand and silt [2]. Other researchers have also found that their models are sensitive to the MUT's SA [3, 4]. Figure 4 shows the re-calculated wet density results using the model adjustments made by the MUT's SA. Table 3 shows the slopes of the wet density calculations without and with the SA adjustment. In five of the six tested materials, when the SA adjustment was applied, the slope of the SDG wet density calculation became closer to one. In addition, the average wet density error between the NDG and the SDG was reduced by 119% when the SA adjustments were applied to the model.

**Table 3. SDG Slope without and with SA Adjustments**

Material	Slope <b>without</b> SA Adjustment	Slope <b>with</b> SA Adjustment
GPGM	0.7059	0.9945
GW	0.3274	1.004
SW	0.8971	1.003
GWGM (7.30% M)	1.15	1.702
GWGM (5.61% M)	0.8173	1.113
ML	0.7812	0.8256



**CONCLUSIONS**

The investigators’ testing and research demonstrated that soil gradation does affect the frequency response of the SDG/EIS instrument. Therefore, soil gradation affects the instrument’s calculation of wet density. By using the gradation information of the tested materials, an adjustment was developed and applied to the empirical algorithm such that a variable was added to modify the slope and offset of the algorithm due to the soil’s gradation, or more specifically, the specific surface area of the MUT. Currently the user enters the gradation of the MUT and the SDG instrument calculates the MUT’s SA and adjusts the empirical inversion model accordingly. The specifics of the SA adjustment are proprietary information. The same method of SA

adjustment is currently being applied to the measurement of moisture in soil. Initial results with the SA adjustment are encouraging and will be reported on at a later date. The SA of clay materials is significantly greater than that of the gravel, sand and fine materials that are typically used in road base and similar construction areas. As the empirical model continues to evolve, the use of the SDG on clay material will be possible.

Future applications of this technology include use as a quality control tool for concrete maturity, Cold in Place Recycled (CIPR) and Warm Mix Asphalt (WMA) road construction projects. This is made possible because of its ability to accurately measure the moisture content of these materials.

### ACKNOWLEDGMENTS

The authors appreciate the support and funding from the Department of Homeland Security (DHS), the New York State Energy Research and Development Authority (NYSERDA), Keyspan (now National Grid) and TransTech Systems, Inc.

### REFERENCES

- [1] Hilhorst, Max, A. (1998). "Dielectric Characterization of Soil". Thesis. ISBN 90-5406-162-6 of the DLO Institute of Agricultural and Environmental Engineering. Wageningen, the Netherlands.
- [2] Jury, William A. and Horton, Robert (2004). Soil Physics. Sixth Edition. John Wiley & Sons, Inc., Hoboken, New Jersey, 2004.
- [3] Or, Dani and Wraith, Jon M. (1999). "Temperature effects on soil bulk dielectric permittivity measured by time domain reflectometry: A physical model." *Water Resources Research*, Vol. 35 (2): 371-384.
- [4] Peterson, L.W., Moldrup, P., Jacobsen, O.H., and Rolston, D.E. (1996). "Relations between specific surface area and soil physical and chemical properties." *Soil Science*, Vol. 161 (1): 9-21.
- [5] Rinaldi, V.A. and Francisca, F.M. (1999). "Impedance Analysis of Soil Dielectric Dispersion (1MHz – 1GHz)." *Journal of Geotechnical and Geoenvironmental Engineering*, Vol. 125 (2): 111-121.
- [6] Hamed, Yasser, Persson, Magnus and Berndtsson, Ronny. (2003). "Soil Solution Electrical Conductivity Measurements Using Different Dielectric Techniques." *Soil Science Society of America Journal*, Vol 67: 1070-1078.
- [7] Hilhorst, M.A., Kirkson, C., Kampers, F.W.H., and Feddes, R.A. (2000). "New Dielectric Mixture Equations for Porous Materials Based on Depolarization Factors." *Soil Science Society of America Journal*, Vol. 64: 1581-1587.
- [8] Topp, G.C., Davis, J.L. and Annan, A.P. (1980). "Electromagnetic Determination of Soil Water Content." *Water Resources Research*, Vol. 16(3): 574-582.

## ULTRASONIC PULSE VELOCITY TESTS ON COMPACTED SOIL

David M. Weidinger<sup>1</sup>, Louis Ge<sup>2</sup>, and Richard W. Stephenson<sup>3</sup>

<sup>1</sup>Staff Geotechnical Engineer, Vector Engineering Inc., 143E Spring Hill Drive, Grass Valley, CA 95945, USA; PH: +1 530-272-2448 ext. 185; FAX: +1 530-272-8533; E-mail: weidinger@vectoreng.com

<sup>2</sup>Missouri University of Science and Technology, Department of Civil, Architectural, and Environmental Engineering, 1401 N Pine Street, Rolla, MO 65409, USA; PH: +1 573-341-7193; FAX: +1 573-341-4729; E-mail: geyun@mst.edu

<sup>3</sup>Missouri University of Science and Technology, Department of Civil, Architectural, and Environmental Engineering, 1401 N Pine Street, Rolla, MO 65409, USA; PH: +1 573-341-6549; FAX: +1 573-341-4729; E-mail: stephens@mst.edu

**ABSTRACT:** In this paper, results of a series of ultrasonic pulse velocity tests on compacted soil were presented and discussed. Ultrasonic pulse velocity tests provide compression and shear wave velocity information that can be used in calculating dynamic elastic moduli such as Young's modulus and shear modulus. From the test results, calculated Poisson's ratio shows a linear relation with the water content in compacted soil, which leads to a linear trend in both P and S wave velocity against water content. Furthermore, presenting plots in bulk density versus wave velocity gives a clearer trend than dry density versus wave velocity.

### INTRODUCTION

Ultrasonic pulse velocity testing is a type of pulse transmission test that propagates high frequency sound waves ranging in frequency from 20 kHz to 1 GHz through a soil specimen to produce strains on the order of  $10^{-4}\%$  (Leong et al., 2004). Ultrasonic pulse velocity testing is a nondestructive testing technique that can be used to determine the dynamic properties of materials capable of transmitting waves. Elastic bodies can transmit three different types of waves: longitudinal or compression waves also known as primary waves (P-waves), shear or transverse waves also known as secondary waves (S-waves), and Rayleigh waves. Rayleigh waves are surface waves that travel on the outside surface (free surface) of a medium. Compression waves move in the same direction as the direction of particle displacement. Shear waves move orthogonal to the direction of particle displacement, and are typically about half the speed of compression and Rayleigh waves. The velocities at which the P-waves and S-waves travel through a specimen are a function of the dry density and elastic constants of the specimen. By measuring the velocity of

the P and S waves through a soil sample, the shear modulus (G), Young's modulus (E), and Poisson's ratio ( $\nu$ ) can be determined for the strain level of  $10^{-4}$  %.

### ULTRASONIC PULSE VELOCITY TESTS

The material used in this study was selected based upon its availability, past experience, and its typical textbook silt-like properties. The soil is a modified loessial, low plastic silt that comes from the Mississippi River Valley near Collinsville, Illinois. The silt has a liquid limit of about 30, a plastic limit close to 24, and natural clay content of 17.0% or so. The material is classified by the Unified Soil Classification System as an ML soil (Izadi, 2006).

The soil was first mechanically pulverized then passed through a #40 sieve (425 mm). The soil was moistened to a predetermined moisture content then allowed to cure for 24 hours. It was then compacted into a 152 mm (6-inch) split proctor mold in three equal height lifts under standard proctor compaction energy (ASTM Standard D 698). An automated compaction device was used for a tighter control on the compaction effort. The soil has a standard proctor optimum moisture content of 15% and a maximum dry density of  $17.1 \text{ kN/m}^3$ . After compaction, the soil was gently extruded from the split mold, wrapped in plastic wrap, placed inside a sealed bag, and allowed to further cure in a moist cure room. Three 152.4-mm (6-inch) diameter proctor specimens were trimmed at each moisture content, so that three independent tests could be conducted.

All pulse velocity measurements determined in this study utilized a GCTS ULT-100 Ultrasonic Velocity Test System (GCTS, 2004). The device consists of sender and receiver transducers housed in the top and bottom platens of a standard triaxial cell. The two, 70-mm diameter test platens are wired to a data acquisition and processing unit. The piezoelectric crystals are arranged for the transmission and reception of P and S-waves. Piezoelectric crystals are small ceramic elements that change shape when a voltage is applied, or produce a voltage when they change shape. These properties transform an electrical wave into a mechanical wave or vice versa. Figure 1 shows a compacted silt specimen in a triaxial cell for the pulse velocity test. The typical pulse velocity measurements are displayed in Figure 2. The determination of P-wave arrival time for the compacted silt within this study was trivial; however, not for the S-wave arrival time determination. As an example given in Figure 2, 4 possible S-wave arrival times were found. After a thorough examination and judgment, the most possible S-wave arrival time can be determined. The detailed discussion on wave arrive time determination can be found in Weidinger (2008).



Figure 1 – Test setup.

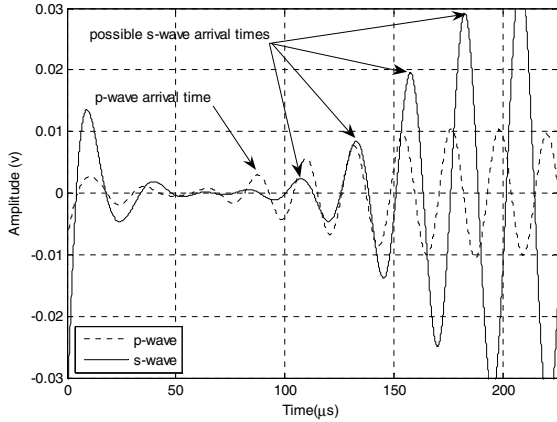


Figure 2 – Typical pulse velocity measurements.

## RESULTS AND DISCUSSION

The standard proctor compaction curve for this particular soil is shown in Figure 3. The calculated Poisson's ratio was compared to an assumed range of values. The actual Poisson's ratio of the silt is unknown, but an appropriate range can be assumed. Typically, Poisson's ratios for sands range from 0.2 for loose sands to 0.4 for dense sands. Poisson's ratios for clays range from 0.4 to 0.5 for saturated clays (Holtz and Kovacs, 1981). The soil used for these tests is a densely compacted low plastic silt with 17% clay content. This places the Poisson's ratio in the range of 0.35 to 0.40, depending on the moisture content (Figure 3).

The Poisson's ratio ranged from 0.41 in the stiff, low moisture content samples to 0.34 for the softer samples at higher moisture contents and lower dry density. The average Poisson's ratio for all tests was 0.38 with a standard deviation of 0.02 which confirmed the assumed range of the Poisson's Ratio was between 0.35 and 0.40. P-wave velocities obtained from ultrasonic pulse velocity measurements were ranging from 260 m/s to 390 m/s (Figure 4) while the S-wave velocities were ranging from 110 m/s to 180 m/s (Figure 5). The maximum shear wave velocities occurred in the soil samples prepared dry of the optimum moisture content and decreased with increasing moisture content and saturation. Finally, presenting plots in bulk density versus wave velocity gives a clearer trend than dry density versus wave velocity.

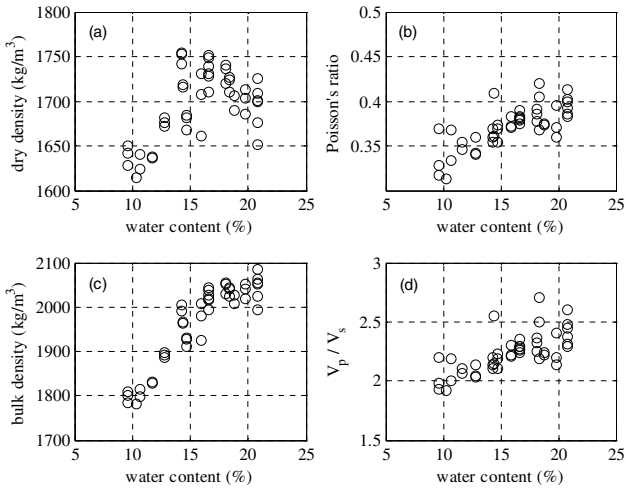


Figure 3 – Density, Poisson's ratio and wave velocity ratio versus water content.

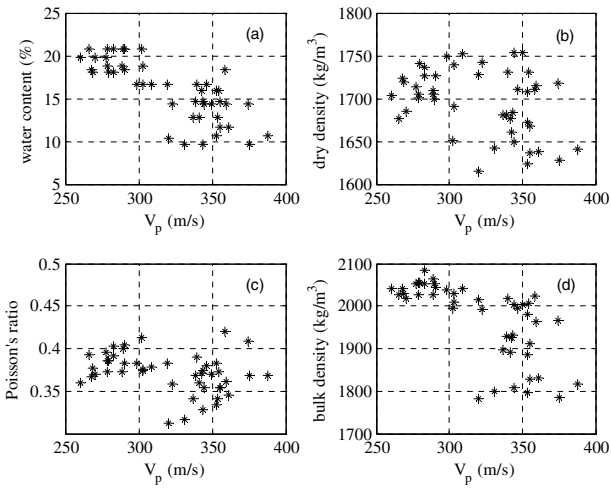


Figure 4 – P-wave velocity measurements.

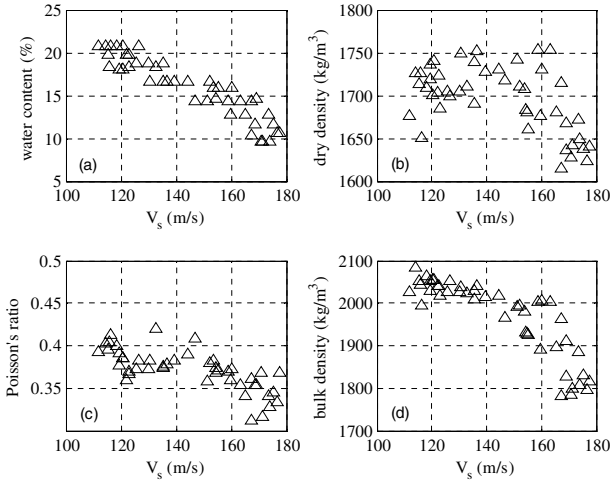


Figure 5 – S-wave velocity measurements

## CONCLUSIONS

Ultrasonic pulse velocity testing is a quick and simple, nondestructive test compared to other conventional geotechnical laboratory tests. From the test results, calculated Poisson's ratio shows a linear relation with the water content in compacted soil, which leads to a linear trend in both P and S wave velocity against water content. Furthermore, presenting plots in bulk density versus wave velocity gives a clearer trend than dry density versus wave velocity. The wave velocities associated with various soils can yield a great deal of information about a soil under dynamic loading.

## ACKNOWLEDGMENTS

The financial support for this research work was by the Senator Bond Fund in Transportation Research through the Missouri Transportation Institute, and is gratefully acknowledged. The technical support from GCTS and the guidance on signal filtering from Dr. Eng-Choon Leong at Nanyang Technology University in Singapore are also greatly appreciated.

## REFERENCES

- ASTM, Standard D698-07, "Standard test method for laboratory compaction characteristics of soil using standard effort (12,400 ft-lb/ft<sup>3</sup> (600 kN-m<sup>3</sup>)),” *Annual Book of ASTM Standards*, ASTM International, West Conshohocken, PA. 2007.

- GCTS (2004). Data Acquisition and Ultrasonic Velocity Software User's Guide.
- Holtz, R.D. and Kovacs, W.D. (1981). An Introduction to Geotechnical Engineering, Prentice-Hall, Inc., Englewood Cliffs, N.J., 733 pp.
- Izadi, A. (2006). Behavior of Undrained Monotonically Loaded Low Plasticity Silt Under Triaxial Compression. Department of Civil, Architectural, and Environmental Engineering, University of Missouri-Rolla. M.S. Thesis.
- Leong, E.-C., Yeo, S.-H., and Rahardjo, H. (2004). "Measurement of wave velocities and attenuation using an ultrasonic test system." *Canadian Geotechnical Journal*, Vol. 41, pp. 844-860.
- Weidinger, D.M. (2008) Laboratory Analysis Of Small Strain Moduli. Department of Civil, Architectural, and Environmental Engineering, Missouri University of Science and Technology. M.S. Thesis.

# Characterization of Early Stage Concrete by Ultrasonic Method

Yan Liu<sup>1</sup>, Bin Zhang<sup>2</sup>, Xinbao Yu<sup>3</sup> and Xiong (Bill) Yu<sup>4\*</sup>

<sup>1</sup> Graduate Assistant, Department of Civil Engineering, Case Western Reserve University, 10900 Euclid Avenue, Bingham 217, Cleveland, OH 44106-7201, [yx1192@case.edu](mailto:yx1192@case.edu).

<sup>2</sup> Graduate Assistant, Department of Civil Engineering, Case Western Reserve University, 10900 Euclid Avenue, Bingham 203B, Cleveland, OH 44106-7201, [xy23@case.edu](mailto:xy23@case.edu).

<sup>3</sup> Graduate Assistant, Department of Civil Engineering, Case Western Reserve University, 10900 Euclid Avenue, Bingham 203C, Cleveland, OH 44106-7201, [bxz26@case.edu](mailto:bxz26@case.edu).

<sup>4\*</sup> Assistant Professor, Department of Civil Engineering, Case Western Reserve University, 10900 Euclid Avenue, Bingham 210, Cleveland, OH 44106-7201, [xyy21@case.edu](mailto:xyy21@case.edu), Corresponding author

**ABSTRACT:** Seismic methods are useful tools to non-destructively assess the integrity of concrete. It has also been applied to characterize the behaviors of curing concrete to provide information for construction decision. This paper shows that freezing of concrete significantly affects the seismic properties of concrete. Attention needs to be paid when applying seismic method to concrete curing in cold weather. In the experimental program ultrasonic tests were conducted on curing concrete subjected to different freezing process. The results indicate while there exists linear correlation between small strain seismic wave velocity and concrete strength under normal curing conditions, such relationships do not hold if the concrete is subjected to freezing process. A correction accounting for the effects of ice on the bulk strength needs to be applied. This correction was found to have linear relationship with water content (or ice content if concrete is completely frozen). Procedures to correct the effects of freezing are proposed, which include the use of Time Domain Reflectometry to measure the water content. Finally the strength of concrete in frozen status can be estimated. This information could be incorporated to determine the magnitude of Winter Load Increase in cold regions.

## INTRODUCTION

The evaluation of mechanical properties of concrete by nondestructive techniques is gaining popularity. Several techniques are currently in use, such as impact echo, ultrasonic test, spectra analyses of surface wave. They are based on the information contained in the propagation of ultrasonic waves. Different wave modes and transeiving methods are explored. For example, Boutin<sup>1</sup> and Arnaud used the speed of longitudinal waves (L-waves, also known as compression waves) of low frequencies from measuring the time of transition between fluid and solid state of cellular cement paste. A new device for monitoring the hydration of cement mortar that measures the transit time and the energy of an L-wave pulse propagating through a mortar sample has been introduced by Reinhardt<sup>2</sup> et al. With this device the setting and hardening process of mortar can be evaluated. Other investigators have applied both, longitudinal and transverse waves (T-waves, also known as shear waves) to examine the hydration of cementitious materials. Sayers<sup>3</sup> and Grenfell found a linear relationship between the effective bulk and shear moduli determined by pulse velocities. D'Angelo<sup>4</sup> et al. detected a considerably higher sensitivity of T-waves to the hydration process compared to L-waves. Boumiz<sup>5</sup> et al. studied the development of elastic modulus, shear modulus and Poisson's ratio as functions of time and degree of hydration.

Most current studies are on concrete under normal service conditions. For cold regions, freezing can have significant effects on the technologies based on seismic waves, especially for concrete in the early stage of curing. Ohio Department of Transportation, for example,

specifies a 5-day thermal curing during winter construction. The concrete can quickly become frozen upon removing the thermal curing. This study aims to determine a NDT test framework to quantify the effects of freezing on seismic wave propagation in curing concrete.

**BACKGROUND**

**Ultrasonic Testing**

Ultrasonic Testing uses high frequency sound wave propagation to measure material and structural responses. This technology has been used for flaw detection, dimensional measurements, material characterization and etc.

A typical UT inspection system (shown in Figure 1) consists of several functional units, such as the pulser and receiver, transducer, and display devices. A pulser and receiver is an electronic device that can produce high voltage electrical pulses. Driven by the pulser, the transducer generates high frequency ultrasonic energy. The sound energy is introduced via couplant to propagate through the materials in the form of seismic waves. From the signal, information about the location, size, orientation of structural features can be obtained.

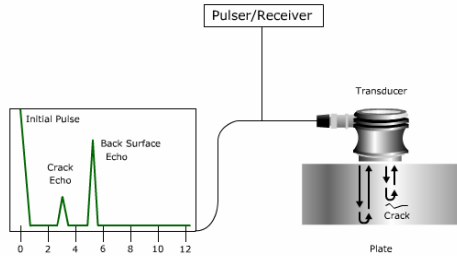


**FIG. 1. Ultrasonic testing inspection system**

In recent years, techniques based on ultrasonic wave propagation are used to assess the strength of early age concrete. Several methods that relate the ability of cementitious materials to transmit ultrasonic waves and their compressive strength gain can be found in the literature. Keating<sup>6</sup> et al investigated the relationship between ultrasonic longitudinal pulse velocity and cube strength for cement slurries in the first 24 hours. For concrete cured at room temperature, it was noted that the relative change in the pulse velocity in the first few hours is higher than the observed rate of strength gain. However, a general correlation between these two parameters could be deduced. Another study about the interdependence between the velocity of L-waves and compressive strength has been presented by Pessiki<sup>7</sup> and Carin. Within the scope of this work concrete mixtures with different water-cement ratios and aggregate contents cured at three different temperatures were examined. The L-wave velocity was determined by using the impact-echo method in a time range of up to 28 days. At early ages the L-wave velocity increases at a faster rate when compared with the compressive strength and at later ages the strength is the faster developing quantity. L-wave velocity is found to be a sensitive indicator of the changes in the compressive strength up to 3 days after mixing.

From the measured ultrasonic velocity, two different types of moduli, i.e, longitudinal and shear modulus can be calculated as follows:

$$L = \rho \cdot v_L^2 \tag{1}$$

$$G = \rho \cdot v_T^2 \tag{2}$$

where  $L$  is the longitudinal modulus,  $G$  the shear modulus and  $v_L$  and  $v_T$  the velocity of L- and T-waves respectively. The moduli  $L$  and  $G$  are related to the direction of particle motion caused by L- and T-waves. The longitudinal modulus relates strain to longitudinally applied stress. The shear modulus describes the elastic behavior of a material subjected to shear strain.

### ***Time Domain Reflectometry***

Time Domain Reflectometry (TDR) is a guided radar technology. It utilizes the propagation of electromagnetic wave to measure materials properties and structural responses. The configuration of a typical TDR system is shown in Figure 2(a), which includes a TDR device (pulse generator and sampler), a connection cable, and a measurement probe. The measurement probe generally consists of multiple conductors embedded in materials whose properties are to be measured. Figure 2(b) shows a schematic plot of typical TDR signal. Information commonly obtained on materials electrical properties include the apparent dielectric constant  $K_a$ , which are related to the speed of electromagnetic wave in the material; and the electrical conductivity  $EC_b$ , which is related to the energy attenuation. Both quantities can be easily obtained from a TDR signal. A brief introduction on determining these quantities are summarized below: the travel velocity,  $v$ , of an electromagnetic wave through media is calculated as follows:

$$v = \frac{c}{\sqrt{K_a}} \quad (3)$$

where  $c$  is the velocity of an electromagnetic wave in free space ( $2.988 \times 10^8$  m/s) and  $K_a$  is the dielectric constant (for TDR measurement in soils, this quantity is generally called apparent dielectric constant). The time for the electromagnetic wave traveling down and back along a metallic waveguide of length,  $L$ , is given by:

$$t = \frac{2L}{v} \quad (4)$$

Substituting equation (4) to (3) yields

$$K_a = \left( \frac{ct}{2L} \right)^2 \quad (5)$$

By defining  $\frac{ct}{2}$  as apparent length  $l_a$ , the apparent dielectric constant can be calculated as

$$K_a = \left( \frac{l_a}{L} \right)^2 \quad (6)$$

In the TDR signal, the apparent length is determined from analyzing the time elapse between reflections. The determination of the apparent length  $l_a$  is illustrated in Figure 2(b). The electrical conductivity of bulk soil sample can be simultaneously obtained from the final signal level (Yu and Drnevich 2004).

### ***Relationship between Dielectric Constant and Gravimetric Water Content***

Water has dielectric constant of around 81, which is much larger than that of soil solids (typically around 3 to 7) or air (around 1). A variety of relationships has been developed between TDR measured dielectric constant and volumetric water content. Siddiqui and Drnevich (1995)<sup>12</sup> developed an equation that relate the TDR measured dielectric constant to the gravimetric water content. The equation accounts for the effects of soil type and density by incorporating two calibration constants. This equation is shown below.

$$w = \frac{1}{b} \left[ \frac{\rho_w}{\rho_d} \sqrt{K_a} - a \right] \tag{7}$$

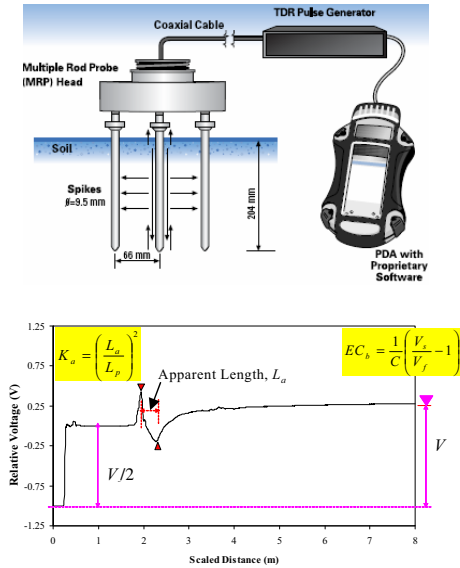


**FIG. 2. a) Schematic plot of TDR measurement system; b) Typical TDR signal and information utilized**

**EXPERIMENT DESIGN**

Experiments were designed to establish the effects of freezing on the strength of concrete. Three representative types of concrete used in Ohio DOT projects were used in the experiment. Concrete mixes were obtained from commercial suppliers THE COLLINWOOD-HORNING CONCRETE COMPANY (<http://www.collinwood-horning.com>). The concrete mixes are designated as ODOT Class C (Ordinary pavement concrete of 4000 psi), High Strength (8000 psi) and Self-consolidating concrete (6000 psi). A list of concrete properties is shown in Table 1.

**Table 1. Concrete Mixes Used in the Experimental Program**

	ODOT Class C	High strength	Self-consolidating
Designed 28-day strength (psi)	4000	8000	6000
Slump (inch)	4	6	6
Designed Water-cement ratio	0.53	0.26	0.31
Accrual w-c ratio	0.648	0.552	0.33
Sand (lb)	1380	1140	1438
Gravel(lb)	1480	1660	#57 Limestone 738 #8 Limestone 783
Cement(lb)	Type 1-5 650	Type 2-3 665	648

Admixture(oz)	AE-260 4	AE-260 7 3500N 32 Super 84	Duraflux33 (SCC Admixture) 10
Water(lb)	76	102	240

Concrete specimens were prepared to determine the mechanical strength at different curing ages. Sufficient numbers of specimens were prepared to ensure at least three repetitive tests can be conducted for each test. All of these samples were kept in the curing room before they were subjected to different freezing processes. In TDR test, 7 specimens were monitored in each group of experiment; each subjected to different curing process. Among these, there were 4 different freezing process produced by placing the specimen into temperature controlled freezer at 1st, 2nd, 4th and 6th day of curing. The remaining 3 specimens are cured under normal curing conditions but with different types of TDR probe design, including a parallel strip design, a four-spike probe design and an insulated four-spike probe design. TDR sensor monitors the electrical conductivity ( $EC_b$ ) and dielectric constant ( $K_d$ ) of concrete specimens subjected to different curing processes. For each of these 7 specimens, thermal couples were used to monitor the temperature process (Figure 3b). The channel assignments are shown in Table 2.



FIG. 3. a) TDR sensor head with cable b) TDR sensor and thermocouple distribution

Table 2. Distribution of Monitoring Channels

TDR Channel No.	TDR sensor type	Sample	When was it frozen	Thermal couple No.
1	Parallel	4-inch	1 <sup>st</sup> day	5
5	Parallel	4-inch	2 <sup>nd</sup> day	2
3	Parallel	4-inch	w/o	3
4	Parallel	4-inch	4 <sup>th</sup> day	4
6	Parallel	4-inch	6 <sup>th</sup> day	6
7	Uninsulated spikes	6-inch	w/o	7
8	Insulated spikes	6-inch	w/o	8
				1 (Environment Temp)

The ultrasonic system includes a high power pulse generator, 1MHz ultrasonic transducers, and a PC-oscilloscope (Fig. 4). The high characteristic frequency ultrasonic transducer ensures a high resolution in determining the ultrasonic wave speed. They are coupled to the concrete specimens via water.



FIG. 4. Ultrasonic testing device and example photos of testing concrete specimen

In conjunction with ultrasonic test and TDR monitoring, the mechanical and physical properties of concrete subjected to different curing procedures are also measured. These are used to determine properties of concrete such as the compressive strength, ultrasonic wave speed and water content of each type of concrete (destructive oven dry method). The details of experiment plan are shown in Table 3. The mechanical and physical properties of virgin samples were tested every day from the beginning to the 7<sup>th</sup> day and then at 28<sup>th</sup> day. For the specimens subjected to freezing, the strength and water content at 3<sup>rd</sup> day, 7<sup>th</sup> day and 28<sup>th</sup> day are measured. The frozen specimens were first defrosted before being tested.

Table 3. Physical Properties Test Schedule of Different Type of Concrete

Sample	1	2	3	4	5	6	7	28
Virgin	*	*	*	*	*	*	*	*
1 <sup>st</sup> frozen			*				*	*
2 <sup>nd</sup> frozen			*				*	*
4 <sup>th</sup> frozen			*				*	*
6 <sup>th</sup> frozen			*				*	*

EXPERIMENT DATA ANALYSIS

Ultrasonic velocity - strength relationship for concrete with normal curing procedures

Figure 5 plots the strength of concrete versus ultrasonic wave velocity for concrete subjected to normal curing conditions. As seen from this plot, there are reasonably linear relationships between both factors. This confirms the observations in many existing literatures. Such relationship can be used to estimate the compressive strength of concrete from ultrasonic measurements.

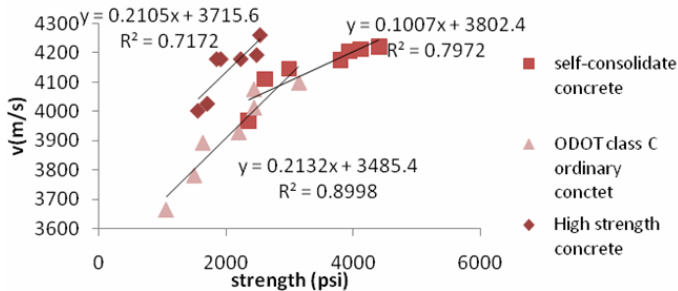
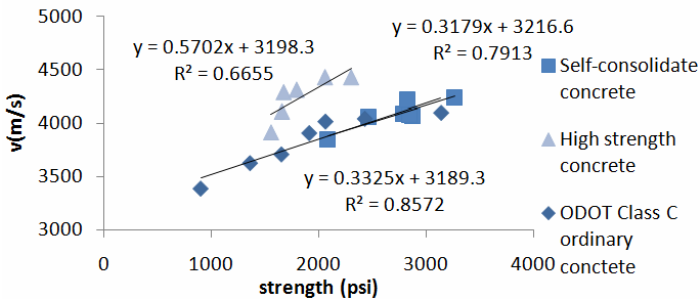


FIG. 5. Relationships between ultrasonic velocity and strength of concrete

**Ultrasonic velocity (after thaw) - strength (after-thaw) relationship for concrete subjected to freezing during the curing process**

In this experiment, concrete specimens were placed in freezer at different curing ages (1-day, 2-day, 3-day, 4-day, 5-day etc). At the end of the 7-th day, the specimens were taken out of the freezing room. Ultrasonic test and compression tests were then conducted on each specimen either in complete frozen status or in complete thaw status. The frozen status is ensured by compressing the specimens immediately after taken out from the freezer; the complete thaw is ensured by subject the specimens to rapid thawing procedures. Figure 6 shows the plots of ultrasonic wave velocity and strength relationship for concrete specimens that are completely thaw. This figure indicates there exist reasonably linear relationship between ultrasonic velocity (after thaw) and strength of concrete (after thaw) subjected to freezing during the curing process.



**FIG. 6. Relationships between ultrasonic velocity (after thaw) and strength of frozen concrete (after thaw)**

**Ultrasonic velocity (before thaw)- strength (before-thaw) relationship for concrete subjected to freezing during the curing process**

Figure 7 plots the ultrasonic velocity (before thaw) versus strength of frozen concrete specimens (either before thaw or after thaw). The large scattering in the data indicates there are no reliable relationships between the ultrasonic velocity (before thaw) and compressive strength for frozen concrete, whether it is frozen or complete thaw. This implies if NDT testing is conducted on concrete while it is frozen, the measured wave speed can not be used to reliably predict the strength of concrete.

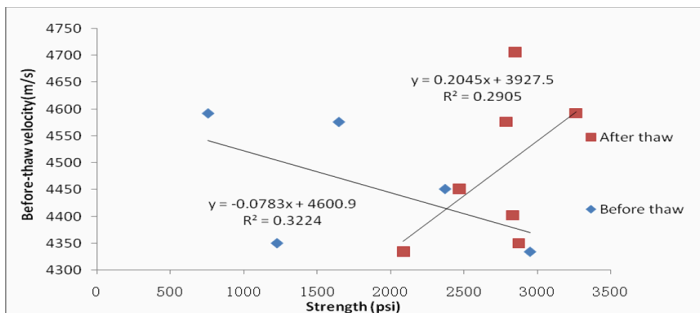


**FIG. 7. The ultrasonic wave velocity of frozen concrete versus strengths of concrete specimens**

The differences observed in Figs. 6 and 7 can be clearly seen from the trend of ultrasonic velocity and strength development in frozen concrete samples (Figs. 8 and 9). Fig. 8 shows the evolution of the strength of concrete (either before thaw or after thaw) with time. Fig. 9 shows the evolution of the ultrasonic velocity (either before thaw or after thaw) with time. The thaw concrete specimens show gradual increasing trend in both compressive strength and ultrasonic velocity. While those of frozen concrete show the opposite trend. This leads to what are observed in Figs. 6 and 7.

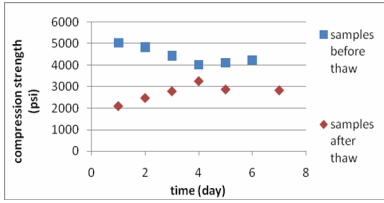


FIG. 8. Evolution of concrete strength with time

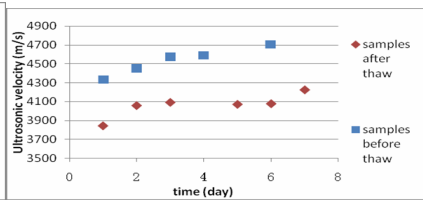


FIG. 9. Evolution of ultrasonic velocity with time

**Estimation of Frozen Concrete Strength**

Fig. 8 shows the frozen early stage concrete has higher strength than those completely thaw. A plot of the differences in the strength of concrete in the complete frozen or thaw conditions is plotted in Fig. 10. Also plotted on Fig. 10 is the evolution of free water content (or free ice content when completely frozen). It is interesting to notice that both curves show similar trends. Fig. 11 directly plots the free water content and the differences in the compressive strength of concrete in complete frozen or thaw status. There appear to exist high linear relationship between both quantities. The relationship between these quantities is probably due to the fact that when the free water in the sample freezes, the strength of ice contributes the bulk strength of frozen concrete specimens.

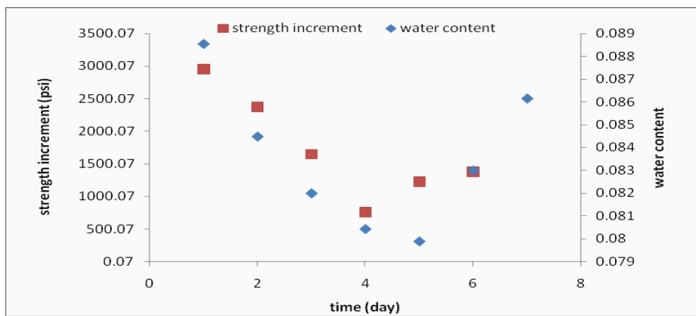
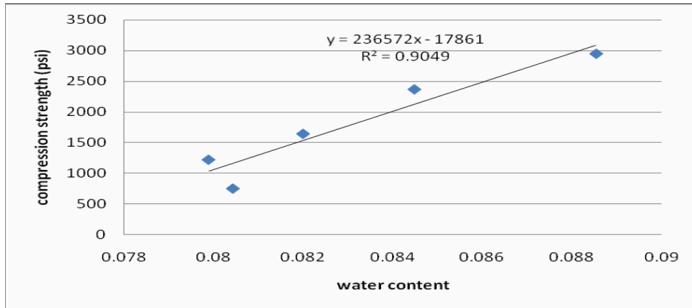


FIG. 10. Free water content and differences in strength of frozen and thaw concrete specimens



**FIG. 11. Difference strength versus free water content (i.e. ice content in completely frozen concrete)**

With the use of relationship such as shown in Fig. 11, an estimation of the strength of frozen concrete from seismic test can be performed in the following sequences:

- 1) Defreeze the concrete
- 2) Estimate the strength of thaw concrete from ultrasonic test (using relationship shown in Fig. 6)
- 3) Use free water content to determine the differences in the strength of concrete between complete frozen and complete thaw status (using relationship shown in Fig. 11)
- 4) Estimate the strength of frozen concrete by adding strength from steps 2) and 3).

A final issue to implement such a procedure is the estimation of the free water content in concrete. This can be achieved by use of NDT technology such as Time Domain Reflectometry (TDR). Previous research by the author shows TDR can be used to reliably estimate the free water content in curing concrete<sup>(15)</sup>. The combination of ultrasonic testing and TDR testing thus provides a way to estimate the strength of frozen concrete in the field. This information can be valuable for pavement open-road decisions in cold regions, where the Winter Load Increases is used to improve freight efficiency. The measured strength of frozen concrete can be incorporated to determine the magnitude of overload that can be allowed on pavements.

## CONCLUSION

The relationship between seismic wave velocity and strength is the basis for application of many NDT technologies based on seismic wave principles. Our experimental data shows while there exist good linear relationships between the compressive strength and the ultrasonic velocity, such relationship does not hold when the concrete is frozen. The strength of frozen concrete does not have direct correlations with ultrasonic wave velocity. The strength of frozen concrete, however, can be estimated from that of thaw concrete and a correction related to the amount of ice (free water). Combination of ultrasonic method and method for water content measurement (such as TDR) provides a nondestructive method to estimate the strength of curing concrete subjected to freezing procedures. This can potentially be used for implement Winter Load Increases in cold regions. More studies are needed to further validate and improve this technology.

## REFERENCE

- Boutin, C. and Amaud, L., "Mechanical characterization of heterogeneous materials during setting." *European Journal of Mechanics, A/Solids* 14 (4) (1995) 633-656.
- Reinhardt, H.-W., Grobe, C. and Herb, A., "Ultrasonic monitoring of setting and hardening of cement mortar - a new device." *Mater.Struet.* 33 (233) (2000) 580-583.
- Sayers, C.M. and Grenfell, R.L., "Ultrasonic propagation through hydrating cements: onset of shear wave propagation." *Ultrasonics* 31 (3)(1993) 147-153.
- D'Angelo, R., Plona, T.J., Schwartz, L.M. and Coveney, P., "Ultrasonic measurements on hydrating cement slurries." *Advanced Cement Based Materials* 2 (1) (1995) 8-14.
- Boumiz, A., Vernet, C. and Tenoudji, F.C., "Mechanical properties of cement pastes and mortars at early ages, evolution with time and degree of hydration." *Advanced Cement Based Materials* 3 (3/4) (1996) 94-106.
- Keating, J., Hannant, O.J. and Hibbert, A.P., "Correlation between cube strength, Ultrasonic pulse velocity and volume change for oil well cement slurries." *Cement and Concrete Research* 19 (5) (1989) 715-726.
- Pessiki, S.P. and Carino, N.J., "Setting time and strength of concrete using the impact-echo method." *ACI Materials Journal* 85 (5) (1988) 389-399.
- Minnesota Department of Transportation, 1996. Frost Resistivity Probe. User Guide
- Ruth L. Roberson and John Siekmeier, 2000. "Determining Frost Depth in Pavement System Using a Multi-Segment Time Domain Reflectometry Probe." *TRB Session*
- Klute et al, 1986. "Method of Soil Analysis: Physical and Mineralogical Methods." NO.9, Part 1. 2nd Edition.
- Topp, G. C., Davis, J. L., and Annan, A. P. (1980), "Electromagnetic Determination of Soil Water Content and Electrical Conductivity Measurement Using Time Domain Reflectometry." *Water Resources Research*, Vol. 16, pp. 574-582.
- Siddiqui, S.I., and Drnevich, V.P., (1995). "A New Method of Measuring Density and Moisture Content of Soil Using the Technique of Time Domain Reflectometry." *Report No.: FHWA/IN/JTRP-95/9*, Joint Transportation Research Program, Indiana Department of Transportation - Purdue University, February, 271 p.
- Drnevich, V.P., Siddiqui, S.I., Lovell, J., and Yi, Q. (2001). "Water Content And Density Of Soil Insitu by the Purdue TDR Method." *TDR 2001: Innovative Applications of TDR Technology*, Infrastructure Technology Institute, Northwestern University, Evanston, IL, September.
- Yu, X. and Drnevich, V.P. 2004. "Soil Water Content and Dry Density by Time Domain Reflectometry." *Journal of Geotechnical and Geoenvironmental Engineering*, ASCE, Vol. 130, No.9, September, pp 922-934.
- Yu, X., Drnevich, V. P. and Olek J., 2004, "Time Domain Reflectometry for Measuring Water-Cement-Ratio of Concrete." *the Proceedings of the 2004 International Symposium: Advances in Concrete through Science and Engineering*, Evanston , Illinois , March 21-24, 2004

## Measuring Dielectric Constant in Highly Conductive Soils Based on Surface Reflection Coefficients

Renpeng Chen<sup>1</sup>, Wei Xu<sup>2</sup>, Yunmin Chen<sup>3</sup> and Wei Chen<sup>4</sup>

<sup>1</sup>Professor, Key Laboratory of Soft Soil and Geoenvironmental Engineering of Ministry of Education, Department of Civil Engineering, Zhejiang University, 388 Yuhang tang Road, Hangzhou, 310058, China. chenrp@zju.edu.cn

<sup>2</sup>Key Laboratory of Soft Soil and Geoenvironmental Engineering, Ministry of Education, Hangzhou 310058, China. E-mail: xyczju@gmail.com

<sup>3</sup>Professor, Key Laboratory of Soft Soil and Geoenvironmental Engineering of Ministry of Education, Department of Civil Engineering, Zhejiang University, 388 Yuhang tang Road, Hangzhou, 310058, China. chenyunmin@zju.edu.cn

<sup>4</sup>Marster candidate, Key Laboratory of Soft Soil and Geoenvironmental Engineering, Ministry of Education, Hangzhou 310058, China. E-mail: chenweizju@126.com

**ABSTRACT:** Time domain reflectometry (TDR) fails in soils with high electrical conductivities, because the attenuation of the signal eliminates the reflection from the end of the probe. This paper describes a new approach for determining dielectric constants in highly conductive soils using TDR measurements. It makes use of information contained in the reflection at the soil surface rather than the reflection at the end of the probe. A relationship between the reflection coefficients at the soil surface with the apparent dielectric constant of the soil was established theoretically. The apparent dielectric constant of the soil can be estimated from the surface reflection coefficient. Results indicate that the dielectric constant can be determined with reasonable accuracy by the proposed approach for soils with high electrical conductivities, where the conventional travel time analysis fails due to significant signal attenuation.

## INTRODUCTION

Soil water content plays an important role for soil engineering property assessment and compaction quality control in geotechnical engineering. Time domain reflectometry (TDR) technology is becoming an established technology in civil engineering for soil moisture measurement (Benson and Bosscher, 1999; Siddiqui et al., 2000; Noborio, 2001; Yu and Drnecich, 2004a; ASTM D6780-05, 2005). The apparent dielectric constant ( $K_a$ ) and the bulk electrical conductivity ( $\sigma_{DC}$ ) are two basic electrical parameters of soil. TDR apparatus can measure the apparent dielectric constant and the electrical conductivity in the same specimen simultaneously, which in

turn can be used to estimate soil water content. Topp et al. (1980) established a relation between soil volumetric water content and soil apparent dielectric constant. However, geotechnical applications require the gravimetric water content. It relates to the volumetric water content by the dry density of the soil. Siddiqui and Drnevich (1995), Yu and Drnevich (2004a), and Yu and Drnevich (2004b) presented efforts to extend the application of TDR for measuring the gravimetric water content and the dry density of soils with the apparent dielectric constant and the electrical conductivity. An ASTM standard, designated ASTM D6780 (2005), describes the details of this method. Figure 1 shows the typical TDR system used in ASTM D6780. The apparent dielectric constant is based on the travel time of the electromagnetic wave traveling along the probe (coaxial cylinder in Fig. 1). The identification of the reflection at the probe end (point D in Fig. 2) is critical for the travel time analysis.

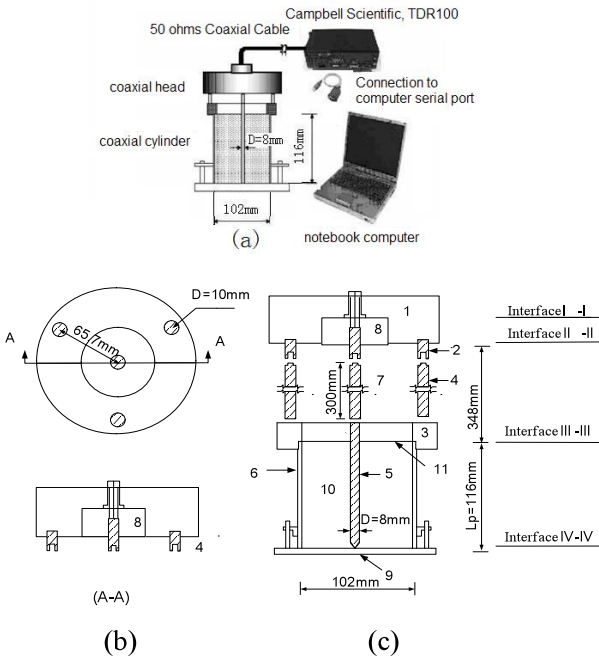


FIG. 1 TDR system used in ASTM D6780 and the probe with extended rods: (a) TDR system, (b) the configuration of the coaxial head, and (c) the configuration of the mold probe with extended rods.

Notes for figure: 1-stainless steel in the coaxial head, 2- studs, 3-stainless ring, 4-extended rods, 5-centre rod, 6-metal mold, 7-air gap, 8-Delrin as the insulating material in the coaxial head, 9-Delrin as the base of the mold, 10-soil or water in the mold, 11-soil or water surface.

It was observed that the travel time analysis is challenging when the tested soil with high electrical conductivity, which causes significant energy attenuation (Topp et al., 1980; Jone and Or, 2004; Chen et al., 2007). This makes it impossible to use the travel time analysis for highly conductive soils such as chemically modified soils, fat clays, and contaminated soils. This paper describes a new approach for determining the apparent dielectric constant from the TDR measurement in highly conductive soils. The new approach makes use of information in the reflection at the surface of the soil.

The apparent dielectric constant measured using the TDR technique is based on the travel time of the electromagnetic wave propagating along the probe. A TDR waveform for deionized water is plotted with solid line in Fig. 2(a). The point B is the start of the reflection at the soil surface. The point D is the reflection at the probe end. An equation is presented in Fig. 2(a) to show how to calculate  $K_a$ , from the travel time of the wave along the probe (time difference between points B and D),  $\Delta t$ , the length of the probe,  $L_p$ , and wave velocity in vacuum,  $c$ . Chen et al. (2007) stated that the small step C is the end of the reflection at the soil surface, and the difference of the reflection coefficient between B and C depends on the dielectric constant of the soil in the mold.

There is an air gap between the coaxial head and the mold (see Fig. 1). The length of the air gap (number 7 in Fig. 1(c)) has a significant impact on the position of the point B (Chen et al., 2007). When the length of the air gap is as short as 48 mm (typical length of the air gap in ASTM D6780 (2005)), the reflections at the coaxial head, the air gap, and the surface of the soil interfere with each other. The reflection at the soil surface could be overlapped with the reflection at the air gap. The longer air gap can separate the reflections at the air gap and the soil surface, then results in a flatter peak B. In this study, four studs in the coaxial head were extended with four 300 mm rods (number 7 in Fig. 1(c)). The extended rods were bolt joint with the studs in the coaxial head. A waveform for deionized water measured with the extended rods probe is plotted in dash-dotted line in Fig. 2(a). It is clear that the peak of the waveform becomes flatter, and the points C and D move up right. But, the time difference between the points B and D are the same.

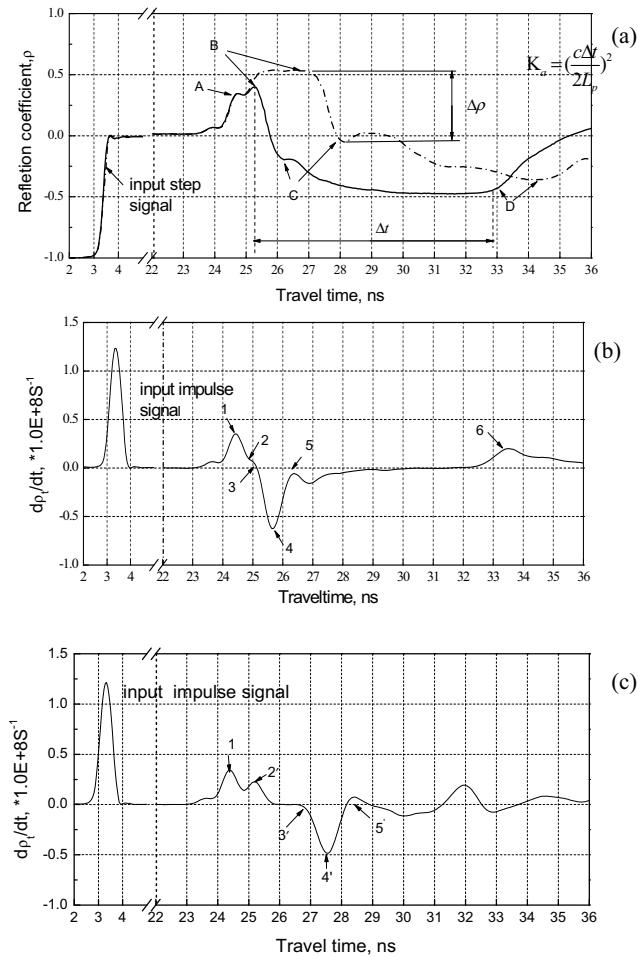


FIG. 2 TDR waveforms measured in deionized water using the probe with the extended rods (short air gap) and without the extended rods (long air gap): (a) TDR waveforms for short air gap (solid line) and long air gap (dash-dotted line), (b) the first derivatives of the TDR waveforms for short air gap, and (c) the first derivative of TDR waveforms measured in the same mold with an extended rods (long air gap).

## Reflection wave and transmission wave in coaxial cable

For the probe used in the study (as shown in Fig. 1(c)), there are four impedance-mismatch interfaces: interface I-I (between the cable and the coaxial head), interface II-II (between the coaxial cable and the air gap), interface III-III (between the air gap and the soil), and interface IV-IV (probe end). If we denote the characteristic impedance of the cable, the coaxial head, the air gap, and the mold as  $Z_b$ ,  $Z_h$ ,  $Z_a$ , and  $Z_m$ , the reflection coefficients at the interfaces ( $\rho_I$ ,  $\rho_{II}$ , and  $\rho_{III}$ ) and transmission coefficients at interfaces ( $\tau_I$ ,  $\tau_{II}$ , and  $\tau_{III}$ ) can be easily obtained.

The dielectric permittivity of soil can be expressed as:

$$K_{asc} = \left( \frac{Z_p}{Z_a} \right)^2 \left( \frac{1 - \rho_{III}}{1 + \rho_{III}} \right)^2 \quad (1)$$

where  $K_{asc}$  is relative dielectric permittivity calculated from the surface reflection coefficient  $\rho_{III}$ ;  $Z_p$  is the geometric impedance of the mold.

The wave phenomena in a TDR measurement include multiple reflections, dielectric dispersion, and attenuation due to the conductive loss and cable resistance (Lin 2003). Dielectric dispersion and attenuation slow down the rise time of the step voltage. Multiple reflections make the total reflection coefficient unequal to the true reflection coefficient at the interface.

We studied the multiple reflections in TDR system, and obtain:

$$\sqrt{K_{asc}} = k \left( \frac{\psi + \Delta\rho}{\psi - \Delta\rho} \right) \quad (2b)$$

$$\psi = (1 - \rho_{II}^2)(1 - \rho_{III}^2) \quad (2c)$$

in which  $k = \frac{Z_p}{Z_a}$  and  $\Delta\rho = \rho_{III} - \rho_{III} \cdot \rho_{II}$ ,  $\rho_{II}$ , and  $\rho_{III}$  is the total reflection coefficient at the time  $t_1$ ,  $t_2$ , and  $t_3$ . It can be found in TDR recorded waveforms (see Fig. 3).  $k$  and  $\psi$  are constants, which depend on the geometry and insulating material of the probe. Their values can be obtained from lab calibration.  $\Delta\rho$  depends on the dielectric constant of the material in the mold, as shown in Fig. 2. Equation (2b) suggests that if the probe constants  $k$  and  $\psi$  are obtained, the dielectric constant  $K_{asc}$  can be determined by the surface reflection coefficient. If the dielectric constants of the materials can be measured by travel time analysis,  $\psi$  can also be calibrated using Eq. (2b). Figure 4 shows the calibration curve of  $\psi$ . From calibration,  $\psi$  is 0.803.

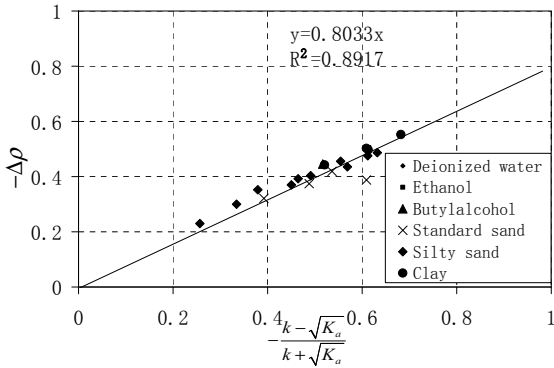


FIG. 4 Calibration of  $\psi$ .

**Dielectric constants  $K_{asc}$  and water content**

Soil samples of standard sand, silt sand, Xiaoshan clay, and Bentonite were used in the experiments. The waveforms for ethanol and butyl alcohol were also measured.

After the calibration of  $k$  and  $\psi$ , Eq. (2) can be used to estimate the dielectric constant  $K_{asc}$ . Figure 5 shows the comparison of  $K_{asc}$  estimated using Eq. (2b) for sands and water to the apparent dielectric constants  $K_a$  obtained by travel time analysis. The data lie within  $\pm 10\%$  of the 1:1 line. It indicates that the proposed approach of estimating  $K_{asc}$  provides satisfactory accuracy.

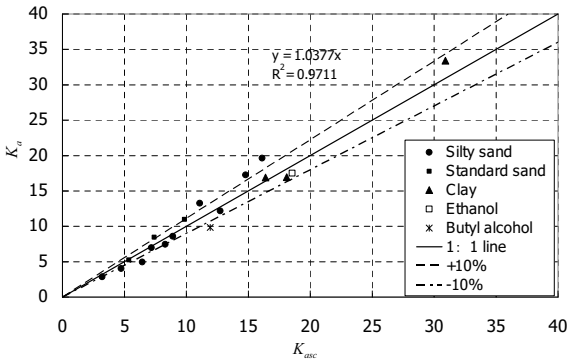


Fig. 5 Comparison of apparent dielectric constant ( $K_a$ ) by travel time analysis compared to the dielectric constant ( $K_{asc}$ ) from the surface reflection coefficient for sands and waters.

Moreover, the high electrical conductivities of clay and Bentonite make the measurements of the apparent dielectric constants difficult as the second reflection is indiscernible. The surface reflection coefficients methods still work satisfactory for situations where the conventional travel time analysis fails due to weak or non-existent second reflections. Note in Fig. 5 water contents calculated by use of  $K_{asc}$  are quite reasonable for situations where it was not possible to measure  $K_a$ . The developed new method appears to have an advantage over the conventional travel time analysis in that it can be applied to soils with high electrical conductivities where second reflections are weak or absent altogether.

## CONCLUSIONS

This paper presents an approach to estimate the apparent dielectric constant from the reflection at the surface of soils by using surface reflection coefficient obtained in time domain signal. This approach can be applied to contaminated soils, chemically modified soils and fat clays which have high electrical conductivities. An improved probe with extended rods is developed first compared to the convention probe in ASTM D6780. The probe with extended rods is used to identify and separate the reflections at the coaxial head and the surface of sample. The reflection of TDR signal at the soil surface is used to obtain the dielectric permittivity of soil by Eq. (2b). The approach was validated with the experimental data on salty water, sand soils, and clay. Major conclusions from this investigation include:

Calculate  $K_{asc}$  from reflection coefficient in time domain is a possible ways to find  $K_a$  from surface reflection. The total reflection coefficient was considered as being obtained from the sum of all the signals reaching the sampling oscilloscope from various successive reflections and transmissions at the line interfaces..The high electrical conductivities of clay and Bentonite make the measurements of the apparent dielectric constants difficult as the second reflection is indiscernible. The surface reflection coefficients methods still work satisfactory for situations where the conventional travel time analysis fails due to weak or non-existent second reflections.

## ACKNOWLEDGMENTS

The authors wish to thank National Basic Research Program of China (2007CB714001) and National Natural Science Foundation of China (research grant: 50425825, and 50538080) for financial support.

## REFERENCES

- ASTM (2005). D6780-05 "Standard Test Method for Water Content and Density of Soil in Place by Time Domain Reflectometry (TDR)." ASTM International.<sup>1</sup>
- Benson, C. H., and Bosscher, P. J. (1999). "Time-domain reflectometry (TDR) in geotechnics: a review." *ASTM Special Technical Publication*, 1350, 113-136.
- Campbell Scientific (2007). *TDR100 Instruction Manual*, Revision 04/07, Campbell Scientific Inc. Logan, Utah.
- Chen, R. P., Drnevich V. P., Yu, X., Robert L.N., and Chen, Y. M., (2007) Time Domain Reflectometry Surface Reflections for Dielectric Constant in Highly

- Conductive Soils. *Journal of Geotechnical and Geoenvironmental Engineering, ASCE*, **133**(12): 1597–1608.
- Jones, S. B. and Or, D. (2004). “Frequency domain analysis for extending time domain reflectometry water content measurement in highly saline soils.” *Soil Science Society of America Journal*, **68**(5), 1568-1577.
- Noborio, K. (2001). “Measurement of soil water content and electrical conductivity by time domain reflectometry: A review.” *Computers and Electronics in Agriculture*, **31**(3), 213-237.
- Siddiqui, S. I. and Drnevich, V. P. (1995). *Use of time domain reflectometry for the determination of water content and density of soil*. FHWA/IN/JHRP-95/9, Purdue University, West Lafayette.
- Siddiqui, S. I., Drnevich, V. P., and Deschamps, R. J. (2000). Time domain reflectometry development for use in geotechnical engineering. *Geotechnical Testing Journal*, **23**(1): 9–20.
- Topp, G. C., Davis, J. L., and Annan, A. P. (1980). “Electromagnetic determination of soil water content: Measurements in coaxial transmission lines.” *Water Resources Research*, **16**, 574-582.
- Yu, X. and Drnevich, V. P. (2004a). “Soil water content and dry density by time domain reflectometry.” *Journal of Geotechnical and Geoenvironmental Engineering*, **130** (9), 922-934.
- Yu, X. and Drnevich V. P. (2004b). “Time domain reflectometry for compaction control of stabilized soils.” *Transportation Research Record*, **1868**, 14-22.

## Comparison of Surface Wave Tests for Pavement System Thicknesses/Moduli

Larry D. Olson<sup>1</sup> M. ASCE, P.E and Patrick Miller<sup>2</sup>

<sup>1,2</sup>Principal Engineer and Project Engineer, Olson Engineering, Inc., 12401 W. 49<sup>th</sup> Avenue, Wheat Ridge, CO 80033-1927 USA; LDOLSON@OLSONENGINEERING.COM

**ABSTRACT:** This paper discusses the comparison of the shear wave velocity results for the concrete, lime treated base and subgrade pavement layers obtained from two separate surface wave test methods at a concrete pavement site. The older Spectral Analysis of Surface Waves (SASW) and newer Multiple Impact of Surface Waves (MISW) test methods were performed at the same concrete pavement forensic investigation project for comparison purposes. Neither the SASW nor MISW test methods require the installation of boreholes to measure the shear wave velocity and layer thickness profiles of asphalt or concrete pavements, and the underlying base and subgrade layers, thus reducing the costs of the tests. The older SASW and newer MISW methods differ only slightly from one another in the equipment used, method of data collection, but involve significantly different data processing. This paper includes a comparison and discussion of the surface wave test results, as well as backgrounds of the MISW and SASW methods. The MISW method is able to provide much more accurate determinations of layer thicknesses (within 4-5 mm for the pavement surfaced layer) and layer thicknesses/moduli for the underlying less stiff base and subgrade layers than the SASW method which greatly overestimates moduli of less stiff base materials immediately below the stiffer asphalt or concrete pavement.

## INTRODUCTION

As pavement design is increasingly being done with mechanistic-empirical design methods, there is an increasing need to measure Young's moduli in situ. This has been possible to do so during construction of each pavement layer using the Spectral Analysis of Surface Waves (SASW) method since its research and development by Dr. Kenneth H. Stokoe, II and his students at the University of Texas at Austin beginning in the late 1970's (Heisey, Stokoe and Meyer, 1982). There are a number of different surface waves methods that have been developed for pavement and geotechnical site investigations including the SASW, frequency wave number ( $f-k$ ) spectrum, multi-channel analysis of surface waves (MASW) and continuous surface waves (CSW). These methods are reviewed in detail along with other surface seismic and borehole seismic methods by Stokoe, Joh and Woods (2004).

Ryden and Lowe (2004) reported a study on guided waves in a layered half-space with large velocity contrasts where a decreasing velocity with depth is presented. They found by calculating multiple mode dispersion curves in the complex wave number domain and taking into consideration the attenuation caused by leakage into the underlying half-space, that they could better resolve the thicknesses and moduli of layered pavement systems with improved matching of the experimental and theoretical phase velocity vs. frequency dispersion curves. This method is called Multiple Impact Surface Waves (MISW) herein. In particular, the lower moduli base and subgrade layers are able to be much better resolved with the MISW approach versus the SASW and other surface wave approaches as reported in this paper for a concrete pavement case history. The test methods are described below along with a comparison of SASW and MISW results for a concrete pavement site.

### **SASW AND MISW SURFACE WAVES METHODS**

The SASW method uses the dispersive characteristics of surface waves to determine the variation of the surface wave velocity (stiffness) of layered systems with depth (Heisey, Stokoe and Meyer, 1982). Shear wave velocity profiles can be determined from the experimental dispersion curves (surface wave velocity versus wavelength) obtained from SASW measurements through a process called forward modeling (an iterative inversion process to match experimental and theoretical results). The SASW method can be performed on any material provided an accessible surface is available for receiver mounting and impacting.

The MISW test method utilizes many of the same principles and equations as the SASW method (Ryden and Lowe, 2004). The data collection of both methods is also similar. The differences between the two methods are predominantly in the data analysis. All of the data taken during MISW testing is analyzed together to create a dispersion image or phase velocity spectrum. As generally seen in the MISW phase velocity spectrum for pavements, the phase velocity increases as a function of frequency. This apparent increase in the dispersive trend at higher frequencies is built up by interference of higher modes of surface waves and it is reported that the data can be more accurately evaluated by taking this effect into account. This effect can be accounted for by modeling to match the dispersion image rather than the fundamental mode dispersion curve primarily analyzed in SASW.

### **Collection of SASW AND MISW Field Data**

In SASW tests, two receivers are placed on the surface, and a hammer is used to generate the acoustic energy (see Fig. 1). Short receiver spacings use accelerometers to sample the shallow layers while for long receiver spacings geophones are used in sampling the deep materials. The source and receiver signals were recorded by an Olson Instruments Freedom Data PC Spectral Analysis of Surface Waves System and stored for further analysis at the concrete pavement site. Two profiles, a forward profile and a reverse profile, are typically obtained in SASW measurements where the accessible surface is struck by a hammer on two opposite sides of the receivers.

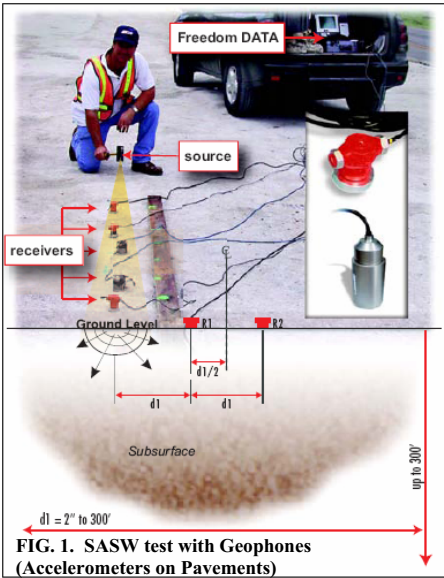


FIG. 1. SASW test with Geophones (Accelerometers on Pavements)

The MISW method is illustrated in Fig. 2 and data was taken with the same instrumentation system. In MISW tests the generated surface waves were measured with a seismic accelerometer fixed at zero offset. Hammer impacts were generated from 0.20 to 5.00 m offset in 0.20 m increments. All recorded signals were then compiled to make an equivalent multichannel record which can be transformed to a phase velocity spectrum similar to the MASW transformation technique (Park et al., 1998).

**SASW and MISW Theoretical Modeling Data Processing**

For both SASW and MISW, in order to determine the shear wave velocity profile from the "apparent" velocities of the dispersion curve, analytical modeling is necessary.

The analytical modeling used herein is a forward modeling process that is iterative and involves assuming a shear wave velocity profile and constructing a theoretical dispersion curve or dispersion image. The experimental (field) and theoretical curves are compared, and the assumed theoretical shear wave velocity profile is adjusted until the two curves or images match.

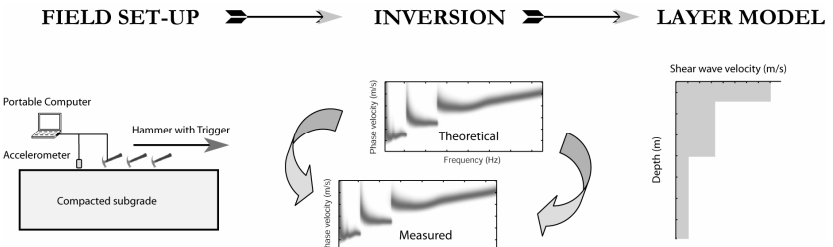
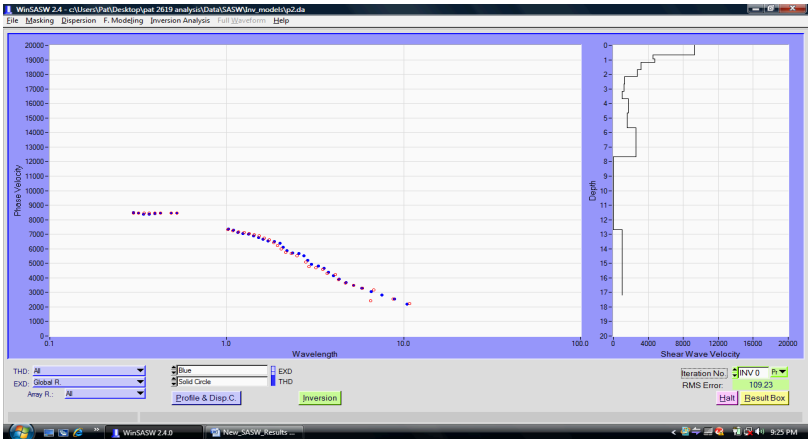


FIG. 2. MISW Data Acquisition, Processing and Shear Wave Velocity Profile

For SASW modeling the interactive computer software WINSASW for both 2-dimensional and 3-dimensional analyses have been developed by Dr. Sung Ho Joh during his Ph.D. research at the University of Texas at Austin to compute a theoretical dispersion curve based upon an assumed shear wave velocity and layer thickness profile. These algorithms have produced reasonable accuracy when comparing velocities determined with the SASW and seismic crosshole methods on soil sites. A

SASW result with a good match between the measured and experimental data and the resulting shear wave velocity profile is presented in Fig. 3 for a concrete pavement.

**FIG. 3.** SASW dispersion curve plot for Concrete Pavement Site (velocity vs. wavelength on left with good match of experimental data – open circles and theoretical match – solid circles) and Theoretical Shear Wave Velocity vs. Depth-right



For MISW modeling, a program developed by Dr. Nils Ryden (Ryden et al 2004) was used for data collection, analysis, and theoretical modeling. The modeling program iteratively adjusts multiple parameters in order to match the experimental dispersion velocity spectrum image. This technique and analysis algorithms have been shown to accurately determine the layer thicknesses and moduli of pavement and soil systems. A MISW result from the same concrete pavement site as tested with the SASW method is presented in Fig. 4 below. The surface wave data is plotted in the left plot as impact point offset from the accelerometer receiver versus time while the phase velocity spectrum of the experimental data is plotted as normalized and not normalized in the two right hand plots. The matching of the experimental phase velocity spectrum with the theoretical phase velocity spectrum is presented in Fig. 5 with the top plot being the measured phase velocity spectrum, the second plot being the best fit theoretical velocity spectrum and the third plot comparing the mismatch between the experimental and theoretical results. The bottom plot on the left is the shear wave velocity profile versus depth while the layer data in terms of thicknesses, shear and compressional wave velocities and Poisson's ratios are summarized in the lower right. Finally, the direct comparison of the theoretically best fit shear wave velocity profiles is presented in Fig. 6. Review of this figure indicates that the SASW method predicted significantly higher shear wave velocity profiles for the lime treated base below the concrete than the MISW method.

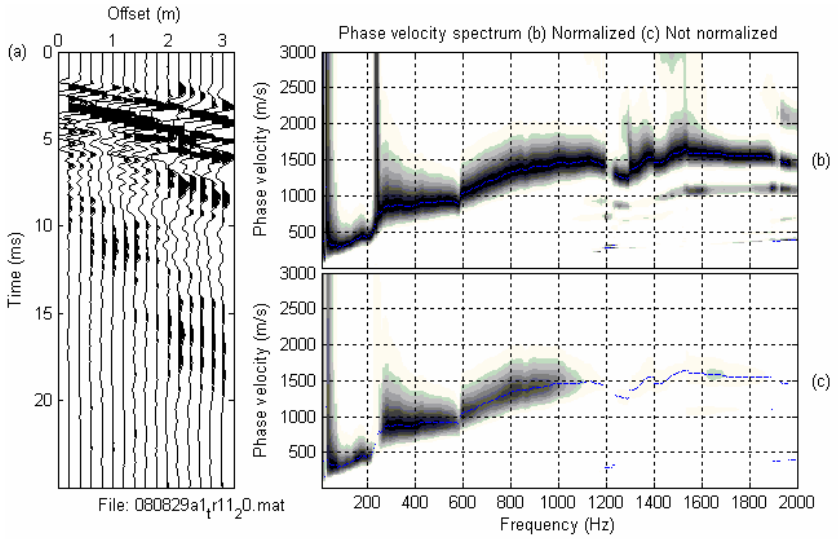


**FIG. 4.** Example MISW results from Concrete Pavement Site with time domain data in left plot and Phase Velocity Spectrum in right plots.

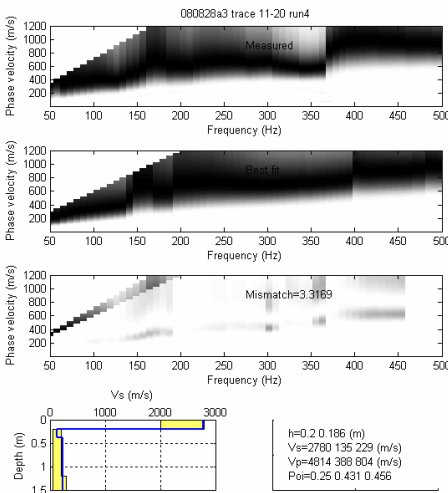
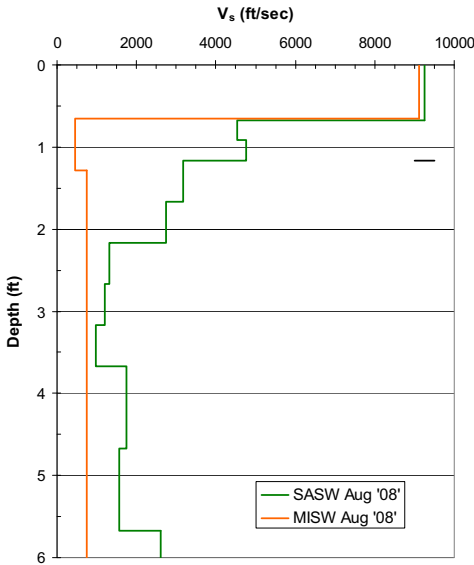


**FIG. 5.** MISW Matching of Phase Velocity Spectrum for Experimental (top) and Theoretical Best-fit (2<sup>nd</sup> plot), and Mismatch (3<sup>rd</sup> plot) with MISW Theoretical Shear Wave Velocity Profile vs. Depth (left-bottom) and Layer Information (right-bottom)

Further examination of Fig. 6 indicates that the shear wave velocity of the lime-treated subgrade was quite high below the concrete in the SASW results (~4500 ft/s or 1500 m/s). However, the MISW results predicted a much slower velocity (500 ft/s or 150 m/s). Unconfined compressive strength tests on samples of the lime-treated base revealed comparatively low strengths at the pavement site. This finding is in agreement with the MISW results as the lime-treated subgrade was found to have similar strengths to the underlying natural clayey subgrade soils that had not been treated.



**CONCLUSIONS**

The case history illustrates the improved accuracy of the MISW methods over the SASW method to accurately measure the shear wave velocity profile versus depth for the difficult case of softer base materials below rigid pavements. The MISW method has similar advantages for asphalt pavements and can also measure asphalt and concrete thicknesses accurately to within 4 to 5 mm. The MISW method can thus be used to determine shear wave velocity profiles from which Young’s moduli and layer thicknesses can be accurately calculated for use in mechanistic-empirical pavement design. The MISW method can be

applied for Quality Assurance/Quality Control (QA/QC) purposes to each layer of a pavement system during construction directly to provide accurate layer thickness and moduli data. In pavement rehabilitation projects, MISW can be used to measure asphalt/concrete moduli and thicknesses as well as the thicknesses and moduli of the underlying base, subbase and subgrade layers of pavement systems. It is also used for seismic shear wave velocity tests of soil/rock.

**REFERENCES**

Heisey, J. S., Stokoe II, K. H., and Meyer, A. H. (1982), “Moduli of pavement systems from spectral analysis of surface waves,” Transportation Research Record No. 852, pp. 22–31.

Ryden, N., and Lowe, M. (2004), “Guided wave propagation in three-layer pavement structures”, *Journal of the Acoustical Society of America*, Vol. 116(5), pp. 2902-2913.

Park, C. B., Miller, R. D., and Xia, J. (1998), “Imaging dispersion curves of surface waves on multi-channel record”, Kansas Geological Survey, 68th Ann. Internat. Mtg. Soc. Expl.Geophys., Expanded Abstracts, pp. 1377-1380.

Stokoe II, K.H., Joh, S.H., Woods, R.D. (2006), “Some Contributions on In Situ Geophysical Measurements to Solving Geotechnical Engineering Problems,” 2<sup>nd</sup> International Conference on SiteCharacterization, Porto, Portugal.

## **Solving the Problems of Differential Settlement of Pavement Structures in the Bangkok Area**

Titi Paveenchana<sup>1</sup> and Manoon Arayasiri<sup>2</sup>

<sup>1</sup> Principal Geotechnical Engineer, Seven Engineering Consultants Co., Ltd., Thailand  
tpaveenchana@yahoo.com, mail@sevenconsultants.com

<sup>2</sup> Principal Geotechnical Engineer, Thai Engineering Consultants Co., Ltd., Thailand  
arayasiri\_m@yahoo.com, tec@tec.co.th

**ABSTRACT:** The Bangkok Area is underlain by 12 to 16 m deep soft compressible clay. Pavements on embankments 1.5 – 2.5 m high commonly undergo a total settlement of 500 - 1 000 mm in 10 years. This causes significant differential settlement problems between the bridge approach embankment and bridge structure founded on long piles with bases in the sand layers. Significant longitudinal or cross-sectional differential settlements of the roadway may also take place due to ground conditions. Stability and settlement are always associated problems on soft ground. Solutions that have been implemented in the past three decades include the use of preload embankments, light weight materials, concrete bearing units on precast piles, preloading with prefabricated vertical drains (PVD), and soil-cement columns. Case histories of investigation and analysis of the soil mechanics problems and design solutions by state-of-the-art methods are presented in this paper.

### **Geotechnical Conditions**

The Bangkok area lies in the southern part of the Chao Phraya river deltaic flood plain. The soil profile through this area from west to east is shown in Fig. 1. The depth of the dark grey soft and compressible Recent marine clay is generally 12 – 16 m. The typical properties of the soft Bangkok clay are summarized in Table 1. Beneath the soft clay is Pleistocene stiff to very stiff clay. It is underlain by the first Bangkok sand layer which begins at 19 – 27 m depth and is 2 – 10 m thick. An interval of hard clay 10 – 20 m thick lies above the second Bangkok sand layer. Alternate strata of clay, sand and gravel are found further down to depths varying from 600 to more than 1 000 m before reaching the bed rock.

### **Differential Settlement Problems**

Pavements in the Bangkok area are typically constructed on embankments with a total height (including pavement) of 1.5 to 2.5 m, and exert pressures of 35 to 55 kPa on the ground surface. This commonly causes a total settlement of 500 to 1 000 mm in 10 years. Bridges and viaducts in this area are founded on 20 to 50 m long piles with bases in the sand layers. Without any ground improvement, a sudden drop in elevation will take place at the joint of the approach embankment with bridge structure. This also happens at pavement approaches to buildings, at intersections or

interfaces with drainage and utility culverts, etc. When a road lies over ponds, canals, ditches, etc., significant longitudinal or cross-sectional differential settlements may take place. Stability problem is always associated with settlement problem on such a soft ground as that covering the Bangkok area.

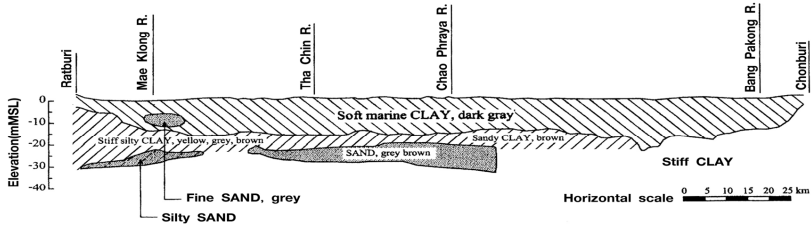


Fig. 1. Soil Profile of the Chao Phraya River Deltaic Plain

Table 1. Typical Properties of the Soft Bangkok Clay at the Suvarnabhumi Airport (after Moh and Associates et al 1995)

Depth (m)	Soil Profile	Unit Weight $\gamma_t$ (kN/m <sup>3</sup> )	Coefficient of Consolidation $c_v$ and $c_d$ (m <sup>2</sup> /day)	Void Ratio $e_c$	Compression Curve										Undrained Modulus $E_u$ (kPa)	$S_u$ (kPa)
					Settlement Strain, $\epsilon$ (%) and Consolidation Pressure, $P'$ (kPa)											
0-1	Weathered Clay	16.2	0.011	2.45	$\epsilon$ (%)	0.00	1.31	1.70	2.11	2.54	3.00	3.92	4.97	2 500	14.0	
					$P'$ (kPa)	3.1	25.0	35.0	45.0	55.0	65.0	85.0	110			
1-7	Very Soft Clay	14.4	0.0018	3.30	$\epsilon$ (%)	0.00	1.66	4.26	7.19	10.11	12.92	20.96	26.68	1 000	11.0	
					$P'$ (kPa)	26.7	35.0	45.0	55.0	65.0	75.0	110.0	150.0			
7-11	Soft Clay	15.8	0.0043	2.61	$\epsilon$ (%)	0.00	0.92	2.07	3.36	4.78	6.25	8.47	11.48	1 800	20.0	
					$P'$ (kPa)	45.4	55.0	65.0	75.0	85.0	95.0	110.0	130.0			
11-15	Soft to Medium Clay	16.3	0.0035	1.80	$\epsilon$ (%)	0.00	0.87	1.94	3.10	4.80	7.14	9.36	13.35	4 200	26.0	
					$P'$ (kPa)	66.6	75.0	85.0	95.0	110.0	130.0	150.0	190.0			

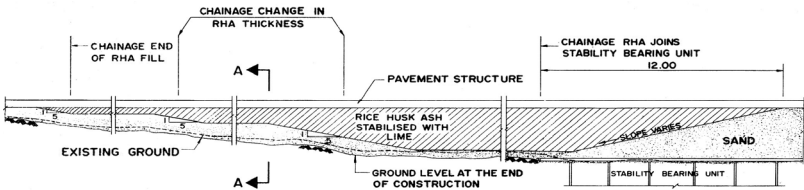
**Solutions**

The objectives are mainly to maintain the minimum requirements of safe sight distance in the design life of the roadway as the vertical curve of its alignment changes with settlement, of the cross-slope of the road surface for safe driving and adequate surface runoff, and of safe and smooth transition between pavements on ground and structures.

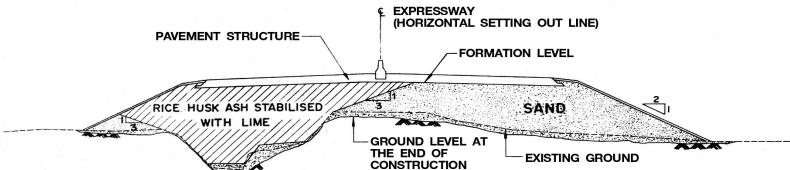
Fig. 2 shows the solution to the above mentioned problem for the design of the First Stage Expressway System in Bangkok in 1977. A *light weight embankment material*, rice husk ash with a compacted unit weight of about 12 kN/m<sup>3</sup>, was used both to alleviate the longitudinal (Fig. 2 (a1)) and cross sectional differential settlements (Fig. 2 (a2)) as well as to improve the embankment stability.

At the approaches to bridge structures founded on long piles, *bearing units* consisting of concrete slabs supported by gradually shorter precast piles were constructed (Fig. 2 (b)). The surface loading including embankment, pavement and traffic loads was transferred to greater depths in the soft compressible clay, thus reducing the amount of settlement. The rows of piles immediately next to the bridge structure reached down to the stiff clay. The pile tips gradually rose up to the very soft clay layer where the bearing unit joined with the rice husk ash embankment as shown in Fig. 2 (a1). Settlement of friction piles in compressible soils would vary

with the length and the distance between piles, and this is the basis of the compensated friction pile foundation method presented by Zeevaert (1973) used for the design of the bearing units. Bearing units were also used to solve the stability problem as seen in Fig. 2(c).

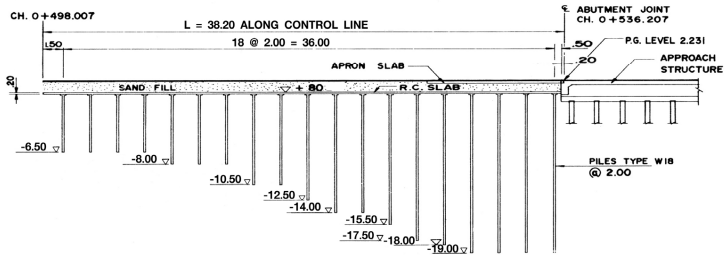


a1) Alleviate Longitudinal Differential Settlement and Improve Embankment Stability

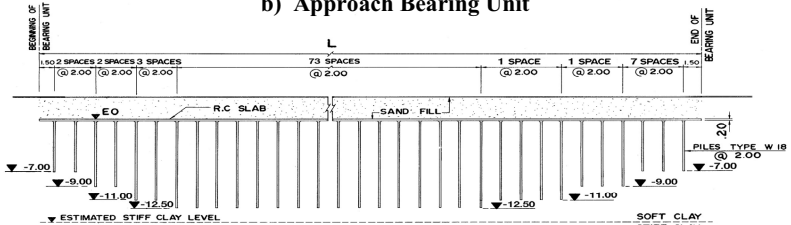


a2) Alleviate Cross Sectional Differential Settlement

a) Typical Rice Husk Ash Fill



b) Approach Bearing Unit



c) Stability Bearing Unit

Fig. 2. Facilities for Solving the Problem of Differential Settlement of Pavement Structures along the Bang Na - Port Section of the First Stage Expressway System in Bangkok (after Freeman Fox & Partners)

Preconsolidation with *preload* embankment has been practiced in Thailand including the expressway project described above. The Suvarnabhumi airport has adopted *preloading with prefabricated vertical drain (PVD)* as the method for ground improvement of the runways, taxiways, and landside roads. PVD is a prefabricated flexible flat band drain consisting of a permeable core and outer filter jacket. Under the preload embankment, the ground water dissipates from the clay stratum horizontally into and then vertically upward through the PVD. The dissipated water enters a sub-drain system consisting of perforated hoses installed within a sand blanket, with pumping wells installed at intervals in the preload areas and at side trenches.

The settlement under the preconsolidation system consists of immediate, primary consolidation and secondary compression settlement. For the landside roads, Moh and Associates et al (1995) analyzed the rate of primary consolidation by vertical pore water flow by the classical Terzaghi theory, and the rate of consolidation by horizontal flow into band-shaped drains by the method modified by Hansbo (1979). They obtained the design parameters by performing back analysis from the full scale embankment tests with PVD carried out by the Asian Institute of Technology. Together with the results of other investigations in the airport area, design soil parameters were adjusted (Table 1), resulting in computed total settlements which were within 5% difference from the monitored results. The stability of the preload embankment was analyzed by means of the simplified Bishop procedure. Stage loading, with which the soft underlying clay can gain an increase in strength through the consolidation process under each level of preloading was designed for the construction of the preload embankment.

Moh and Associates performed trial analyses for various factors including PVD spacing, PVD depth, and height of preload embankment. The effect of embankment width, and the construction schedule were also taken into consideration. Fig. 3 shows the results of analysis for preload embankments nominally 2.0 – 4.5 m high. The design criterion of the rate of settlement of the embankment, for assuring the effectiveness of ground improvement, was less than 5 mm per month (excluding land subsidence) before the construction of the pavement. It can be seen that for preloading to take place until the settlement rate meets this criterion the preload period may take up to 320 – 450 days. In practice, it was specified that the preload embankment should be removed when the preload period was greater than 180 days and the settlement was less than 30 mm in 30 days. The design minimum factor of safety of the embankment during and after ground improvement was 1.2. The cross-section of the typical design preload embankment is presented in Fig. 4.

A more rapid method of ground improvement than that of preload with PVD is *soil-cement columns*. They are constructed by deep soil mixing with either cement slurry or dry cement powder. The settlement is reduced by the mechanism of load transfer to greater depths in the soft compressible clay in the same way as the bearing units on piles. The total settlement of a soil-cement column includes column shortening and consolidation settlement. For the at-grade roads at the Suvarnabhumi airport, MAA Consultants et al (2003) analyzed the consolidation settlement by means of the conventional equivalent raft foundation method. The resulting estimate was 40 – 90 mm under embankments 1.0 – 1.8 m high for cement columns 10 - 14 m

long. The column shortening which occurred during filling was estimated to be 30 – 70 mm. The design adopted a soil-cement column under cement stabilized aggregate mat system as shown in Fig. 5. Its stability was analyzed in terms of the column capacity; and flexural strength, punching and bearing capacity of the column/mat system. The slope stability was also analyzed.

**Regional Land Subsidence**

The Bangkok area has been undergoing regional land subsidence due to deep well pumping. In the past 50 years, the piezometric pressure has declined from the hydrostatic state to almost zero at 20 m below ground surface before it resumes the hydrostatic trend. Moh and Associates et al (1995) reported 20-60 mm/year subsidence in the vicinity of the Suvarnabhumi airport. Since the deep subsoil strata in the Bangkok area contribute to 50-70% total subsidence (Nguyen Anc Duc 1999),

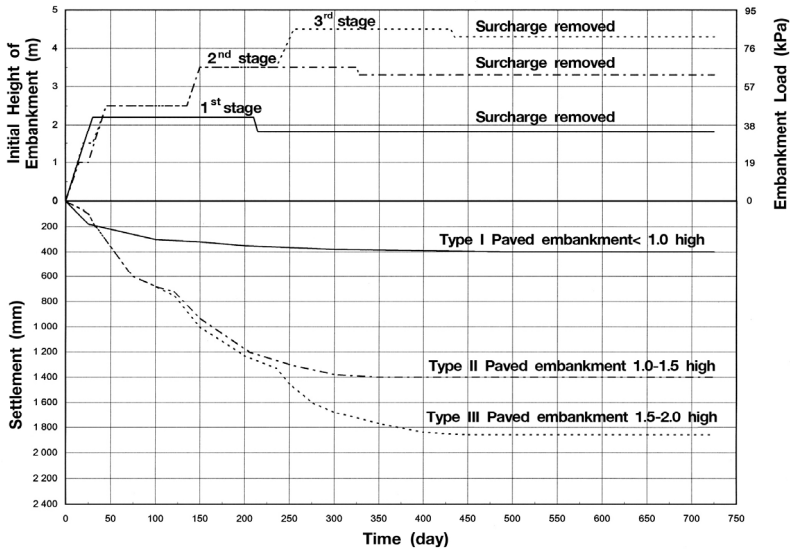


**Fig. 3. Load – Settlement Relationship at Base Center of Preload Embankment with PVD (after Moh and Associates et al 1995)**

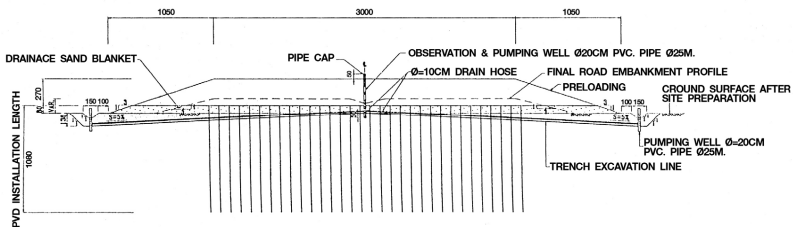


**Fig. 4 . Cross Section of Typical Preloading Embankment with PVD (after Moh and Associates et al 1995)**

this will be a cause of significant differential settlement between paved embankments and structures founded on long piles based in the deep soil layers even after soft ground improvement.

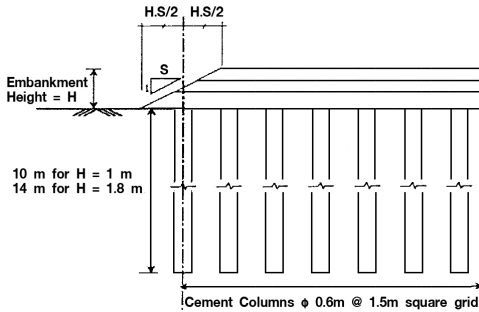


**Fig. 5. Typical Cross Section of Embankment with Soil Cement Columns**  
(after MAA Consultants et al 2003)

## CONCLUSIONS

Engineering solutions to the problems of differential settlement of pavement structures by state-of-the-art methods have been carried out in the Bangkok area for at least thirty years. In the early days, the methods included preloading, light weight embankment materials, and concrete bearing units on precast piles. In the last decade, preloading with prefabricated vertical drains (PVD) and soil-cement columns have been employed.

## REFERENCES

- Freeman Fox & Partners and Thai Engineering Consultants Co., Ltd. (1977). "Contract drawings, Bang Na – Port Section, First Stage Expressway System in Bangkok." *Expressway and Rapid Transit Authority of Thailand*, Bangkok.
- Hansbo, S. (1979). "Consolidation of clays by band-shaped prefabricated drains." *Ground Engineering*, v. 1, no. 5, pp. 16 – 25.
- MAA Consultants Co., Ltd. and Seven Associated Consultants Co., Ltd. (2003). "Final design report, At-Grade Frontage Roads to the Passenger Terminal Complex", Second Bangkok International Airport (Suvannabhumi Airport), TRA2-FR-01. *New Bangkok International Airport Co., Ltd.*, Bangkok.
- Moh and Associates, Inc., MAA Consultants Co., Ltd., National Engineering Consultants Co., Ltd., and Prasat Consultant Co., Ltd. (1995). "Final report on ground improvement" and "Specifications on ground improvement", Landside Road System, Second Bangkok International Airport, LR2-FR-01/1/D. *Airports Authority of Thailand*, Bangkok, v. 1.
- Nguyen Anh Duc (1999). "Updating and analysis of Bangkok land subsidence caused by deep well pumping with emphasis on shallow soil settlement." *Thesis, Asian Institute of Technology*. Bangkok.
- Zeevaert, L. (1973). "Foundation engineering for difficult subsoil conditions." *Van Nostrand Reinhold Company*, New York.

## Contribution of loamy soil treatment to improve embankments performance

Régis De Bel<sup>1</sup>, Antonio Gomes Correia<sup>2</sup> and Jean-Claude Verbrugge<sup>3</sup>

<sup>1</sup> Belgian Road Research Center, Sterrebeek, Belgium, [r.debel@brrc.be](mailto:r.debel@brrc.be)

<sup>2</sup> University of Minho, Guimarães, Portugal, [agc@civil.uminho.pt](mailto:agc@civil.uminho.pt)

<sup>3</sup> Université Libre de Bruxelles, Bruxelles & Gembloux Agronomical University, Gembloux, Belgium, [jverbrug@ulb.ac.be](mailto:jverbrug@ulb.ac.be) & [verbrugge.jc@fsagx.ac.be](mailto:verbrugge.jc@fsagx.ac.be)

**ABSTRACT:** This paper shows for a loamy soil the benefits of lime treatment on the evolution of the geomechanical properties governing the slope stability and the resistance against erosion of embankments. The main results indicate that the effective internal friction angle ( $\phi$ ) is quite unchanged through time, while the effective cohesion ( $c'$ ) strongly increases. Furthermore, erosion tests using the LCPC erodimeter on slopes between 0 and 30 degrees, and for a curing time up to 112 days, have shown that the treated soil becomes insensitive to erosion after a few days. These results clearly establish the benefits of lime treatment in safety and serviceability of embankments for highways and high speed trains and, consequently, have an important impact on the reduction of their life cycle costs.

## INTRODUCTION

Lime treatment of fine soils is a common practice in many countries to reuse very wet or soft soils as embankments or capping layers among others. After adding the lime, two mechanisms develop: an instantaneous granulation referred to as soil improvement and a long term development of pozzolanic reactions inducing soil stabilization.

In European practice, only improvement of soil properties is usually expected to increase workability and to assist compaction during earthworks; long term effects of lime treated soils being generally not taken into account in the design. However, even mixing rather low amounts of lime with soil induces pozzolanic reactions that may continue throughout years, resulting in a continuous increase of strength (Little 1995, Cabane 2004, Bollens & al. 2005, De Bel 2006, De Bel & al. 2007). Neglecting this evolution after improvement has a direct impact on costs of earthworks, mainly for slope stability and erosion.

In this study saturated isotropically consolidated undrained (ICU) triaxial tests have been performed after different curing times on a loamy soil treated with 0, 1.5, 3 and 4.5% quicklime. Because of a lack of space, only the results for 3% lime are presented, as they correspond to the minimal lime content to reach, in the Eades and

Grim test (Eades and Grim 1960), a pH value of 12.4 required by the pozzolanic reactions. The soil-lime mixtures were prepared by dry mixing of air dried soil and lime prior to add the water. Each treated soil sample was statically compacted at 98.5% of its standard Proctor maximum dry density and at the corresponding optimum water content. Curing process was carried out in a controlled temperature room at 20°C up to 448 days.

The erosion tests were performed in the LCPC erodimeter for 3 curing times and 3 slopes.

## MATERIALS

### Soil

Silt sampled in Marche-les-Dames, near the city of Namur in Belgium has been chosen to be representative of those mostly encountered in Belgium but also in neighbouring countries. The main identification and SPO values are summarized (De Bel 2006) as follow: natural moisture content (w): 22%; particles size material distribution: 98% finer than 80  $\mu\text{m}$  and 16% clay (<2  $\mu\text{m}$ ); organic matter (through DCO method): 0.2%; unit weight of solid particles ( $\gamma_s$ ): 27.18 kN/m<sup>3</sup>; Atterberg limits (NF P 94-051): liquid limit ( $w_L$ ): 31%, plasticity index ( $I_p$ ): 11%; Methyl Blue Value (VBS) according to NF P 94-068 : 1.8 g/100g; classification according to the French standard NF P 11-300 : A1; optimum values of the standard Proctor (SPO) test measured according to French standard NF P 94-093 are  $\gamma_{\text{max}} = 18.09 \text{ kN/m}^3$  and  $w_{\text{opt}} = 15.1\%$ .

### Lime

The tests were performed using a quicklime CL 90 Q according to EN 459-1, normally used for soil stabilisation in earthworks. The main properties here presented, were determined, (with several exceptions mentioned under brackets), according to the EN 459-2 standard. It largely fulfils all the requirements of Belgian and European standards: refuse on sieves: 0,02% and 17% respectively for 2mm and 80 $\mu\text{m}$ ; available lime content : 91.2% (>90% - according to EN 459); reactivity to water :  $t_{60} = 2,17$  minutes (< 10 minutes - NBN B13-204 / < 25 minutes EN 459-2).

### Treated soil

Consistency limits and compaction characteristics of the treated soil are: Atterberg limits: liquid limit ( $w_L$ ): 31%; plasticity index ( $I_p$ ): 8 %; optimum values of the standard Proctor (SPO)  $\gamma_{\text{max}} = 17.6 \text{ kN/m}^3$  and  $w_{\text{opt}} = 17.1\%$ .

## EXPERIMENTAL RESULTS

### Shear strength parameters

Isotropically consolidated undrained (ICU) triaxial tests, with measurement of pore

water pressure on saturated samples were performed for the determination of the effective values for the ultimate shear parameters, cohesion ( $c'$ ) and internal friction angle ( $\phi'$ ). Their evolution is shown in Figure 1 for curing times up to 448 days. It shows an immediate increase of strength parameters as already presented by various authors for UCS tests (Verhasselt 1978, 1990, Little 1995, Cabane 2004, Bollens & Verbrugge 2005). The increase of cohesion is much more important than the internal friction angle; this last seeming less modified. Furthermore, the evolution is not monotonic with time but occurs at varying rate, as put in evidence for the cohesion by the plateau followed by a significant increase. The trend of these results is in accordance with the results on UCS tests and the statement of Estéoule & Perret (1979) and Perret (1979) that the pozzolanic reactions between lime and clay particles develop along 2 or 3 successive processes depending on the curing temperature.

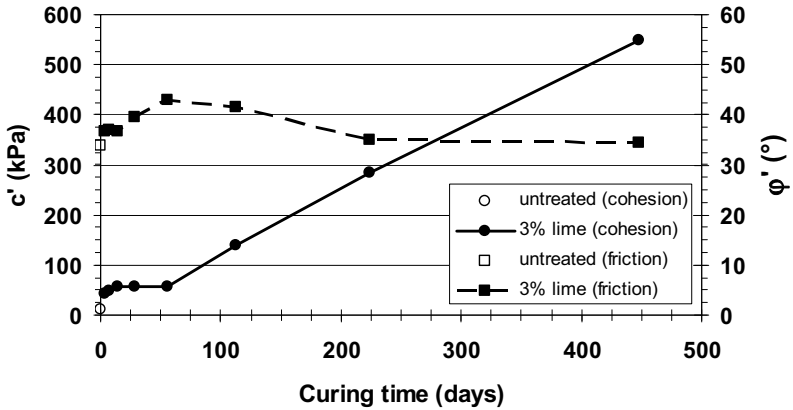


FIG. 1. Evolution of shear parameters with curing time.

Thus long-term strength gain is important as the cohesion is almost ten times higher after one year curing time than directly after mixing. Also experiences have underscored that the strength resistance keeps rising up to 448 days and probably even more. For the sample at this last curing time, the strength was so high that a rock triaxial testing device was used instead of the classical soil triaxial. It is obvious that because of the influence of cohesion in slope stability, this long-term strength gain should be taken into account in the simulation design of embankments.

### Erosion

In addition to the triaxial tests, erosion tests using a LCPC-erodimeter (Henensal & al. 1990) have also been performed.

In addition to the natural soil, three curing times have been chosen for the tests: 1, 14 and 112 days. This corresponds roughly to the immediate influence of treatment, during the works and at the end of them. As slopes are mainly concerned by erosion,

tests were performed at three angles of slope: 0, 15 and 30°. The tests have been performed on samples directly compacted in the moulds fitted for the erosion testing device (D = 15.2 cm and h = 6 cm) at the same density and water content as those of the triaxial tests.

During each test, losses of materials have been measured after 2 minutes erosion by water jets at a pressure of 2 bars in the LCPC erodimeter. This corresponds to a heavy rain for the Belgian climate (intensity 15 to 20 mm/hour; drops diameter = 1.5 mm, falling speed of drops = 5m/sec) (Juanos Cabanas 2007). The mean values of the results on sets of 3 samples are shown on Figure 2. These results clearly establish the beneficial effects of the lime treatment even after one day. This is important at the early ages of the embankment slope when no vegetation has yet developed on it. After 2 weeks, it may be considered that the erosion has no more effect on the slope.

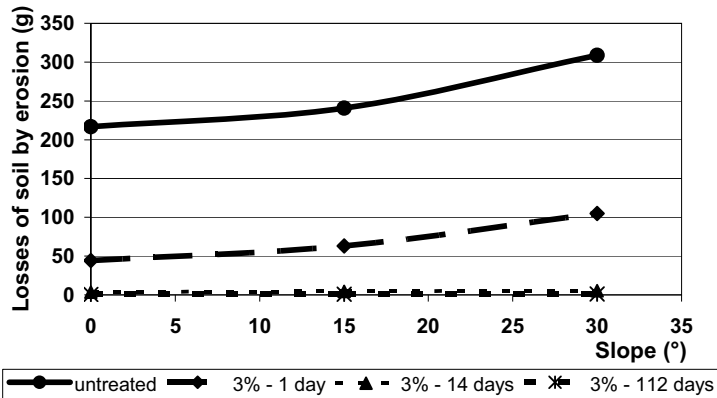


FIG. 2. Influence of curing time and slope in losses of untreated soil versus treatment.

**EMBANKMENT MODELLING**

Some design simulations have been carried out in order to compare a conventional solution with natural soil to lime-treatment. The strength parameters used ( $c'$  and  $\phi$ ) are those of figure 1. This academic case of study considers a homogeneous embankment of 15 m height without ground water (Figure 3). The slope was calculated with the parameters of the untreated soil to give a safety factor of 1.5.

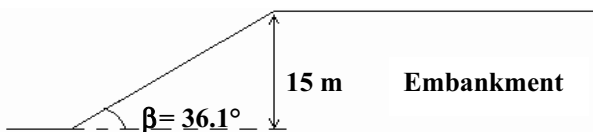
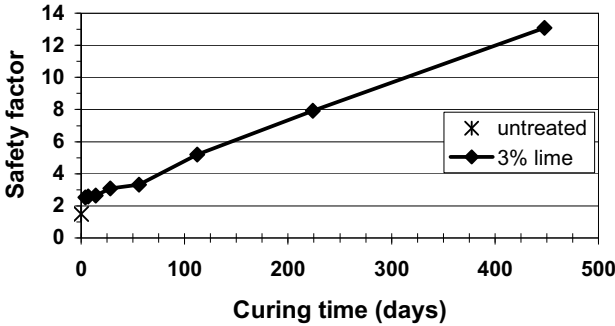


FIG. 3. Schematic representation of the simulated embankment.

Figure 4 shows the evolution of the safety factor with curing time for the embankment for the cases of untreated and treated soil.



**FIG. 4. Evolution of the safety factor with curing time of untreated and treated soil.**

## DISCUSSION – CONCLUSIONS

The very beneficial effect of lime treatment is clearly put in evidence in Figure 4, even early after construction, as for instance 4 days curing time where the safety factor rises from 1.5 for the untreated soil to 2.5 for the treated soil. This evolution grows on with time and values close to 4 and 10 are reached respectively after 3 months and one year. These delays, corresponding roughly to the construction period and the first months of service, are indeed very short considering the total lifetime of the embankment. Thus, using lime to increase workability and to assist compaction during earthworks, but neglecting the subsequent evolution for the design gives way to a money loss. Of course, these considerations are made from a pure academic case and other factors (type of soil, frost, cycles of wetting-drying,) have to be taken into account before to allow for a final conclusion. Nevertheless, these results show on one hand that even at usual dosages (3% quicklime) used for soil improvement, a durable increase of the mechanical properties may be expected. On the other hand, the increase of the cohesion induces an immediate positive influence of lime treatment against erosion which becomes negligible after only a few days. This is a good mean of protection against erosion in order to keep the slope integrity, mainly during the construction and immediately after, when no vegetation has yet developed.

The conclusion of this paper is that the initial over-cost of the lime-treatment can be counterbalanced by other advantages related to the durability of the earthwork which can be demonstrated by a proper life cycle costs analysis.

## ACKNOWLEDGMENTS

The results presented in this paper are issued from the COGESTAC project supported by the European Social Fund (FSE) and the General Directorate for

Technology, Research and Energy (DGTRE) of the Ministry of Walloon Region in Belgium. The industrial partner of this research is LHOIST R&D. The authors acknowledge strongly all these contributors.

## REFERENCES

- Bollens Q., Verbrugge J.C. (2005) "Time dependant evolution of the shear strength of a silty soil treated with lime", Paper n° C008, *Proceedings International Symposium on Treatment and Recycling of Materials for Transport Infrastructures (TREM TI)*, Association Mondiale de la Route (PIARC), Paris
- Cabane N. (2006) "Sols traités à la chaux et aux liants hydrauliques : Contribution à l'identification et à l'analyse des éléments perturbateurs de la stabilisation". *PhD thesis* - Ecole Supérieure Nationale des Mines de Saint-Etienne (France)
- De Bel R., Bollens Q., Duvigneaud P.H., Verbrugge J.C. (2005) "Influence of curing time, percolation and temperature on the compressive strength of a loam treated with lime", Paper n° C022, *Proceedings International Symposium on Treatment and Recycling of Materials for Transport Infrastructures (TREM TI)*, Association Mondiale de la Route (PIARC), Paris
- De Bel R. (2006) "Etude des sols traités à la chaux, à l'échelle microscopique et à l'échelle macroscopique" *DEA thesis*, Université Libre de Bruxelles
- De Bel R., Bollens Q., Gomes Correia A., Duvigneaud P.H., Verbrugge J.C (2007) "Time and temperature dependency of the geomechanical properties of silty soils treated with lime", *Proc. Int. Conf. on Advance Characterization of Pavment and Soil Materials*, Athènes, Taylor & Francis / Balkema, Vol 1, pp 513-521
- Eades J.L., Grim R.E. (1960) "A quick test to determine lime requirements for soil stabilisation", *Highway Research Record N°139*
- Estéoule J., Perret P. (1979) "Etude expérimentale des phénomènes de stabilisation des sols fins par la chaux" *Bull. Liaison Laboratoires des Ponts et Chaussées*, n° 99, pp 99-109
- Henensal P., Duchatel F. (1990) "L'érodimètre à jets mobiles" *Bull. Liaison Laboratoires des Ponts et Chaussées*, n°167, pp 47-52
- Juanos Cabanas C. (2007) "Etude de l'érodabilité des sols traités à la chaux", *Master thesis*, Université Libre de Bruxelles
- Little D. (1995) "Stabilization of pavement subgrade and base courses with lime" *Kendall/Hunt Publishing Compagny*, Dubuque, Iowa, USA, 219p.
- Perret P. (1979) "Application pratique des nouvelles données expérimentales relatives à la stabilisation des sols fins par la chaux" *Bull. Liaison Laboratoires des Ponts et Chaussées*, n° 99, pp 110-118
- Verhasselt A. (1978-a) "Stabilisation à la chaux (Traitement des sols cohésifs humides par la chaux - I)", *Rapport de Recherche n° 176/VA/1978*, Centre de Recherches Routières (CRR), Bruxelles, Belgique
- Verhasselt A. (1978-b) "Stabilisation à la chaux (Traitement des sols cohésifs humides par la chaux - II)" *Rapport de Recherche n° 177/VA/1978*, Centre de Recherches Routières (CRR), Bruxelles, Belgique.

*This page intentionally left blank*

# Author Index

Page number refers to the first page of paper

- Ali, Liaqat, 86  
Ali, Sarfraz, 86  
Arayasiri, Manoon, 180
- Bhandari, Anil, 47  
Bilyeu, John, 116  
Bulut, Rifat, 1
- Cao, Xue-shan, 33  
Chao, Sao-Jeng, 40  
Chen, Can, 138  
Chen, Dar-Hao, 116  
Chen, Guoyuan, 60  
Chen, Jian-Feng, 68  
Chen, Liangbiao, 13  
Chen, Renpeng, 166  
Chen, Tung-Tsan, 92  
Chen, Wei, 7, 166  
Chen, Yunmin, 166  
Cheng, Yingying, 109  
Correia, Antonio Gomes, 186
- De Bel, Régis, 186  
Deng, An, 78
- Farhad Eftekharzadeh, S., 53  
Fei, Chen, 109  
Feng, Jin-Rong, 78
- Gao, Yan-xi, 129  
Ge, Louis, 150
- Han, Jie, 47, 68  
Hewitt, John W., 144  
Hsu, Yao T., 92  
Huo, Yuan-Yuan, 99
- Li, Liang, 99
- Li, Lin, 13  
Li, Xia, 129  
Liu, Jinyuan, 123  
Liu, Yan, 156
- Mabirizi, Daniel, 1  
Maqbool, Ammar, 86  
Miao, Kun, 99  
Miller, Patrick, 174  
Mustapha Rahmaninezhad, S., 53
- Olson, Larry D., 174
- Paveenchana, Titi, 180  
Pluta, Sarah E., 144
- Qiu, Tong, 7
- Shahaboddin Yasrobi, S., 53  
Stephenson, Richard W., 150
- Tang, Xue-song, 26  
Tao, Mingjiang, 20  
Tumay, Mehmet T., 20
- Verbrugge, Jean-Claude, 186
- Wang, Chun-Yuan, 92  
Wang, Fang, 109  
Wang, Fei, 47  
Weidinger, David M., 150  
Wimsatt, Andrew, 116
- Xu, Wei, 166
- Yan, Xiao-Qiang, 26  
Yang, Xiao-Li, 99  
Yin, Zong-ze, 33

Yu, Song-Bo, 68  
Yu, Xinbao, 156  
Yu, Xiong (Bill), 156

Zeng, Ming-hua, 26  
Zhang, Bin, 156

Zhang, Jie, 138  
Zhang, Xiong, 13  
Zhang, Zhongjie, 20  
Zhao, Bing, 26  
Zheng, Ying-ren, 26

# Subject Index

Page number refers to the first page of paper

- Algorithms, 99
- Alignment, 99
- Arches, 47
- Assessments, 138
  
- Bridges, highway, 60
  
- Centrifuge models, 68
- China, 33, 109
- Clays, 13
- Coefficients, 166
- Cohesive soils, 20
- Comparative studies, 1
- Concrete, 129, 156
- Constitutive models, 13
- Construction industry, 92
  
- Damage, 26
- Differential settlement, 180
- Dynamic response, 68
  
- Ecology, 92
- Embankments, 47, 68, 186
- Energy, 20, 26
  
- Fills, 78
- Filters, 1
- Footings, 123
  
- Geogrids, 60
- Geomaterials, 78
- Geosynthetics, 40, 47, 53
- Geotechnical engineering, 123
- Gradients, 26
- Granular materials, 78
  
- Highway and road construction, 109
- Highway and road design, 99
  
- Highway and road structures, 116
- Hydraulic conductivity, 7
- Hydraulics, 13
  
- In situ tests, 86
  
- Laboratory tests, 60
- Landfills, 86
- Lime, 186
- Load bearing capacity, 40
  
- Measurement, 1, 123, 144, 166
- Mechanical properties, 156
- Moisture, 138
- Monte Carlo method, 7
  
- Nondestructive tests, 144, 156
- Numerical models, 68
  
- Optimization, 53, 99
  
- Pavement design, 174
- Pavements, 138, 180
- Permeability, 33
- Piles, 47
- Pore water, 1
- Probability, 7
- Problem solving, 180
  
- Radar, 116, 129
- Reinforcement, 40, 53, 60
- Research, 60
  
- Safety, 116
- Sand, 53, 78
- Shallow foundations, 40, 53
- Shear tests, 86
- Shear waves, 174

- Slope stability, 109
- Soil compaction, 20, 150
- Soil compression, 7
- Soil conditions, 166
- Soil consolidation, 7, 33
- Soil deformation, 123
- Soil properties, 144, 166
- Soil stabilization, 40, 53
- Soil structures, 47
- Soil suction, 1
- Soil treatment, 186
- Soil water, 144, 166
- Solid wastes, 86
- Stochastic processes, 7
- Surface waves, 174
- Sustainable development, 92, 109
- Swelling, 20
- Thailand, 180
- Thermodynamics, 26
- Tires, 78
- Tunnel linings, 129
- Ultrasonic methods, 150, 156
- Unsaturated soils, 1, 13, 33
- Velocity, 150, 174
- Voids, 116